N°d'ordre NNT : 2023ISAL0103

THESE de DOCTORAT DE L'INSA LYON, membre de l'UNIVERSITE DE LYON

délivré en partenariat international avec
Politecnico di Torino

Ecole Doctorale N° 034
ED Matériaux de Lyon

Spécialité / discipline de doctorat :
Matériaux

Soutenue publiquement le 01/12/2023, par :
Valentina Cavallo

Tailoring intermolecular interactions in methacrylate-based copolymers and nanocomposites: Effect on molecular dynamics and thermal properties

Devant le jury composé de :

LACABANNE, Colette	Professeure	Université Toulouse 3	Examinatrice
HERNANDEZ SANTANA, Marianella	Professeure	Instituto de Ciencia y Tecnología de Polímeros	Rapporteuse
LO RE, Giada	Professeure	Chalmers University of Technology	Rapporteuse
PRUVOST, Sébastien	Professeur	INSA Lyon	Directeur de thèse
GERARD, Jean-François	Professeur	INSA Lyon	Co-directeur de thèse
FINA, Alberto	Professeur	Politecnico di Torino	Co-directeur de thèse

INSTITUT NATIONAL DES SCIENCES APPLIQUÉES LYON

Département de la Formation par la Recherche et des Études Doctorales **(FEDORA)**

Bâtiment INSA direction, 1er étage
37, av. J. Capelle
69621 Villeurbanne Cédex
fedora@insa-lyon.fr

Référence : TH1033_CAVALLO Valentina

L'INSA Lyon a mis en place une procédure de contrôle systématique via un outil de détection de similitudes (logiciel Compilatio). Après le dépôt du manuscrit de thèse, celui-ci est analysé par l'outil. Pour tout taux de similarité supérieur à 10%, le manuscritest vérifié par l'équipe de FEDORA. Il s'agit notamment d'exclure les auto-citations, à condition qu'elles soient correctement référencées avec citation expresse dans le manuscrit.

Par ce document, il est attesté que ce manuscrit, dans la forme communiquée par la personne doctorante à l'INSA Lyon, satisfait aux exigences de l'Etablissement concernant le taux maximal de similitude admissible.

Département FEDORA – INSA Lyon - Ecoles Doctorales

SIGLE	ECOLE DOCTORALE	NOM ET COORDONNEES DU RESPONSABLE
CHIMIE	**CHIMIE DE LYON** **https://www.edchimie-lyon.fr** Sec. : Renée EL MELHEM Bât. Blaise PASCAL, 3e étage secretariat@edchimie-lyon.fr	**M. Stéphane DANIELE** C2P2-CPE LYON-UMR 5265 Bâtiment F308, BP 2077 43 Boulevard du 11 novembre 1918 69616 Villeurbanne **directeur@edchimie-lyon.fr**
E.E.A.	**ÉLECTRONIQUE, ÉLECTROTECHNIQUE, AUTOMATIQUE** **https://edeea.universite-lyon.fr** Sec. : Stéphanie CAUVIN Bâtiment Direction INSA Lyon Tél : 04.72.43.71.70 secretariat.edeea@insa-lyon.fr	**M. Philippe DELACHARTRE** INSA LYON Laboratoire CREATIS Bâtiment Blaise Pascal, 7 avenue Jean Capelle 69621 Villeurbanne CEDEX Tél : 04.72.43.88.63 **philippe.delachartre@insa-lyon.fr**
E2M2	**ÉVOLUTION, ÉCOSYSTÈME, MICROBIOLOGIE, MODÉLISATION** **http://e2m2.universite-lyon.fr** Sec. : Bénédicte LANZA Bât. Atrium, UCB Lyon 1 Tél : 04.72.44.83.62 secretariat.e2m2@univ-lyon1.fr	**Mme Sandrine CHARLES** Université Claude Bernard Lyon 1 UFR Biosciences Bâtiment Mendel 43, boulevard du 11 Novembre 1918 69622 Villeurbanne CEDEX **sandrine.charles@univ-lyon1.fr**
EDISS	**INTERDISCIPLINAIRE SCIENCES-SANTÉ** **http://ediss.universite-lyon.fr** Sec. : Bénédicte LANZA Bât. Atrium, UCB Lyon 1 Tél : 04.72.44.83.62 secretariat.ediss@univ-lyon1.fr	**Mme Sylvie RICARD-BLUM** Institut de Chimie et Biochimie Moléculaires et Supramoléculaires (ICBMS) - UMR 5246 CNRS - Université Lyon 1 Bâtiment Raulin - 2ème étage Nord 43 Boulevard du 11 novembre 1918 69622 Villeurbanne Cedex Tél : +33(0)4 72 44 82 32 **sylvie.ricard-blum@univ-lyon1.fr**
INFOMATHS	**INFORMATIQUE ET MATHÉMATIQUES** **http://edinfomaths.universite-lyon.fr** Sec. : Renée EL MELHEM Bât. Blaise PASCAL, 3e étage Tél : 04.72.43.80.46 infomaths@univ-lyon1.fr	**M. Hamamache KHEDDOUCI** Université Claude Bernard Lyon 1 Bât. Nautibus 43, Boulevard du 11 novembre 1918 69 622 Villeurbanne Cedex France Tél : 04.72.44.83.69 **hamamache.kheddouci@univ-lyon1.fr**
Matériaux	**MATÉRIAUX DE LYON** **http://ed34.universite-lyon.fr** Sec. : Yann DE ORDENANA Tél : 04.72.18.62.44 yann.de-ordenana@ec-lyon.fr	**M. Stéphane BENAYOUN** Ecole Centrale de Lyon Laboratoire LTDS 36 avenue Guy de Collongue 69134 Ecully CEDEX Tél : 04.72.18.64.37 **stephane.benayoun@ec-lyon.fr**
MEGA	**MÉCANIQUE, ÉNERGÉTIQUE, GÉNIE CIVIL, ACOUSTIQUE** **http://edmega.universite-lyon.fr** Sec. : Stéphanie CAUVIN Tél : 04.72.43.71.70 Bâtiment Direction INSA Lyon mega@insa-lyon.fr	**M. Jocelyn BONJOUR** INSA Lyon Laboratoire CETHIL Bâtiment Sadi-Carnot 9, rue de la Physique 69621 Villeurbanne CEDEX **jocelyn.bonjour@insa-lyon.fr**
ScSo	**ScSo*** **https://edsciencessociales.universite-lyon.fr** Sec. : Mélina FAVETON INSA : J.Y. TOUSSAINT Tél : 04.78.69.77.79 melina.faveton@univ-lyon2.fr	**M. Bruno MILLY** Université Lumière Lyon 2 86 Rue Pasteur 69365 Lyon CEDEX 07 **bruno.milly@univ-lyon2.fr**

Abstract

A correlation between the strength of the intermolecular interactions and physical properties has been reported for amorphous polymers. In particular, an increment of thermal conductivity has been associated to the addition of stronger interactions compared with weak van der Walls, *i.e.* hydrogen and ionic bonds. In this work, an attempt to tailor thermal conductivity in amorphous polymers has been made by engineering intermolecular interactions.

Poly(methylmethacrylate) PMMA was used as standard and poly(methylmethacrylate-*co*-methacrylic acid) (PMMA-*co*-MAA) copolymers were synthesised by free radical copolymerization in order to introduce inter-chain hydrogen bonds and, after neutralisation, ionic bonds. Copolymers were successfully obtained up to 30wt% of MAA and characterized. Also, different comonomers were used to evaluate the influence of a flexible unit bringing H-bonds, 2-hydroxyethylmethacrylate (HEMA) or 2-carboxyethylacrylate (CEA). Thermal conductivity slightly increased increasing MAA and HEMA content, while for CEA copolymers the presence of defects prevented the measurement.

Later, PMMA-*co*-MAA was used as a matrix for cellulose-based nanocomposites to tailor filler compatibility, thanks to the presence of H-bonds between MAA unit and cellulose surface. Cellulose nanofibers (CNF) up to 15wt% were efficiently dispersed by solvent casting in a mixture of two solvents (tetrahydrofuran/methanol). Thermal conduction showed no significant changes following the introduction of CNF.

Dynamic mechanical analysis (DMA) and broadband dielectric spectroscopy (BDS) were used in combination to fully characterize the macromolecular mobility of PMMA-*co*-MAA following the introduction of inter-chain H-bonds and the subsequent addition of CNF. An additional β'-relaxation, characterized by an activation energy (E_a) nearly four times higher than the $E_a(\beta)$, was found for the nanocomposites and ascribed to the establishment of H-bonds between the -COOH

groups of the matrix and the hydroxyl groups of CNF, as confirmed by the lower values found for the thermal expansion coefficient of the free volume and the fragility of the material. A deeper investigation about the α-relaxation was able to reveal the influence of CNF confirming the presence of interfacial H-bonds. Indeed, despite the similar glass transition temperatures characterising the matrix and the nanocomposites, a shift of their relaxation times to higher temperatures was observed following the addition of CNF.

Results reported in this thesis evidenced that the enhancements of thermal conductivity obtainable by the modification of the interchain interactions between chains in amorphous matrices remains an extremely complex challenge.

French summary

Une corrélation entre l'intensité et la nature des interactions intermoléculaires et les propriétés physiques, comme la conductivité thermique, a été rapportée pour des polymères amorphes. En particulier, une augmentation de la conductivité thermique a été associée à l'ajout d'interactions plus fortes par rapport aux liaisons de Van der Walls faibles, c'est-à-dire des liaisons hydrogène et ioniques. Dans ce travail, une tentative d'adapter la conductivité thermique dans les polymères amorphes a été réalisée par ingénierie des interactions intermoléculaires.

Le poly(méthylméthacrylate) PMMA a été utilisé comme modèle et des copolymères poly(méthylméthacrylate-*co*-acide méthacrylique) (PMMA-*co*-MAA) ont été synthétisés par copolymérisation radicalaire afin d'introduire des liaisons H inter-chaînes et, après neutralisation, des liaisons ioniques. Des copolymères ont été obtenus avec succès jusqu'à 30 % en poids de MAA et caractérisés. Différents comonomères ont été utilisés pour évaluer l'influence d'une unité flexible apportant des liaisons H, le 2-hydroxyéthylméthacrylate (HEMA) ou le 2-carboxyéthylacrylate (CEA). La conductivité thermique a légèrement augmenté en augmentant la teneur en MAA et HEMA, tandis que pour les copolymères CEA, la présence de défauts a empêché la mesure. Le copolymère PMMA-*co*-MAA a été utilisé comme matrice pour les nanocomposites à base de cellulose afin d'adapter la compatibilité des charges, grâce à la présence de liaisons H entre l'unité MAA et la surface de la cellulose. Des nanofibres de cellulose (CNF) jusqu'à 15 % en poids ont été efficacement dispersées par coulée de solvant dans un mélange de deux solvants (tétrahydrofurane/méthanol). La conduction thermique n'a montré aucun changement significatif après l'introduction des CNF. L'analyse mécanique dynamique (DMA) et la spectroscopie diélectrique à large bande (BDS) ont été utilisées en combinaison pour caractériser pleinement la dynamique

moléculaire du PMMA-*co*-MAA copolymère suite à l'introduction de liaisons H inter-chaînes et à l'ajout ultérieur de CNF. Une relaxation β' supplémentaire, caractérisée par une énergie d'activation (E_a) presque quatre fois plus élevé que le $E_a(\beta)$, a été trouvée pour les nanocomposites et attribuée à l'établissement de liaisons H entre les groupes -COOH de la matrice et les groupes hydroxyles du CNF, comme confirmé par les valeurs inférieures trouvées pour le coefficient de dilatation thermique du volume libre et la fragilité du matériau. Ainsi, une étude plus approfondie de la relaxation α a permis de révéler l'influence du CNF confirmant la présence de liaisons H interfaciales. En effet, malgré les températures de transition vitreuse similaires caractérisant la matrice et les nanocomposites, un décalage de leurs temps de relaxation vers des températures plus élevées a été observé suite à l'ajout de CNF.

Les résultats rapportés dans cette thèse ont mis en évidence que les améliorations de la conductivité thermique obtenues par la modification des interactions entre les chaînes dans les matrices amorphes restent un défi extrêmement complexe.

Acknowledgment

First and foremost, I want to profoundly thank my supervisors, Prof. Sébastien Pruvost, Prof. Alberto Fina and Prof. Jean-François Gerard, for the amazing work they have done mentoring me during the last three years. Their guidance not only has been essential for the development of this work, but also for the evolution of my professional profile as researcher as a result of numerous scientific discussions. Nonetheless, they took a great care of me as a human being supportive during the tough moments that this project has brought me through, for this, I would never be grateful enough.

I would like to thank Prof. Colette Lacabanne, Prof. Giada Lo Re and Prof. Marianella Hernández Santana for their contributions as committee members.

Next, thanks to Stine and Laura, the ones who firstly guided me to discover and enjoy the universe of scientific research. They inspired my curiosity for this mysterious world and if it was not for them I would probably not being here writing this manuscript.

Thanks also to Aurélien Roggero for his precious and kind help in developing my knowledge about dielectric spectroscopy and, with Sébastien, transmitting their passion to me for this very complicated subject. I am grateful also to Carolina for the long discussions about our dielectric results which supported my progresses.

I would like to thank the Centre Technologique des Microstructures de l'Université Lyon 1 for the access to the TEM microscope and Pierre Alcouffe for his help in performing the observations, the Axel'One Campus for the access to NMR analysis and Fernande Da Cruz-Boisson and Carlos Fernandez de Alba for their precious help in the interpretation of my results.

I would like to express my gratitude also to Dario Pezzini for helping me with SEM observations and Daniele Battegazzore for his help with long and complex DMA measurements.

Then, I want to deeply thank my first co-bureaux Amélie, Adrien, Victor for the warm welcome when I moved to Lyon and their precious friendship shown along the way. Thanks also to all the amazing colleagues I have met in France, Liu,

David, Guillaume, Martin, Xavier, Gabriel, Matheus, Clémence and all the others. All of them contributed to make this journey at IMP and in Lyon remarkable and helped me patiently to improve my French. Merci à vous.

I would like to thank also Rossella, Chiara, Fulvia and Giulia for their patience supporting me when this work was challenging me and for being always there for me. Also, thanks to Francesco, Peppe, Chiara, Giusi, Massimo, Tian, Lorenza and all the beautiful colleagues I have met in Alessandria who supported me during this work.

I may not be able to list the names of all whom I feel grateful to, but I would like to express my gratitude to all the extraordinary people I have met in Lyon and in Alessandria during these years, this work would have not been possible without you.

At more personal level, I would like to thank my family for being a constant source of motivation and encouragement to keep doing my best. I am grateful also to my dearest friends Martina and Davide, Chiara and Vito, Alice, Fra, Luciano and Michele, all of you always stand by me.

And, last but not least, my innermost gratitude goes to Gra, who has been my greatest source of encouragement, thank you for believing in me even before I did.

“If we knew what we were doing , it wouldn't be called research, would it?”

Albert Einstein

Contents

1. State of the art 1
1.1 Thermal transport in polymers 2
1.1.1 Thermal conductivity measurements 8
1.1.1.1 Transient plane source method 9
1.1.1.2 Transient plane source method applied to thin films 13
1.1.2 Thermal conductivity of amorphous polymers 16
1.1.2.1 Effect of the strength of inter- and intra-chain interactions on thermal transport 18
1.1.2.2 Polymethacrylates as amorphous polymer model 23
1.2 Polymer nanocomposites for tailored properties 25
1.2.1 Thermal conduction in polymer nanocomposite 26
1.2.2 Cellulose-based fillers and their application 31
1.2.3 Methacrylate-based cellulose nanocomposites 35
2. Materials and methods 39
2.1 Materials 39
2.2 Preparation methods 40
2.2.1 Bulk polymerization 40
2.2.1.1 Thermally activated bulk polymerization 40
2.2.1.2 Room temperature bulk polymerization 41
2.2.1.3 Cobalt-mediated bulk co-/polymerization 41
2.2.2 Films preparation for thermal conductivity measurements 43
2.2.3 Neutralisation 43
2.2.4 Nanocomposites films preparation via solvent casting 43
2.2.4.1 Preparation from THF/water suspensions 44

2.2.4.2 Solvent exchange 44
2.2.4.3 Preparation from THF/MeOH suspensions 45
2.2.4.4 Films preparation for macromolecular mobility analysis 45
2.3 Characterizations 46
2.3.1 Macromolecular architecture 46
2.3.2 Molecular masses 46
2.3.3 Thermal analysis 47
2.3.4 Morphology of the films 47
2.3.5 Macromolecular mobility 48
3. Acrylate copolymers with tailored intermolecular interactions 49
3.1 MMA-MAA copolymers 50
3.1.1 PMMA from thermally activated polymerization 52
3.1.2 PMMA by room temperature polymerization 54
3.1.3 PMMA and PMMA-*co*-MAA from cobalt-mediated co-/polymerization 56
3.1.3.1 Thermal stability of PMMA-*co*-MAA copolymers 63
3.1.3.2 H-bond influence on copolymer properties 68
3.1.3.3 Neutralized MMA-MAA copolymers 73
3.2 Alternative comonomers: an evaluation of the influence of chain flexibility on the desired properties 76
3.2.1 MMA-HEMA copolymers 77
3.2.1.1 Thermal stability of PMMA-*co*-HEMA copolymers 79
3.2.1.2 H-bond influence on copolymer properties 81
3.2.2 MMA-CEA copolymers 84
3.2.2.1 Thermal stability of PMMA-*co*-CEA 88
3.2.2.2 H-bond influence on copolymer properties 90
3.2.2.3 Neutralized PMMA-*co*-CEA copolymers 92
3.3 Conclusions 93
4. Methacrylate-based CNF nanocomposites 97
4.1 Dispersion of CNF in a copolymer matrix 98
4.2 Thermal events in PMMA, PMMA-*co*-MAA and nanocomposite films 106
4.3 Influence of CNF on molecular mobility 110

4.3.1 Secondary relaxations analysed by dielectric spectroscopy.....113
4.3.2 Alpha relaxation analysis from dynamic mechanical spectroscopy 117
4.4 Thermal conductivity of thin films.....122
4.5 Conclusions.....123
Conclusions.....127
References.....131
Annexe.....149
Résumé de la thèse en Français.....149

List of Tables

Table 1. Comparison between steady and non-steady state techniques. 8
Table 2. Molar masses of PMMA polymerized at room temperature by BPO/DMT initiation. 56
Table 3. Copolymers composition determined by ^{1}H NMR analysis. 59
Table 4. Molar masses of PMMA-*co*-MAA copolymers after synthesis obtained by SEC measurements in THF applying multidetector method. 62
Table 5. TGA data for PMMA and PMMA-*co*-MAA copolymers under $N_{2(g)}$ and air. 63
Table 6. Assignment of IR peaks in PMMA and PMMA-*co*-MAA copolymers spectra. 69
Table 7. T_gs values of PMMA-*co*-MAA (0-30wt% MAA) measured on the second heating ramp of DSC and theoretical values calculated applying Fox's equation. 71
Table 8. Temperatures of second-order transitions from second heating DSC for PMMA-*co*-MAA neutralized with NaOH. 75
Table 9. TGA data for PMMA and PMMA-*co*-HEMA copolymers under $N_{2(g)}$ and air. 79
Table 10. T_gs values of PMMA-*co*-HEMA (14-39wt% HEMA) measured on the second DSC heating ramp and theoretical values calculated applying the Fox's equation. 82
Table 11. Molar masses PMMA-*co*-CEA polymerized applying different temperature profiles. 88
Table 12. TGA data for PMMA and PMMA-*co*-CEA copolymers under $N_{2(g)}$ and air. 89
Table 13. T_gs values of PMMA-*co*-CEA (15-41wt% CEA) measured on the second heating ramp of DSC and theoretical values calculated applying Fox's equation. 91

Table 14. T_gs values of PMMA, PMMA-*co*-MAA (30wt% MAA), and nanocomposites measured during a first and a second heating ramp by DSC. ...106
Table 15. TGA data for PMMA, PMMA-*co*-MAA and nanocomposites copolymers under $N_{2(g)}$ and air. 110
Table 16. Activation energies for γ, β, and β' relaxation of polymers and related nanocomposites.....115
Table 17. Fitting parameters from WLF. 117
Table 18. VFT parameters from fit determined for copolymer and related nanocomposites.....121
Table 19. Thermal conductivities measured on thin films by Hot Disk method for PMMA, PMMA-*co*-MAA, and nanocomposite with 10wt% of CNF. 122

List of Figures

Figure 1. Scheme of spring-mass analogy for unidimensional polymer chain. Heat is transferred from the hottest atom (red sphere) efficiently in the chain and in a less efficient way to the vicinal chains. *Reprinted from Engineering polymers with metal-like thermal conductivity—Present status and future perspectives, 233, Guo Y., Zhou Y., Xu Y., 124168, Copyright (2021), with permission from Elsevier.* 3

Figure 2. Scheme of interatomic force between two adjacent atoms, bonding and non-bonding contributions (a). Schematic thermal pathway in macromolecules by the contributions of covalent bonding interactions, non-bonding interactions and polymer chains translation (b). *Reprinted from Engineering polymers with metal-like thermal conductivity—Present status and future perspectives, 233, Guo Y., Zhou Y., Xu Y., 124168, Copyright (2021), with permission from Elsevier.* 5

Figure 3. Scheme of intramolecular interactions and vibration modes which affect thermal conduction. *Reprinted from Thermal conductivity of polymers and polymer nanocomposites, 132, Huang C., Qian X., Yang R., 1-22, Copyright (2018), with permission from Elsevier.* 6

Figure 4. Heat transfer at molecular level. Heat carrier scattering in amorphous polymer due to the presence of defects and disorder in the structure (a). Efficient thermal conduction along the chains in crystalline domains (b). *Reprinted from Engineering polymers with metal-like thermal conductivity—Present status and future perspectives, 233, Guo Y., Zhou Y., Xu Y., 124168, Copyright (2021), with permission from Elsevier.* 6

Figure 5. Effect of crystallinity on PE simulated and experimentally measured thermal conductivity. *Reprinted from Engineering polymers with metal-like thermal conductivity—Present status and future perspectives, 233, Guo Y., Zhou Y., Xu Y., 124168, Copyright (2021), with permission from Elsevier.* 7

Figure 6. Thermal conductivity measurement methods classification. 8

Figure 7. Thermal conductivity and temperature working intervals for thermal conductivity measurement methods. *Reprinted from Thermal conductivity measurement techniques for characterizing thermal energy storage materials – A review, 108, Palacios A., Cong L., Navarro M.E., Ding Y., Barreneche C., 32-52, Copyright (2019), with permission from Elsevier.* 9
Figure 8. Scheme of TPS apparatus. 10
Figure 9. Schematic configuration of samples and TPS probe. *Reprinted from "Thermal conductivity measurement techniques for characterizing thermal energy storage materials – A review, 108, Palacios A., Cong L., Navarro M.E., Ding Y., Barreneche C., 32-52" Copyright (2019), with permission from Elsevier.* 11
Figure 10. Temperature variation in the sensor and on the sample surface. ...12
Figure 11. TPS sensor designed for thin film methods (a). Schematic configuration of the thin film measurement in TPS technique (b). *Reprinted from An improved transient plane source method for measuring thermal conductivity of thin films: Deconvoluting thermal contact resistance, 96, Ahadi M., Andisheh-Tadbir M., Tam M., Bahrami M., 371-380, Copyright (2016), with permission from Elsevier.* 13
Figure 12. Deconvolution of the single effects contributing to the total thermal resistance in TPS thin film setup. *Reprinted from An improved transient plane source method for measuring thermal conductivity of thin films: Deconvoluting thermal contact resistance, 96, Ahadi M., Andisheh-Tadbir M., Tam M., Bahrami M., 371-380, Copyright (2016), with permission from Elsevier.* 15
Figure 13. Physical factors determining the mechanism of thermal conduction in polymers. 16
Figure 14. Structure of reference polymer (polynorbornene, PNb) and the bottlebrush (BB) polymers with different side chain length (a). Thermal conductivity along the chain orientation direction and its dependency on the length of the side chains (b). *Reprinted from Effects of polymer topology and morphology on thermal transport: A molecular dynamics study of bottlebrush polymers, 110, Ma H., Tian Z., 091903, Applied Physics Letters, 2017, with the permission of AIP Publishing.* 17
Figure 15. Thermal conductivity dependency on molecular weight. Experimental results for PS (□) and PIB (○), MD simulation results for monodisperse (□) and polydisperse (⊠) PS. *Reprinted from Thermal conductivity of amorphous polymers and its dependence on molecular weight, 228, Kiessling A., Simavilla D.N., Vogiatzis G.G., Venerus D.C., 123881, Copyright (2021), with permission from Elsevier.* 18

Figure 16. Thermal conductivity as function of sound speed for different classes of polymers characterized by different inter-chain interactions. *Reprinted figure with permission from "Xie X., Yang K., Li D., Tsai T.-H., Shin J., Braun P.V., Cahill D.G., High and low thermal conductivity of amorphous macromolecules, Phys. Rev. B, 95, 035406, 2017" Copyright (2017) by the American Physical Society.* 19

Figure 17. Chemical structures of the analysed polymers (a). Measured thermal conductivity of a function of the calculated minimal one for water-soluble polymers (■) and non-water-soluble polymers (▲). The blue short dashed line corresponds to the minimal thermal conductivity, and the red ones shows the best fit linear relationship. *Reprinted with permission from "Xie X., Li D., Tsai T.-H., Liu J., Braun P.V., Cahill D.G., Thermal Conductivity, Heat Capacity, and Elastic Constants of Water-Soluble Polymers and Polymer Blends, Macromolecules, 49, 972-978, 2016". Copyright 2016 American Chemical Society.* 20

Figure 18. Intermolecular connection via H-bonding in PVA/gelatin/lignin blend. *Reprinted with permission from "Mu L., He J., Li T.J., Mehra N., Shi Y., Zhu J., The Molecular Origin of Efficient Phonon Transfer in Modulated Polymer Blends: Effect of Hydrogen Bonding on Polymer Coil Size and Assembled Microstructure, J. Phys. Chem. C, 121, 14204-14212, 2017". Copyright 2017 American Chemical Society.* 20

Figure 19. Thermal conductivity variation according to the composition in PAP:PAA blends (a). Schematic illustration of thermal path in heterogeneously and homogeneously distributed inter-chain thermal connections (b). *Reproduced from [46] with permission from Springer Nature.* 21

Figure 20. Thermal conductivity as function of pH in ionizable PAA and non-ionizable PVP (a). IR spectra of PAA films manufactured at different pH corresponding to different neutralization degrees as showed by the intensity of the peak at 1594 cm^{-1} corresponding to the neutralized unit (b). Schematic illustration of chain conformation in polymer PAA films and factors affecting thermal conduction: unionized PAA (left) and ionized PAA (right) (c). *Reproduced from [49] in agreement with Creative Commons Attribution-Non Commercial license.* 22

Figure 21. Esters (left) and salts (right) of poly methacrylic acid (PMAA). ..23

Figure 22. Scheme of polymer nanocomposite preparation by *in situ* polymerization. 25

Figure 23. Composite thermal conductivity from Bruggeman's prediction as function of the particle content for different matrix thermal conductivities (Kp). *Reprinted from Thermal conductivity of polymer-based composites: Fundamentals*

and applications, 59, Chen H., Ginzburg V.V., Yang J., Yang Y., Liu W., Huang Y., Du L., Chen B., 41-85, Copyright 2016, with permission from Elsevier. 28

Figure 24. Interfacial thermal conductance in PP-base nanocomposites as a function of van der Waals strength. *Reprinted from Enhancement of Thermal Energy Transport Across Graphene/Graphite and Polymer Interfaces: A Molecular Dynamics Study, 22, Luo T., Lloyd J.R., 2495-2502, Copyright (2012), with permission from John Wiley and Sons.* 30

Figure 25. Thermal conductivity in pristine epoxy resin and in its nanocomposites (with 5wt% of BN) according to BN surface functionalization. *Reprinted from Interfacial modification of boron nitride nanoplatelets for epoxy composites with improved thermal properties, 53, Yu J., Huang X., Wu C., Wu X., Wang G., Jiang P., 471-480, Copyright 2012, with permission from Elsevier.* 31

Figure 26. Schematic representation of hierarchical structure of cellulose for CNC and CNF production. *Reprinted from Lignocellulosic biomass from agro-industrial residues in South America: current developments and perspectives, 13, Magalhães A.I., de Carvalho J.C., de Melo Pereira G.V., Karp S.G., Câmara M.C., 1505-1519, Copyright (2019), with permission from John Wiley and Sons.* 32

Figure 27. Intra and inter-chain H-bonding in cellulose structure. *Reproduced from Ref. [107] with permission from the Royal Society of Chemistry.* 33

Figure 28. Dynamic mechanical behaviour of CNF/PMMA nanocomposite films for different CNF vol% at 1 Hz. *Reprinted from Large specific surface area and rigid network of nanocellulose govern the thermal stability of polymers: Mechanisms of enhanced thermomechanical properties for nanocellulose/PMMA nanocomposite, 16, Fujisawa S., Togawa E., Kimura S., 105-110, Copyright (2018), with permission from Elsevier.* 36

Figure 29. Preparation of PMMA/CNF nanocomposites via Pickering emulsion. Nanocomposite particles are firstly synthesised in Pickering emulsion in water, successively washed in methanol and water to remove the excess of monomer, initiator and CNF. Next, a nanocomposite film is made by compression moulding. *Reprinted from Nano-dispersed cellulose nanofibrils-PMMA composite from pickering emulsion with tunable interfacial tensions, 247, Kim D.W., Shin J., Choi S.Q., 116762, Copyright (2020), with permission from Elsevier.* 36

Figure 30. Schematic structure in pristine CNF blended with PMMA (CNF-b-PMMA), modified CNF blended with PMMA (mCNF-b-PMMA), and grafted with PMMA (mCNF-*g*-PMMA). Allyl glycidyl ether (AGE) used for CNF modification (mCNF). *Reprinted with permission from Nanostructural Effects in High Cellulose Content Thermoplastic Nanocomposites with a Covalently Grafted*

Cellulose−Poly(methyl methacrylate) Interface, 20, Boujemaoui A., Ansari F., Berglund L.A., 598-607. Copyright 2019 American Chemical Society. 37
Figure 31. Stress strain curves for neat PMMA, pristine CNF blended with PMMA (CNF-*b*-PMMA), modified CNF blended with PMMA (mCNF-*b*-PMMA), and grafted with PMMA (mCNF-*g*-PMMA). *Reprinted with permission from Nanostructural Effects in High Cellulose Content Thermoplastic Nanocomposites with a Covalently Grafted Cellulose−Poly(methyl methacrylate) Interface, 20, Boujemaoui A., Ansari F., Berglund L.A., 598-607. Copyright 2019 American Chemical Society.*.....38
Figure 32. Scheme of the mould used for polymerization, U-shape silicone frame 5mm-thick in between two glass plates.....41
Figure 33. Scheme of the mould used for polymerization, squared shape silicone frame 5mm-thick in between two glass plates. 42
Figure 34. Structure evolution correlated to the introduction of H-bonds and ionic bonds in the macromolecular microstructure.....50
Figure 35. Schematic free radical polymerization of MMA. Radicals (R•) formation from the initiator (I) (a), chain initiation (b), propagation step (c) and termination reactions (d).....51
Figure 36. BPO thermal decomposition to form radicals. *Reproduced from [173] with permission from Royal Society of Chemistry.* 52
Figure 37. NIR spectra of reactive mixture MMA + BPO 0.13mol% after 2, 4, and 6h of reaction and chemical structure of MMA.....53
Figure 38. Polymerized PMMA samples in presence of 0.13 (a) and 0.30mol% (b) of BPO.....54
Figure 39. Activation mechanism correlated to the reaction between BPO and a tertiary amine. *Reproduced from [160] with permission from Royal Society of Chemistry.* 54
Figure 40. Bulk polymerized PMMA in presence of 1 (a) and 1.5mol% (b) of BPO/DMT initiator complex. 55
Figure 41. Molar masses distribution PMMA polymerized with 1 and 1.5mol% of BPO/DMT (PS standard, DMF as eluent and viscosimeter detection). 55
Figure 42. Radicals formed by alkoxyl radical decomposition.....57
Figure 43. Reaction of acetyl and propoinyl radical. 57
Figure 44. PMMA polymerized in glass mould at 55/80°C (a), in aluminium mould at 55/80 (b) and at 55/70°C (c). 58
Figure 45. PMMA-*co*-MAA 70:30wt% polymerized in aluminium mould at 55/70°C. Transparency is highlighted by the small cube visible behind the sample. 58

Figure 46. PMMA-*co*-MAA 60:40wt% after bulk copolymerization. 59
Figure 47. ^{1}H NMR spectra at 25°C for MMA (a) and MAA (b) and at 90°C for PMMA (c), PMMA-*co*-MAA 10 (d), 20 (e), and 30wt% (f) MAA after copolymerization (400 MHz, DMSO-*d6*).....61
Figure 48. Molar mass distributions for PMMA and PMMA-*co*-MAA 10 and 20wt% of MAA (THF as eluent and IR detection).....62
Figure 49. Molar masses distribution for PMMA-*co*-MAA 30wt% of MAA (PS standard, DMF as eluent and viscosimeter detection). 63
Figure 50. Thermogravimetric analyses of PMMA in N_2 and in air (heating rate 10°C/min).....64
Figure 51. PMMA thermal degradation mechanism. *Reproduced from "Suresh, S.S. et al.; Investigation into the Mechanical and Thermal Properties of Poly(Methyl Methacrylate) Recovered from Light Guidance Panels with a Focus on Future Remanufacturing and Sustainable Waste Management*." [186] *with permission from Springer Nature.* 65
Figure 52. Reactions between the macroradicals and O_2 during thermal degradation.....66
Figure 53. Thermogravimetric analyses of PMMA-*co*-MAA 30wt% MAA in N_2(a) and in air (b) (heating rate 10°C/min).....67
Figure 54. Reaction of anhydride formation via a transition state and decarboxylation of anhydride rings. 68
Figure 55. IR spectra (ATR mode) of PMMA-*co*-MAA copolymers after copolymerization reaction with MAA content from 0 to 30wt%. 68
Figure 56. Scheme of interactions between MMA and MAA carbonyl and related absorption bands. *Reprinted from Comparison of hydrogen bonding interaction between PMMA/PMAA blends and PMMA-co-PMAA copolymers, 44, Huang C.-F., Chang F.-C., 2965-2974, Copyright 2003, with permission from Elsevier.* 69
Figure 57. DSC thermograms of PMMA, PMMA-*co*-MAA 10, 20, and 30wt% (heating rate 10°C/min). 70
Figure 58. T_g versus composition curves of PMMA-*co*-MAA based on experimental data fitted by Kwei's equation and theoretical prediction by Fox's equation.....72
Figure 59. Thermal conductivity in PMMA-*co*-MAA copolymers variation with MAA content. 73
Figure 60. IR spectra (ATR mode) of pristine PMMA-*co*-MAA and neutralised with NaOH hydroxide 1:1.....74

Figure 61. DSC thermograms of the second heating ramp for PMMA-*co*-MAA 70/30wt% neutralized with NaOH (heating rate 10°C/min).....74
Figure 62. Scheme showing the restricted mobility region in a multiplet. *Reprinted with permission from "A New Multiplet-Cluster Model for the Morphology of Random Ionomers, 23, Eisenberg A., Hird B., Moore R.B., 4098-4107, 1990". Copyright 1990 American Chemical Society.*.....75
Figure 63. Chemical structure of PMMA and designed copolymers.....76
Figure 64. PMMA-*co*-HEMA 39wt% of HEMA from bulk polymerization. 77
Figure 65. ^{1}H NMR spectra at 25°C for MMA (a) and at 90°C for HEMA (b), PMMA (c), PMMA-*co*-HEMA 14 (d), 28 (e), and 39wt% (f) of HEMA after copolymerization. (400 MHz, DMSO-*d6*). PMMA and comonomers reference spectra are reported to help in peak assignment. 78
Figure 66. Thermogravimetric analyses of PMMA-*co*-HEMA 39wt% HEMA compared to PMMA ones in N_2 (a) and in air (b) (heating rate 10°C/min).....80
Figure 67. Decomposition reactions occurring in the side chain of HEMA units. *Reprinted from A detailed study of thermal degradation of poly(2-hydroxyethyl methacrylate), 72, Demirelli K., Coşkun M., Kaya E., 75-80, Copyright (2001), with permission from Elsevier.* 80
Figure 68. IR spectra (ATR mode) of PMMA-*co*-HEMA copolymers after copolymerization reaction with HEMA content from 14 to 39wt% compared to PMMA. 81
Figure 69. DSC thermograms of PMMA-*co*-HEMA at 14, 28, and 39wt% of HEMA (heating rate 10°C/min).....82
Figure 70. T_g versus composition curves of PMMA-*co*-HEMA based on experimental data fitted by Kwei's equation and theoretical prediction by Fox's equation.....83
Figure 71. Scheme of intermolecular interactions in PMMA-*co*-HEMA.....83
Figure 72. Thermal conductivity in PMMA-*co*-HEMA. 84
Figure 73. PMMA-co-CEA 41wt% of CEA polymerized at 55/70°C.....85
Figure 74. Bubbles evolution for PMMA-*co*-CEA 59/41wt% treated at 50/60 (A), 30/40/60 (B), and Troom/25/30/35/40/45/60°C (C). 85
Figure 75. ^{1}H NMR spectra at 25°C for MMA (a) and at 90°C for CEA monomer (b), PMMA (c), PMMA-*co*-CEA 15 (d), 30 (d), and 41wt% (f) of CEA after copolymerization. (400 MHz, DMSO-*d6*). PMMA and comonomers reference spectra are reported to ease peak assignment. 87
Figure 76. Molar mass distribution for PMMA, PMMA-*co*-CEA 15 and 30 (a) and 41wt% of CEA (b) polymerized applying different temperature profiles (PS standard, DMF as eluent and viscosimeter detection). 88

Figure 77. Thermogravimetric analyses of PMMA-*co*-CEA 41wt% CEA compared to PMMA ones in N_2 (a) and in air (c) (heating rate 10°C/min). 89
Figure 78. IR spectra (ATR mode) of PMMA-*co*-CEA copolymers after copolymerization reaction with CEA content from 15 to 41wt% compared to PMMA. 90
Figure 79. DSC thermograms of PMMA-*co*-CEA at 15 (a), 30 (b), and 41wt% of CEA (heating rate 10°C/min). 91
Figure 80. T_g versus composition curves of PMMA-*co*-CEA based on experimental data fitted by Kwei's equation and theoretical prediction by Fox's equation. 92
Figure 81. IR spectra (ATR mode) of pristine PMMA-*co*-CEA 41wt% of CEA and neutralized with NaOH 1:1. 93
Figure 82. SEM images (secondary electrons) of PMMA-*co*-MAA + 5wt% of CNF evaporated from THF/water at 77/23vol%. 99
Figure 83. SEM images of neat PMMA-*co*-MAA evaporated from THF/water at 77/23vol% (a), 95/5vol% (azeotropic composition) (b) with details of spherical inclusions (c) and from pure THF (d). 100
Figure 84. SEM images of neat PMMA-*co*-MAA casted from THF/MeOH 90/10 (a), 70/30 (b) and 50/50vol% (c) solutions. 101
Figure 85. TGA thermograms for CNF water suspension and MeOH-wetted CNF after third washing (5°C/min). 101
Figure 86. SEM images of fractured PMMA-*co*-MAA + 5 (a), 10 (b) and 15wt% (c) of CNF film casted from THF/MeOH 85/15vol% solutions. 102
Figure 87. FE-SEM (a) and TEM (b) micrographs of PMMA-*co*-MAA + CNF 10wt% nanocomposites processed from THF/MeOH 85/15vol% solution. FE-SEM (c) and TEM (d) micrographs of PMMA-*co*-MAA + CNF 10wt% processed from THF/MeOH 66/34vol% solutions. 103
Figure 88. SEM micrograph showing residual porosity after solvent casting (THF/MeOH 66/34vol%) in PMMA-*co*-MAA + 10wt% CNF film before compression moulding. 103
Figure 89. Transparent film of PMMA-*co*-MAA after compression moulding at 230°C (a) and with the addition of 10wt% of CNF after compression moulding at 230°C (b). 104
Figure 90. UV spectra of compression moulded films of PMMA-*co*-MAA (5, 10 and 15wt% of CNF). 104
Figure 91. ^{1}H NMR spectrum at 25°C for PMMA-*co*-MAA after compression moulding of the film (400 MHz, DMSO-*d6*). 105

Figure 92. ATR spectra of PMMA-*co*-MAA 30wt% MAA before and after compression moulding at 230°C for 8 min and PMMA-*co*-MAA + 10wt% CNF after compression moulding at 230°C for 8 min.....105
Figure 93. DSC thermograms for PMMA (a), PMMA-*co*-MAA (30wt% MAA) (b), and nanocomposites films with 5 (c), 10 (d) and 15 (e) wt% of CNF (heating rate 10°C/min).....107
Figure 94. Thermogravimetric analyses on films of PMMA (a), PMMA-*co*-MAA (30wt% MAA) (b) and nanocomposite with 5 (c), 10 (d) and 15 (e) wt% of CNF in air and N_2 (heating rate 10°C/min).....109
Figure 95. Relaxations in MMA units described in literature and possible relaxations in MAA units.....111
Figure 96. Dielectric relaxations maps for PMMA (a), neat PMMA-*co*-MAA (30wt% MAA) (b) and filled with 5 (c), 10 (d), and 15wt% (e) of CNF. Relaxation processes are indicated by white lines. 112
Figure 97. Dielectric thermogram, isofrequency at 0.04Hz of polymers and related nanocomposites. The presence of β'-relaxation is indicated (black arrows) for PMMA and PMMA-*co*-MAA.....114
Figure 98. Arrhenius diagram of the secondary relaxations processes of polymers and related nanocomposites. 114
Figure 99. Schematic interactions between MAA carboxylic group in PMMA-*co*-MAA and CNF surface hydroxyl groups and water molecules.....116
Figure 100. Storage (solid dots) and loss modulus (open dots) master curves of copolymer and related nanocomposites.....118
Figure 101. Arrhenius plot of alpha relaxations of copolymer and related nanocomposites.....119
Figure 102. Stickel diagram for copolymer and related nanocomposites. 120
Figure 103. Thermal conductivity of PMMA-*co*-MAA copolymers in bulk and as thin films as function of MAA content and for PMMA-*co*-MAA with 10wt% of CNF.....123

List of Abbreviations

ATR	Attenuated total reflectance
BDS	Broadband dielectric spectroscopy
BHT	Butylhydroxytoluene
BN	Boron nitride
BNC	Bacterial nanocellulose
BPO	Benzoyl peroxide
CEA	2-carboxyethyl acrylate
CNC	Cellulose nanocrystals
CNF	Cellulose nanofibers
CNT	Carbon nanotubes
DHEPT	2,2'-(4-methylphenylimino)diethanol
DMF	*N,N*-dimethylformamide
DMSO	Dimethyl sulfoxide
DMSO-*d6*	Deuterated dimethyl sulfoxide
DMT	4,*N,N*-trimethylaniline
DMTA	Dynamic mechanical thermal analysis
DSC	Differential scanning calorimetry
E_a	Activation energy
$E_{a\text{-}app}$	Apparent activation energy
EMT	Effective Medium Theory
FE-SEM	Field emission SEM
H-bonds	Hydrogen bonds
HBP	Hyperbranched aromatic polyamide
HEMA	2-hydroxyethyl methacrylate
IR	Infrared
$LiNTf_2$	Bis(trifluoromethane) sulfonimide lithium salt
MAA	Methacrylic acid
MD	Molecular Dynamics
MeHQ	Hydroquinone monomethyl ether
MEKP	Methyl ethyl ketone peroxide
MeOH	Methanol
MMA	Methyl methacrylate
M_n	Number average molecular weight

M_w	Weight average molecular weight
NIR	Near-Infrared
NMR	Nuclear magnetic resonance
ODA	Octadecylamine
PAA	Polyacrylic acid
PAP	Poly(*N*-acryloyl piperidine)
PCEA	Polycarboxyethyl acrylate
PE	Polyethylene
PHEMA	Polyhydroxyethyl methacrylate
PIB	Polyisobutylene
PMA	Polyacrylamide
PMAA	Polymethacrylic acid
PMMA	Polymethyl methacrylate
PMMA-*co*-CEA	Poly(methyl methacrylate-*co*-carboxyethyl acrylate)
PMMA-*co*-HEMA	Poly(methyl methacrylate-*co*-hydroxy ethyl methacrylate)
PMMA-*co*-MAA	Poly(methyl methacrylate-*co*-methacrylic acid)
PP	Polypropylene
PS	Polystyrene
PSS	Poly(4-styrenesulfonic acid)
PU	Polyurethane
PVA	Polyvinylalcohol
PVP	Poly(N-vinyl pyrrolidone)
PVPA	Polyvinylphosphonic acid
q	Kwei parameter
SEC	Size exclusion chromatography
SEM	Scanning electron microscope
TCR	Thermal contact resistance
TEM	Transmission electron microscope
T_g	Glass transition temperature
TGA	Thermogravimetric analysis
THF	Tetrahydrofuran
TPS	Transient plane source
TTS	Time temperature superposition
UPyMA	2-ureido-4[1H]-pyrimidinone methyl methacrylate
UV	Ultra-Violet
vdW	van der Waals
VFT	Vogel–Fulcher–Tammann
WLF	William–Landel–Ferry
α	thermal diffusivity
α_T	shift factor in TTS
κ	Thermal conductivity
τ	Relaxation time

Chapter 1

State of the art

Polymer are traditionally considered as thermal insulating materials given their low bulk thermal conductivity ranging in between 0.1 and 0.5 $W \cdot m^{-1} \cdot K^{-1}$ [1–5]. However, the possibility to improve this property would open up the field to new set of applications, especially in electronic and energetic fields, *e.g.* packaging for light-emitting diode and electronic components, heat exchangers with corrosion resistance, heat sink applications where electrical insulation is required [4,6]. The great interest in making polymer thermally conductive lies in their unique combination of properties which cannot be obtained in other thermo-conductive materials, such as chemical resistance, ease of processability in complex shapes, flexibility and electrical insulation [2–4,6–10]. Therefore, in the last decades a great interest has been showed in the understanding of the heat conduction mechanism in polymeric materials which, however, is not yet fully elucidated. Once an adequate knowledge will be achieved, it will be possible to act on factors determining the heat transport and obtain an adequate thermal conduction making polymers suitable for specific applications where thermo-conductive properties are required [4,5].

Multiple factors have been recognized to play a role on polymers thermal conduction, including crystallinity, chain orientation, chain stiffness, and molar mass [1,6,8,9,11] Therefore, an intense research is needed in order to clarify the relation between each factor and the final thermal conductivity of the material. Moreover, it must be considered that polymers are not intrinsically poor heat conductor. In fact, the low bulk thermal conductivity mainly results from the frequent scattering of heat carriers at the chain ends and entanglements [2,4,6,8]. Instead, the polymer chains structure is principally made by carbon-carbon covalent bonds similar to diamond one, which exhibits a thermal conductivity close to 2000 $W \cdot m^{-1} \cdot K^{-1}$ [12], suggesting the potential of this class of materials [6]. Indeed, many studies have been published reporting an excellent thermal conductivity along the polymer backbone encouraging the scientific community to pursue the research in this field [4,6,8,13–17]. For example, molecular dynamics (MD) simulations suggest a thermal conductivity along a single polyethylene (PE) chain that is close

to 350 $W \cdot m^{-1} \cdot K^{-1}$ about 1000 times higher than bulk PE (0.35 $W \cdot m^{-1} \cdot K^{-1}$) [6,15]. Indeed, as abovementioned, the loss of conduction is determined by the disordered structure which is a common feature for polymers. Based on these considerations, some attempts have been done in order to obtain highly ordered structures, comparable to single crystalline fibre, and measure their thermal conductivity. For example, Shen *et al.* prepared ultra-drawn PE fibers having a thermal conductivity about 104 $W \cdot m^{-1} \cdot K^{-1}$, about 300 times higher than bulk PE [16].

In this context, this chapter aims to give an overview about the actual knowledge regarding thermal conduction in polymers and the main factors affecting this property. Then, thanks to the design of a copolymer where inter-chain interactions can be easily modified, a correlation between the strength of these interactions and the thermal conduction is investigated. Ideally, the addition of stronger hydrogen bonds (H-bonds) interactions to van der Waals (vdW) ones is expected to show a positive contribution to the thermal transport and the subsequent substitution with ionic interactions may further increase the thermal conductivity of the material [8]. The modification of the strength and the density of inter-chain interactions is designed to lead to a tuneable thermal conductivity. Additionally, given the recent attention to sustainable materials based on renewable resources, a fully organic nanocomposite with engineered interactions at the matrix/filler interface is designed. Between the organic nanoparticles, cellulose nanofibers are selected accordingly to the promising thermal conductivity showed by the single fibers, *i.e.* close to 1.7 – 2.2 $W \cdot m^{-1} \cdot K^{-1}$, one order of magnitude greater than polymer one [18,19]. The role of H-bonds established between the matrix and the nanofibers is explored and its influence on macromolecular mobility and thermal conduction is disclosed.

1.1 Thermal transport in polymers

Thermal conductivity can be defined as "the rate at which heat is transferred by conduction through a unit cross-section area of a material, when a temperature gradient exits perpendicular to the area" [11]. In isotropic material, the heat flux (q) can be defined by the Fourier's law:

$$q = -\kappa \nabla \mathrm{T} \tag{1}$$

where ∇T is the temperature gradient and κ is the thermal conductivity [4,7,11]. The thermal conductivity is the sum of the different contributions to the heat transfer in the material and can be express as:

$$\kappa = \kappa_e + \kappa_p \tag{2}$$

where κ_e is the electron conductivity and κ_p is the phonon conductivity [7]. According to the material structure, one of the contributions is predominant: for example, in metals κ_e is the factor determining the final κ value given the large number of electronic carriers. As polymers are typically electrical insulator, the

main contribution to heat transfer is attributable to the propagation of vibrational modes in the material [2,3,6,8]. The mechanism behind the thermal transport in polymer materials is still not fully understood and, given the amorphous structure, it is not possible to accurately describe the atomic vibration as phonons [6,20]. However, despite this consideration, thermal conductivity is generally expressed by the equation based on relaxation time models and the approximation of Debye-like density of vibrational states, which can be simplified in the following equation:

$$\kappa = \frac{Cvl}{3} \tag{3}$$

where C specific heat capacity per unit volume, v is the average velocity of heat carriers, and l is the carrier mean free path [4,6,7,21].

The macromolecular chain can be schematized as a series of atoms bonded by springs with a given restoring force where the heat transfer is more efficient along the chain (Figure 1) [6,22].

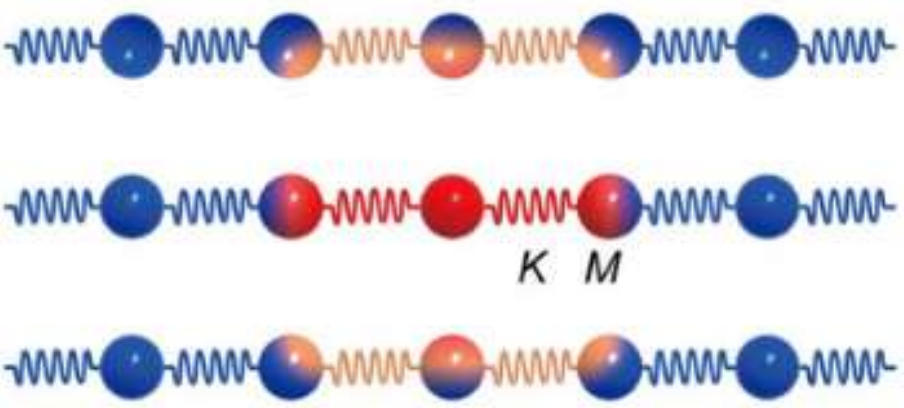


Figure 1. Scheme of spring-mass analogy for unidimensional polymer chain. Heat is transferred from the hottest atom (red sphere) efficiently in the chain and in a less efficient way to the vicinal chains. *Reprinted from Engineering polymers with metal-like thermal conductivity—Present status and future perspectives, 233, Guo Y., Zhou Y., Xu Y., 124168, Copyright (2021), with permission from Elsevier.*

Therefore, the atomic vibration corresponds to a coupled harmonic oscillator. In this representation, the sound velocity (v_s) in the macromolecule can be described as:

$$v_s \approx x\sqrt{\frac{K}{\bar{M}}} = \sqrt{\frac{2\bar{E}}{\overline{M_b}}} \tag{4}$$

where x is the atomic distance, K is the spring constant, M average atomic mass, M_b average backbone atomic mass, and E average binding energy of the backbone.

From v_s, an estimation of the lower limit of thermal conductivity (κ_{min}) has been proposed for amorphous polymer in the high-temperature limit where all vibrational modes are activated:

$$\kappa_{min} = \sqrt[3]{\frac{\pi}{48}} k_b n^{\frac{2}{3}} (v_l + 2v_t) \quad (5)$$

where k_b is the Boltzmann's constant, n is the atomic density, v_l and v_t are the sound velocity in the longitudinal and transversal direction respectively [6–8,21]. Instead, the thermal conductivity along the chain (κ_{chain}) can be expressed as:

$$\kappa_{chain} = \frac{213 \bar{E} \delta}{\overline{M_b}^{0.48} \overline{M_s}^{0.02} P^3 V^{2/3} T} \quad (6)$$

where δ is the in-plane bond ratio, Ms the average atomic mass of side chains, P is the rotation ratio, V the volume of the unit cell, and T the temperature. Considering the relation expressed in equations (4) and (6), the thermal conductivity along the macromolecules is directly influenced by the inter-atomic binding energy. In a similar way, the inter-chain thermal transport will be affected by the strength of the established intermolecular interactions. In fact, the inefficiency of thermal transport between the chains is hardly surprising considering the fact that inter-chain interactions are usually weak vdW forces, characterized by much lower energy (2 – 4 kJ/mol [6]) compared to carbon covalent bonds present in the chain (close to 350 kJ/mol [23]) [6,8].

It is also clear from equation (4) that for polymer material, the binding energy is a major determinant in the thermal transport. The interatomic force between two adjacent atoms results as the sum of two contributions (Figure 2a): the covalent bonding interaction ($f_{cov\text{-}bond}$) and the non-bonding interaction ($f_{non\text{-}bond}$) [1,6,9]. The first contribution is related to the C-C covalent bonds of the backbone, while the second contribution is attributable to vdW, H-bonding, or Coulomb interactions [1]. Therefore, the total thermal conductivity (κ_{tot}) consists of the contribution of covalent bonding interactions ($\kappa_{cov\text{-}bond}$), non-bonding interactions ($\kappa_{non\text{-}bond}$), and polymer chains translations (κ_{tran}) (Figure 2b). The main contribution is represented by $\kappa_{cov\text{-}bond}$ [6,9].

$$\kappa_{tot} = \kappa_{cov-bond} + \kappa_{non-bond} + \kappa_{tran} \quad (7).$$

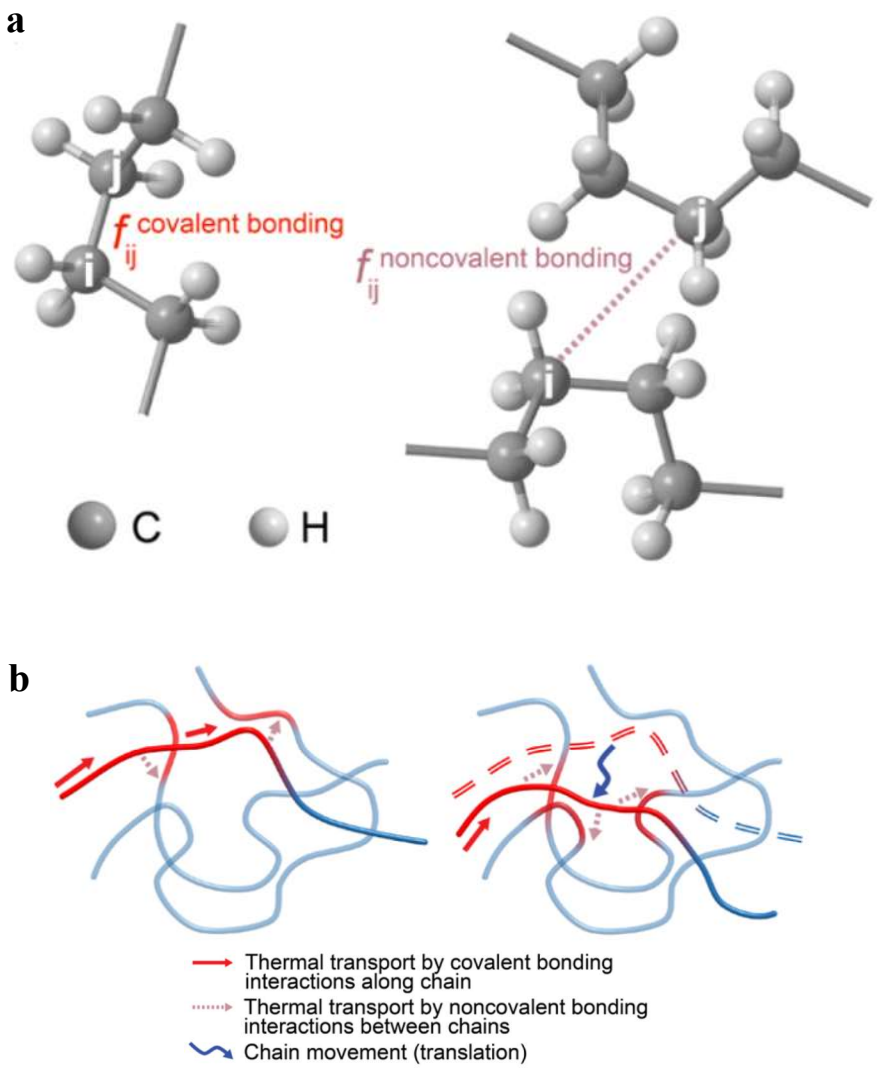


Figure 2. Scheme of interatomic force between two adjacent atoms, bonding and non-bonding contributions (a). Schematic thermal pathway in macromolecules by the contributions of covalent bonding interactions, non-bonding interactions and polymer chains translation (b). *Reprinted from Engineering polymers with metal-like thermal conductivity—Present status and future perspectives, 233, Guo Y., Zhou Y., Xu Y., 124168, Copyright (2021), with permission from Elsevier.*

Moreover, the covalent bond energy has an impact on the conformational structure which plays as well an important role in determining the polymer thermal conductivity along the chain. Indeed, the bond stretching ($E_{stretching}$) and the angular bending (E_{angle}) influence the flexibility of the chain and the presence of chain entanglements, while the dihedral energy ($E_{dihedral}$) shows a large effect on the chain rotation (Figure 3). Larger $E_{stretching}$ and E_{angle} are associated to stiffer backbones which lead to more efficient thermal transport. The $E_{dihedral}$ is negligible compared to $E_{stretching}$ and E_{angle}. However, $E_{dihedral}$ corresponds to the energy barrier to the segmental rotation and is directly correlated to the radius of gyration, its increase causes the restrain of segmental rotation improving thermal conduction [1,6,9].

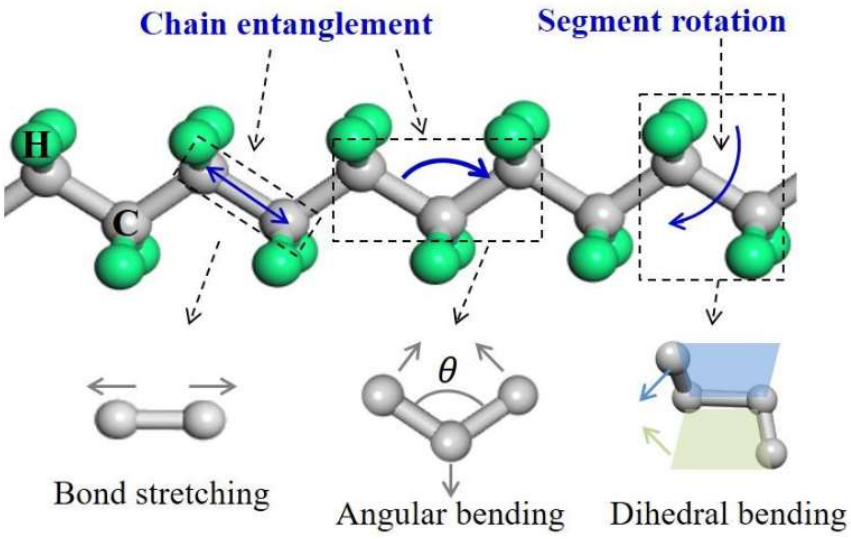


Figure 3. Scheme of intramolecular interactions and vibration modes which affect thermal conduction. *Reprinted from Thermal conductivity of polymers and polymer nanocomposites, 132, Huang C., Qian X., Yang R., 1-22, Copyright (2018), with permission from Elsevier.*

An important distinction needs to be done between the thermal transport in the crystalline domains and amorphous regions of polymers (a scheme is offered in Figure 4) [6]. In amorphous regions, the presence of multiples scattering sites (such as chain ends, entanglements and voids) determines a shorter phonon mean free path and a higher frequency of scattering events [4,6–9]. In this context, chain alignments could be beneficial in terms of thermal conductivity. However, it results in higher thermal conductivity along the main chain and consequently anisotropic thermal conduction [6,8].

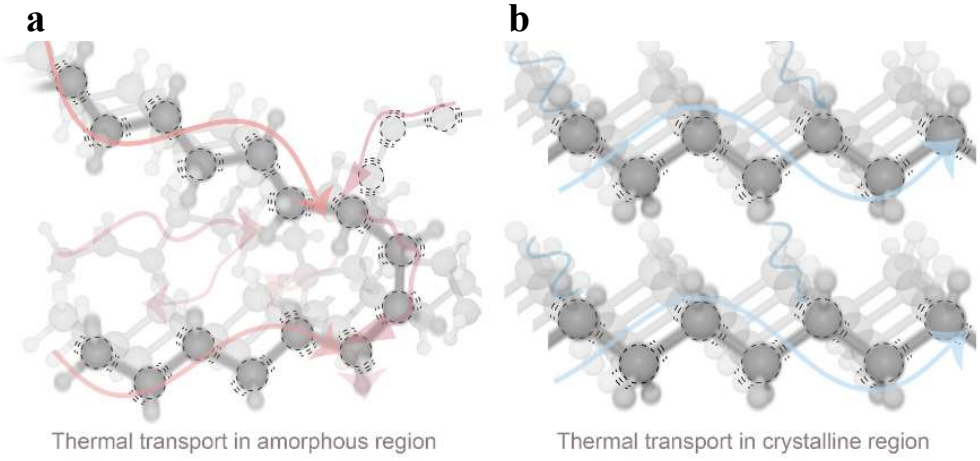


Figure 4. Heat transfer at molecular level. Heat carrier scattering in amorphous polymer due to the presence of defects and disorder in the structure (a). Efficient thermal conduction along the chains in crystalline domains (b). *Reprinted from Engineering polymers with metal-like thermal conductivity—Present status and future perspectives, 233, Guo Y., Zhou Y., Xu Y., 124168, Copyright (2021), with permission from Elsevier.*

Instead, the thermal transport in the crystalline domain propagates along the crystal directions [1,6,8]. Likewise, usually higher crystallinity and larger crystal size lead to higher thermal conductivity given the higher order present in the material. For example, different studies have been published about the influence of crystallinity on thermal conductivity of PE (Figure 5). The values, either obtained by simulation or measured experimentally, clearly show that thermal conductivity increases with increasing crystallinity [6]. It is worth mentioning that a difference is observed for high crystallinity % between the experimental values and calculated ones which, in this case, can be ascribed to the higher order present in the structure for the experimental measures due to stretching performed during the sample preparation [6,24].

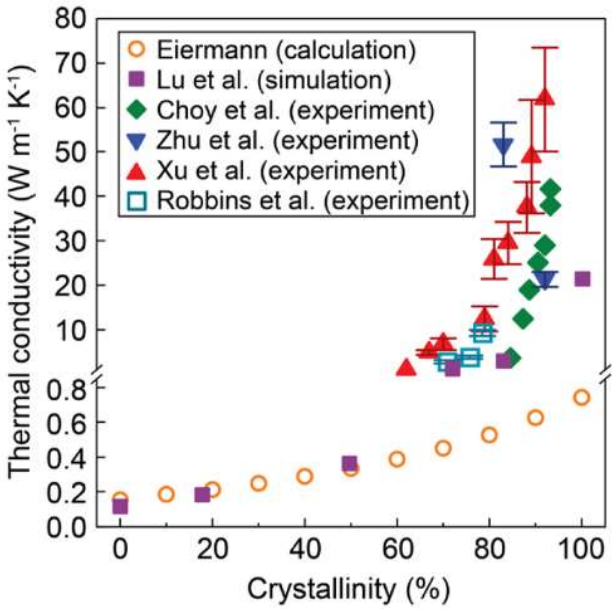


Figure 5. Effect of crystallinity on PE simulated and experimentally measured thermal conductivity. *Reprinted from Engineering polymers with metal-like thermal conductivity—Present status and future perspectives, 233, Guo Y., Zhou Y., Xu Y., 124168, Copyright (2021), with permission from Elsevier.*

Nonetheless, it must be taken in consideration that usually higher crystallinity content could result from a stretching process which influence the chain orientation and thus positively affecting the bulk thermal conductivity [4,6,24]. Moreover, heat carriers scattering is observed at the interface crystal/amorphous region which must be reduced acting on the crystal size in order to maximize the thermal conduction [4,6].

Multiple other factors influence the thermal conductivity in polymers. For example, κ also increases with molar mass given the lower number of chain terminations which can be responsible for scattering events [6].

1.1.1 Thermal conductivity measurements

The techniques applied to measure thermal conductivity can be grouped in two main categories (Figure 6): steady state techniques and non-steady state techniques (or transient methods) [4,8,11,25,26].

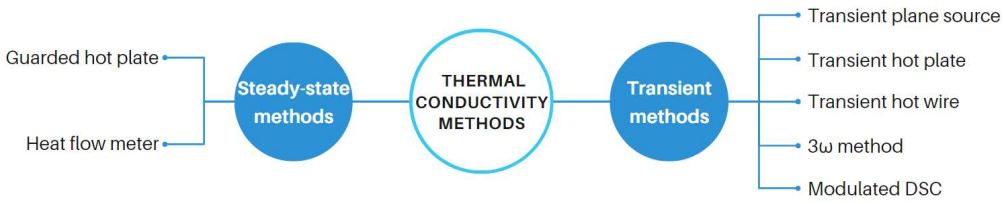


Figure 6. Thermal conductivity measurement methods classification.

The steady state methods are based on measurement performed in a complete thermal equilibrium state and a steady heat flow established across the sample. Usually they are based on simpler mathematical equations compared to transient methods, but higher measuring time is required in order to reach the thermal equilibrium. Generally, the temperature difference (ΔT) across the sample is measured and the thermal conductivity is directly extracted applying the Fourier's law (equation (1)) and assuming a unidirectional flux [7,11,26]. Despite the wide use of these methods, one of its main limitation relies in the fact that it is highly sensible to thermal contact resistance (TCR) and parasitic heat losses which may affect the measurement [7].

In non-steady state techniques, the thermal properties of the material are measured during a transient state of heat exchange and they can be further divided, according to the nature of the heat source, into periodic heat flux or transient heat flux resulting in a periodic or transient temperature variation in the sample [11,26–28]. The transient methods measure the heat transfer rate in the sample and determine the thermal diffusivity of the material, therefore they are usually based on more complex physical models compared to steady-state methods [11].

A comparison between the main advantages and disadvantages of the two methods is reported in Table 1.

Table 1. Comparison between steady and non-steady state techniques.

	Steady state	**Non-steady state**
Sample preparation	-	+
Measuring time	-	+
Theoretical equations	+	-
Cost	-	+

Thermal conductivity can vary in a very broad range of values. Therefore, different instruments are designed for specific range of testing conductivities (Figure 7). Moreover, the main methods can be further grouped in three categories

according to the temperature range for which they have been optimized: 1/ room temperature, 2/ low temperature (down to -180°C), and 3/ high temperature (above 600°C) [26].

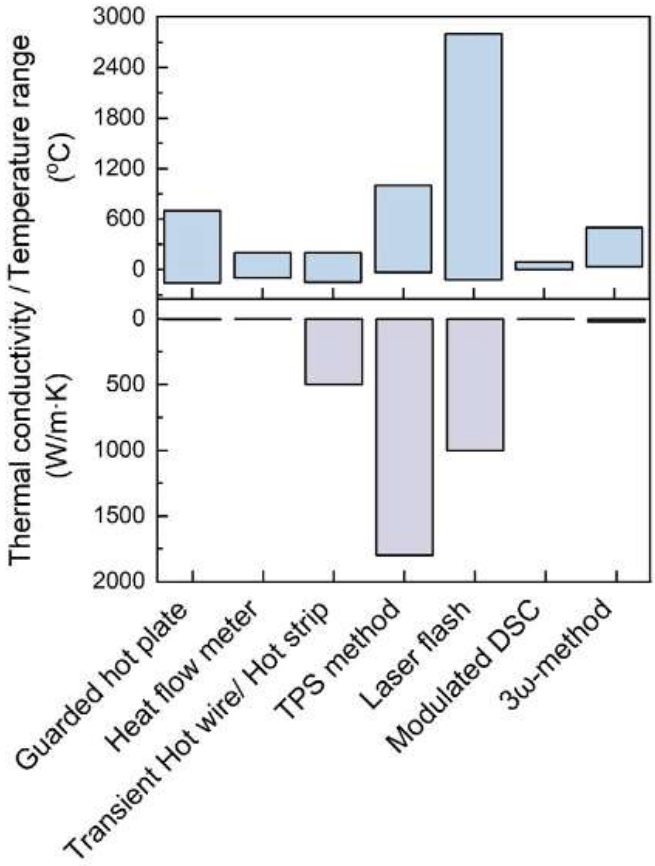


Figure 7. Thermal conductivity and temperature working intervals for thermal conductivity measurement methods. *Reprinted from Thermal conductivity measurement techniques for characterizing thermal energy storage materials – A review, 108, Palacios A., Cong L., Navarro M.E., Ding Y., Barreneche C., 32-52, Copyright (2019), with permission from Elsevier.*

The transient plane source method represents one of the most used techniques given the widest working interval in terms of measured thermal conductivities. The theoretical principles and a variant of the methods will be discussed hereinafter.

1.1.1.1 Transient plane source method

The transient plane source (TPS), also known as hot disk analyser or Gustafsson probe, is an experimental technique widely used for the determination of thermal conductivity and diffusivity [4,29,30]. The method ensures accurate measurements in a large interval of temperature (30-1200K) for materials with κ from 0.005 to 500 $W \cdot m^{-1} \cdot K^{-1}$ [26].

The apparatus (Figure 8) includes a constant voltage source (V), two voltmeters (V_1 and V_2), a standard resistor ($R_{e,s}$) and a sensor with its own resistance (R_e) [31,32].

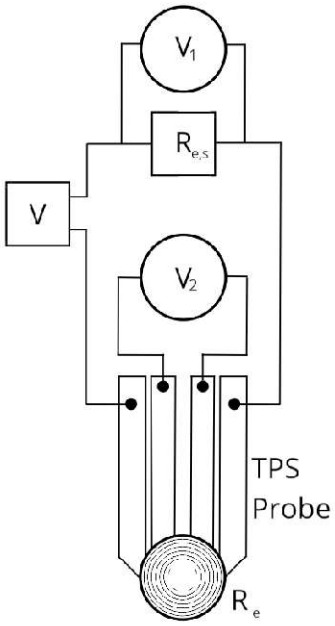


Figure 8. Scheme of TPS apparatus.

The sensor is made of a double spiral of nickel (10μm-thick with a diameter between 0.5 and 30 mm) encapsulated in between two Kapton® or mica films which act as support and guarantee electrical insulation [33]. The possibility to use different sensor sizes for the measurement allows the measurement for different sample sizes. Moreover, compared to other techniques, the required sample size is usually smaller [26,29]. In any case, some geometrical and morphological requirements must be taken in consideration. In fact, to perform the measure, the surface should be smooth and planar in order to ensure a proper thermal contact with the probe [29,31]. Furthermore, the testing parameters and setup should be defined according to the probing depth (D_p) which can be expressed as function of the material's thermal diffusivity and the measuring time set for the measurement [29,34]:

$$D_p = \beta(\alpha t)^{1/2} \quad (8)$$

where β is an integer constant according to the accuracy, α is the thermal diffusivity mm^2/s and t is the measuring time in s. In order to assume that the probe is surrounded by infinite sample in all the directions, the measuring time and the sample dimensions should be selected ensuring the following conditions [29]:

- sample width > $2 \cdot D_p$ + sensor diameter
- sample thickness > D_p.

Prior to the measure, the sensor is placed in between two samples (Figure 9) for a time sufficient to ensure the achievement of isothermal conditions and the testing parameters (output power and measuring time) are fixed. The output power has to be chosen, according to the κ value of the material, in order to ensure a total temperature increase between 2 and 5 K [33].

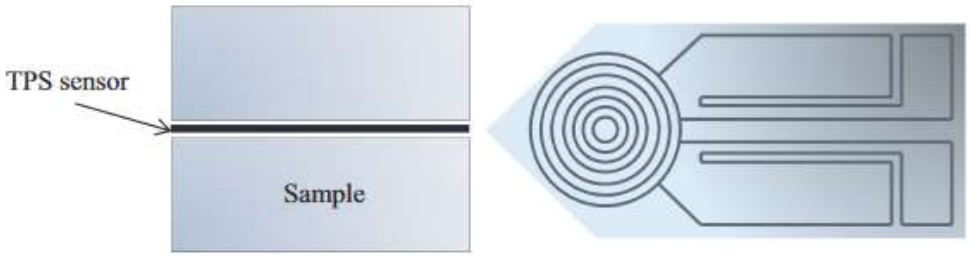


Figure 9. Schematic configuration of samples and TPS probe. *Reprinted from "Thermal conductivity measurement techniques for characterizing thermal energy storage materials – A review, 108, Palacios A., Cong L., Navarro M.E., Ding Y., Barreneche C., 32-52" Copyright (2019), with permission from Elsevier.*

The sensor has a double nature: heat source to increase the sample temperature and resistance thermometer in order to record the time-temperature dependence. In fact, during the measurement, a constant current is imposed in the spiral determining a temperature increase dependent on the heat capacity and thermal conductivity of the two samples in contact with the probe. Therefore, by recording the temperature variation of the sensor and its time dependence, the thermal properties of the sample can be extracted [30,31].

The measurement of the probe temperature increase is obtained by monitoring the increase in time of the thermal resistance of the nickel spiral $R(\tau_d)$ which can be express as

$$R(\tau_d) = R_0[1 + \alpha_{TCR}\Delta T(\tau_d)] \quad (9)$$

where R_0 is the initial electrical resistance, α_{TCR} is the temperature coefficient of resistance (TCR) of the probe calibrated prior the measure, and $\Delta T(\tau_d)$ is the mean temperature increase of the probe which consist in two contributions:

$$\Delta T(\tau_d) = \Delta T_s(\tau_d) + \Delta T_i(\tau_d) \quad (10)$$

where $\Delta T_s(\tau_d)$ is the temperature increase on the sample surface and $\Delta T_i(\tau_d)$ is the temperature drop between the nickel spiral and the sample-sensor interface which is assumed to be constant after a short initial time (Δt_{corr}) (Figure 10) [33].

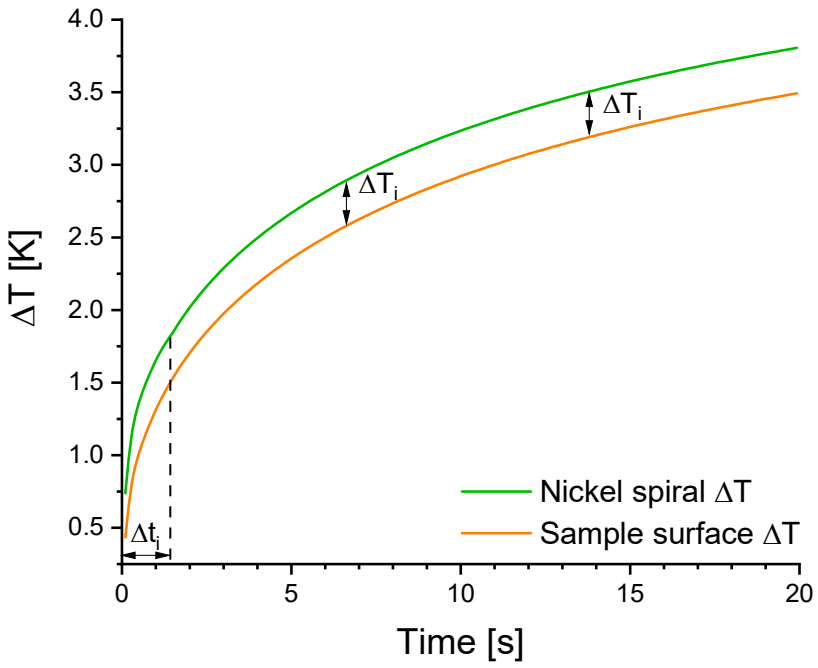


Figure 10. Temperature variation in the sensor and on the sample surface.

With the assumption that the sensor can be approximated by several concentric and equally spaced circular rings with zero thickness, the $\Delta T_s(\tau_d)$ is described by the following equation:

$$\Delta T_s(\tau_d) = \frac{P_0}{\sqrt{\pi^3} r \kappa} D(\tau_d) \tag{11}$$

where P_0 is the total output power, r is the radius of the double spiral on the outer concentric circle, κ is the thermal conductivity of the material. The dimensionless specific time function $D(\tau_d)$ is defined as:

$$D(\tau_d) = \frac{1}{[m(m+1)]^2} \int_0^{\tau} \sigma^{-2} d\sigma \left[\sum_{l=1}^{m} l \sum_{k=1}^{m} k \exp\left\{ -\frac{l^2 + k^2}{4m^2\sigma^2} \right\} I_0\left(\frac{lk}{2m^2\sigma^2} \right) \right] \tag{12}$$

where m is the number of spirals in the probe, σ is the integration variable, and I_0 is the modified Bessel function. The mean temperature increase $\Delta T(\tau_d)$ and the specific time function $D(\tau_d)$ are function of the dimensionless time (τ_d) which is defined as

$$\tau_d = \sqrt{\frac{t\alpha}{r^2}} \tag{13}$$

where t is the real time of the measurement and α is the thermal diffusivity of the testing material.

The optimal time of the measurement should ensure the relation:

$$0.3 \leq \frac{t\alpha}{r^2} \leq 1 \qquad (14).$$

On the basis of the previous relations described, the thermal properties can be derived by fitting the experimental data obtained for temperature $\Delta T(\tau_d)$ vs $D(\tau_d)$ which described a straight line and κ of the material can be extracted by its slope thank to the equation (11) [29,30,33]. Since the thermal diffusivity of the material is not known, the final curve is obtained by an iteration process which allows the derivation at the thermal conductivity and diffusivity from a single measurement [29].

1.1.1.2 Transient plane source method applied to thin films

The thermal conductivity of thin films of electric insulating material can be measured by TPS method thanks to a variant of the method used for bulk samples [4,31,35–38]. Compared to the other techniques which can be used to measure κ for thin films, the advantage of the TPS is the less stringent requirements in terms of sample size and shape and the unrequired pre-treatment of the sample surface [36]. However, in order to obtain an accurate values some requirements must be followed: thermal conductivity of the sample has to be lower than 2 $W \cdot m^{-1} \cdot K^{-1}$ and the film thickness should be in the range of 20 – 600 μm with thickness value known with an accuracy of 1 μm [36,37]. The thin film sensor differs from the conventional ones in terms of design. In fact, squared naked-nickel sensor can be used to increase sensibility or round with a different design of the nickel double spiral (an example is showed in Figure 11a) [37]. The setup of the measure is made up with the probe placed in between two thin films of the testing material and then sandwiched between two cylindric blocks of a thermally conductive background materials, which is usually stainless steel (Figure 11b) [35].

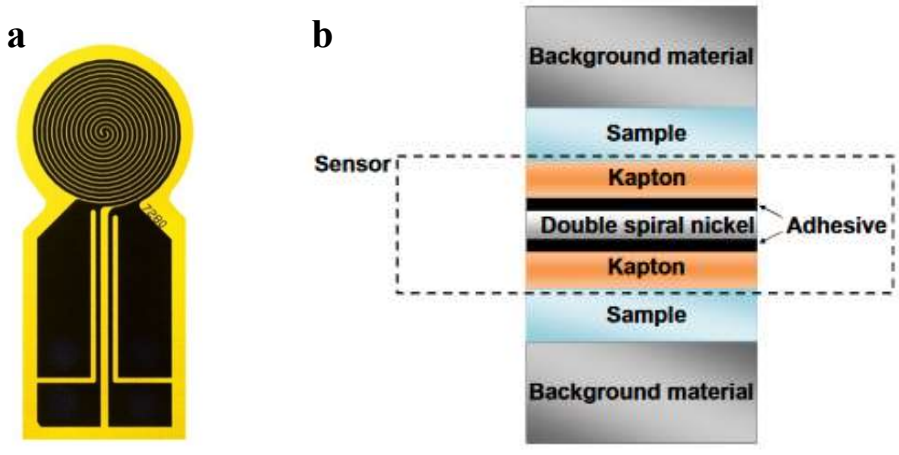


Figure 11. TPS sensor designed for thin film methods (a). Schematic configuration of the thin film measurement in TPS technique (b). *Reprinted from An improved transient plane source method for measuring thermal conductivity of thin films: Deconvoluting thermal contact resistance, 96, Ahadi M., Andisheh-Tadbir M., Tam M., Bahrami M., 371-380, Copyright (2016), with permission from Elsevier.*

Prior to measurement, the setup is assembled and it is left free to reach isothermal condition. Then the measure is performed: a current passes through the nickel spiral leading to a temperature rise, then the electrical resistance, which follows the equation (9), is recorded and in this specific configuration can be written as:

$$R(\tau_d) = R_0\left[1 + \alpha_{TCR}(\Delta T_{p-bm}(\tau_d) + \Delta T_{avg,bm}(\tau_d))\right] \quad (15)$$

where $\Delta T_{p\text{-}bm}(\tau_d)$ is the temperature difference between the probe surface and the background material and $\Delta T_{avg,bm}(\tau_d)$ is the average temperature increase of the background material surface. The term $\Delta T_{p\text{-}bm}(\tau_d)$ is found to be constant after a small interval, Δt_i, defined as:

$$\Delta t_i = \frac{h_{p-bm}^2}{\alpha_{p-bm}} \quad (16)$$

where $h_{p\text{-}bm}$ and $\alpha_{p\text{-}bm}$ are the overall thickness and the thermal diffusivity of the material between the probe and the background material respectively, *i.e.* the film samples, the Kapton foils, and the adhesive.

In this configuration, the temperature increase of the probe calculated from $R(\tau_d)$ during the measurement can be expressed as followed:

$$\Delta T(\tau_d) = \Delta T_{p-bm}(\tau_d) + \frac{P_0}{\sqrt{\pi^3} r \alpha_{bm}} D(\tau_d) \quad (17)$$

where α_{bm} is the thermal diffusivity of the background material.
After an initial time equal to Δt_i, the term $\Delta T_{p\text{-}bm}(\tau_d)$ becomes constant and the term $\frac{P_0}{\sqrt{\pi^3} r \alpha_{bm}}$ is constant for a given measurement configuration, therefore the equation (17) shows a linear dependence of $\Delta T(\tau_d)$ on $D(\tau_d)$. Once the measure is performed and the $\Delta T(\tau_d)$ is obtained, τ_d is calculated by the software allowing the derivation of $D(\tau_d)$ and the plot $\Delta T(\tau_d)$ vs $D(\tau_d)$. As abovementioned, the curve $\Delta T(\tau_d)$ vs $D(\tau_d)$ shows, after an initial transient state (Δt_i) where the heat is conducted across the Kapton foils and the sample, a linear dependency characterized by a slope equal to $\Delta T_{avg,bm}(\tau_d)$ and an intercept equal to $\Delta T_{p\text{-}bm}(\tau_d)$. Once $\Delta T_{p\text{-}bm}(\tau_d)$ is derived, the effective thermal conductivity (κ_{eff}) of the layers between the nickel spiral and the background can be calculated as followed:

$$\kappa_{eff} = \frac{P_0 h_{p-bm}}{2A\Delta T_{p-bm}} \quad (18)$$

where A is the probe surface area.

To extract the thermal conductivity of the thin film, the measure has to be performed in two steps. Firstly, the effective thermal conductivity of the Kapton®

layer and the adhesive ($\kappa_{Kapt+adh}$) is derived by a pre-test where the probe is directly place in between the two stainless steel cylinders. In the subsequent step, the thin films of the analysed material are place in between the probe and the cylinders and the effective thermal conductivity (κ_{eff}) of the layers contained between the nickel spiral and the background material (Kapton®, adhesive and sample) is derived. Finally, the thermal conductivity of the thin film (κ_f) is obtained thanks to the following relation:

$$R = R_f + R_{Kapt+adh} = \frac{h_f + h_{Kapt+adh}}{\kappa_{eff} A} = \frac{h_f}{\kappa_f A} + \frac{h_{Kapt+adh}}{\kappa_{Kapt+adh} A} \qquad (19)$$

where is R_f is the bulk resistance of the thin film, $R_{Kapt+adh}$ is the bulk thermal resistance of the Kapton foils and the adhesive, h_f is film thickness, and $h_{Kapt+adh}$ is respectively the thickness of the Kapton® and the adhesive [35,36].

The testing parameters should be chosen in order to ensure a temperature difference across the thin film ranged between 1 and 3 K. For this reason, the output power is usually fixed in the range of 1-3 W and, when stainless steel is used aa background material, the measuring time between 5 and 10 s [37]. Moreover, the stiffness of the material can affect the quality of the measurement. Flexible films lead to optimal measurement conditions since they could better fill the volume between the probe and the metallic cylinders, while for stiff materials it should taken into account that air gaps could be trapped between the different layers affecting the measured thermal conductivity. For these reasons, the application of mounting pressure in the setup could be beneficial in terms of accuracy [36,37].
It must be also considered that the thermal contact resistance between the films and the background material ($R_{c,bm-s}$), the films and the probe ($R_{c,s-Kapt}$), and the probe and the adhesive ($R_{c,adh-p}$) are neglected in the derivation of the equations and their contributions are included in the value of κ_f. For this reason, the κ_f results affected by a higher incertitude compared to the TPS measurement performed in bulk [35]. To overcome these effects and improve the accuracy of the method, Ahadi *et al.* proposed a procedure starting from the deconvolution of TCR in the TPS thin film setup [35]. In fact, they schematized the thermal resistance in the TPS setup as the contribution of the bulk thermal resistance (R_b) and the contact thermal resistance (R_c) of each contribution (Figure 12). Therefore, the total thermal resistance (R_{tot}) can be expressed as the sum of the contributions.

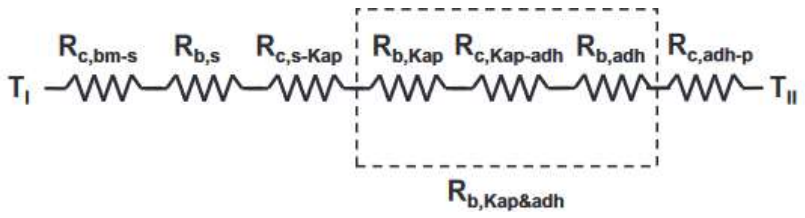


Figure 12. Deconvolution of the single effects contributing to the total thermal resistance in TPS thin film setup. *Reprinted from An improved transient plane source method for measuring thermal conductivity of thin films: Deconvoluting thermal contact resistance, 96, Ahadi M., Andisheh-Tadbir M., Tam M., Bahrami M., 371-380, Copyright (2016), with permission from Elsevier.*

Then the procedure is articulated in three steps: 1/enter h_f, $h_{Kapt+adh}$ and $\kappa_{Kapt+adh}$ in the software, 2/perform the measurement and obtain κ_f, and 3/ calculate the R from equation (19). Once the measurement is performed at least for two samples characterized by two different thicknesses, a correlation R_{tot} vs thickness can be obtained where the slope and the intercept correspond respectively to the thermal resistance of the bulk sample and the thermal resistance of the different contributions except the film one. The method described by Ahadi *et al.* has the advantage of measuring the bulk thermal conductivity of the thin film with higher accuracy and without the contribution of the TCR between the different layers. However, it requires multiple samples with different thicknesses which could potentially be unavailable [35].

1.1.2 Thermal conductivity of amorphous polymers

The fundamental of thermal transport in polymers has been presented in Chapter 1.1. Here, the main aspects regarding thermal conductivity in amorphous polymers will be discussed.

The importance of understanding the mechanisms underlying thermal transport in amorphous polymers resides in the possibility of precisely design materials with controlled thermal conductivity. However, it is not entirely understood yet and the definition of a model able to properly predict the bulk thermal conductivity in amorphous polymers remains challenging given the multitude of factors playing a role in its determination (Figure 13). Indeed, several factors have been recognized to play a role on thermal conduction, *e.g.* molar mass, morphology, chain orientation, side chains [4,6,9,39].

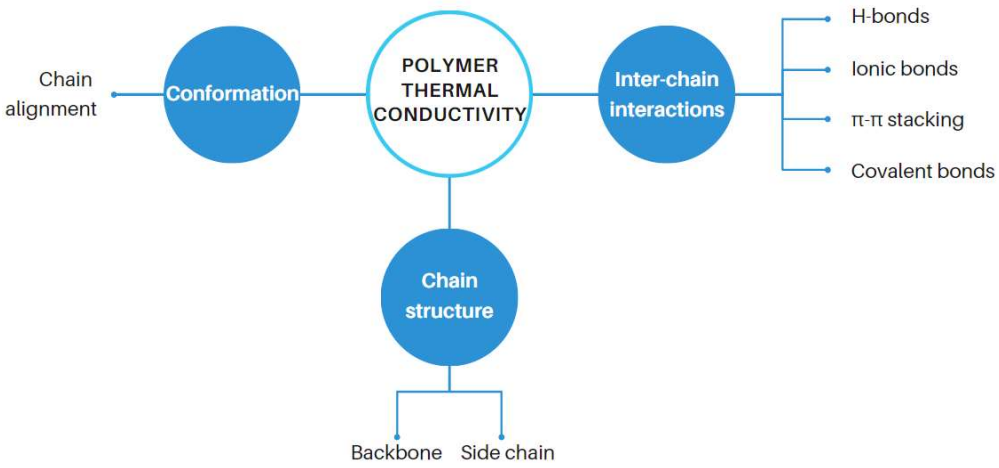


Figure 13. Physical factors determining the mechanism of thermal conduction in polymers.

Therefore, multiple studies have been conducted and reported in literature in order to identify a relationship between each parameter and the final thermal conduction; the main conclusions are reported in the current section.

The disordered structure typical of amorphous polymer causes an intense localization of vibrational modes which are responsible for the heat transfer

resulting in a scarce thermal conduction. Therefore, the possibility to act on chain orientation in order to increase the structural order and consequently the thermal transport has attracted attention in the scientific community [1,4]. Several methods have been explored in order to enhance chain alignment, *e.g.* mechanical stretching or thermal annealing [1]. For example, Singh *et al.* reported thermal conductivity equal to 4.4 $W \cdot m^{-1} \cdot K^{-1}$ for amorphous polythiophene, *i.e.* a 20 fold increase compared to the bulk value, obtained thanks to a strong chain orientation achieved due to the electro-polymerization of the fibres performed in nanochannels [14]. Canetta *et al.* obtained high degree of chain alignment in polystyrene (PS) fibres applying electrospinning process which led to a strong enhancement of thermal conduction, indeed κ passed from 0.15 $W \cdot m^{-1} \cdot K^{-1}$ for the bulk PS to more than 6.6 $W \cdot m^{-1} \cdot K^{-1}$ measured along the fibre axis [40].

As abovementioned, the macromolecular structure has a large influence on thermal conduction [1,4–6,9]. Zhang *et al.* investigated by MD simulations the role of chain conformation on thermal conduction in amorphous polymers [9]. They found that κ depends on by the radius of gyration: higher radius of gyration corresponds to more extended and stiff chains and thus more efficient heat transfer.

Another factor affecting the vibrational dynamics and therefore the bulk thermal conduction is the presence of side group on the main chain. In general, thermal conductivity decreases increasing the mass of the side group [1]. In fact, the addition of side chains theoretically leads to an increase of phonon localization and scattering events [1,41]. A study based on MD simulation in support of this has been reported by Ma *et al.* for amorphous bottlebrush polymers (Figure 14a). They showed that κ in the chain direction clearly decreases when the side chain length increases (Figure 14) [41].

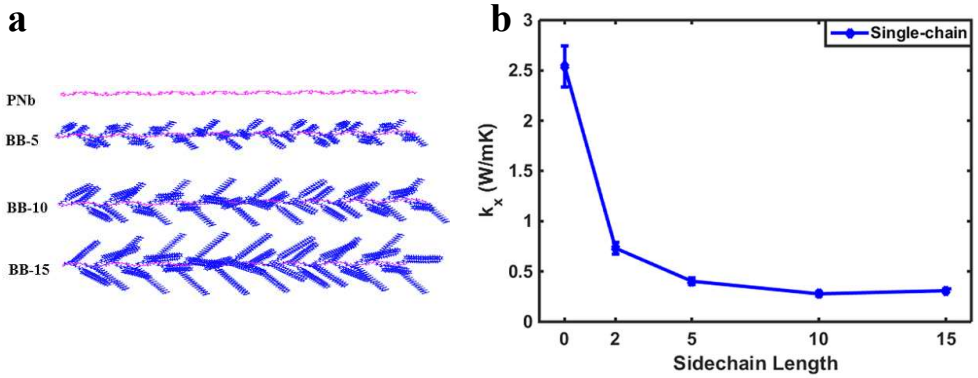


Figure 14. Structure of reference polymer (polynorbornene, PNb) and the bottlebrush (BB) polymers with different side chain length (a). Thermal conductivity along the chain orientation direction and its dependency on the length of the side chains (b). *Reprinted from Effects of polymer topology and morphology on thermal transport: A molecular dynamics study of bottlebrush polymers, 110, Ma H., Tian Z., 091903, Applied Physics Letters, 2017, with the permission of AIP Publishing.*

However, in some cases, the addition of a side chain could lead to an increase in thermal conductivity due to the induction of higher order in the structure [1,42–44]. For example, Guo *et al.* reported an increment of thermal conductivity about 160% in conjugated polymers when modified with long and linear side chain compared to short ones thanks to the achievement of higher degree of crystallisation [42].

Regarding the molar mass influence, Kiessling *et al.* reported the correlation between molar mass (M_w) and thermal conduction measured experimentally and predicted by MD simulations in PS and polyisobutylene (PIB) (Figure 15) [39]. For experimentally obtained values, a virtually constant value of κ is observed for the whole M_w range, while a stronger dependency on the M_w is observed in the values obtained by MD simulation for low values. In both cases, a constant value of κ is observed for high molecular weights.

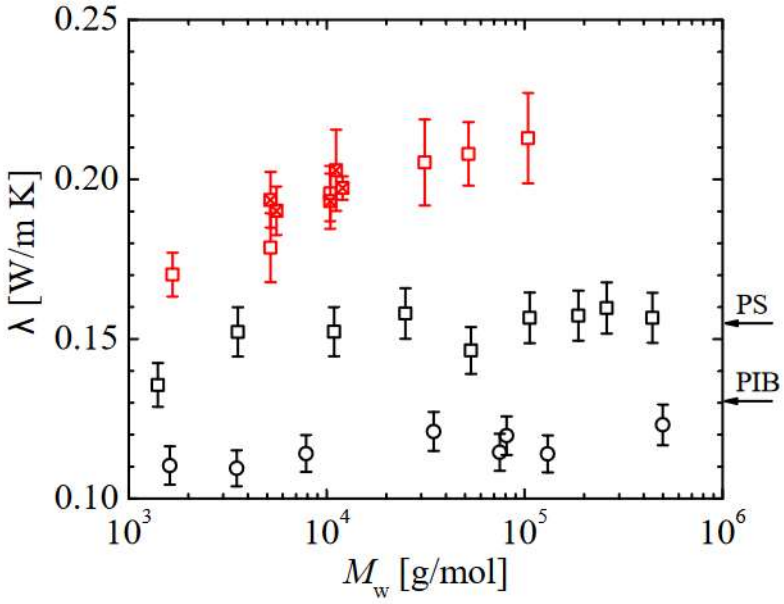


Figure 15. Thermal conductivity dependency on molecular weight. Experimental results for PS (□) and PIB (○), MD simulation results for monodisperse (□) and polydisperse (⊠) PS. *Reprinted from Thermal conductivity of amorphous polymers and its dependence on molecular weight, 228, Kiessling A., Simavilla D.N., Vogiatzis G.G., Venerus D.C., 123881, Copyright (2021), with permission from Elsevier.*

The MD results are in agreement with the well-established hypothesis of favoured thermal path along the main chain in amorphous polymers which should lead to a thermal conductivity strongly dependent on M_w, while the values obtained experimentally are in contrast. Indeed, as abovementioned, a deeper investigation of the mechanisms at the basis of thermal conduction is needed.

1.1.2.1 Effect of the strength of inter- and intra-chain interactions on thermal transport

The low thermal conductivity of polymers is attributable to the losses associated to weak inter-chain interactions and recurrent phonon scattering [6,8]. Therefore, the addition of strong inter-chain interactions to vdW ones could lead to an increase in thermal conductivity thanks to two effects: 1/improved inter-chain thermal conductance, 2/stiffening of the chain and consequential suppression of segmental rotation leading to lower scattering [4–6,8].

Xie *et al.* reported a correlation between the intermolecular bonding strength and thermal conductivity [45]. Indeed, they reported thermal conductivity for several amorphous polymers characterized by the same backbone and different side

groups to define different types of inter-chain bonds (Figure 16). Among the others, PS and PMMA showed the lowest values, owing the weak vdW secondary interactions. Moreover, PS is characterized by a lower κ compared to PMMA according to the presence of C=O bond in PMMA characterized by a slightly higher polarity compared to the C-H covalent non-polar bonds present in PS [45]. A second group of materials composed by H-bonded polymers (polyvinylalcohol (PVA), polyacrylic acid (PAA), and polyvinylphosphonic acid (PVPA)), showing κ values in the range between 0.3 and 0.5 $W \cdot m^{-1} \cdot K^{-1}$. Also in this case, the trend appears representative of the strength of inter-chain interactions. Indeed, the lower κ is presented by PVA and PAA, then a higher value is found for PVPA which is characterized by a higher amount of H-bonds [45]. The last group of polymers characterized by the highest conductivity is then represented by the polymer salts, *i.e.* PAA and PVPA calcium and lithium salts. In fact, the presence of stronger ionic bonds, compared to vdW and H-bonds, results in an improved thermal conductivity. In addition, it is possible to identify a nearly linear correlation between κ and the speed of sound, as suggested by equation (5) [45].

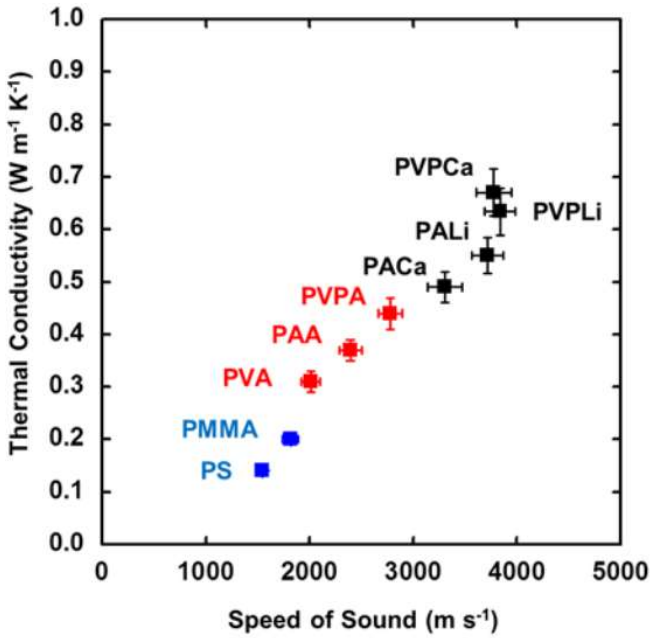


Figure 16. Thermal conductivity as function of sound speed for different classes of polymers characterized by different inter-chain interactions. *Reprinted figure with permission from "Xie X., Yang K., Li D., Tsai T.-H., Shin J., Braun P.V., Cahill D.G., High and low thermal conductivity of amorphous macromolecules, Phys. Rev. B, 95, 035406, 2017" Copyright (2017) by the American Physical Society.*

Different studies have been performed to further elucidate the effect of H-bond introduction on thermal conduction [1,4,8,45–48]. Xie *et al.* reported thermal conductivity for a set of water-soluble polymers, *i.e.* PVA, PAA, polyacrylamide (PAM), poly(vinylpyrrolidone) (PVP), methyl cellulose (MC), poly(4-styrenesulfonic acid) (PSS), and two non-water-soluble polymers, poly(*N*-acryloyl piperidine) (PAP), PMMA (Figure 17a) [47]. The authors measured the highest thermal conductivity for water-soluble polymers due to their ability to form inter-

chain H-bonds (Figure 17b). Moreover, the highest values corresponds to the polymers characterized by higher H-bonds concentration, *i.e.* 0.37 $W \cdot m^{-1} \cdot K^{-1}$ for PAA, 0.38 $W \cdot m^{-1} \cdot K^{-1}$ for PAM and PSS [47].

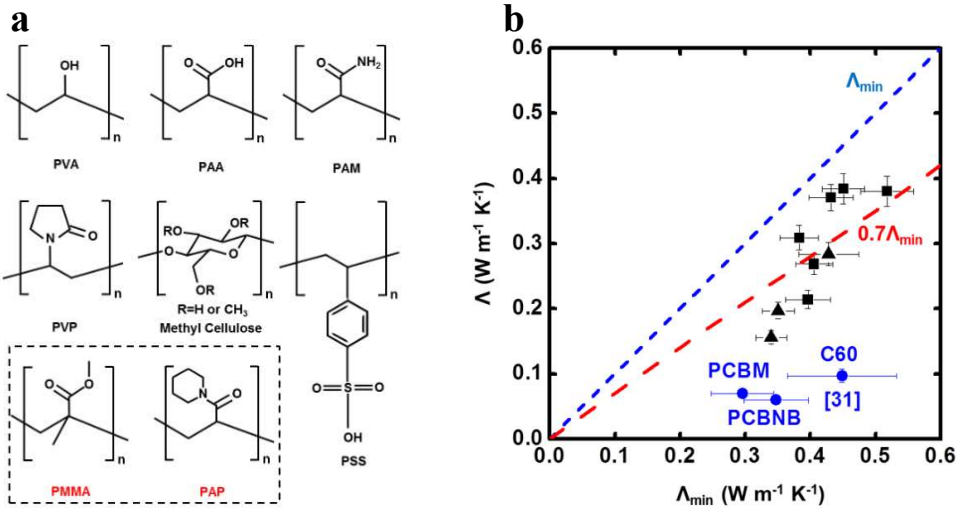


Figure 17. Chemical structures of the analysed polymers (a). Measured thermal conductivity of a function of the calculated minimal one for water-soluble polymers (■) and non-water-soluble polymers (▲). The blue short dashed line corresponds to the minimal thermal conductivity, and the red ones shows the best fit linear relationship. *Reprinted with permission from "Xie X., Li D., Tsai T.-H., Liu J., Braun P.V., Cahill D.G., Thermal Conductivity, Heat Capacity, and Elastic Constants of Water-Soluble Polymers and Polymer Blends, Macromolecules, 49, 972-978, 2016". Copyright 2016 American Chemical Society.*

Mu *et al.* blended PVA with gelatin and lignin and attributed the enhancement (about 184% compared to pristine PVA) of thermal conductivity to the formation of a continuous coils via H-bonding (Figure 18) [48]. This work confirmed that the presence of a continuous thermal path is fundamental in amorphous polymer to achieve better thermal conductive performance [48].

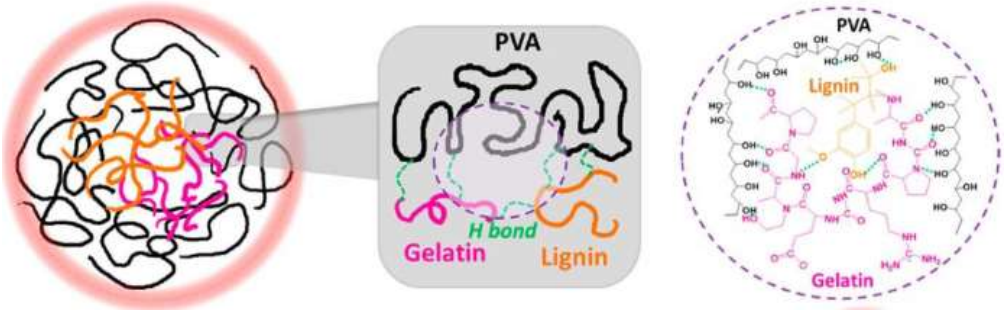


Figure 18. Intermolecular connection via H-bonding in PVA/gelatin/lignin blend. *Reprinted with permission from "Mu L., He J., Li T.J., Mehra N., Shi Y., Zhu J., The Molecular Origin of Efficient Phonon Transfer in Modulated Polymer Blends: Effect of Hydrogen Bonding on Polymer Coil Size and Assembled Microstructure, J. Phys. Chem. C, 121, 14204-14212, 2017". Copyright 2017 American Chemical Society.*

Kim *et al.* reported an enhanced thermal conduction in amorphous blends related to the establishment of inter-chain H-bonds [46]. They showed that the achievement of a homogenous distribution of inter-chain interactions able to efficiently transfer the heat led to a large improvement of thermal conductivity with a value close to

1.5 $W \cdot m^{-1} \cdot K^{-1}$ in PAP:PAA blends (Figure 19a). This configuration can be reached under specific conditions, *i.e.* homogenous distribution of H-bonds, interpenetration of the two blend components (Figure 19b), and optimal blend composition.

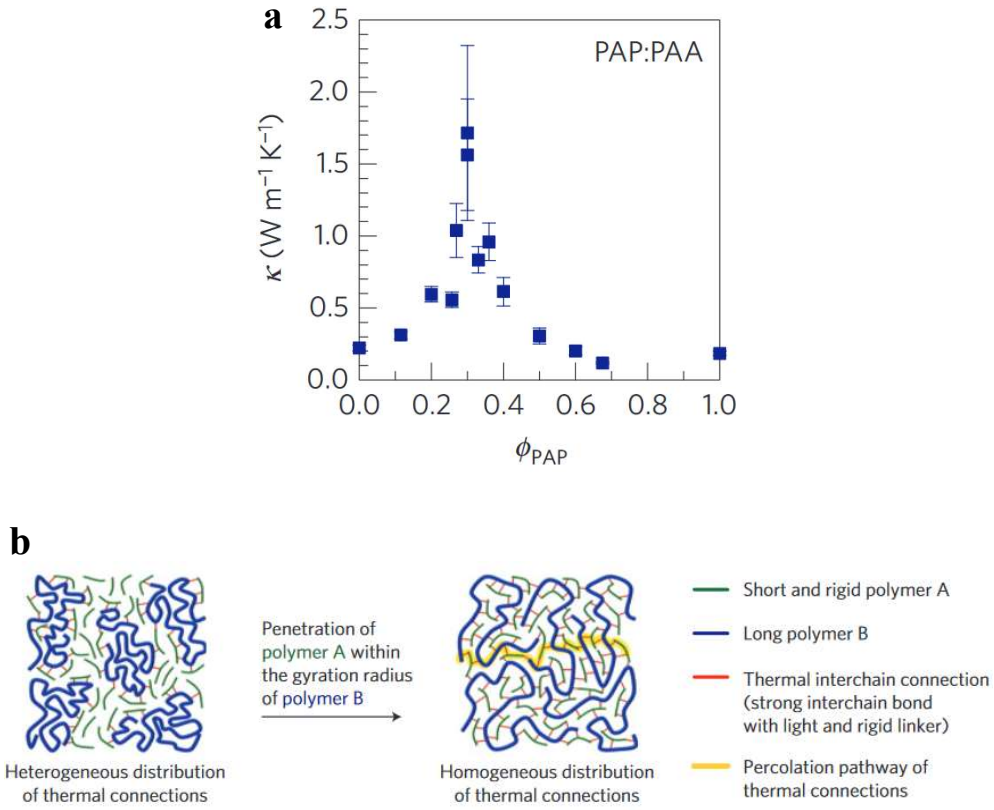


Figure 19. Thermal conductivity variation according to the composition in PAP:PAA blends (a). Schematic illustration of thermal path in heterogeneously and homogeneously distributed inter-chain thermal connections (b). *Reproduced from [46] with permission from Springer Nature.*

However, it has to been taken into account that the introduction of H-bonds is not sufficient to enhance thermal transport. In fact, the system has be designed in order to guarantee a continuous thermal network (Figure 19) [1,46]. Indeed, in the studies reported by Kim *et al.*, the thermal conductivity variation was evaluated in different polymeric blends characterized by different H-bonding conditions. As abovementioned, the enhancement of thermal conduction is reported only when a homogenous distribution of thermal links is obtained and the inter-chain interactions are established by short chemical linkers [46].

The effect of inter-chain ionic bonding on thermal conductivity in neutralized PAA has been also investigated by Shanker *et al.* [49]. They reported the effect of pH variation on thermal conductivity for PAA and PVP (Figure 20), where PVP was used as negative control given the absence of ionizable units in the chain. In fact, in PAA, a different pH can be associated with a different degree of neutralization, as confirmed by the IR spectroscopy (Figure 20b). Therefore, it is clear that higher values of κ, found at higher pH, can be associated to the higher content of ionic bonds. These authors also associated the different thermal

conduction to the different chain conformations induced by the neutralization. Indeed, the ionized PAA chains are more extended at the molecular level compared to the coiled pristine PAA ones due to the presence of repulsive coulombic forces (Figure 20c).

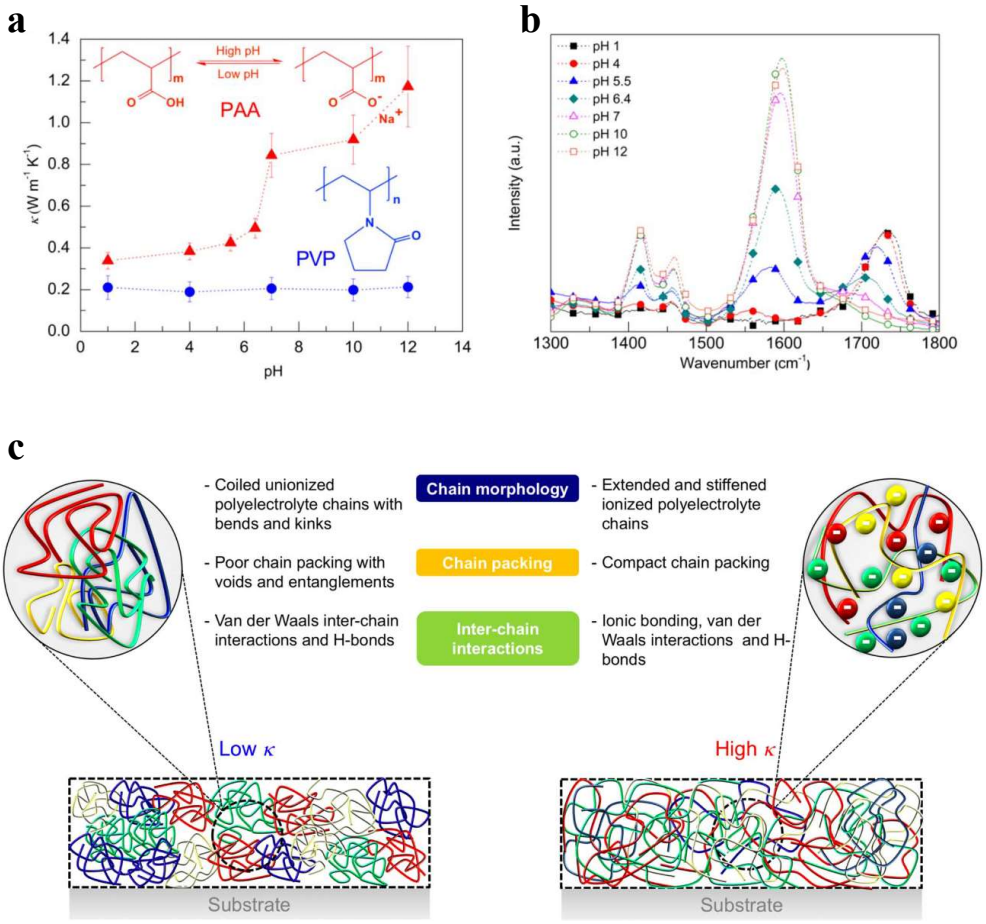


Figure 20. Thermal conductivity as function of pH in ionizable PAA and non-ionizable PVP (a). IR spectra of PAA films manufactured at different pH corresponding to different neutralization degrees as showed by the intensity of the peak at 1594 cm^{-1} corresponding to the neutralized unit (b). Schematic illustration of chain conformation in polymer PAA films and factors affecting thermal conduction: unionized PAA (left) and ionized PAA (right) (c). *Reproduced from [49] in agreement with Creative Commons Attribution-Non Commercial license.*

Xu *et al.* reported an improved thermal conduction and moderate electrical conductivity in conjugated poly(3-hexylthiophene) via strong inter-chain π-π stacking [23]. Indeed, they measured a κ of 2.2 $W \cdot m^{-1} \cdot K^{-1}$ and hypothesized that the presence of inter-chain π-π stacking is responsible for the enhanced thermal transport in the designed macromolecular structure.

Regarding covalent bonds, MD simulations have been performed showing a higher thermal conduction in crosslinked materials [6]. Even if the introduction of inter-chain covalent bonds should be beneficial in terms of thermal transport, it must be taken into account that it could also lead to an increase of scattering events. In fact, for example in the case of PE, the experimental results contradict the MD simulations [6,50]. MD simulations studies predict a thermal conductivity

enhancement with increasing the crosslinking density. However, at the same time, thermal conductivities measured experimentally result in values which decrease increasing the crosslinking density, likely due to a reduction of the degree of crystallinity. Instead, Tang *et al.* reported tuneable thermal conductivity in polyacrylamide hydrogel which is improved increasing the crosslinking density, in agreement with the theorical predictions [51]. Despite the necessity of further investigations, it has been already widely demonstrated that the increase of inter-chain interactions strength results beneficial in terms of heat conduction in amorphous polymers.

1.1.2.2 Polymethacrylates as amorphous polymer model

The terms methacrylate refers to salts or esters of methacrylic acid (Figure 21) [52]. Polymethacrylates represent a class of materials employed in various fields, *e.g.* biomedical implants, electronic applications, etc. Their physical and chemical properties can strongly vary depending on the nature of the substituents of the side chain. Moreover, the presence of the α-methyl group directly bonded on the main chain (Figure 21) prevents the crystallization and free rotation around the C-C backbone leading to an amorphous structure [53].

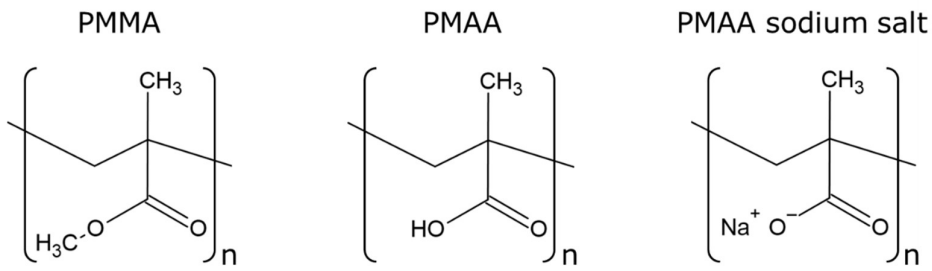


Figure 21. Esters (left) and salts (right) of poly methacrylic acid (PMAA).

The ester of polymethacrylic acid (PMAA), polymethylmethacrylate (PMMA), is currently the most used methacrylate polymer thanks to the combination of its physical and chemical properties [52–54]. Indeed, it is characterized by optical transparency, high thermal stability (in the range -70–100°C), and easy processability [52,54]. Furthermore, it shows a good resistance to chemical (*e.g.* strong acids and bases), UV lights, and humidity. Also, given its structure, usually polar organic solvents are suitable for PMMA dissolution, *e.g.* tetrahydrofuran (THF), *N,N*-dimethylformamide (DMF), and chloroform ($CHCl_3$). PMMA can be obtained by the polymerization of methyl methacrylate by different techniques, *i.e.* bulk, solution, suspension or emulsion, based on radical or anionic polymerization starting from the reaction of the monomer vinyl bond [53]. The general mechanism behind the radical polymerization of PMMA will be presented in Chapter 3.

In general, thanks to its optical transparency, relatively high Young's modulus and biocompatibility, the main application of PMMA regards the its use in the production of transparent rigid packaging and in the biomedical field [52–54].

At the same time, PMAA and its salts, also known as polymethacrylic electrolytes, are mainly used in the preparation of hydrogels thanks to their capacity to by swollen by a large amount of water. In PMAA, the water uptake is also possible thanks to the establishment of H-bonds between the polymer chain and water molecules. In addition, the presence of the side carboxylic group gives them high biocompatibility and antibacterial properties. Therefore, they have been widely investigated to be used in biomedical applications [52,55].

Thanks to the possibility to be easily synthesised by copolymerisation with other monomers, polymethacrylates offer a combination of different properties easy to be achieved [52,54]. Moreover, given their amorphous structure, they are good candidates for the design of a system in which the evaluation of a single factor on the final properties can be investigated. Indeed, the absence of crystalline phase, which shows a distinct additional contribution, allows an easier isolation of the contribution of a single factor, *i.e.* the introduction of H-bond forming groups or reinforcing agents. For example, the effect of the introduction of H-bonds between polymethacrylate chain has been already reported in different PMMA-based copolymers. The main modification obtained following the introduction of H-bond forming groups is the influence on the macromolecular mobility which causes an increase in terms of T_g [56,57]. In fact, when MMA is copolymerised with comonomers such as methacrylic acid (MAA), methacrylamide, or 2-ureido-4[1*H*]-pyrimidinone methyl methacrylate (UPyMA), a large positive deviation from the theoretical calculation of T_g is observed and can be correlated with the presence of intermolecular H-bonds [56,58–60]. Furthermore, the effect of ionic interactions had been reported in literature, mainly for copolymers of methyl methacrylate and methacrylic acid (polymethylmethacrylate-*co*-methacrylic acid PMMA-*co*-MAA). The changes of properties in this type of polymers are correlated with the charge density, type of cation, and neutralization degree. Tsou *et al.* investigated the relationship between charge density and mechanical properties in neutralized PMMA-*co*-MAA copolymers when blended with PMMA [61]. They proved that the addition of the neutralized copolymer leads to better mechanical properties acting as reinforcement agent, *i.e.* higher tensile modulus, fracture toughness, and better thermal stability. In a similar way, Nah *et al.* found for sodium neutralized PMMA-*co*-MAA that the rubbery modulus increases with increasing the ion content and the rubbery plateau shifts to higher temperature thanks to the ionic bonds introduced between chains [62]. For the same copolymer, Ma *et al.* studied the influence of different type of cations on the mechanical properties, *i.e.* sodium and calcium [63]. They observed in both cases, a reinforcing effect in the rubbery state with a more extended rubbery plateau for the calcium neutralized form thanks to the stronger ionic interactions established.

Regarding bulk thermal conductivity, the thermal transport in amorphous polymer has been discussed above. For PMMA, thermal conductivity has been widely reported in literature: 0.20 $W \cdot m^{-1} \cdot K^{-1}$ [21,47,64–68]. At the beginning of this section dedicated to the state of the art, the achievement of enhanced thermal conductivity in PMMA has been discussed only concerning the preparation of various composites and nanocomposites using a thermo-conductive filler [69–73].

However, despite polymethacrylates allow an easy replacement or introduction of different interchain interactions (*i.e.* vdW, H-bonds, ionic bonds) and it has been already proved that a relation between them and thermal conduction in amorphous polymers exists, a systematic study on the evaluation of thermal conductivity variation in this class of polymers is still lacking.

1.2 Polymer nanocomposites for tailored properties

Nanocomposite materials have been intensively studied in the last decades thanks to their promising combination of final properties and the possibility to be proposed for a wide range of applications, *e.g.* electronics, automotive, medical, etc. [74,75]. The different types of nanocomposites can be classified by the nature of the matrix, *i.e.* ceramic, metallic, or polymer-based. In this work, we will focus on polymer nanocomposites. The addition of nanoparticles in polymer matrices has been reported to enhance various properties, such as tensile strength, thermal stability, chemical resistance, thermal or electrical conductivity [74–78]. Nanoparticles are usually in form of spheres, fibres, or whiskers from natural or synthetic materials and are characterized by at least one dimension in the nanometric scale (<100 nm) [76,78,79]. The peculiarity of the nanosized fillers is the high surface to volume ratio exhibited which usually results in enhanced properties compared to the traditional composite materials [75].

The achievement of a proper nanofiller dispersion is essential in order to take advantage of the potential of nanoparticles (from individual to percolated aggregates dispersion state). For this reason, the preparation method must be carefully selected according to the matrix processability, type of nanoparticles to be dispersed, and desired final properties [75,80]. Considering the multitude of matrices and nanofillers, polymer nanocomposites can be prepared from very different methods. Between them, the mainly used ones can be grouped in *in situ* polymerization and blending methods [81,82]. The *in situ* polymerization involves polymer chains growing in the presence of the nanoparticles which are dispersed in the reactive monomers mixture [75,81]. A scheme of the process is offered in Figure 22. One of the advantages of this preparation technique is the possibility to consider high nanoparticles contents [80,81].

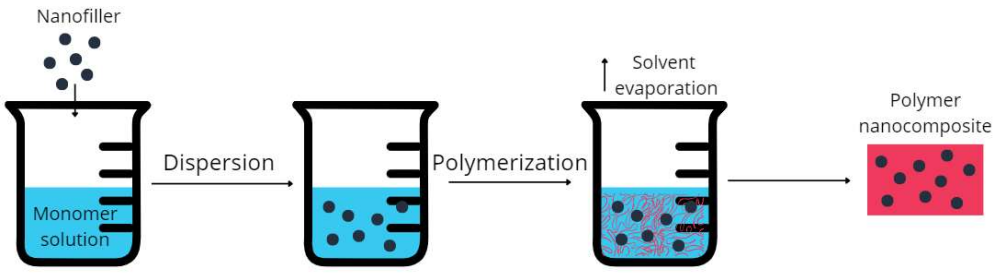


Figure 22. Scheme of polymer nanocomposite preparation by *in situ* polymerization.

Dispersion by blending process is widely used due to the simplicity of the method and can be performed either in solution or in molten state. In solvent blending, the

dispersion is achieved in a solvent where the two components can be properly dissolved or suspended. The process has three steps: 1/ dispersion of nanofiller in a good solvent for the matrix, 2/mixing with the polymer, and 3/solution casting to allow solvent evaporation. The energy to promote homogenous dispersion can be provided in different ways, *e.g.* by ultrasound or magnetic stirring [75,81]. It must be also taken into consideration that the use of excessive power could lead to a reduction of the nanofillers aspect ratio. A good dispersion can be obtained by solvent mixing. However, a common solvent should be found, possibly easily removable, and aggregation of the nanoparticles may occur upon solvent removal [75,81]. Melt blending involves the use of polymer processing tools, such as extruders, which lead to the dispersion of nanoparticles in the molten polymer thanks to the application of a shear forces. This solvent-free process is suitable for the matrix/nanofiller combinations for which a common solvent cannot be identified. Direct mixing in the molten state usually leads to the achievement of a good dispersion as the polymer chains/nanofiller surface interactions are achieved, *e.g.* by surface grafting. However, aggregation may occur at relatively high nanoparticles loading [80]. Moreover, one of the main challenges is the necessity to induce the break of the nanofiller aggregates directly in the molten state [75,81].

Different reviews have been published about the potential applications of polymer nanocomposites [74,77,78,78,81,83–86]. For examples, Kausar *et al.* reported the state of the art of polymer nanocomposites designed for packaging applications in particular in electronics and food industry [83]. Indeed, the addition of nanoparticles can lead to some properties required for these applications, *i.e.* barrier properties (reduced oxygen and moisture permeability) and mechanical reinforcement. Kumar *et al.* described the advantages in terms of mechanical properties of CNTs and graphene-based nanocomposites, *i.e.* increase of tensile and flexural strength and fracture toughness [84]. Shameem *et al.* reviewed the nanocomposite preparation and potential applications for solar cells to microbial applications [78].

Considering the aim of this work, a deeper investigation regarding the design of polymer nanocomposites to enhance thermal conduction will be developed in the next section. The actual knowledge about the mechanisms behind the heat conduction in such materials will be firstly described. Next, a brief description of the many factors governing the nanocomposite thermal conductivity will be presented.

1.2.1 Thermal conduction in polymer nanocomposite

Focusing on thermal properties and in particular on thermal transport mechanism, the preparation of nanocomposites has been a promising strategy in order to improve thermal conductivity of polymers thanks to the addition of thermo-conductive fillers. It is important to keep in mind that the thermal conductivity of the designed nanocomposites will depend not only on the intrinsic conductivity of the components, but also on multiple factors such as the amount of filler, the dispersion state, and the matrix/filler interactions [1,2,4,10]. Moreover, the

variation of nanoparticles concentration has an impact also on the possibility to form a network which significantly affects the thermal transport in the final material. For all these reasons, the description of a mathematical model able to efficiently predict the final value of thermal conductivity remains challenging [1,10]. The main models will be briefly presented, starting from the parallel and the series models which are usually applied in order to define an upper and a lower limit of the expected values. The models currently used can be divided in two main categories: 1/analytical models, 2/finite elements models [4]. In analytical models the composite thermal conductivity is expressed by constitutive equations as a function of the matrix and filler ones usually using morphological approximations. The easiest approach is based on the use of parallel and series models. The parallel model, also known as linear mixing rule, is founded upon the assumption of a uniform temperature gradient and a heat flux coming from the sum of the matrix and filler heat fluxes proportional to their volume fractions. The composite thermal conductivity (κ_c) can be calculated as follows [4,87]:

$$\kappa_c = (1 - \Phi)\kappa_m + \Phi\kappa_f \tag{20}$$

where κ_m and κ_f are respectively the thermal conductivities of the matrix and the filler and Φ is the volume fraction of the filler. The series model, also known as inverse mixing rule, assumes a uniform heat flux and a temperature gradient which is the weighted sum of the matrix and filler ones. The κ_c is given by the equation [4,87]:

$$\kappa_c = \left[\frac{(1 - \Phi)}{\kappa_m} + \frac{\Phi}{\kappa_f}\right]^{-1} \tag{21}.$$

Both models are based on the assumption of an independent contribution from each phase and a perfect transfer at the matrix/filler interface. Therefore, the parallel model often results in an important overestimation of the composite thermal conductivity, while the series model underestimates it. However, experimental values usually fall in between the two predictions which can be effectively considered as an upper and lower limit. Based on series model, different more complex models have been proposed. These models usually rely on the effective medium theory (EMT) which considers the composite as a uniform medium where filler particles are non-interacting. The first EMT model was proposed by Maxwell-Garnett who described the composite thermal conductivity through the following equation [4]:

$$\kappa_c = \kappa_m \left[1 + \frac{3\Phi(\delta - 1)}{2 + \delta - \Phi(\delta - 1)}\right] \tag{22}$$

where

$$\delta = \kappa_f / \kappa_m \tag{23}.$$

Adequate predictions are given by Maxwell-Garnett's equation in the limit of spherical particles for low content and good dispersion [87]. Next, Bruggeman's model has been introduced in order to take into account the interactions between the particles which can affect the thermal transport [4]:

$$\Phi \left[\frac{\kappa_f - \kappa_c}{\kappa_f - 2\kappa_c} \right] + (1 - \Phi) \left[\frac{\kappa_m - \kappa_c}{\kappa_m - 2\kappa_c} \right] = 0 \tag{24}.$$

Bruggeman's equation describes a non-linear trend of the composite thermal conductivity as function of the filler content (Figure 23): for low particles content the composite thermal conductivity depends on the matrix one, while for high loadings it reaches the filler one.

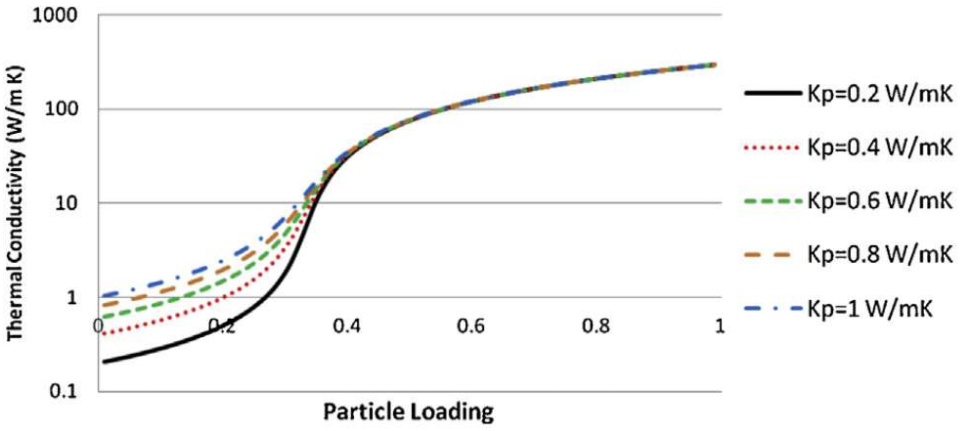


Figure 23. Composite thermal conductivity from Bruggeman's prediction as function of the particle content for different matrix thermal conductivities (Kp). *Reprinted from Thermal conductivity of polymer-based composites: Fundamentals and applications, 59, Chen H., Ginzburg V.V., Yang J., Yang Y., Liu W., Huang Y., Du L., Chen B., 41-85, Copyright 2016, with permission from Elsevier.*

Compared to the Maxwell-Garnett's equation which is a good approximation at low filler fraction, Bruggeman's model is able to give a better prediction for larger filler contents. However, the main limitations of Maxwell-Garnett's and Bruggeman analytical models are in neglecting the interfacial thermal resistance and the approximation of nanoparticles morphology. This leads to predictions which usually result higher than the experimental values [4,87]. Indeed, based on the equations (22) and (24), various models have been proposed in order to obtain a better approximation of the value considering other parameters as the nanoparticle shape and interfacial thermal resistance, details can be find elsewhere [4,87–90]. Recently, finite element models based on numerical approaches have been proposed to predict composite thermal conductivity with higher accuracy since they are able to take into account the real morphology of the composite. However, the composite

morphology must be known and, as for the analytical models, a critical issues is represented by the interfacial thermal resistance which is neglected [4]. The interfacial thermal resistance is referred to the heat carriers backscattering phenomenon observed at the interface matrix/filler, due to a difference in their quantum states, which leads to a loss in terms of thermal conduction [4]. The models which take into account interfacial thermal transport are based on Kapitza's theory whom firstly observed a loss of thermal transport at the metal-liquid interface, more details can be found in literature [4,88,91–93]. In any case, the prediction of thermal conductivity for composites remains challenging and the actual models usually result in an overestimation of the value [4,10,87].

The most common nanoparticles used in order to improve thermal conduction can be divided according to their chemical nature in three main categories: metallic, ceramic, and carbon-based nanoparticles [1,2,4]. Metallic nanoparticles are usually copper, silver, or aluminium fibers or particles [1,2]. However, the addition of metallic particles to a polymer matrix usually determines an increase of weight and electrical conductivity which may be not desirable in some applications and could lead to processability issues [2]. Ceramic nanofillers are often preferred especially in electronic applications, considering their high thermal stability and the electrical insulation properties. They can be oxide or nitride from aluminium, boron, or silicon and their thermal conductivity is usually between 260 and 320 $W \cdot m^{-1} \cdot K^{-1}$. In addition, carbon-based fillers as carbon black, graphite, and carbon nanotubes, have attracted considerable attention thanks to the possibility to preserve lightness and obtain high thermal conductivity along with electrical conduction [1,2]. Indeed, they are characterized by high thermal conductivity, *e.g.* 1000-3000 $W \cdot m^{-1} \cdot K^{-1}$ for CNT [94–96] and close to 800 $W \cdot m^{-1} \cdot K^{-1}$ for graphite [97].

Besides the filler thermal conductivity, other factors play an important role in the determination of composite thermal conductivity, *i.e.* aspect ratio and nanofiller content and distribution. The composite thermal conductivity usually increases with a non-linear dependency with the increase of the filler content, as shown by the Bruggeman's model. Few attempts have been done in order to describe the changes of thermal conductivity in terms of percolation theory [4,98,99]. The latter has been widely applied for electrical conductivity in nanocomposite where nanoparticles characterized by high aspect ratio show a sharp enhancement of properties for a small variation of filler content as a percolative network is formed. However, despite the similitude in the two transport properties, *i.e.* electrical and thermal ones, the increase observed in the thermal conductivity are considerably smoother compared with the electrical ones [4]. Indeed, given the important role played by the interfaces and their quality in thermal transport, it must be taken into account that the absence of contact between the nanoparticles, *i.e.* a physical percolation, and the loss of conduction at each interface are responsible for a decrement of the final value in a greater extent compared to electrical conduction. Therefore, given the controversial results and interpretations found in literature, the validity of the percolation theory applied to thermal conduction in nanocomposites remains doubtful [4].

Also, it must be taken into account that the high thermal conductivity of the nanofillers will not always lead to high thermo-conductive nanocomposites. Indeed, as abovementioned, the thermal resistance at the interface matrix/nanoparticle could lead to a significant loss in terms of heat conduction. Therefore, surface functionalization has been proposed as a strategy in order to maximize the effect of the nanoparticles addition aiming to reduce the thermal contact resistance by ensuring good interfacial interactions [1,2,4,9]. Various studies have proved that increasing the strength of matrix/nanoparticle interfacial bonding leads to a more efficient heat conduction through the interface. Luo *et al.* investigated the effect of the strength of matrix/nanoparticle interactions on thermal conductivity in PP filled with graphene and graphite [100]. Indeed, they calculated interfacial thermal conductance by MD simulations and found that the increase of the strength of matrix/nanoparticle interactions can improve the interfacial thermal conductance (Figure 24).

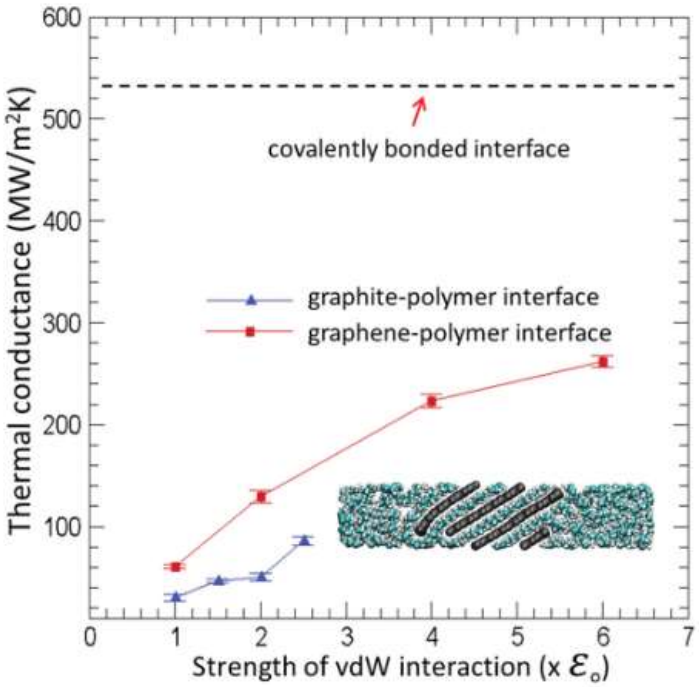


Figure 24. Interfacial thermal conductance in PP-base nanocomposites as a function of van der Waals strength. *Reprinted from Enhancement of Thermal Energy Transport Across Graphene/Graphite and Polymer Interfaces: A Molecular Dynamics Study, 22, Luo T., Lloyd J.R., 2495-2502, Copyright (2012), with permission from John Wiley and Sons.*

Yu *et al.* reported the role of different types of functionalisation of boron nitride (BN) nanoplatelets [101]. Indeed, these authors prepared a nanocomposite whose thermal conductivity depends on the strength of the interfacial interactions, *i.e.* weak for pristine BN, intermediate for BN functionalized with octadecylamine (BN-ODA), and strong covalent bonds for BN functionalized with hyperbranched aromatic polyamide (BN-HBP) (Figure 25). Indeed, compared with the neat matrix, the lowest thermal conductivity increase was reported for pristine BN, whereas a

large enhancement was observed for BN-ODA. The large effect was noticed for BN-HBP due to a better dispersion state and a good interfacial thermal conductance.

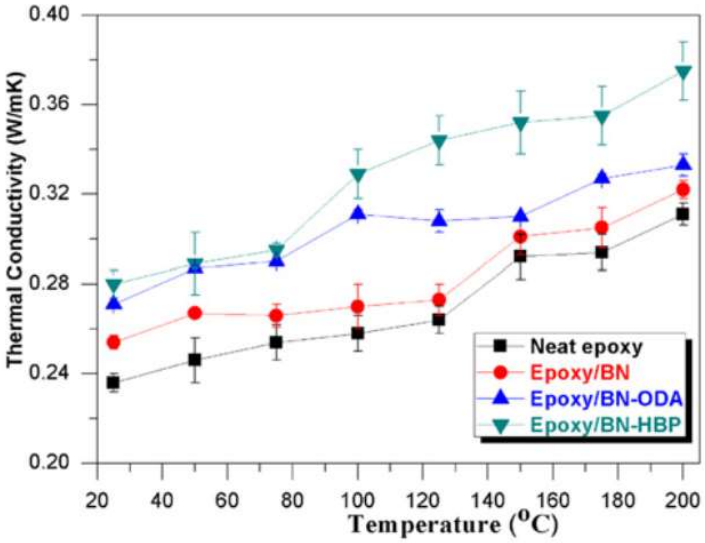


Figure 25. Thermal conductivity in pristine epoxy resin and in its nanocomposites (with 5wt% of BN) according to BN surface functionalization. *Reprinted from Interfacial modification of boron nitride nanoplatelets for epoxy composites with improved thermal properties, 53, Yu J., Huang X., Wu C., Wu X., Wang G., Jiang P., 471-480, Copyright 2012, with permission from Elsevier.*

Besides the nanoparticles traditionally proposed in the design of thermo-conductive nanocomposites, there has been growing attention to the possibility to enhance thermal conductivity in fully organic nanocomposites [18,102–104]. Among others, cellulose-based nanofillers have been identified as promising thermo-conductive fillers due to their crystalline structure formed by unidirectional aligned cellulose macromolecules forming strongly packed structure thanks to interchain H-bonds formation. Indeed, thermal conductivity has been reported equal to 2.2 $W \cdot m^{-1} \cdot K^{-1}$ for the single nanofiber [18] and 1.9 $W \cdot m^{-1} \cdot K^{-1}$ along the nanocrystal [19].

1.2.2 Cellulose-based fillers and their application

Cellulose is a bio-based polymer derived from abundant and renewable resources, which has attracted considerable attention in the last decade thanks to its combination of unique properties including excellent mechanical and thermal properties and versatile surface chemistry [105–107]. As pristine cellulose is not processable in molten state, owing to its secondary interactions which lead to very strong aggregations, its valorisation was traditionally carried out via the extensive chemical modifications to obtain thermoplastic polymers [106,108,109] or by their use as fibers as reinforcing agent in polymers. Within this second approach, the possibility to produce cellulose nanoparticles brought a great attention, owing to their high aspect ratio, high crystallinity, low density and thermomechanical stiffness [110,111]. Cellulose nanoparticles represent a fascinating option for the preparation of "all-polymer" composites. This is particularly relevant for designing

sustainable materials, including biobased and biodegradable polymers. Therefore, nanocellulose have been widely proposed to design nanocomposites for a large set of applications for numerous types of matrices, such as polyolefins, polyurethanes (PUs), polystyrenes (PSs), and polymethylmethacrylates (PMMAs) [112–114]. For example, reinforcement in transparent and lightweight materials, barrier agents for membranes, fully biodegradable nanocomposite films, nanocellulose-based scaffolds for tissue regeneration were prepared from such nanocellulose [82,115–117].

Nanosized cellulose can be mainly divided in three categories: *i*/cellulose nanocrystals (CNC) characterized by a rod-like nanostructure with high degree of crystallinity (50-90%), *ii*/cellulose nanofibers (CNF) long from 1 to 10 µm with nanosize diameter composed by both amorphous and crystalline phases, and *iii*/bacterial nanocellulose (BNC) produced from bacteria as ribbon shape objects of 20-100 nm length [117,118]. CNC and CNF are commonly produced from a chemical pre-treatment of cellulose (*i.e.* acidic hydrolysis, TEMPO-mediated oxidation, enzymatic pre-treatment) that aims to release cellulose nanofibers from the other components initially present in the lignocellulosic biomass, *i.e.* to remove amorphous cellulose phase (Figure 26). The chemical treatments can be preceded and/or followed by a mechanical fibrillation (*i.e.* high-pressure homogenization, grinding, sonication) [119–121].

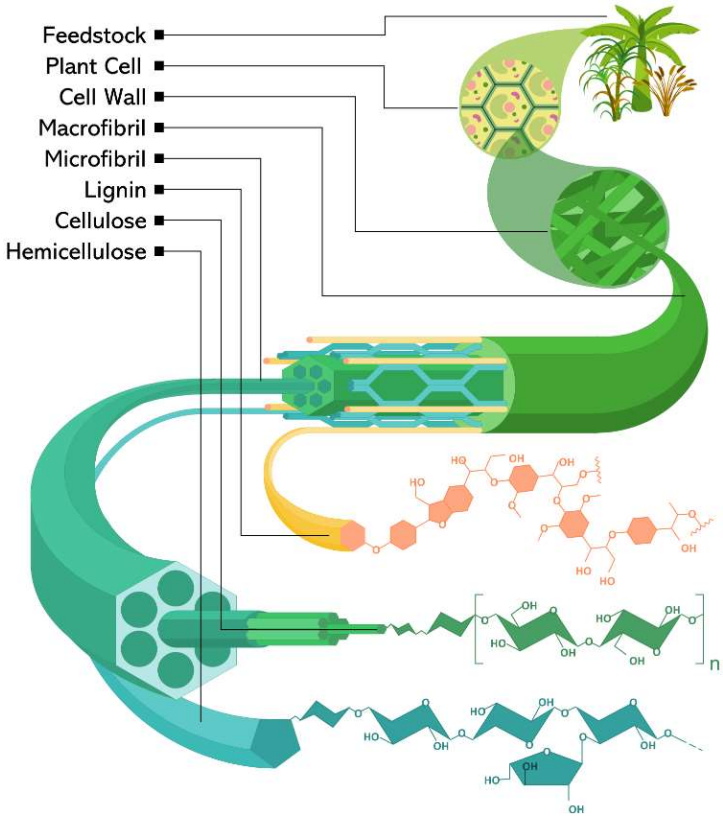


Figure 26. Schematic representation of hierarchical structure of cellulose for CNC and CNF production. *Reprinted from Lignocellulosic biomass from agro-industrial residues in South America: current developments and perspectives, 13, Magalhães A.I., de Carvalho J.C., de Melo Pereira G.V., Karp S.G., Câmara M.C., 1505-1519, Copyright (2019), with permission from John Wiley and Sons.*

Unfortunately, processing of cellulosic fibers and particularly nanocellulose is extremely challenging, owing to strong secondary interactions (Figure 27) causing poor compatibility with conventional thermoplastic polymers which can be considered as matrices. A great challenge of numerous researches was to prepare cellulose nanocomposites via melt compounding [122–124] or solvent casting [110,115].

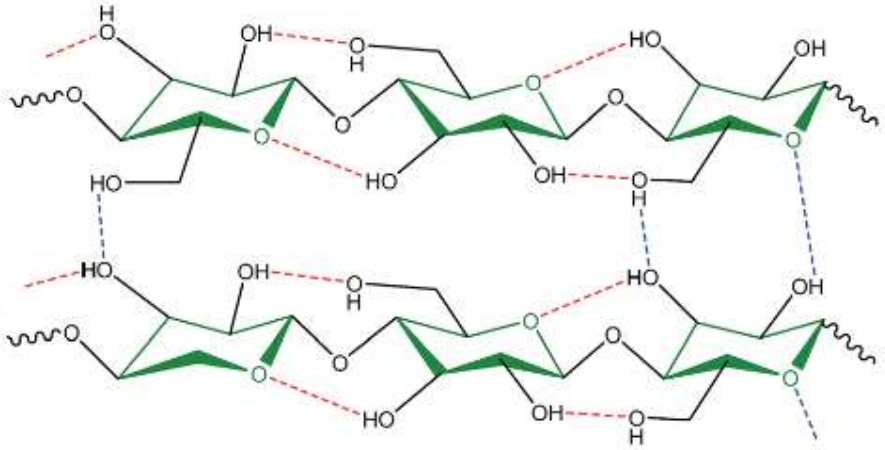


Figure 27. Intra and inter-chain H-bonding in cellulose structure. *Reproduced from Ref. [107] with permission from the Royal Society of Chemistry.*

From an industrial point of view, melt processing techniques are of interest since it could be easily scaled up. The cellulose component can be directly feed in to the extruder minimizing the risk of nanoparticles volatilization [110,122,124]. However, during manufacturing processes where water removal is involved, agglomeration of cellulose nanoparticles related to drying processes, also known as hornification, easily takes place. In these conditions, the water removal modifies the microstructure of cellulosic fibers and results in a lower capacity to retain water and a higher amount of energy necessary for re-dispersion [125,126]. To weaken interactions between cellulose, suspensions of cellulose in water can be used by direct addition during the melt mixing. Upon heating, water is removed while cellulose is mixed within the polymer, possibly establishing interactions to limit its self-aggregation [127]. Chemical functionalization of cellulose [128,129] or the use of compatibilizing agents [130] may be considered to enhance interactions with the polymer and to reduce self-interactions.

Although these routes have been widely investigated. The achievement of a well dispersed nanocellulose in a polymer remains challenging in many non-highly polar matrices and typically requires the addition of a polar compatibilizing agent [123,128,131]. This is particularly relevant for polyolefin matrices where addition of maleic anhydride-grafted polymers or copolymers [132] as coupling agent have been identified as one of the most effective method to achieve a proper dispersion of CNF [103,131,133,134].

Solvent casting methods can also be applied to nanocellulose dispersion processing. In particular, water-soluble polymers are conveniently used as matrices,

as the two components, *i.e.* polymer and CNF, can be directly mixed in an aqueous suspension. As a consequence, strong matrix-nanocellulose interactions are ensured according to the polar nature of both components. For non-water soluble polymers, nanocellulose-based composites preparation by solvent-based techniques is used due to the simplicity of the method at the lab scale. In this case, the nanofillers could rearrange to form a percolative network during the slow evaporation of the solvent [110,115,135]. The formation of a filler network results also from the establishment of H-bond interactions between the nanoparticles [110,115,136]. However, the strong hydrophilic nature of nanocellulose strongly restricts the selection of solvents alternative to water [110]. Several attempts have been done to increase hydrophobicity of cellulose fillers in order to include non-polar polymers in the set of possible matrices. The two main used strategies can be divided into two ways: *i*/addition of surfactants in the mixture or *ii*/chemical functionalization of cellulose surface hydroxyl groups [82,137]. As for chemical functionalization, different processes have been proposed through the years, including functionalization as acetylation [138], esterification [128,129], silanization [139], or grafting of monomers on the cellulose surface [140–142]. For these reasons, functionalization of the cellulose can be crucial for the achievement of adequate matrix-filler interactions. As a consequence, a pre-treatment of the filler is usually required in the preparation of the nanocomposites to guarantee a proper dispersion state.

Despite the necessity of pre-treatments, the addition of CNF has been reported for different goals: enhanced mechanical properties, higher thermal stability, and high gas barrier properties [82,110,143]. For example, the reinforcement effect of cellulose fillers in polymeric matrices has been extensively reported in literature [103,112,115,134,144]. Peng *et al.* described the reinforcement effect in CNF/PP nanocomposites. In fact, they obtained improved mechanical properties, such as an increase of the tensile and flexural moduli and impact strength, following the addition of CNF in maleic anhydride-grafted PP [134]. Furthermore, compared to nanocomposites prepared with neat PP, the authors reported an improvement of interfacial adhesion and a better dispersion in presence of maleic anhydride which led to higher mechanical properties. Pei *et al.* reported higher thermal stability and eight-times increase in tensile strength following the addition of 1wt% of CNC in PU [114]. Robles *et. al.* investigated the effect of surface-modified CNF addition in poly(lactic acid), which results in more than 20% increase of strain to fracture with 0.5wt% of nanofibers [128]. Peterson *et al.* reinforced ethylene-acrylate copolymer with CNC obtaining a dynamic network, *i.e.* a material with high deformation resistance at moderate load and thermoplastic-like flowability under high shear stress conditions, which showed a thermoset-like behaviour without decreasing the material processability [145].

In parallel with reinforcement, different authors reported as well an improvement of thermal properties, *e.g.* thermal stability regarding degradation. Lin *et al.* investigated the degradation in PS reinforced with CNC and showed an increase in stability with an initial degradation temperature shifted to higher temperatures (more than 30°C) for the nanocomposite compared to the neat matrix [113]. Trovatti *et al.* observed a substantial increment in thermal stability of acryl

resin-based nanocomposite related to the addition of cellulose nanofibers. Indeed, the maximum temperature of degradation reported a shift to higher temperatures ranging between 24 and 34°C for a filler content about 10wt% [146].

As abovementioned, the effect of cellulose nanoparticles on thermal conductivity has been poorly investigated. Shimazaki *et al.* prepared a transparent fully organic nanocomposite by dispersing CNF in an epoxy resin characterized by high in-plane thermal conductivity. In fact, the addition of CNF led to an increment close to one order of magnitude compared to the next matrix, *i.e.* from 0.15 to 1.1 $W \cdot m^{-1} \cdot K^{-1}$ [104]. Lu *et al.* reported an enhanced thermal stability in PAA/CNC nanocomposite membranes due to the high thermal conductivity of CNC [147]. Bahar *et al.* investigated the influence of the incorporation of CNC in PP matrix in terms of mechanical and physical properties. They reported, in addition to a mechanical reinforcement effect, an enhancement in thermal conductivity which in presence of 15wt% of CNC was found to increase about 60% compared to neat PP (from 0.27 to 0.42 $W \cdot m^{-1} \cdot K^{-1}$) [103].

1.2.3 Methacrylate-based cellulose nanocomposites

Various studies have been reported about the preparation of nanocellulose-based composites using a methacrylic matrix. In particular, PMMA has been intensively studied mostly due to the necessity to overcome its main limitation related to its poor mechanical strength [112,140,148–156]. Moreover, as abovementioned, PMMA is a well-known amorphous polymer characterized by optical transparency. For this reason, a common goal in the studies concerning the nanocomposite preparation is the achievement of a good dispersion of the nanoparticles in order to preserve the matrix transparency.

Fahma *et al.* prepared nanocomposite sheets by immersion precipitation with different nanofibers contents. They showed a positive trend on mechanical, *i.e.* tensile modulus and strength, and thermal properties, *i.e.* thermal stability and T_g, with the increasing content of nanofibers [157]. Fujisawa *et al.* prepared transparent PMMA/CNF films, up to 25vol% of CNF, with enhanced thermal stability and a storage modulus which increases with the content of CNF [155]. Furthermore, they identified the formation of a CNF percolative network in PMMA/CNF films starting from 0.5vol% as suggested by the appearance of a second plateau in the storage modulus vs temperature (Figure 28).

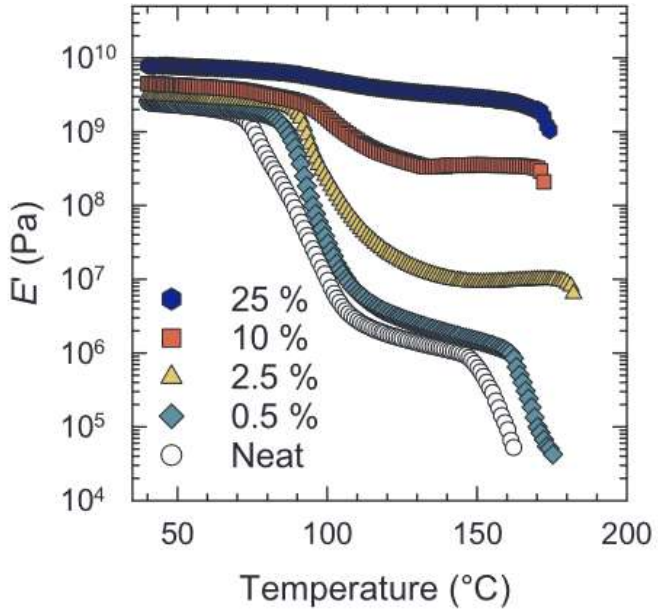


Figure 28. Dynamic mechanical behaviour of CNF/PMMA nanocomposite films for different CNF vol% at 1 Hz. *Reprinted from Large specific surface area and rigid network of nanocellulose govern the thermal stability of polymers: Mechanisms of enhanced thermomechanical properties for nanocellulose/PMMA nanocomposite, 16, Fujisawa S., Togawa E., Kimura S., 105-110, Copyright (2018), with permission from Elsevier.*

Kim *et al.* proposed a method for the preparation of PMMA/CNF nanocomposite based on a pickering emulsion-based method [158]. The method (schematized in Figure 29) is based on the *in situ* emulsion polymerization of methyl methacrylate (MMA). The authors optimized the synthesis conditions by selecting an oil/water couple characterized by an interfacial tension suitable to achieve the absorption of CNF onto the oil phase. The obtained nanocomposites with various CNF contents exhibiting high thermal stability and increased Young's modulus.

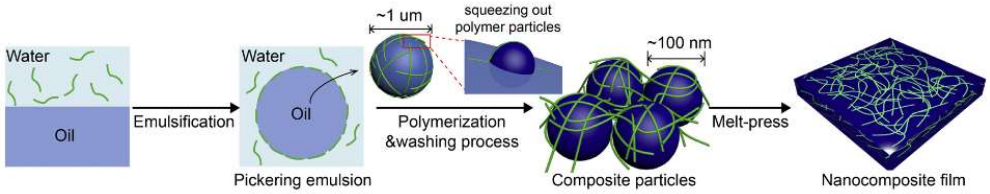


Figure 29. Preparation of PMMA/CNF nanocomposites via Pickering emulsion. Nanocomposite particles are firstly synthesised in Pickering emulsion in water, successively washed in methanol and water to remove the excess of monomer, initiator and CNF. Next, a nanocomposite film is made by compression moulding. *Reprinted from Nano-dispersed cellulose nanofibrils-PMMA composite from pickering emulsion with tunable interfacial tensions, 247, Kim D.W., Shin J., Choi S.Q., 116762, Copyright (2020), with permission from Elsevier.*

However, one of the main difficulties in the achievement of a good dispersion is the poorly polar nature of PMMA which leads to a scarce compatibility with highly polar nanoparticles as CNF. Therefore, the nanoparticles are usually surface modified in order to be homogeneously dispersed. For example, Banerjee *et al.* grafted MMA on CNF to improve dispersion in PMMA and analysed the difference between nanocomposite obtained by *in situ* polymerization and *ex situ* dispersion,

i.e. from a solution [154]. They found better properties when the preparation was made by *in situ* polymerization compared to *ex situ* technique. The addition of CNF results into an improved thermal stability and an increment of T_g (from 107°C to 126°C), tensile strength and Young's modulus which increased respectively about 15 and 39%. In a similar way, Shih *et al.* dispersed CNF-grafted with MMA in PMMA obtaining transparent nanocomposite films characterized by improved impact strength, *i.e.* increase of 23% compared to neat PMMA with the addition of 1wt% of CNF [153]. Sain *et al.* reported the influence of CNF surface functionalization with maleic anhydride and MMA on mechanical properties. Tensile strength and modulus showed the highest increase when MMA was grafted on CNF thanks to a higher matrix/nanofiber compatibility [159]. Anžlovar *et al.* grafted MMA from the CNCs surface to improve dispersion in PMMA matrix, i.e. for reducing CNCs tendency to agglomeration [140]. Jamaluddin *et al.* reported acylation of CNF leading to reinforced PMMA, demonstrating that functionalization with acetyl group enhanced interactions with ester groups of PMMA [112]. Wang *et al.* demonstrated that a more homogenous dispersion of cellulose nanocrystals can be obtained when carboxyl groups are grafted on their surface, thanks to the possibility to increase the numbers of H-bond interactions between PMMA and cellulose [152]. For instance, Dong *et al.* processed a transparent PMMA nanocomposite reinforced with homogeneously dispersed CNF (surface functionalized with carboxylic acid). This work confirmed that the presence of polymer-nanoparticles H-bonds plays a significant role on the increase of tensile strength as well as the achievement of a more ductile behaviour compared to the neat polymer [115]. Boujemaoui *et al.* performed a study on the effect of different nanoparticle/matrix interfaces in PMMA/CNF nanocomposites (Figure 30) with high CNF content (30-38 wt%) [156]. The nanofibers were firstly functionalized using epoxide molecules with allyl moieties and successively dispersed in PMMA (mCNF-*b*-PMMA) or bonded with the matrix via covalent bonds (mCNF-*g*-PMMA). As a reference unmodified CNF were also dispersed into the matrix (CNF-*b*-PMMA). They found higher transparency, a lower hygroscopicity, and a better thermal stability for the nanocomposite where covalent bonds are established at the interface.

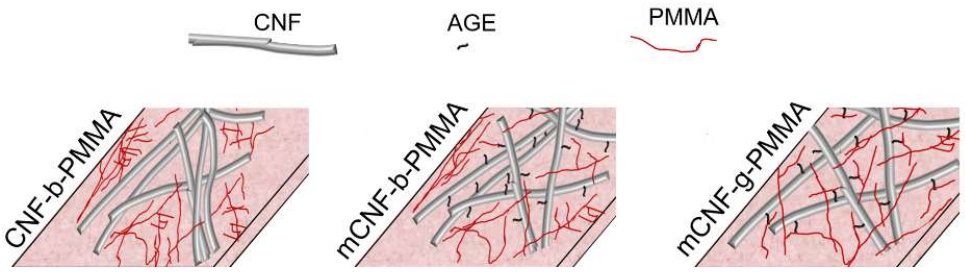


Figure 30. Schematic structure in pristine CNF blended with PMMA (CNF-b-PMMA), modified CNF blended with PMMA (mCNF-b-PMMA), and grafted with PMMA (mCNF-*g*-PMMA). Allyl glycidyl ether (AGE) used for CNF modification (mCNF). *Reprinted with permission from Nanostructural Effects in High Cellulose Content Thermoplastic Nanocomposites with a Covalently Grafted Cellulose−Poly(methyl methacrylate) Interface, 20, Boujemaoui A., Ansari F., Berglund L.A., 598-607. Copyright 2019 American Chemical Society.*

Moreover, mechanical properties in dry conditions showed similar results for the modified CNF either blended or grafted to the matrix (Figure 31), with a tensile modulus 3 times higher than the PMMA one. Instead, under water soaking conditions, the blended nanocomposites lost the reinforcing effect, showing a tensile modulus identical to the one of the neat matrix. On the contrary, the mCNF-*g*-PMMA thanks to the presence of covalent bonds at the interface showed a lower reduction of tensile modulus which still resulted 2-times higher than PMMA one.

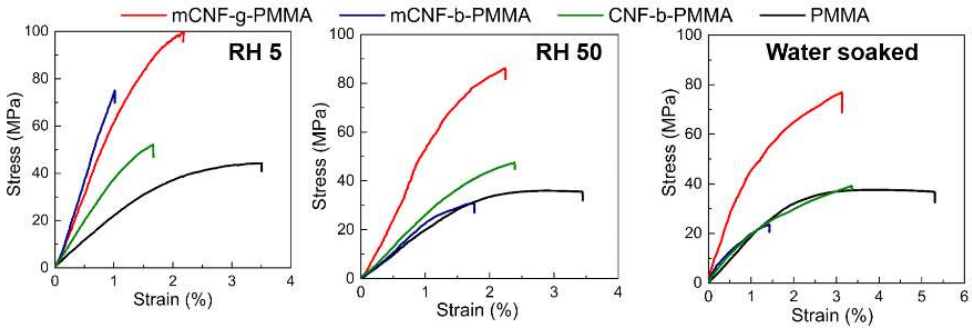


Figure 31. Stress strain curves for neat PMMA, pristine CNF blended with PMMA (CNF-*b*-PMMA), modified CNF blended with PMMA (mCNF-*b*-PMMA), and grafted with PMMA (mCNF-*g*-PMMA). *Reprinted with permission from Nanostructural Effects in High Cellulose Content Thermoplastic Nanocomposites with a Covalently Grafted Cellulose−Poly(methyl methacrylate) Interface, 20, Boujemaoui A., Ansari F., Berglund L.A., 598-607. Copyright 2019 American Chemical Society.*

The main objective of these studies was to report the influence of cellulose nanoparticles addition on mechanical, optical, and thermal properties in methacrylate-based nanocomposites. Regarding thermal properties, the reported results refer exclusively to thermal stability and T_g modification. At the beginning of this work, results about thermal conductivity in methacrylate-based CNF nanocomposites have not been reported yet.

Chapter 2

Materials and methods

In the present work, an attempt to tailor thermal conductivity in amorphous polymers has been made by tailoring intramolecular interactions. PMMA was selected as a polymer matrix model, thanks to the possibility of MMA monomer to easily copolymerize with different comonomers. The addition of inter-chain H-bond interactions to vdW ones has been achieved by the addition carboxylic acid groups in the chain via the copolymerization of MMA with MAA. Different ratios MMA:MAA were explored in order to tailor the content of H-bonds introduced and establish a correlation between their content and the final thermal conductivity exhibited by the copolymer.

Next, a neutralisation process was set up in order to replace H-bonds with stronger inter-chain interactions, *i.e.* ionic bonds, in the copolymer with the higher content of MAA units. Thin films of pristine PMMA and PMMA-*co*-MAA and sodium neutralised PMMA-*co*-MAA were prepared by solvent casting techniques and used to perform thermal conductivity measurements.

In a next stage, the MAA comonomer was replaced with new comonomers (2-hydroxyethyl methacrylate HEMA and 2-carboxyethyl acrylate CEA) in order to evaluate the influence of a higher chain flexibility when intermolecular H-bonds were present. Moreover, in PMMA-*co*-CEA, the effect of higher flexibility was also evaluated on the neutralised copolymer with the highest content of CEA.

In the last stage, PMMA-*co*-MAA with the highest MAA content (30wt%) was selected for the preparation of a fully organic nanocomposite with the addition of cellulose nanofibers (CNF). Nanofibers dispersion was performed in solution based on a mixture of solvents. Nanocomposite films with different content of CNF (5, 10, and 15wt%) were processed by solvent casting. The dispersion was evaluated in films casted from different solvents mixtures. Next, changes in macromolecular mobility and in thermal conductivity were studied for the different CNF contents.

2.1 Materials

Methyl methacrylate (MMA, 99%, inhibited with 30 ppm hydroquinone monomethyl ether (MeHQ)), methacrylic acid (MAA, 99%, inhibited with 100-250 ppm MeHQ), 2-hydroxyethyl methacrylate (HEMA, 97%, inhibited with ≤250 ppm of MeHQ), 2-carboxyethyl acrylate (CEA, inhibited with 900-1100 ppm MEHQ), Luperox® A75 (benzoyl peroxide BPO, 75%, remainder water), Luperox® DHD-9 (methyl ethyl ketone peroxide (MEKP) solution, ~32wt% in phthalate-free plasticizer mixture), 4,N,N-trimethylaniline (DMT, 99%), 2,2'-(4-

methylphenylimino)diethanol (DHEPT, ≥97.0%), tetrahydrofuran (THF, ≥99%, inhibited with 250 ppm butylhydroxytoluene (BHT)), sodium hydroxide (NaOH, ≥98%, reagent grade, pellets, anhydrous), and bis(trifluoromethane) sulfonimide lithium salt ($LiNTf_2$, ≤100%) were purchased from Sigma-Aldrich (Germany). Lithium chloride (LiCl, 99%, for analysis, anhydrous) was purchased by Acros Organics (Part of Thermo Fisher Scientific, France). Methanol (MeOH, anhydrous) and *N,N*-dimethylformamide (DMF, isocratic grade) were purchased from Carlo Erba (France). Accelerator NL-51P (Cobalt(II) 2-ethylhexanoate, 6wt% cobalt in solvent mixture) was purchased from AkzoNobel (The Netherlands). CNF water suspension (2wt%, aqueous suspension) standard enzymatic grade was purchased from RISE (Sweden). Deuterated dimethyl sulfoxide (DMSO-*d6*, 99.8%, water<0.02%) for nuclear magnetic resonance analyses was purchased from Eurisotop (Cambridge). All the products were used as received. Deionised water was obtained from a milli-Q dispenser (Merck Millipore, USA).

2.2 Preparation methods

2.2.1 Bulk polymerization

In this subchapter, the co-/polymerization process of PMMA and PMMA-*co*-MAA is presented. In order to fulfil the requirements for the measurement of bulk thermal conductivity (dense and defect-free samples with planar surface and minimum dimensions of 40x40x4 mm^3), free radical co-/polymerization in bulk was selected and different initiation mechanisms were evaluated. The different synthesis procedures will be described in the next section. The first method is based on a simple reactive mixture consisting of the monomer and a diacyl peroxide, commonly used for thermally activated radical polymerizations, *i.e.* MMA and BPO, respectively. The second synthesis method is a polymerization performed at room temperature where the activation is based on a redox reaction between BPO and a tertiary amine which results in the formation of radicals. The last synthesis is based on a more complex initiation reaction containing a diacyl peroxide (*i.e.* MEKP) and a metal-coordinate accelerator. More details about the mechanism will be given in Chapter 3.1.

2.2.1.1 Thermally activated bulk polymerization

PMMA was synthesized by bulk polymerization using BPO as initiator. Each sample was prepared starting by 15 g of MMA with the addition of 0.13 or 0.3 mol of BPO for 100 mol of total unsaturations. The two components were mixed and stirred for few minutes to promote homogenisation of the solution, then the formulations were poured in a U-shaped silicone mould sandwiched in between two glass plates (scheme in Figure 32).

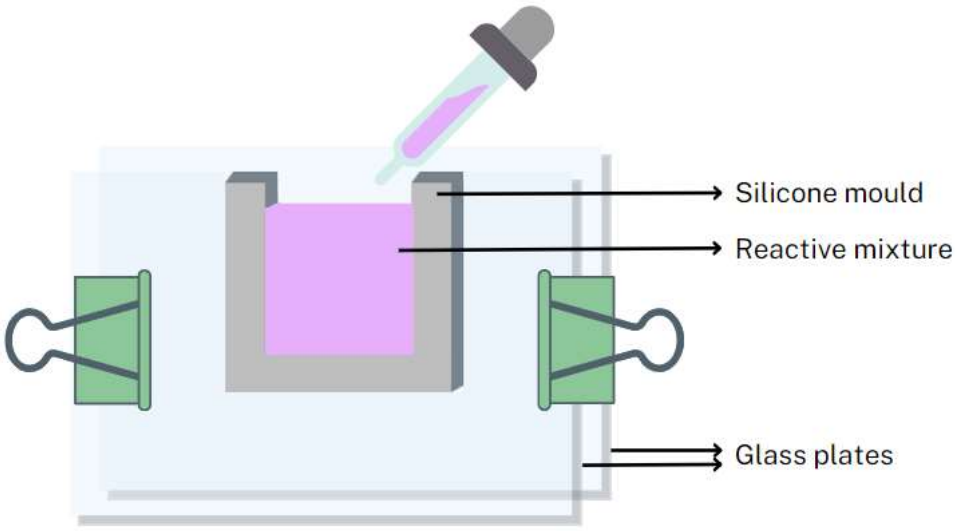


Figure 32. Scheme of the mould used for polymerization, U-shape silicone frame 5mm-thick in between two glass plates.

Moulds with formulation were placed in an oven where the polymerization proceeded applying a temperature profile made of multiple isothermal steps (2h each 10°C between 40 and 80°C or 2h at 55 and 70°C) to gradually induce BPO scission into radicals. Complete reaction was ensured by two additional isothermal steps at higher temperature performed for 2h at 110 and 140°C.

An averaged value of the total evaporated mass during thermal treatment was estimated weighing the initial liquid formulation introduced in the mould and the final weight after polymerization.

2.2.1.2 Room temperature bulk polymerization

PMMA was prepared by bulk polymerization at room temperature. For each sample, 15 g of comonomers were weighed, BPO was added in a quantity of 0.25, 1, and 1.5 mol% and next the selected amine (DMT or DHEPT) was added in a concentration equal to BPO. Formulations were stirred for few minutes, then poured in a mould similar to the one described in section 2.2.1.1 and left free to react for 185 min, corresponding to the polymerization time for the combination with the slowest kinetics (BPO/DMT at 0.25 mol%) [160]. In similar conditions, PMMA-*co*-MAA 90/10wt% was prepared with BPO/DMT initiator and a content fixed at 1mol%.

An averaged value of the total evaporated mass during thermal treatment was estimated weighing the initial liquid formulation introduced in the mould and the final weight after polymerization

2.2.1.3 Cobalt-mediated bulk co-/polymerization

PMMA and PMMAcoMAA were synthesized in bulk by cobalt-mediated radical copolymerization with different MMA:MAA ratios up to 40wt% of MAA. Each sample was prepared from 15 g of comonomers with the addition of 0.36 mol of peroxide initiator (MEKP) for 100 mol of total unsaturations and cobalt(II) 2-

ethylhexanoate equivalent to 15wt% of MEKP. Formulations were stirred for few minutes to homogenise the composition and then injected with the aid of a syringe in a silicone squared frame in between two glass defining a 50x50 mm^2 cavity with a thickness of 5 mm (scheme in Figure 33). The use of a closed silicon frame, compared to the previous one (open), allowed a better control of the evaporation of the reactive mixture during the synthesis. Later, aiming to optimize the synthesis parameters, the glass plates were replaced by aluminium plates ensuring a better control of the dissipation of the heat generated during the reaction.

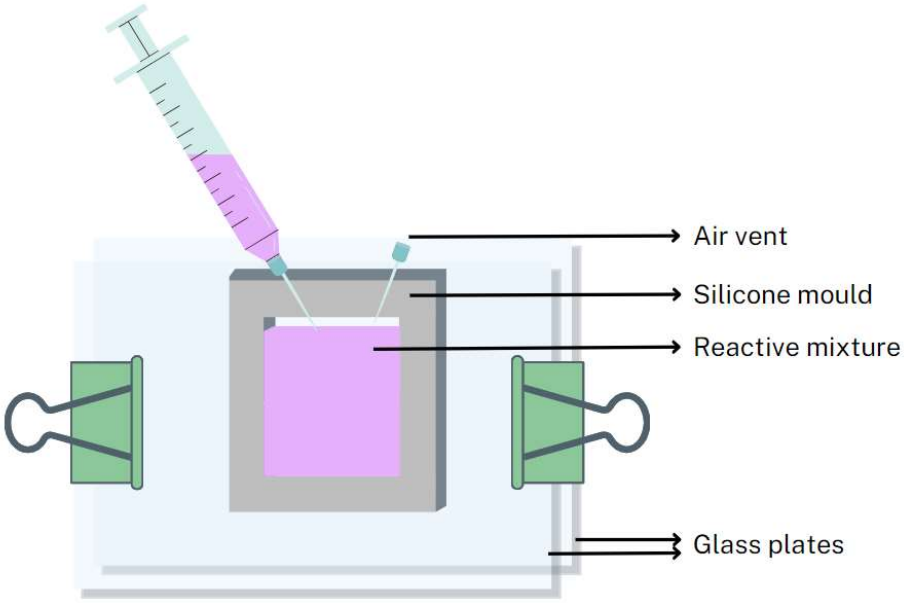


Figure 33. Scheme of the mould used for polymerization, squared shape silicone frame 5mm-thick in between two glass plates.

Moulds filled with the reactive systems were then placed in an oven and reaction was thermally activated thanks to two isothermal steps of 2h: the first one at 55°C and the second one at 70 or 80°C. Complete conversion was ensured by two additional isothermal steps at higher temperature performed for 2h at 110°C and 2h at 140°C.

Initial liquid formulations introduced in the mould and corresponding final samples were weighed in order to estimate an average value of the total evaporated mass.

PMMA-*co*-HEMA and PMMA-*co*-CEA copolymers were synthesized according to the same protocol. The ratios were chosen in order to have a molar ratio corresponding to 10, 20, and 30wt% of MAA in PMMA-*co*-MAA, *i.e.* corresponding to 14, 28, and 39wt% of HEMA and 15, 30, and 41wt% of CEA.

PMMA-*co*-HEMA copolymers were synthesized applying the conditions previously optimized for PMMA-*co*-MAA copolymers, *i.e.* a mould sandwiched between aluminium plates following a temperature profile of 2h at 55 and 70°C followed by two steps at higher temperature to ensure complete conversion (2h at 110 and 2h at 140°C). PMMA-*co*-CEA copolymers were synthesised in a mould

containing aluminium plates and with different temperature profiles in order to control the heat produced during the reaction and obtained a fully dense material. The different temperature profiles were characterized by 2h isothermal steps at T_{room}/25/30/35/40/45/60, 30/40/60, 55/60, and 55/70; and two steps at higher temperature to ensure complete conversion of (2h at 110 and 2h at 140°C).

2.2.2 Films preparation for thermal conductivity measurements

Thin films of PMMA, PMMA-*co*-MAA 70/30wt%, and PMMA-*co*-CEA (15, 30, and 41wt%) for thermal conductivity measurements were prepared via solution casting. PMMA was solubilised in THF. For the copolymers, given the different polarity of the two units, a better solubilisation was ensured using a mixture of two solvents. Therefore, PMMA-*co*-MAA was solubilised in THF/MeOH 90/10vol% and PMMA-*co*-CEA 15, 30 and 41wt% of CEA in THF/MeOH 70/30vol%. Solutions were poured in an aluminium dish and let evaporate overnight under fume hood. Next, the films were peeled-off from the aluminium dish and compression moulded in order to get a constant thickness and remove residual porosity. PMMA films were compression moulded at 200°C, while PMMA-*co*-MAA films were processed at 230°C and PMMA-*co*-CEA at different temperatures, *i.e.* between 100 and 170°C.

2.2.3 Neutralisation

The PMMA-*co*-MAA copolymer with the highest content of carboxylic acid was selected to perform neutralization. Therefore, PMMA-*co*-MAA 70/30wt% was solubilized in THF/MeOH 90/10vol% and methanolic solution of NaOH was added to perform a neutralization of the acidic units at 1:1 Na^+:COOH molar ratio [161,162].

PMMA-*co*-MAA solution were neutralized with 0.2M NaOH. After hydroxide solution addition, the neutralized solution was stirred for 2h and then poured in an aluminium dish to allow overnight evaporation of the solvents. Subsequently, the obtained films were placed in a vacuum oven (30 mbar) for 2h to remove residual solvents. Finally, the dried films were compression moulded to homogenise the thickness and densify them. Different temperatures (up to 300°C) were tested in order to find the optimal processing parameters.

In a similar manner, PMMA-*co*-CEA 41wt% was solubilized in a THF/MeOH 70/30vol% solution and neutralized with NaOH 0.3M. Then, the resulting material was compression moulded under different temperatures in order to reach homogenous thickness all over the film.

2.2.4 Nanocomposites films preparation via solvent casting

PMMA-*co*-MAA (30wt% of MAA) + CNF nanocomposites were prepared with different content of nanofibers, *i.e.* 5, 10, and 15wt%. For these ones, a proper

matrix/nanofibers interaction is ensured by the presence of carboxylic acid units able to form H-bonds with the hydroxyl groups of the nanofiber surface. The dispersion of polar nanofibers in a mostly hydrophobic matrix was achieved by a simple solvent casting method based on a mixture of solvents able to simultaneously dissolve the matrix and suspend the CNF. The first solvent chosen was THF given the good solubility showed by MMA units, while the second one was chosen between the solvents miscible with THF and forming a stable CNF suspension. Therefore, the first choice was water given the commercially availability of CNF aqueous suspension and the second one was methanol (MeOH) given the possibility to replace it to water thanks to a solvent exchange method described in literature [163].

Then, the dispersion state was evaluated using microscopy techniques. Once it was identified the range of THF/MeOH ratios in which a good dispersion of CNF in PMMA-*co*-MAA is achieved, films of PMMA, PMMA-*co*-MAA, and nanocomposites were prepared. Next, a complete investigation of their influence on macromolecular mobility was performed combining several tools, *i.e.* dynamic mechanical and dielectric spectroscopies. Finally, the influence of the nanofibers introduction on the thermal conductivity has been evaluated.

2.2.4.1 Preparation from THF/water suspensions

Prior to the CNF dispersion, the stability of PMMA-*co*-MAA solution in a THF/water mixture at room temperature was studied. PMMA-*co*-MAA copolymer was solubilized in THF and water was gradually added until precipitation occurred.

Pristine PMMA-*co*-MAA films were prepared from THF/water mixtures at different volume ratios (95/5 and 77/23vol%, both suitable to retain PMMA-*co*-MAA in solution) and in pure THF. The solutions were poured in an aluminium dish to allow overnight under hood solvents evaporation. Films were further dried under vacuum (30 mbar) for 2h at 100°C and compression moulded at 230°C.

For nanocomposites preparation, a given amount of PMMA-*co*-MAA was solubilized in THF overnight and deionised water was added in different amounts (from 0 to 0.1vol%). The additional amount of water was considered as coming from the subsequent aqueous suspension addition in order to keep the ratio THF/water at 77/23vol% in the final mixture. Next, the CNF aqueous suspension was added in the matrix solution at different contents (from 5 to 25wt% of polymer). The mixture was stirred for 2h and then poured in an aluminium dish to allow overnight under hood solvents evaporation to produce films. Films were further dried under vacuum (30 mbar) for 2h at 100°C, peeled from the aluminium dish and compression moulded at 230°C to remove porosity.

2.2.4.2 Solvent exchange

CNF suspension in MeOH was obtained starting from CNF aqueous suspension following the procedure described by Roman *et al.* [163]. Briefly, CNF aqueous suspension was diluted with the addition of MeOH in a proportion of MeOH:aqueous suspension 3:1 (by weight) at room temperature. Ultra-Turrax

homogeniser T25 basic (Ika Werke, 10min, 9000 rpm) was used to obtain a dispersion where interactions between CNF and MeOH could occur. Then, the mixture was centrifugated (Centrifuge 5702, Eppendorf) for 10min at 4000 rpm, allowing the precipitation of MeOH-wetted CNF. The excess of solvents was removed. The residual CNF suspension followed the same procedure two additional times to ensure complete solvent exchange.

After the third cycle, TGA analysis coupled with infrared (IR) spectroscopy (TGA 4000 Thermogravimetric analyser coupled with Spectrum Two IR spectrometer and Red-Shift chiller and transfer line, Perkin-Elmer) was carried out on the MeOH-based suspension to verify the complete water substitution. The analysis was performed from 50 to 150°C under nitrogen atmosphere with a heating rate of $5°C \cdot min^{-1}$.

CNF content in MeOH was calculated from the weight of residual solid after overnight evaporation of the solvent and additional drying in vacuum oven for 2h under vacuum (30 mbar) at 100°C.

2.2.4.3 Preparation from THF/MeOH suspensions

In a similar manner to the method described above in 2.2.4.1 (Preparation from THF/water suspension), stability of matrix solution in the mixture THF/MeOH was defined.

Pristine PMMA-*co*-MAA films were prepared for in THF/MeOH at different volume ratios (90/10, 70/30 and 50/50vol%, all ratios being suitable to maintain PMMA-*co*-MAA in solution) following the same procedure described for THF/water.

PMMA-*co*-MAA copolymer in a given amount was added in a mixture of THF/MeOH (between 75 and 97vol% THF) and left solubilize overnight, where the amount of MeOH varied in relation to the final designed ratio. Next, CNF suspension in MeOH was added as 5, 10 and 15wt% of filler in the final composition. Nanocomposite films were prepared following the same procedure described above for the preparation by THF/water suspension.

2.2.4.4 Films preparation for macromolecular mobility analysis

Films for the neat polymers were prepared dissolving a given amount of PMMA in THF and PMMA-*co*-MAA in THF/MeOH 90/10vol%. Nanocomposites films were prepared dissolving PMMA-*co*-MAA in THF/MeOH 90/10vol% overnight and next adding CNF suspension in MeOH to have a CNF content of 5, 10, and 15wt% of the matrix. For PMMA-*co*-MAA, the use of THF/MeOH 90/10vol% solution ensured a faster dissolution compared to pure THF given the double nature of the copolymer having a non-polar (MMA) and a polar (MAA) unit. Besides, the addition of CNF resulted, before the evaporation, in a final ratio of THF/MeOH included (between 85/15 and 75/25vol%) in the range where dispersion of CNF in the matrix was studied.

All the solutions were then poured in aluminium dishes and placed under hood overnight to allow solvents evaporation. Next, all samples were vacuum dried for

2h at 100°C and 30 mbar, peeled off the aluminium dishes, and compression moulded to obtain homogenisation and densification. Moulding temperature was set at 200°C for PMMA and at 230°C for PMMA-*co*-MAA and nanocomposites.

2.3 Characterizations

2.3.1 Macromolecular architecture

Near IR (NIR) analyses were performed on the reactive mixture containing BPO as initiator to confirm reaction progress. Spectra were collected between 6300 and 4700 cm^{-1} in transmission mode (16 scans, resolution 4 cm^{-1}) using a Spectrum Two (PerkinElmer) spectrometer.

For polymerized samples, IR spectroscopy was used to investigated the chemical structure. Spectra were collected from 4000 to 400 cm^{-1} via the attenuated total reflectance (ATR) method (16 scans, resolution 4 cm^{-1}) with a Nicolet iS10 spectrometer (Thermo Scientific) equipped with a diamond crystal. The spectra are reported after being normalized at 1448 cm^{-1}, corresponding to the absorption for the bending vibration for CH in α-CH_3 groups.

^1H nuclear magnetic resonance spectroscopy (NMR) (64 scans in DMSO-*d6* with Bruker 400 Avance III spectrometer, 400 MHz) was performed for all the monomers used in the synthesis and on copolymers in order to confirm ratio between comonomers and calculate percentage of potential residual monomers. Between the suitable solvents, DMSO-*d6* was chosen in order to guarantee the absence of superimposition between the peaks of the solvent and the ones of the polymers. Similar analyses were also performed for PMMA-*co*-MAA film at 25°C to evaluate the presence of remaining solvents from the manufacturing process. Testing temperature (25 or 90°C) was chosen taking into account the solvent stability and the solubility of the component.

2.3.2 Molecular masses

For the determination of number average molar mass (M_n), samples, either in bulk and film form, were solubilized overnight in THF. Then, size exclusion chromatography (SEC) measurements were carried out using a Shimadzu SEC instrument equipped with three columns (for M_n<15000 $g \cdot mol^{-1}$: Styragel HR 2 (WAT044237), Styragel HR 1 (WAT044234), Styragel HR 0,5 (WAT044231); for 10000<M_n<100000 $g \cdot mol^{-1}$: 3xStyragel HR 5E (WAT044228)) and multiples detectors (IR, UV, viscosimeter and light scattering detectors). THF was used as eluent with a flow rate of 1 $mL \cdot min^{-1}$ at 35°C. M_n was estimated applying a multi-detector method.

Alternatively, the samples were solubilized overnight in DMF + $LiNTf_2$ with the addition of 0.75wt% of LiCl in order to prevent intramolecular H-bonds to facilitate filtration. Then, SEC measurements were carried out using a Malvern SEC instrument equipped with a ViscoGEL I-MBHMW-3078 column and a viscosimeter detector. A solution of DMF + $LiNTf_2$ was used as eluent with a flow

rate of 0.7 mL·min^{-1} at 50°C. M_n and distribution of molar masses were estimated applying a calibration method using PS standards.

2.3.3 Thermal analysis

Differential scanning calorimetry (DSC) measurements were performed using a TA Q20 instrument (TA Instruments) calibrated with Indium Calibration Standard, applying a heating ramp of 10°C·min^{-1} from -50 to 200°C under nitrogen atmosphere. For each sample (about 4.5 mg), T_g was determined from a second heating ramp recording.

Thermogravimetric analysis (TGA) curves were recorded using a TA Instruments Q500 TGA (TA Instruments) at 10°C/min from room temperature to 700°C under nitrogen or air atmosphere.

Thermal conductivities of the samples were measured using a Hot Disk TPS 2200 for bulk measurement and Hot Disk TPS 2500 S for thin films (Hot Disk AB). A probe characterized by a 2.001 mm radius (probe number 7577) was placed between two identical samples. The system was let at least 15 min to ensure temperature equilibrium. Next, the measurements were performed in isotropic mode fixing the output power at 20 mW and the measuring time at 20 s.

In the case of thin films, prior to the measurement, the thermal resistance of the background material was measured. Therefore, a 7852 probe (radius 10.48 mm) was placed between two stainless-steel cylinders and closed in between two metal plate. Prior to measure, the system was placed in a thermostatic bath and let at least 30 min to reach temperature equilibrium. Next, two sample films were placed between the stainless-steel cylinders and the probe and their thermal conductivity was measured applying an output power of 2 W and a measuring time of 10 s.

2.3.4 Morphology of the films

Scanning electron microscope (SEM) EVO 15 SEM Zeiss (acceleration voltage 20 kV) and a SEM equipped with a field emission gun (FE-SEM, Zeiss Merlin 4248, acceleration voltage 3 kV, probe current 10 pA, working distance 3 mm) were combined to properly investigate the polymethacrylate matrix and nanocomposite films morphologies. The fracture surfaces were obtained after immersion in liquid nitrogen for 3 min to ensure a brittle fracture. The observations of secondary electrons were performed on the cross-section of the film after the deposition of a thin gold layer to ensure charge drain.

Dispersion state of CNF in the matrix was evaluated from transmission electron microscopy (TEM, JEOL 1400 Flash operating at 120 kV as acceleration voltage). For the observation, films were embedded in an epoxy resin and sliced as thin layers (70 nm thick) using an Ultramicrotome UC7 (Leica).

For a quantitative evaluation of the samples transparency, transmission UV-vis spectra of the films were recorded using a UV2600 spectrophotometer (Shimadzu) from 780 to 380 nm using air as blank. From these measurements, absorption was derived, normalized on the film thickness and converted in transmittance %. The

area under the curves is reported as percentage of the area corresponding to a fully transparent sample in the analysed range of wavelengths.

2.3.5 Macromolecular mobility

Dynamic mechanical thermal analyses (DMTA) were performed using a Q800 TA Instruments in tensile mode. To study the alpha relaxation by the application of time-temperature superposition (TTS) principle, the measurements were obtained recording isotherms with a frequency sweep from 100 to 0.1 Hz (acquiring 5 pt/decade) and a temperature step of 2°C in an interval of 50°C centred on T_g values obtained on the second heating of the DSC measurements. Strain was set at 0.05% and sample dimensions were 6x20 mm^2 with an average thickness of 0.18 mm. Reference temperatures were fixed at the T_g of the second heating of DSC and shift factors were determined using TRIOS software from TA Instruments.

Dielectric relaxation spectra were recorded with a Novocontrol instrument equipped with an ALPHA Analyzer under nitrogen flow and isothermal conditions each 2°C from -100°C to a different temperature chosen according to the composition of the materials. The temperature of the cryostat was controlled using a Novocontrol Quatro system controller. The frequency ranged from 10^6 to $4 \cdot 10^{-2}$ Hz at 3V RMS. Prior to test, films were gold-coated with a metallizer Q300T D (Quorum Technologies) applying a current of 20 mA for 300 s to ensure good electrical contacts.

Chapter 3

Acrylate copolymers with tailored intermolecular interactions

Relationships between strength of the intermolecular interactions and physical properties have been widely reported in literature [1,45,46,49,164] as previously discussed in Chapter 1. In particular, focusing on thermal conduction in amorphous polymers, the addition of stronger interactions compared with weak vdW ones could lead to the establishment of a continuous thermal network arising from an increase in the thermal conductivity [1,23]. The main positive consequence related to the introduction of stronger inter-chain interactions is the "bridging" effect between different macromolecules which may create additional thermally conductive paths and the possibility to decrease macromolecular mobility with consequent reduction of phonon scattering [5,165]. In this context, the influence of specific intermolecular interactions such as H-bonds [46] or ionic interactions [45,49] has been already discussed. Therefore, it appears that, in amorphous polymers one factor that plays an essential role determining the final value of thermal conductivity is the strength of intermolecular interactions, especially considering that low thermal conductivity values are not the result of bad conduction along the polymer backbone but it mainly results from phonon scattering [10,15].

Based on these findings, in the present work, an attempt to tailor thermal conductivity in amorphous polymers has been made by engineering intermolecular interactions. In this study, PMMA has been selected as amorphous model thanks to its well-known chemistry which allows an easy control of the interactions between macromolecular chains. The introduction of H-bonds forming moieties in the microstructure has been achieved thanks to the copolymerization of MMA with a comonomer (MAA) having a -COOH groups (Figure 34). Moreover, the copolymerization of MMA and MAA in different ratios gives the possibility to vary the amount of H-bonds introduced along the chain and to establish relationships between H-bonds content and final physical properties of the copolymers. Besides, the possibility to neutralize the -COOH groups leading to the introduction of ionic interactions (Figure 34), where the cations can form multiplets, *i.e.* acting as crosslinks [166], allows to explore the effect of stronger intermolecular interactions on the thermal conduction. At the same time, the remaining -COOH units could preserve H-bonding interactions observed in the pristine copolymer.

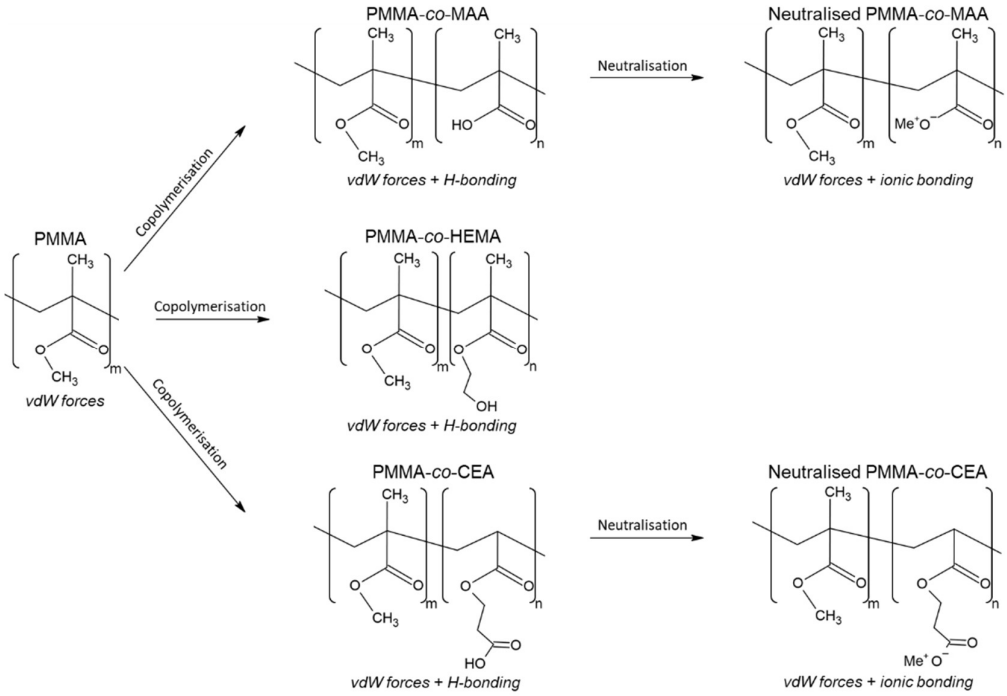


Figure 34. Structure evolution correlated to the introduction of H-bonds and ionic bonds in the macromolecular microstructure.

Given the requirements for the measurement of thermal conductivity as a bulk property reported in Chapter 2.2.1, bulk radical polymerization method has been selected. It has the advantage of being a near net shape process without the necessity of additional steps of solvent removal or sample shaping.

In a later stage, the MAA comonomer was replaced by different comonomers (Figure 34) and the influence of the chain flexibility when intermolecular H-bonds are present was evaluated. The two comonomers chosen are characterised by existence of a hydroxyl and a carboxylic acid group at the end of the ethyl side chain of HEMA and CEA, respectively.

3.1 MMA-MAA copolymers

Methacrylic monomers are widely employed in free radical polymerization given the cost-effectiveness and the simplicity of the method [167–170]. A general scheme of the free radical polymerization reaction for MMA is reported in Figure 35. The polymerization reaction can be performed in suspension, emulsion, solution, or bulk. Its mechanisms have been widely described as the sequence of three main steps: 1/initiation, 2/chain propagation, 3/termination [171,172]. The first step is the formation of radicals (a) starting from the initiator molecules which undergo a decomposition reaction induced by an external stimulus, *i.e.* UV radiation or heat. During the chain initiation (b), the formed radicals react with the unsaturation present in the monomer creating an active centre by the transmission of the radical on the monomer molecule. At this stage, other monomer molecules

react with the active centre giving rise to a growing chain which keeps growing during the propagation step (c). The macromolecule is built up by the continuous addition of monomer molecules on the active centre and the transfer of the active centre on the attached new unit. Once the monomer is consumed, the growing chain undergoes termination reactions (d), which can follow either a recombination or a disproportion reaction. The first one is the radicals combination of two different growing chains to create a unique longer and stable macromolecule. The second termination reaction is referred to the transfer of a hydrogen atom from one chain to another in order to form two stable molecules [171].

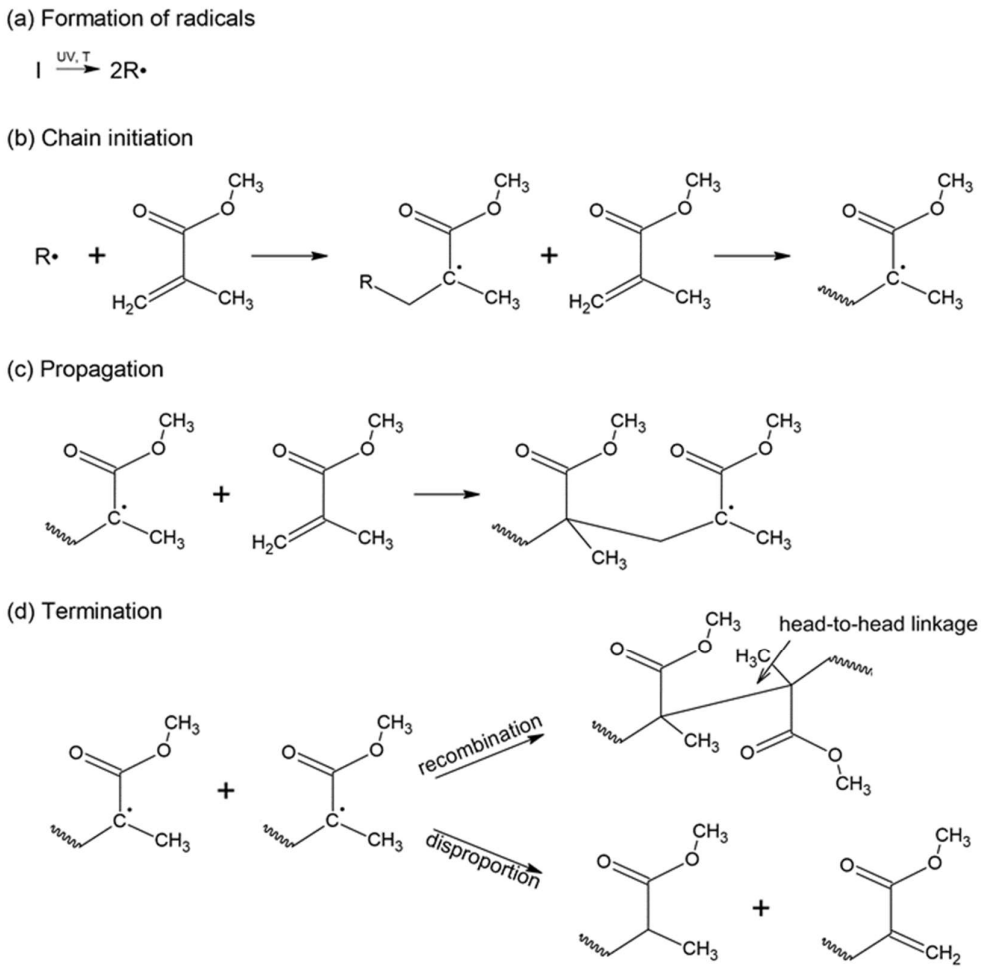


Figure 35. Schematic free radical polymerization of MMA. Radicals (R•) formation from the initiator (I) (a), chain initiation (b), propagation step (c) and termination reactions (d).

In this subchapter, the polymerization process leading to PMMA and PMMA-*co*-MAA copolymers is presented. Free radical polymerization in bulk was selected for the synthesis of these new materials and three different methods characterized by a different initiation mechanism will be presented. The first method is based on a simple formulation consisting of the monomer and a diacyl peroxide, commonly used for radical polymerization, *i.e.* MMA and BPO respectively. Secondly, the polymerization at room temperature is activated by a redox reaction between BPO

and a tertiary amine. Lastly, a more complex formulation containing a diacyl peroxide (*i.e.* MEKP) and a metal-coordinate accelerator is considered. Then, a complete characterization of the obtained copolymers is presented with a focus on the influence of the introduction of H-bonds on final properties. Moreover, the carboxylic acid units of PMMA-*co*-MAA copolymer was neutralized allowing an addition of stronger ionic interactions to H-bonds already present in the system and subsequent characterizations aiming to establish relationships between the strength of the inter-chain interactions and the final physical properties of the copolymers.

3.1.1 PMMA from thermally activated polymerization

In a first attempt, PMMA has been polymerized thanks to a thermally activated process using a simple formulation consisting of the monomer and a diacyl peroxide initiator (general formula $R_1C(O)OOC(O)R_2$, BPO) added in two different contents, 0.13 and 0.30 mol%.

The activation of the reaction was ensured by thermal decomposition of BPO to form radicals, following the reaction [173]:

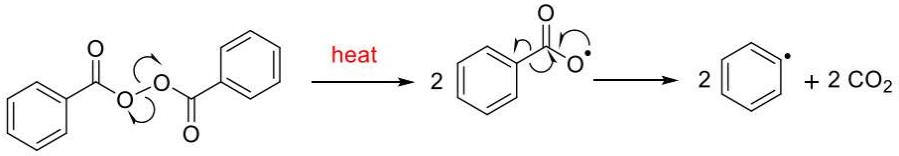


Figure 36. BPO thermal decomposition to form radicals. *Reproduced from [173] with permission from Royal Society of Chemistry.*

In fact, under the influence of heat, BPO reacts to break the O-O bond forming two radical species, which can further proceed with the decomposition in a CO_2 molecule and a phenyl radical [173,174]. However, as Buback *et al.* reported, the R-(CO)O• radical is sufficiently stable at 95°C to perform the initiation reaction with the monomer before proceeding with decarboxylation. Given the moderate temperature involved in the synthesis process, it is possible to claim that the benzoyloxy radical reacts directly with MMA double bond to initiate the polymerization reaction. The decomposition rate of BPO is directly influenced by the temperature [173]. For this reason, during the designed temperature profile, it is possible to gradually induce and control the concentration of radicals thanks to isothermal steps of rising temperature (2h each 10°C from 40 to 80°C).

From a visual observation of the formulation during the reaction, the temperature step in which the reactive mixture becomes solid was identified at 70°C. At the same time, in order to investigate the progression of the polymerization reaction during the temperature profile, qualitatively NIR spectroscopy analyses have been performed on the formulation with the lower initiator content. The spectra recorded at the end of the first three isothermal steps at 40, 50, and 60°C (corresponding to 2, 4, and 6h) are reported in Figure 37. The two spectra at 2 and 4h result identical, except for the region between 5200 and 5300 cm^{-1}, while the spectrum recorded at 6h shows a main reduction in the intensity for the peaks at

4750, 5940, and 6170 cm^{-1}. The analysis of the main peaks results in the attribution of the two peaks at 4750 and 6170 cm^{-1} respectively to a combination of the stretching (ν) and the bending (δ) modes of the double bonded CH_2 present in MMA (Figure 37) and to the first overtone of the ν for the double bonded CH_2 [167]. The peak between 5200 and 5300 cm^{-1} can be associated with the presence of water [175]. Conversely, the attribution of the peak at 5940 cm^{-1} remains doubtful. Although it corresponds to the absorption of the aromatic ring present in BPO [176], the attribution to the initiator is unlikely taking into account its scarce concentration and the peak intensity observed in the spectrum. Furthermore, the significant intensity decrease suggests the attribution to a bond present in the monomer molecules. The unchanged peak intensity between the first two steps indicates that the decomposition rate of BPO during the second step is insufficient to properly start the reaction, suggesting as well that the monomer is not reacting during the first isothermal step. When the temperature overcomes 50°C, the polymerization takes place converting the MMA monomers into growing macromolecular chains, in agreement with the intensity reduction of the peaks corresponding to the absorption of the MMA double bond.

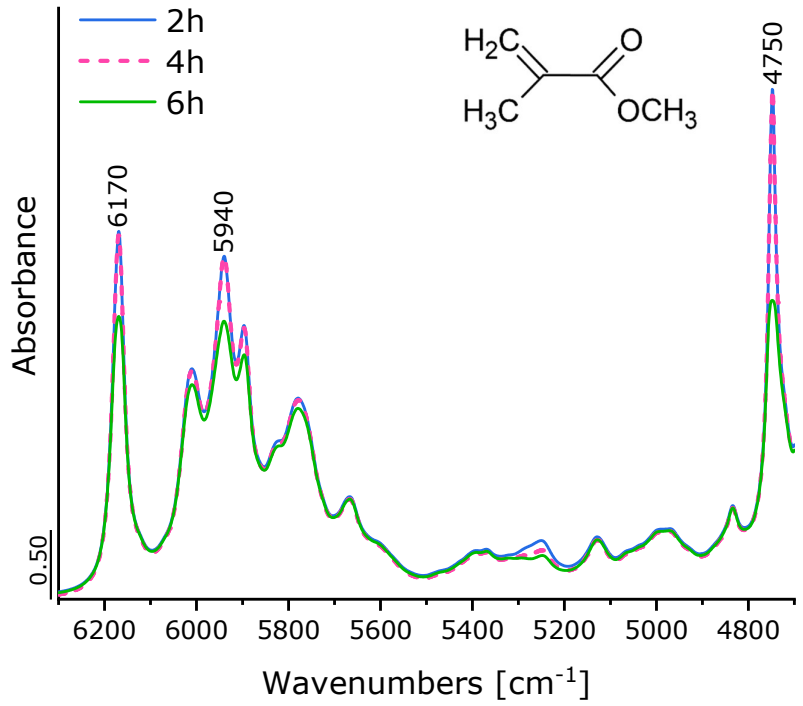


Figure 37. NIR spectra of reactive mixture MMA + BPO 0.13mol% after 2, 4, and 6h of reaction and chemical structure of MMA.

The resulting materials from polymerization are showed in Figure 38. Regardless the amount of peroxide used in the formulation, the samples result as highly porous materials, unsuitable for the following characterizations. As expected, in the open reactor used, monomer evaporation occurred in competition with polymerization. Indeed, the mass loss during polymerization was calculated and is equal to 55%.

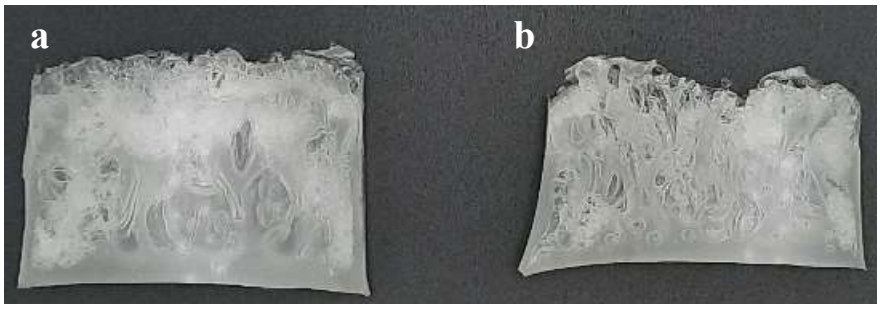


Figure 38. Polymerized PMMA samples in presence of 0.13 (a) and 0.30mol% (b) of BPO.

For these reasons, this polymerization method was discarded and new formulations with different initiation mechanisms were designed. Moreover, considering the high volatility of the monomer at high temperatures, activation mechanisms based on different principles, other than peroxide thermal decomposition, were evaluated.

3.1.2 PMMA by room temperature polymerization

PMMA was polymerized at room temperature thanks to a peroxide/amine redox activation [160,168]. In fact, the activation of the radical polymerization in this system is based onto a complex reaction between a peroxide and a tertiary amine (Figure 39), which can be summarized in the following steps: *i*/amine nucleophilic attack on the BPO peroxide bond, *ii*/BPO/amine redox reaction, and *iii*/creation of benzoyloxy and an anilinomethyl radicals [160].

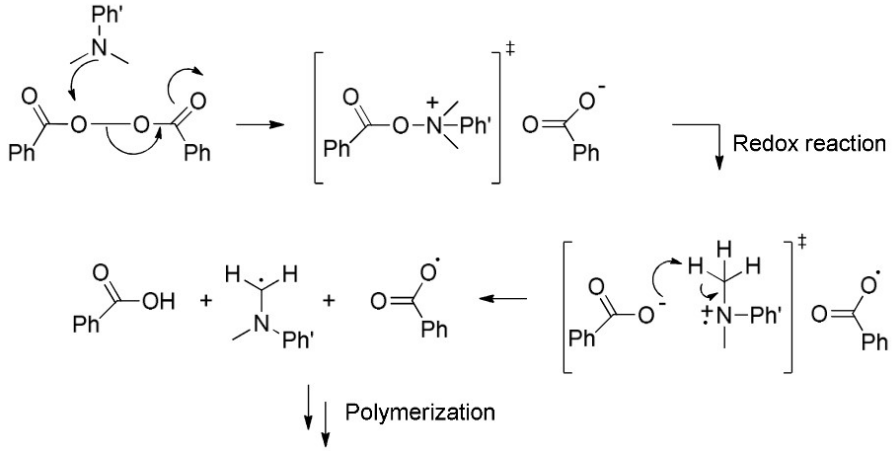


Figure 39. Activation mechanism correlated to the reaction between BPO and a tertiary amine. *Reproduced from [160] with permission from Royal Society of Chemistry.*

In the present work, two different tertiary amines were used, dimethyl-p-toluidine (DMT) or dihydroxyethyl-p-toluidine (DHEPT), the different chemical structures between the two amines result in a different decomposition kinetics of the complex BPO/amine during the initiation reaction [160].

PMMA obtained from the BPO/DHEPT activation led to a highly viscous liquid, regardless the amine concentration (0.25-1.5mol%). Similar results were

obtained using BPO/DMT in a concentration of 0.25mol%. Solid samples were processed with the initiator content fixed at 1 and 1.5mol% (Figure 40). The mass loss during polymerization was calculated to be equal to 4.5%. However, it can be seen that the samples show some defects related to the shrinkage of the formulation during polymerization.

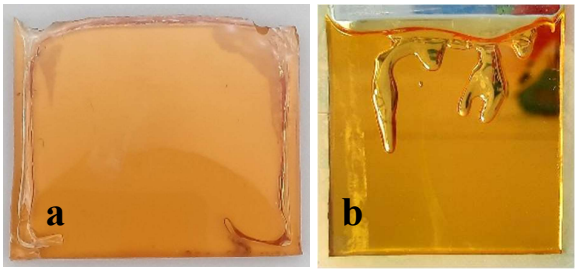


Figure 40. Bulk polymerized PMMA in presence of 1 (a) and 1.5mol% (b) of BPO/DMT initiator complex.

To confirm the successful polymerization and the achievement of a molar mass comparable with the data already reported in literature [160], the molar masses were evaluated by SEC in DMF (Figure 41). For the two analysed conditions, the curve shows a bimodal distribution and the molar mass distribution shifts to smaller molar masses when a higher content of DMT is added.

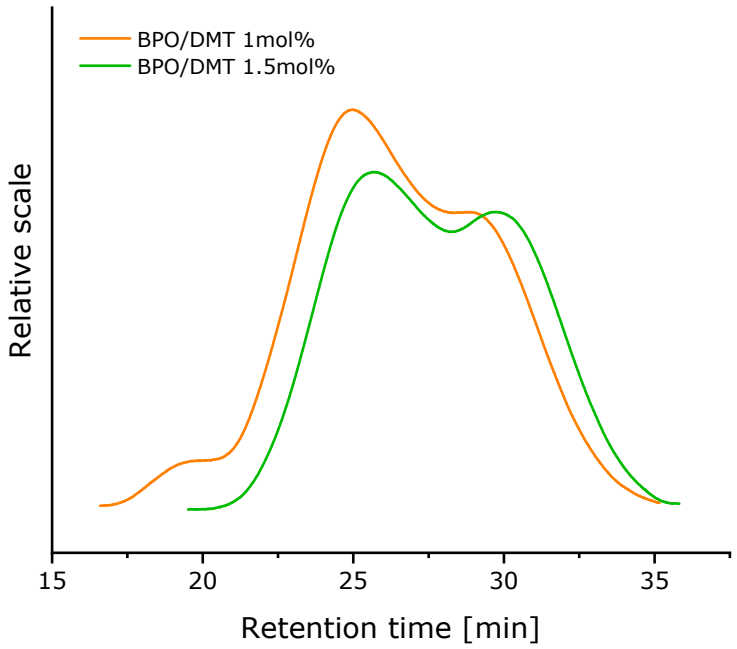


Figure 41. Molar masses distribution PMMA polymerized with 1 and 1.5mol% of BPO/DMT (PS standard, DMF as eluent and viscosimeter detection).

These results are in agreement with the experimental findings reported by Zoller *et al.* [160]. At the onset of the reaction, a first population of macromolecules is formed and the resulting average molar mass is affected by the initiator content. The polymerization increases the viscosity of the system until it reaches the gel point. The macroradicals present in the formulation in these conditions are not able

to follow the termination reaction and give rise to a population characterized by higher molar masses [160]. The M_n (determined using DMF solutions) reported in Table 2 are in agreement with the experimental values reported by Zoller *et al.* [160].

Table 2. Molar masses of PMMA polymerized at room temperature by BPO/DMT initiation.

Composition	**M_n (g/mol)**	**M_n from ref.** [160] **(g/mol)**
PMMA – BPO/DMT 1mol%	28300	24500
PMMA – BPO/DMT 1.5mol%	18100	16800

PMMA has been successfully polymerized at room temperature leading to a final result consistent with the results already reported in the literature (Table 2, similar M_n final values and distributions). Moreover, performing the polymerization at room temperature ensured the overcoming of the issue related to monomer evaporation during the reaction reported for the previous syntheses. Therefore, an attempt to apply similar synthesis conditions to copolymerise MMA and MAA was made. PMMA-*co*-MAA 90/10wt% was prepared proceeding with BPO/DMT with a content of 1mol% and led to a similar result to PMMA one. However, the achievement of defect-free samples remained challenging and a proper control on the synthesis parameters were not reached leading to the presence of randomly distributed voids in the material. In order to have a better control of the reaction, a more complex formulation was subsequently investigated.

3.1.3 PMMA and PMMA-*co*-MAA from cobalt-mediated co-/polymerization

MMA was polymerized by cobalt-mediated radical polymerization which is thermally activated by the decomposition of a peroxide molecule, MEKP. The commercially available MEKP is produced starting from butanone thanks to a complex reaction of peroxidation. The reaction results difficult to control and as a consequence MEKP is usually the mixture of various peroxides characterized by either a hydroperoxide (ROOH) or an alkyl peroxide (R-OO-R) structure. The MEKP catalysed by Cobalt(II) 2-ethylhexanoate (MEKP/Co^{2+}) represents one of the most used initiator especially for unsaturated polyesters where styrene or methacrylate are used as reactive diluents [177–179]. However, the understanding of the polymerization initiation mechanism remains challenging due to the complex MEKP composition and the lack of techniques able to investigate the radical formation with high sensitivity. Therefore, a detailed and complete description of the mechanism is still not disclosed.

Guo *et al.* analysed the initiation mechanism of MEKP/Co^{2+} system in styrene radical polymerization, simplifying the system by using a single species of peroxide (monomeric MEKP) extracted from the commercial mixture [178]. The decomposition reaction of MEKP in presence of cobalt salts starts at room temperature. The high complexity of the mechanisms besides also in the fact that

the reaction is passing by the formation of numerous intermediate species which will themselves react to form radicals. The first reactive specie formed is the alkoxyl radical which results highly unstable and reacts leading to the formation of different radicals (Figure 42).

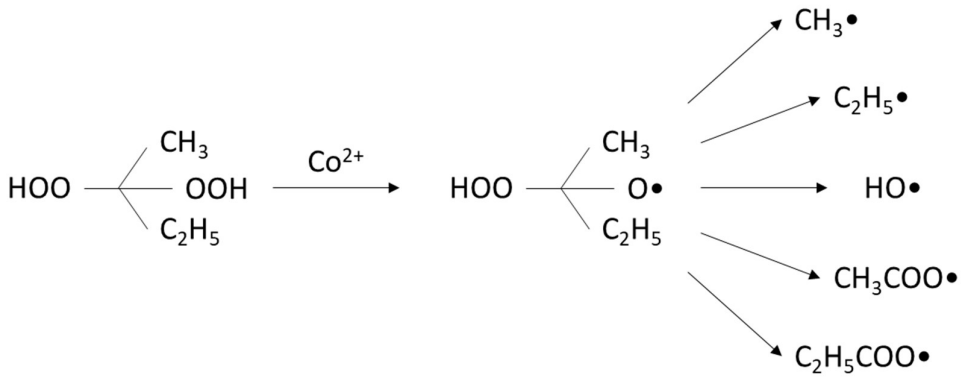


Figure 42. Radicals formed by alkoxyl radical decomposition.

Between the possible species, the formation of $C_2H_5COO•$ and $CH_3COO•$ radicals is detected in negligible amounts. Moreover, they can also react to form smaller radicals (Figure 43). For this reason, the main radicals formed overall from the MEKP/Co^{2+} initiator system are methyl, ethyl, and hydroxyl radical, which will be the species responsible for the activation of the polymerization [178].

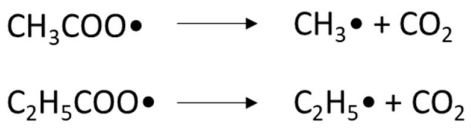


Figure 43. Reaction of acetyl and propoinyl radical.

The PMMA synthesized between glass plates following a temperature profile of 2h at 55°C and 2h at 80°C led to bubble inclusions in the samples as showed in Figure 44a. Assuming that the heat generated during the exothermic reaction is not properly evacuated by the glass plates, the monomer mixture may heat up to the boiling point while the reactive mixture is reaching a high viscosity, yielding bubbles inside the PMMA plate. For this reason, different attempts have been made in order to control the heat generated during the reaction and improve its dissipation.

Firstly, the mass of the reactive mixture was decreased in order to reduce the amount of reactive species simultaneously present and limits the increase of temperature. However, no differences were observed when the reactive mass was reduced by one-third of the initial one (from 15 to 10 g of reactive mixture). These findings supported the element causing the mixture overheating is the inefficient dissipation of the heat through the mould (according to the thermal conductivity of glass) toward the exterior of the system.

In a second attempt, the glass plates were substituted with plates made of a higher thermo-conductive material. Therefore, aluminium plates were used as heat

sinks and dissipators to limit overheating of the mixture during polymerization. However, PMMA synthesized in aluminium mould applying the same temperature profile (55°C for 2h and 80°C for 2h) shows similar bubble inclusions which are smaller in this case (Figure 44b). In fact, in these conditions, this result suggests that a better control of the heating generated during the reaction is performed.

Next, the role of the temperature was considered. Therefore, the temperature profile was modified decreasing the temperature of the second step from 80 to 70°C. In these new conditions, PMMA results in rigid, fully dense and transparent 5mm-thick materials (Figure 44c). It is worth mentioning that a slight difference of the samples colour is observed (Figure 44) which is correlated with a different surface quality that derives from the preparation with moulds, *i.e.* glass or aluminium plates.

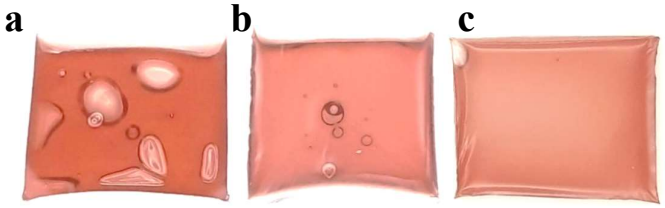


Figure 44. PMMA polymerized in glass mould at 55/80°C (a), in aluminium mould at 55/80 (b) and at 55/70°C (c).

Once the optimal configuration was set for PMMA, all the copolymer formulations (10, 20, and 30wt% of MAA) were successfully copolymerized applying the same parameters and resulting in fully dense and transparent samples (an example is reported in Figure 45 for the composition with the highest MAA content). It is worth mentioning that a different colour is obtained in the copolymer compared to PMMA. This effect can be attribute to the different environment, more or less acidic, in which the Cobalt complex shows a different coloration [180].



Figure 45. PMMA-*co*-MAA 70:30wt% polymerized in aluminium mould at 55/70°C. Transparency is highlighted by the small cube visible behind the sample.

Also, compared to BPO formulation, the use of a closed squared frame where the reactive mixture was injected and the reduction of 60% of the reaction time allowed a decrease of the evaporated monomer mass which dropped from 55 to 12wt%.

An attempt to further increase the ratio in terms of MAA content was done copolymerizing PMMA-*co*-MAA 60:40wt%. However, it was observed that when MAA content exceeds 30wt%, white inclusions appear (Figure 46). Huang *et al.* observed for the same ratio a phase separation occurring into the mixtures of the two homopolymers [60]. In a similar way, during bulk polymerization, a phase separation can occur between chains richer in MMA or MAA units, *i.e.* the generated copolymers are not fully statistical.



Figure 46. PMMA-*co*-MAA 60:40wt% after bulk copolymerization.

After synthesis, ^{1}H NMR analyses were performed on the copolymers. In the spectra, it is possible to identify the resonances corresponding to MMA at 6, 5.7, 3.7, and 1.9 ppm (Figure 47a). Residual monomer is still present at the final stage. From the integration of these peaks, residual MMA results lower than 1.5mol%, while no evidence of residual MAA was found (Figure 47b). By ^{1}H NMR, it is also possible to determine copolymer compositions (Figure 47d-f) for the ratio MMA:MAA which were found to be 87:13, 74:26 and 63:37mol% for the copolymerized 10, 20 and 30wt% of MAA, respectively (Table 3) [181]. Compared to the expected values (11, 23, and 33mol% corresponding to 10, 20, and 30wt% of MAA), a lower concentration of MMA units is obtained experimentally, as a consequence of the higher volatility of MMA compared to MAA (boiling point is 101°C for MMA and 163°C for MAA).

Table 3. Copolymers composition determined by ^{1}H NMR analysis.

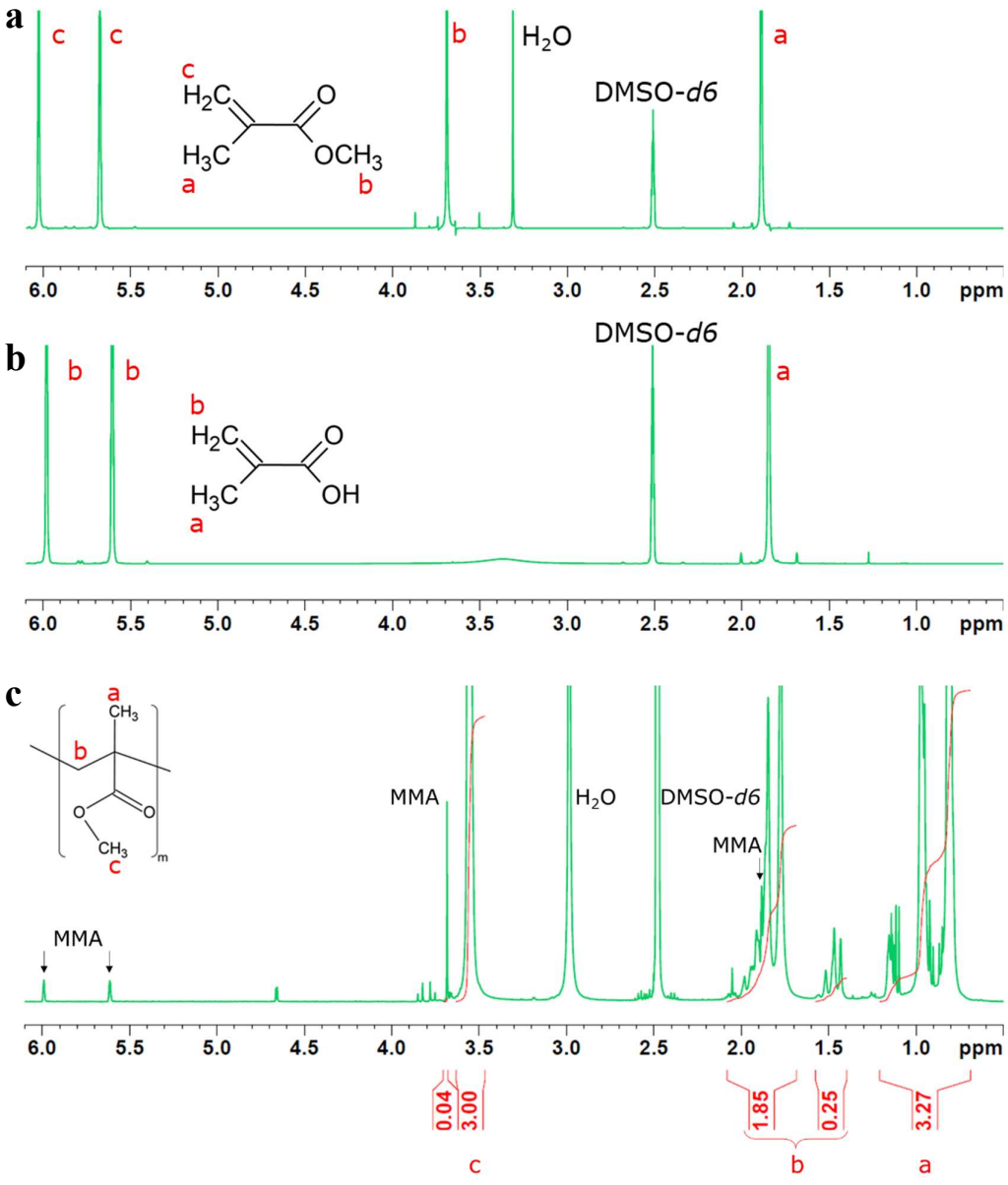
Initial ratio MMA/MAA (wt%)	Ratio from ^{1}H NMR MMA/MAA (wt%)	Initial ratio MMA/MAA (mol%)	Ratio from ^{1}H NMR MMA/MAA (mol%)
90/10	87/13	89/11	85/15
80/20	74/26	77/23	71/29
70/30	63/37	67/33	64/36

Regarding the macromolecular microstructure, based on the copolymerization constants reported from Krul *et al.* (r_{MMA}=0.84 and r_{MAA}=0.62) defined as the ratio between the rate constant of the propagation reaction where the unit added at the end of the growing chains is similar to the one already present ($k_{MMA\text{-}MMA}$ or $k_{MAA\text{-}MAA}$) to the rate constant for the addition of the other comonomer ($k_{MMA\text{-}MAA}$):

$$r_{MMA} = \frac{k_{MMA-MMA}}{k_{MMA-MAA}} \tag{25}$$

$$r_{MAA} = \frac{k_{MAA-MAA}}{k_{MMA-MAA}} \tag{26}$$

and given their product <1, it is possible to predict the formation of the random copolymer microstructure [182].



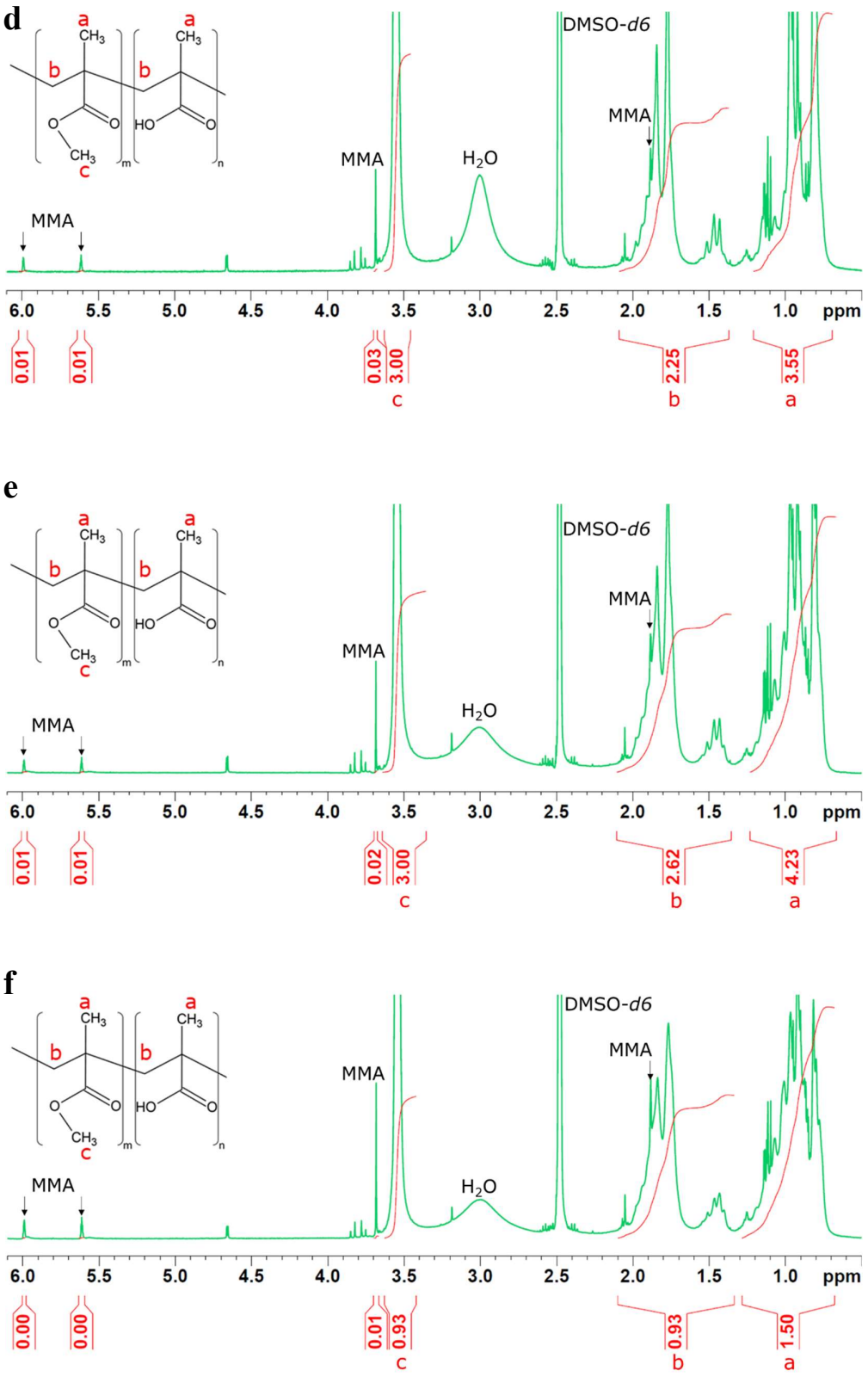


Figure 47. ^{1}H NMR spectra at 25°C for MMA (a) and MAA (b) and at 90°C for PMMA (c), PMMA-*co*-MAA 10 (d), 20 (e), and 30wt% (f) MAA after copolymerization (400 MHz, DMSO-*d6*).

Monomodal distributions of molar masses were found for PMMA and PMMA-*co*-MAA with 10 and 20wt% of MAA (Figure 48) and values using THF as eluent are reported in Table 4.

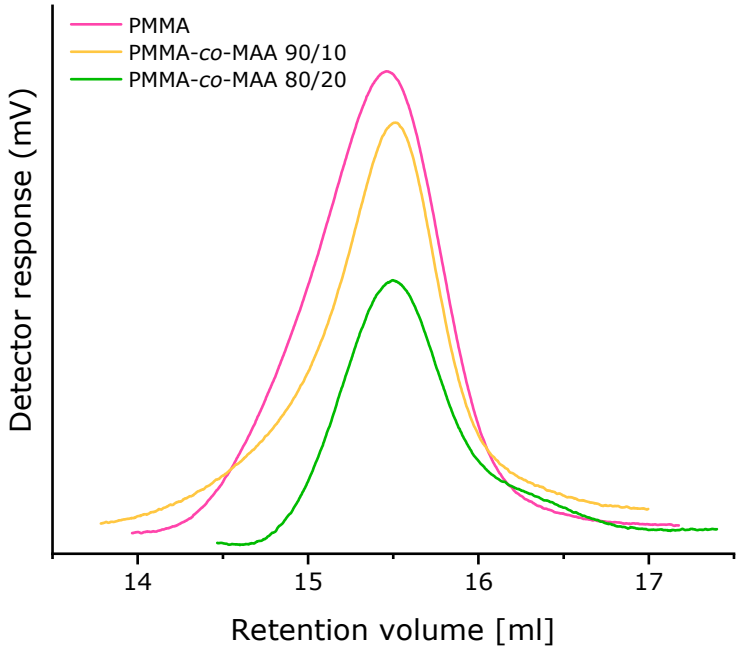


Figure 48. Molar mass distributions for PMMA and PMMA-*co*-MAA 10 and 20wt% of MAA (THF as eluent and IR detection).

The addition of 10 and 20wt% of MAA did not affect significantly the final M_n (Table 4). However, for higher content of MAA (30wt%), the obtained M_n values resulted much higher than the upper limit of the columns. Likely, the M_n is higher than the detection limit of the columns leading to a retention time too low to be analysed with the considered standard. Polydispersity indexes (Table 4) are found, for PMMA, comparable with the ones reported in literature (1.2 – 1.5) [183], while the copolymers ones did not show a specific trend.

Table 4. Molar masses of PMMA-*co*-MAA copolymers after synthesis obtained by SEC measurements in THF applying multidetector method.

Composition	**M_n (g/mol)**	**M_w/M_n**
PMMA	261000	1.6
PMMA-*co*-MAA 90/10	135000	2.9
PMMA-*co*-MAA 80/20	98000	1.3

For this reason, PMMA-*co*-MAA 30wt% MAA M_n was also evaluated in DMF. Molar masses distribution from SEC in DMF is found to be a non-gaussian (Figure 49) at an elution time close to the upper limit of the column. In a similar way to THF, M_n has a value much higher than the upper limit identified by the calibration curve of PS, suggesting that M_n of PMMA-*co*-MAA is higher than the detection limit (equal to $1.35 \cdot 10^6$ g/mol). The reliability of the values obtained remains

doubtful, however the hypothesis is that, similarly to the results obtained in THF, the M_n is higher than the detection limit of the columns.

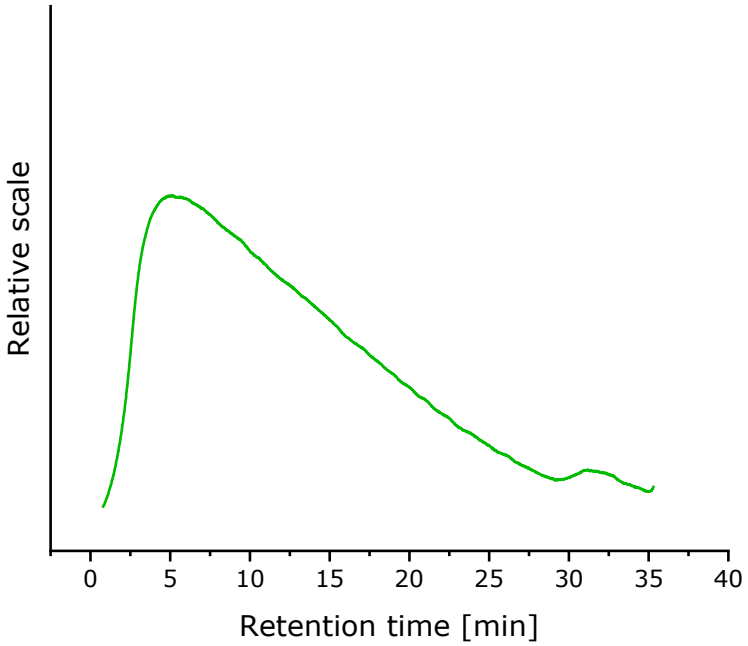


Figure 49. Molar masses distribution for PMMA-*co*-MAA 30wt% of MAA (PS standard, DMF as eluent and viscosimeter detection).

3.1.3.1 Thermal stability of PMMA-*co*-MAA copolymers

Thermal stability was investigated by TGA for PMMA and PMMA-*co*-MAA copolymers. From the thermograms (Figure 50 and Figure 53), it is possible to identify the temperature corresponding to a weight loss of 5%, taken at the onset temperature for polymer decomposition, and the temperature at which the derivative TGA curves is maximum. The onset temperature for the degradation is included between 251 and 264°C, while the maximum weight loss rate is in the range of 372 and 404°C. In both cases, limited temperature differences are observed between the inert and oxidative atmosphere. These temperatures for all the compositions are listed in Table 5. Moreover, the final residual weight is lower than 0.4% at temperatures higher than 500°C in both atmospheres.

Table 5. TGA data for PMMA and PMMA-*co*-MAA copolymers under $N_{2(g)}$ and air.

Composition	**$T_{5\%}$ (°C)**		**T_{max} (°C)**	
	N_2	**Air**	**N_2**	**Air**
PMMA	258	265	372	372
PMMA-*co*-MAA 90/10	251	253	398	378
PMMA-*co*-MAA 80/20	264	264	404	384
PMMA-*co*-MAA 70/30	253	253	401	384

PMMA is characterized by a well-known mechanism of depolymerization which lead to the conversion of the whole initial mass into volatile species and is not affected by the presence of oxygen as suggested by the close temperature of the peaks for the main weight loss in the two atmospheres [184].

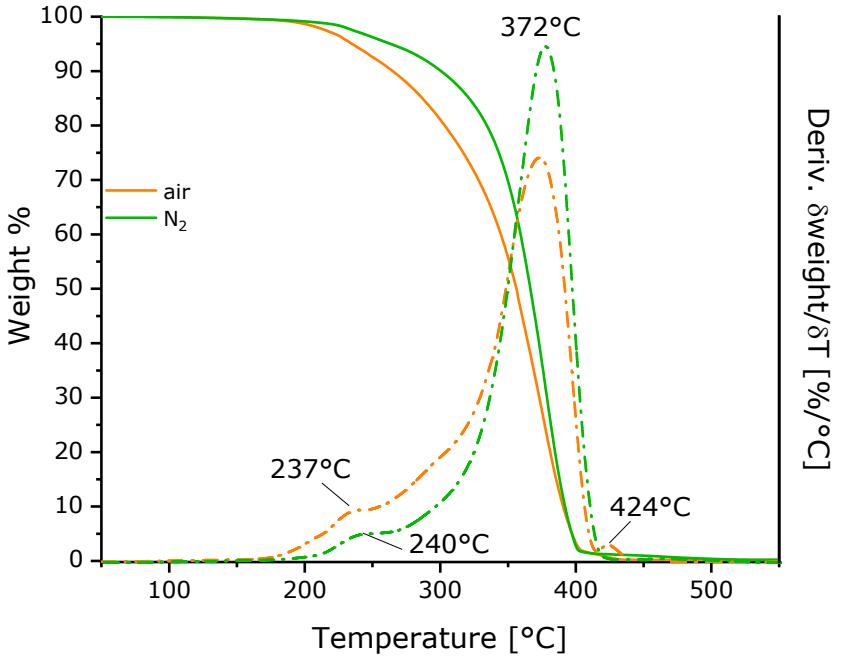


Figure 50. Thermogravimetric analyses of PMMA in N_2 and in air (heating rate 10°C/min).

Kashiwagi *et al.* [185] analysed the thermal degradation of PMMA and reported three mechanisms under inert atmosphere (Figure 51). For PMMA obtained by radical polymerization, they found a first degradation close to 195°C corresponding to an initial scission at head-to-head linkages characterized by lower dissociation energy. The second mechanism of degradation appears close to 255°C and they ascribed it to the depolymerization started by the unsaturated vinylidene chain ends which result by disproportion reaction of termination. Instead, the scission of C-C from the backbone starts close to 300°C. In any case, the reaction (I) give rise to primary and tertiary radicals.

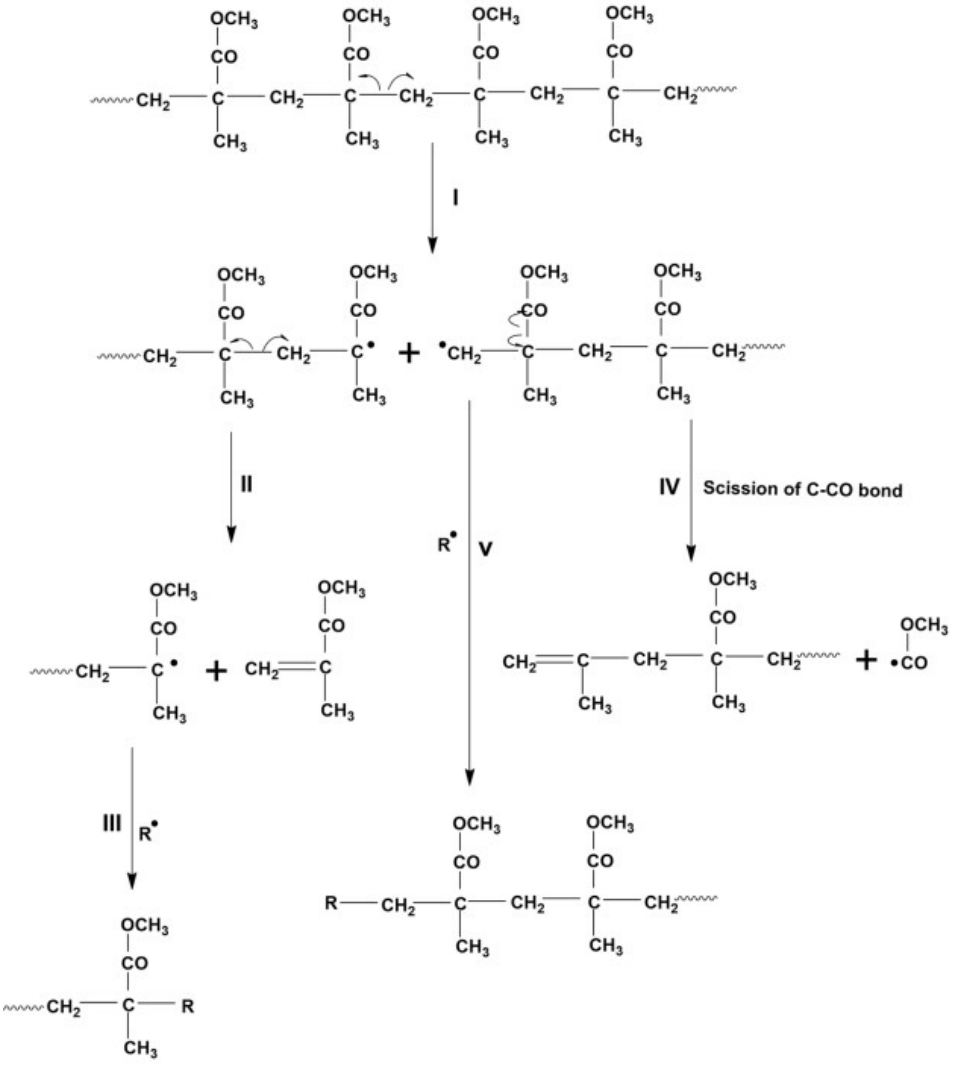


Figure 51. PMMA thermal degradation mechanism. *Reproduced from "Suresh, S.S. et al.; Investigation into the Mechanical and Thermal Properties of Poly(Methyl Methacrylate) Recovered from Light Guidance Panels with a Focus on Future Remanufacturing and Sustainable Waste Management."* **[186]** *with permission from Springer Nature.*

The tertiary radicals decompose by a homolytic scission (II) into monomer molecules (MMA) and another tertiary radical which can continue depolymerization or can recombine with another radical (III). The primary radical formed during reaction I reacts to form a stable chain and a methoxy carbonyl radical (C•O-OCH_3) by cleavage of the C-CO bond (IV). It can either recombine with other radicals (V) to form a stable molecule [185,186]. The main product of the degradation reaction is the monomer, MMA.

In presence of oxygen, the radicals formed due to the chain scission can react with O_2 forming a peroxide radical mainly with the macroradicals formed by head-to-head linkages cleavage at lower temperature [185]. A scheme of the possible reactions between the macroradicals and O_2 is offered in Figure 52.

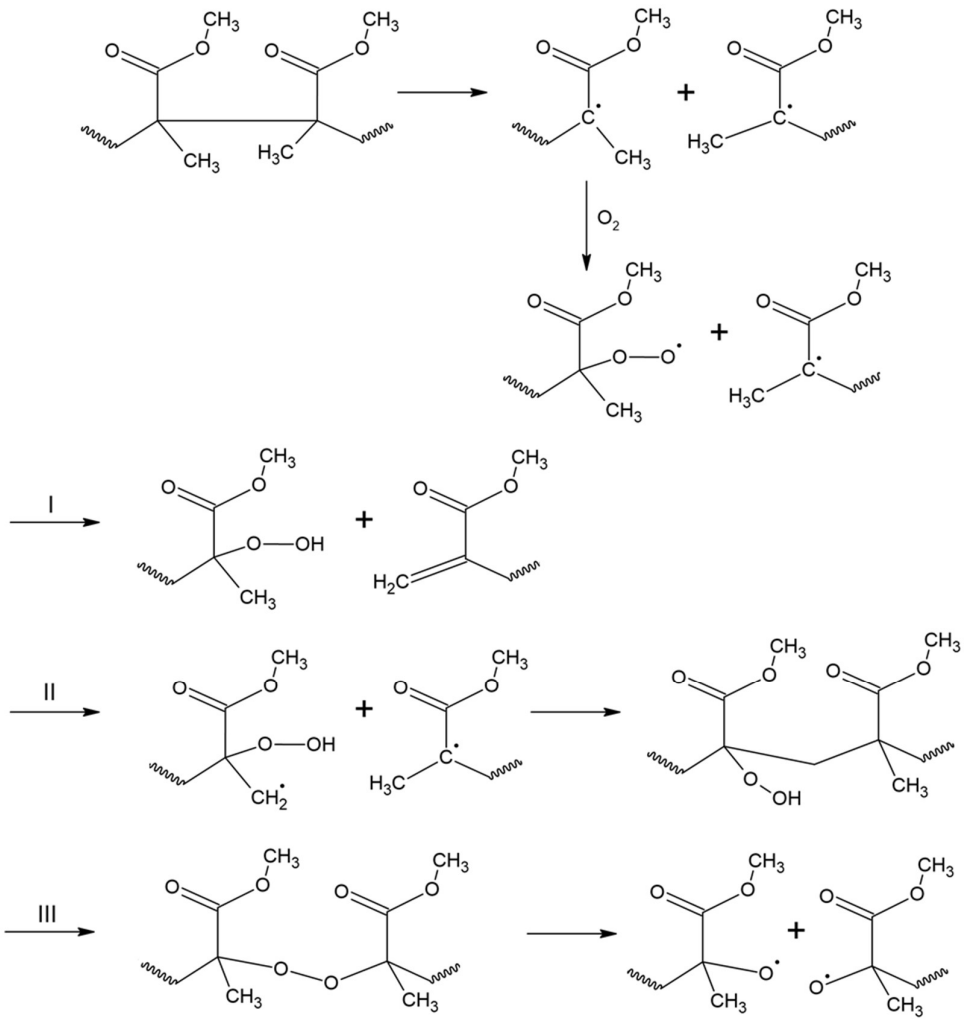


Figure 52. Reactions between the macroradicals and O_2 during thermal degradation.

These reactions affect the degradation reactions at low temperature (close to 195°C) preventing depolymerization and usually result in a slight delay of the degradation beginning [185,187]. The ROO• generated subsequently can react to capture an hydrogen and forms ROOH species which can decompose leading to the formation of RO• and •OH radicals which proceed degradation attacking the other chains [185,188]. Indeed, $T_{5\%}$ was found to be slightly higher in air compared to nitrogen atmosphere (265 °C vs 258°C). The main product of degradation in oxidising atmosphere remains the monomer and, in addition, other volatile species are formed, *i.e.* 2-methyl-oxirane carbonic acid methyl ester, methyl pyruvate and dimethyl itaconate [53,187].

In the present study, the degradation starts around 195°C giving rise to a first peak while the second and third mechanisms appear overlapped and the temperature of main degradation remains coherent with the ones described in literature. Besides, it has to be taken into account that the temperatures associated with the degradation, regardless the atmosphere, may vary according to the multiple factors, such as tacticity, molar mass, and polymerization method which determines a different content and nature of chain ends [185].

For all the copolymers, the relevant temperatures associated to thermogravimetric curves are listed in Table 5. Moreover, TGA thermograms are reported in Figure 53 for the copolymer with the highest MAA content (30wt%). The derivative TGA curves (Figure 53) show, either in nitrogen and air, *i*/a first degradation between 200 and 330°C, *ii*/a main weight loss peak, and *iii*/a last peak (between 490 and 650°C in nitrogen and 420 and 455°C in air) leading to a ~0 final residual weight. From the comparison of the two curves, it is clear that oxygen presence has a strong effect on the last degradation step which occurs at lower temperature compared to nitrogen atmosphere.

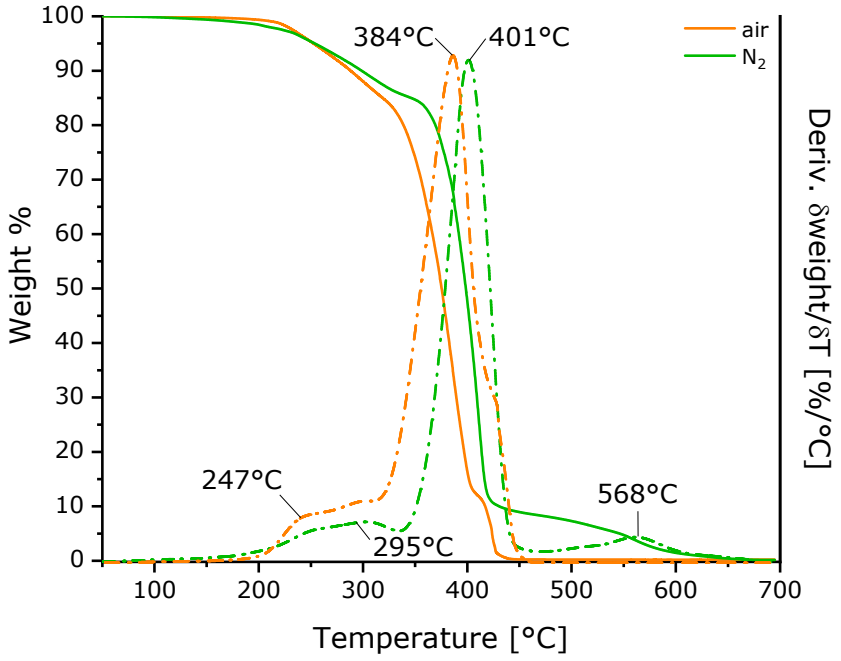


Figure 53. Thermogravimetric analyses of PMMA-*co*-MAA 30wt% MAA in N_2(a) and in air (b) (heating rate 10°C/min).

The degradation mechanism that occurs in MMA-MAA copolymers has been previously descried by Krul and Jamieson [182,189]. PMMA-*co*-MAA copolymers were reported to release volatile products above 220°C and the chemical species formed can be different depending on the involved paths (Figure 54): two acidic units react to eliminate a water molecule, while when MMA-MAA are adjacent, a MeOH molecule is released. In any case, this condensation reaction leads to the same anhydride structure. The reaction mechanism (Figure 54) is reported only for the intrachain anhydride formation since it corresponds to the favoured reaction, however, to a lower extent, it can take place also between interchain units [189].

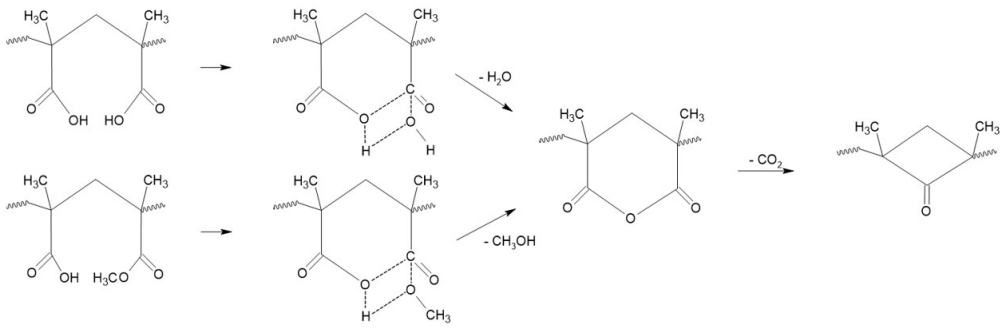


Figure 54. Reaction of anhydride formation via a transition state and decarboxylation of anhydride rings.

Above 300°C, the degradation mechanism refers to the decomposition of the anhydride structure which occurs simultaneously with the beginning of polymer backbone volatilization by depolymerization. At this stage, additional volatile species (CO_2, CO, methane) are formed either due to fragmentation of anhydride segments or degradation of the remaining MMA-MMA adjacent units [182,189]. The anhydride rings can partially decarbonise leading to the formation of a more stable fraction which will be volatilized in thermoxidative conditions above 400°C or at higher temperature in inert atmosphere as shown by TGA. This mechanism explains the experimental observation described above, with limited temperature differences which can occur for the same composition and can be due to the multiple factors, including molar mass and tacticity [190].

3.1.3.2 H-bond influence on copolymer properties

Further investigations on the chemical structure of the copolymer were performed using infrared spectroscopy. The reported IR spectra (Figure 55) are normalized at 1448 cm^{-1} which corresponds to the absorption for the bending vibration of CH in α-CH_3 groups.

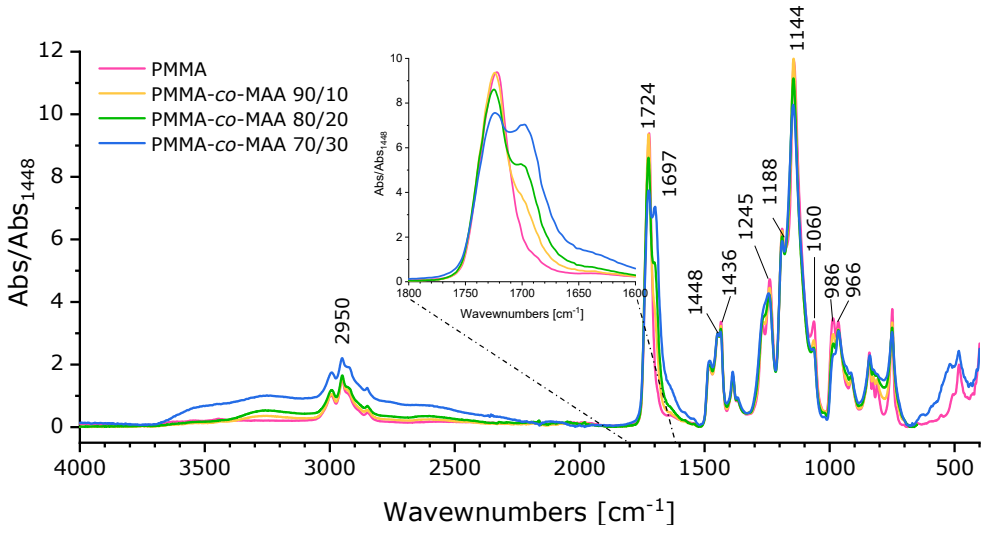


Figure 55. IR spectra (ATR mode) of PMMA-*co*-MAA copolymers after copolymerization reaction with MAA content from 0 to 30wt%.

The assignment of the absorption peaks identified in the IR spectrum is reported in Table 6 [191].

Table 6. Assignment of IR peaks in PMMA and PMMA-*co*-MAA copolymers spectra.

Wavenumber (cm^{-1})	Assignment
966	rocking deformation of the α-CH_3
986	bending of C-O-C combined with OCH_3 group
1060	symmetric vibration of C-C
1144, 1188	vibration of -C-O-C-
1245	symmetric vibration of -C-C-O-
1436	bending of CH in -O-CH_3
1697, 1724	stretching of -C=O
2950	stretching of CH

Focusing on the carbonyl absorption region, the peak at lower wavenumber (1697 cm^{-1}) can be attributed to the acidic units, while the one at 1724 cm^{-1} is related to the ester group in MMA. Moreover, the peak corresponding to the carboxylic group shows an intensity directly related to the MAA content. These assignments are in agreement with the results reported by Huang *et al.* [60]. These authors described the two signals as the superimposition of four signals corresponding to the absorption of the free carbonyl for MAA and for MMA and H-bonded carbonyl between MMA-MAA and MAA-MAA (Figure 56). They assigned the peak between 1670 and 1710 cm^{-1} to the carboxyl in MAA forming H-bonds [60]. Therefore, the appearance of a peak at 1697 cm^{-1} confirms the presence of H-bonded -COOH groups.

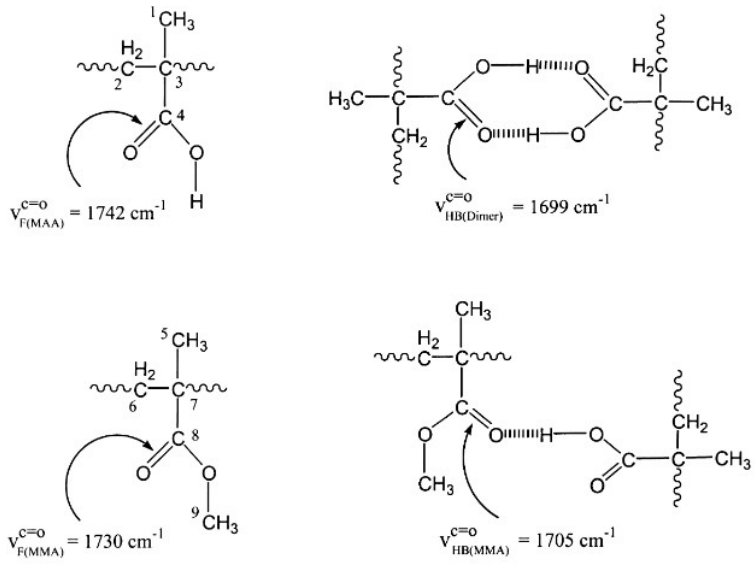


Figure 56. Scheme of interactions between MMA and MAA carbonyl and related absorption bands. *Reprinted from Comparison of hydrogen bonding interaction between PMMA/PMAA blends and PMMA-co-PMAA copolymers, 44, Huang C.-F., Chang F.-C., 2965-2974, Copyright 2003, with permission from Elsevier.*

A peak shoulder also appears in this range for lower wavenumbers and can be attributed to the presence of water (water bending is close to 1640 cm^{-1}) absorbed due to the presence of the acidic comonomer [192]. The amount of absorbed water increases with the increasing of the MAA content in the copolymer given the higher content of the hydrophilic comonomer.

DSC thermograms (Figure 57) show a single T_g for all the compositions which is included in the range 100 – 150°C and increases with the MAA content, the precise values are reported in Table 7.

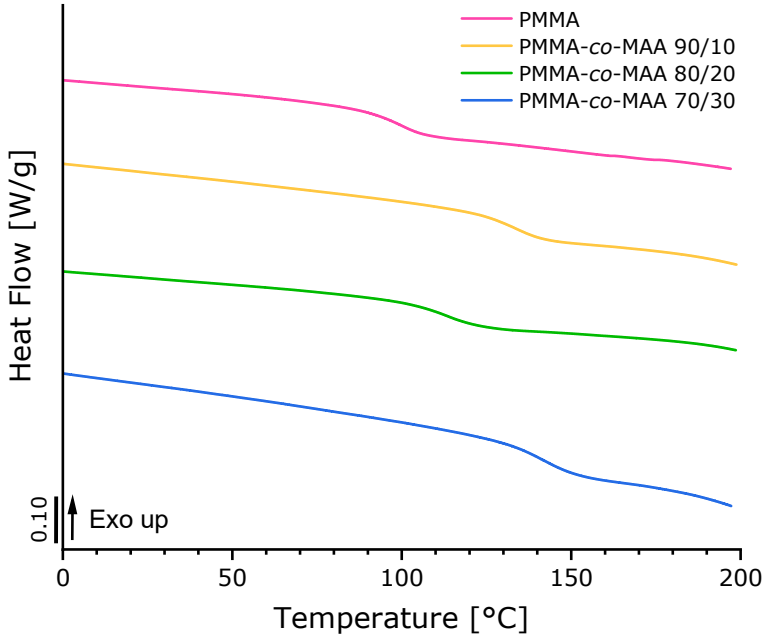


Figure 57. DSC thermograms of PMMA, PMMA-*co*-MAA 10, 20, and 30wt% (heating rate 10°C/min).

PMMA has a T_g of 100°C, close to value reported by Huang *et al.* [60]. For all the analysed copolymer compositions, a theoretical T_g was calculated applying Fox's equation (Figure 58):

$$\frac{1}{Tg} = \frac{w_1}{Tg_1} + \frac{w_2}{Tg_2} \tag{27}$$

where w_1 and w_2 are the weight fraction of the components and T_{g1} and T_{g2} correspond respectively to their T_g [193]. It is worth mentioning that the Fox's equation is valid for miscible polymer blends and statistical copolymers without aggregation or specific interactions [60]. In fact, for the copolymers, the experimental values are higher than the value predicted from Fox's equation (Table 7). For example, in the case of 37wt% of MAA, the Fox's theory predicts a T_g equal to 119°C calculated from the actual copolymer composition and considering the T_g of PMMA equal to 100°C, as experimentally obtained, and 170°C for PMAA, as measured by Huang *et al.* [60,194].

Table 7. T_gs values of PMMA-*co*-MAA (0-30wt% MAA) measured on the second heating ramp of DSC and theoretical values calculated applying Fox's equation.

Composition	T_g DSC (°C)	T_g Fox's eq. (°C)
PMMA	100	-
PMMA-*co*-MAA 90/10	113	106
PMMA-*co*-MAA 80/20	134	112
PMMA-*co*-MAA 70/30	150	119

Based on the Fox's equation, Gordon and Taylor developed a new equation introducing a parameter k_{GT} to better represent the unequal contribution of the two components of the mixture [195]:

$$Tg = \frac{w_1 Tg_1 + k_{GT} w_2 Tg_2}{w_1 + k_{GT} w_2} \quad (28).$$

However, the Gordon-Taylor's equation is still based on the assumption on non-interacting components, therefore the experimental values in interacting mixtures deviate from the prediction. In order to take into account the contribution of the intermolecular interactions, Kwei introduced another term in the following equation [56,60,196]:

$$Tg = \frac{w_1 Tg_1 + k w_2 Tg_2}{w_1 + k w_2} + q w_1 w_2 \quad (29)$$

where k and q are fitting parameters. This approach is the most used equation for blends and copolymers in which H-bonds are present allowing a quantitative evaluation of specific interactions present in the system. The k parameter is introduced in the equation to take into account the unequal contribution of the mixture components, while q can be associated to the balance between the breaking of self-associations and the establishment of inter-association interactions [60,195]. The Kwei's equation was used to fit the experimental trend (Figure 58) and derive the parameters k and q which are respectively equal to 1 and 131, in agreement with values previously reported by Huang *et al.* for the same copolymers [60,193,196].

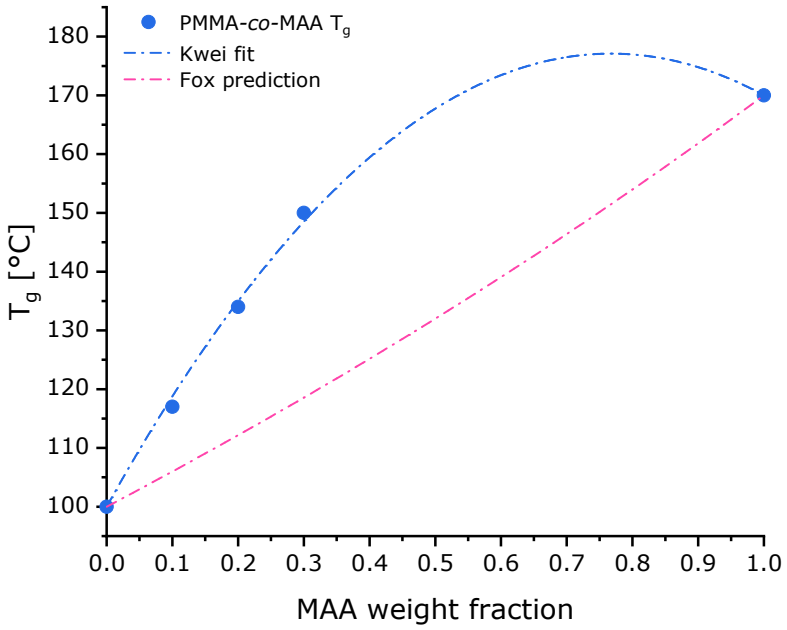


Figure 58. T_g versus composition curves of PMMA-*co*-MAA based on experimental data fitted by Kwei's equation and theoretical prediction by Fox's equation.

In fact, the T_g exhibited by PMMA-*co*-MAA exceeds about 30°C the theoretical value due to the effect of intermolecular H-bonding on macromolecular mobilities. As expected, the Fox's equation is not able to take into account the additional contribution of such specific and strong interactions. Indeed, the application of Kwei's equation results in a positive value of *q* parameter suggesting that intermolecular interactions are stronger than self-association ones as a further confirmation of the presence of H-bonds formed between MMA and MAA units. The value of *k* equal to 1 indicates that the two units are equally contributing to the glass transition phenomenon. Furthermore, the presence of intermolecular H-bonds was confirmed by IR spectroscopy with the appearance of a peak at 1697 cm^{-1} which can be assigned to the interaction via H-bond involving carboxylic groups [60].

At this point, the influence of the introduction of such intermolecular interactions on thermal conductivity were evaluated. The thermal conductivity shows a positive trend with increasing MAA content. Thermal conductivities (average of 3 measured values) were found equal to 0.209 for PMMA and 0.213, 0.221, and 0.227 $W \cdot m^{-1} \cdot K^{-1}$ respectively for 10, 20, and 30wt% of MAA (Figure 59).

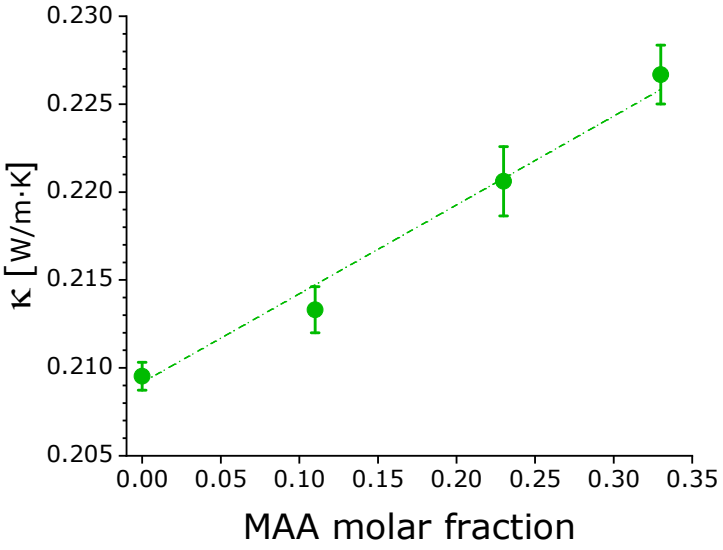


Figure 59. Thermal conductivity in PMMA-*co*-MAA copolymers variation with MAA content.

The slight increase observed can be correlated to the addition of stronger intermolecular interactions, *i.e.* H-bonds, to weak ones already present, *i.e.* vdW. In fact, it has been already proven by Kim *et al.* a correlation between the strength of intermolecular interactions and the thermal conductivity in amorphous polymers [46]. However, despite the positive trend observed in this system, the increment (Figure 59) results limited, as compared to previous thermal conductivity variation associated to inter-chain H-bonds described in literature [46,164]. Indeed, the increase of κ obtained with the addition of 30wt% of MAA in the copolymer is about 9%, while Kim *et al.*, for example, obtained in PAA blends an increase about 580% (from 0.22 to 1.5 $W \cdot m^{-1} \cdot K^{-1}$) due to inter-chain H-bonding. The addition of stronger H-bonds interactions to vdW ones may be not sufficient if the H-bonds are not present in high density [1,46].

3.1.3.3 Neutralized MMA-MAA copolymers

Neutralization of PMMA-*co*-MAA (30wt% MAA) with 0.2M NaOH was checked by ATR analysis. The copolymer resulted successfully neutralized; in fact, the carboxylic groups peak at 1697 cm^{-1} present in the pristine PMMA-*co*-MAA disappears and a new peak at 1560 cm^{-1} appears (Figure 60), which is assigned to the asymmetric stretching of the carboxylate $-COO^-$ groups in MAA [49,60,161]. At the same time, the intensity of the peak at 1724 cm^{-1} notably decreases. This peak is the result of the convolution of the -C=O stretching in the ester group in MMA (1724 cm^{-1}) and in the H-bonded carboxylic group in MAA (1697 cm^{-1}). Therefore, once the peak at 1697 cm^{-1} is removed, the one at 1720 cm^{-1} decreases its intensity due to the loss one of the two contributions. Also, compared to the pristine PMMA-*co*-MAA, a broad peak between 3100 and 3700 cm^{-1} appears. This observation may suggest a higher content of absorbed water due to the higher hydrophilic behaviour of the copolymer when it is neutralized.

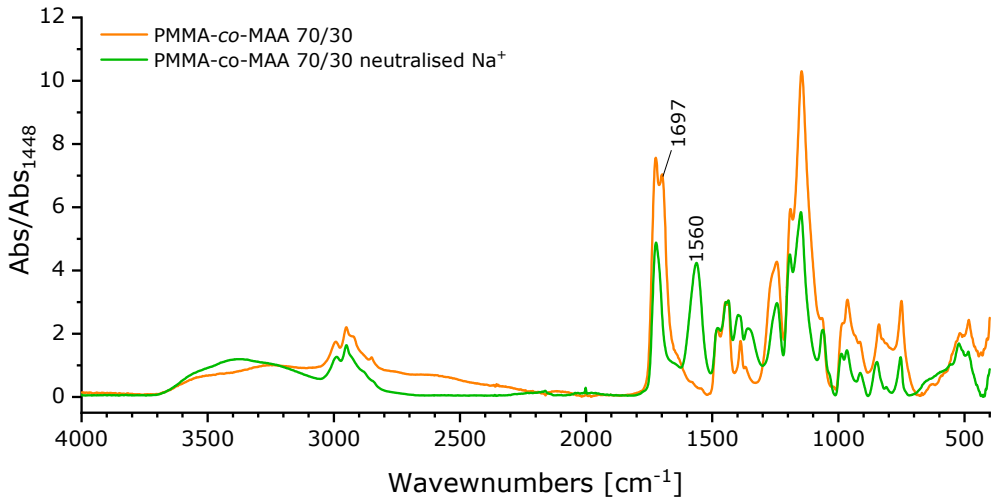


Figure 60. IR spectra (ATR mode) of pristine PMMA-*co*-MAA and neutralised with NaOH hydroxide 1:1.

DSC thermogram shows the presence of two second-order transitions (Figure 61), respectively close to 130 and 160°C (Table 8). Despite, the signals are associated with very low intensities, their presence was confirmed in multiple replicas and detectable on the curve part corresponding to the cooling ramp. Moreover, it is worth mentioning that the trend of the heat flow is in contrast with the one already observed for similar systems [197,198], *i.e.* the trend should be descending.

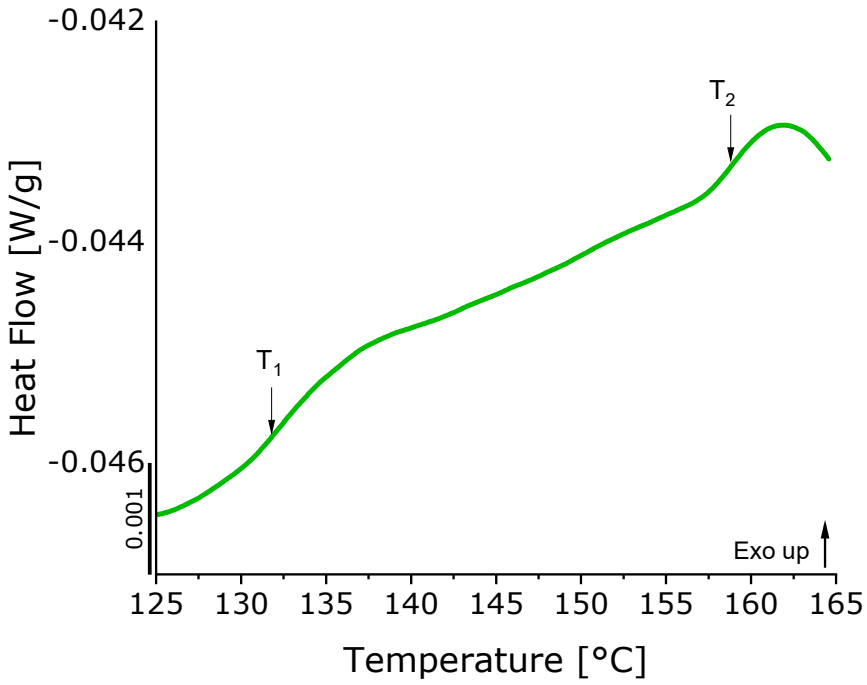


Figure 61. DSC thermograms of the second heating ramp for PMMA-*co*-MAA 70/30wt% neutralized with NaOH (heating rate 10°C/min).

Table 8. Temperatures of second-order transitions from second heating DSC for PMMA-*co*-MAA neutralized with NaOH.

Composition	T_1 (°C)	T_2 (°C)
PMMA-*co*-Na^+MAA	132	159

However, supposing that the two phenomena are associated with a glass transition, the presence of a second glass transition would be coherent with the multiplet-cluster model described by Eisenberg and Moore for random ionomers [166]. These authors theorised the existence of multiplets when neutralization is performed, where a multiplet is referred to an ion aggregate which can be created when the ion content is sufficiently high to induce electrostatic attraction. The presence of a multiplet gives rise in the surrounding layer to a region of restricted mobility in the hosting polymer (a schematic example is proposed by Eisenberg *et al.* for poly(styrene-*co*-sodium methacrylate) ionomer and it is reported in Figure 62).

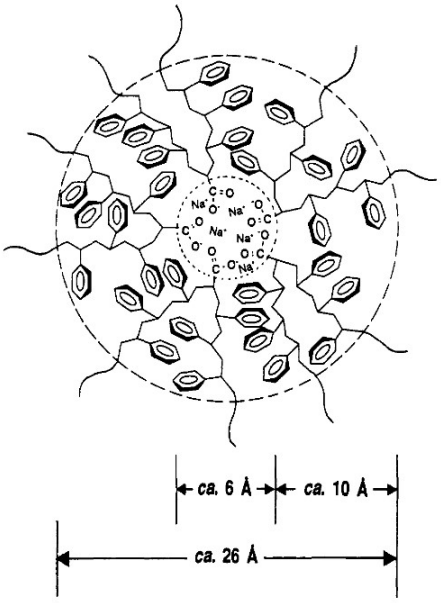


Figure 62. Scheme showing the restricted mobility region in a multiplet. *Reprinted with permission from "A New Multiplet-Cluster Model for the Morphology of Random Ionomers, 23, Eisenberg A., Hird B., Moore R.B., 4098-4107, 1990". Copyright 1990 American Chemical Society.*

The extension of the restricted mobility layer is determined by the macromolecule flexibility and the strength of the electrostatic interactions. In flexible chains, the layer will be thinner, while smaller ions result in stronger interactions. For higher ion concentration, the amount of multiplets increases and they start be sufficiently close to overlap their restricted mobility layers. At this point, they create clusters which constitute a second "independent" phase. Indeed, a second T_g is observed by DSC when the cluster dimension is higher than 50-100 Å [166] . The two T_gs can be attributed to the glass transition of the matrix and the cluster phase [166,199]. Therefore, assuming the appearance of a second glass transition phenomenon in

PMMA-*co*-MAA neutralized with Na^+ the successful addition of stronger ionic interactions to intermolecular H-bonds present in the system would be confirmed.

The neutralized films obtained after overnight evaporation of the solvents were then compression moulded at different temperature, *i.e.* from 180 to 300°C. This step is essential in order to perform thermal conductivity measurements which require a high degree of homogeneity of the film thickness. However, despite the numerous attempts to increase the moulding time and temperature, it has been not possible to obtain a final result suitable for testing. Regardless of the high temperature used, no flowing of the matrix was observed. Indeed, the presence of clusters appears to act as crosslinkers, resulting in a not-processable, *i.e.* thermoset-like, material [166].

3.2 Alternative comonomers: an evaluation of the influence of chain flexibility on the desired properties

New comonomers (Figure 63) were explored in order to design polymers where H-bonding forming moieties are present in a more flexible chain and concurrently overcome the issues related to the non-processability of PMMA-*co*-MAA copolymers. In particular, MAA units were replaced either by 2-hydroxyethyl methacrylate (HEMA) or 2-carboxyethyl acrylate (CEA).

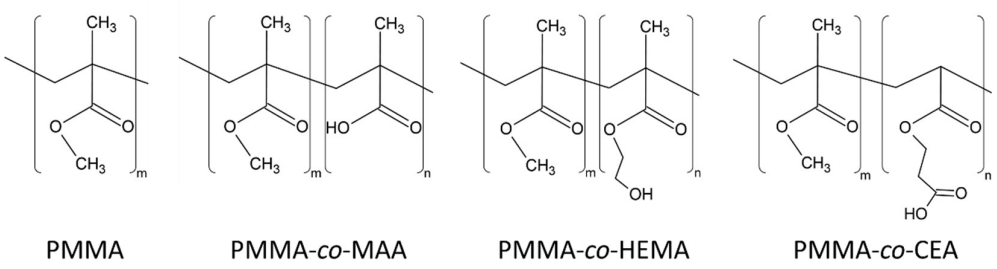


Figure 63. Chemical structure of PMMA and designed copolymers.

HEMA comonomer leads to the possibility of designing a new set of copolymers where the H-bonding forming moieties are brought by a hydroxylic group present at the end of an ethyl side chain.

The second option, *i.e.* the copolymerisation of MMA with CEA, contains a similar side chain but brings a carboxylic acid function in the macromolecule such as in MAA. In both copolymers, it will be possible to evaluate the influence of the addition of a longer side chain and the consequent increase in flexibility on the final properties while intermolecular H-bonds are still present. Additionally, in CEA-based copolymers, the effect of higher flexibility on neutralized copolymer with higher CEA content and its properties will be investigated. For both cases, the MMA/comonomer ratios were chosen to have the same mol% as for MAA in PMMA-*co*-MAA, namely at 11, 23, and 33mol% which corresponds to 14, 28, and 39wt% of HEMA and 15, 30, and 41% of CEA, respectively.

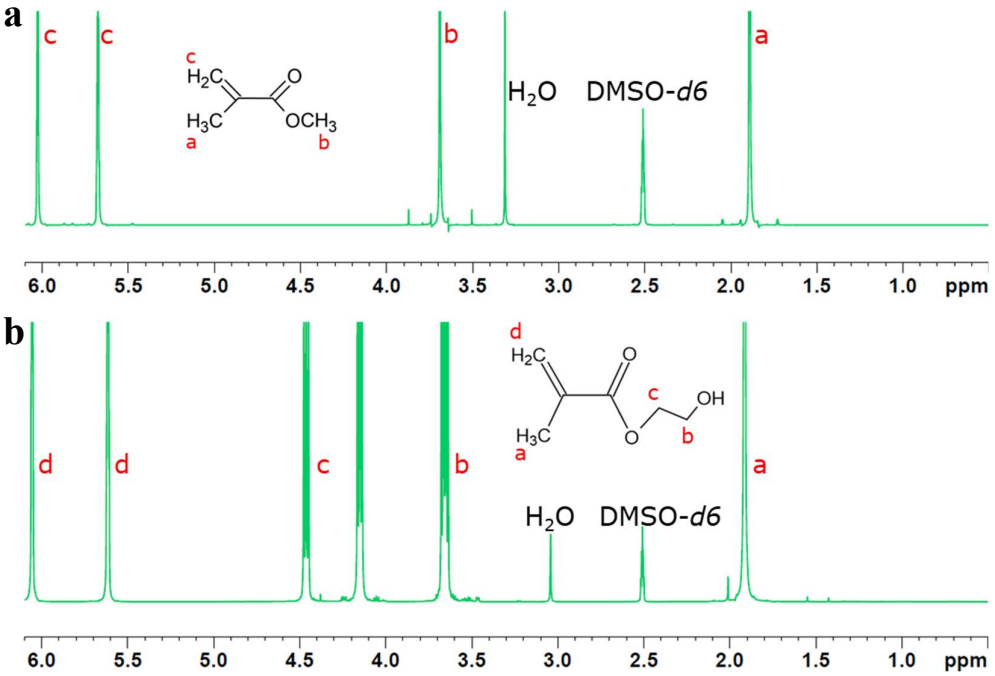
3.2.1 MMA-HEMA copolymers

PMMA-*co*-HEMA copolymers for 14, 28, and 39wt% of HEMA were successfully copolymerized by cobalt-mediated polymerization maintaining identical synthesis conditions as those optimized for PMMA and PMMA-*co*-MAA. Rigid, fully dense, and transparent samples were obtained for all the three compositions (an example for the higher content of HEMA is reported in Figure 64).



Figure 64. PMMA-*co*-HEMA 39wt% of HEMA from bulk polymerization.

The chemical structure was investigated by ^{1}H NMR spectroscopy (Figure 65). From the comparison with the spectra of the pure MMA and HEMA (reported in Figure 65a and b respectively), residual monomers are found in the copolymer. The peaks corresponding to MMA and HEMA are identified respectively at 6, 5.7, 3.7, 3.4 and 3.2 ppm and at 6.1, 5.7, and 4.7 ppm. In all the analysed compositions, the spectrum shows the resonances from both units corresponding to the α-methyl between 0.8 and 1.4 ppm and the -CH_2 from the backbone between 1.6 and 2.2 ppm. Moreover, the resonance corresponding to the methyl of the side chain in PMMA can be identified at 3.6 ppm and the -CH_2 from the pending group in HEMA close to 3.6 and 3.9 ppm.



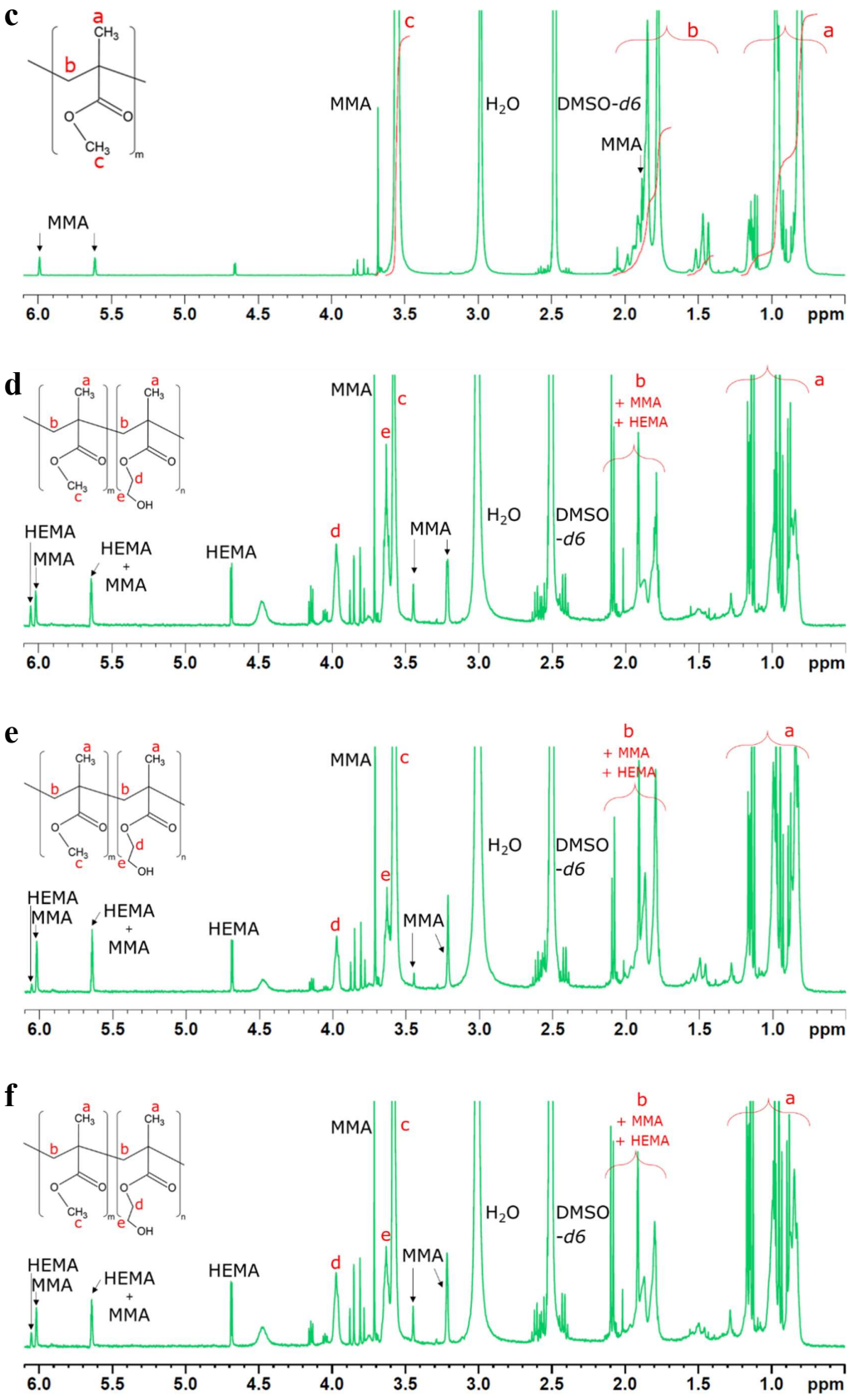


Figure 65. ^{1}H NMR spectra at 25°C for MMA (a) and at 90°C for HEMA (b), PMMA (c), PMMA-*co*-HEMA 14 (d), 28 (e), and 39wt% (f) of HEMA after copolymerization. (400 MHz, DMSO-*d6*). PMMA and comonomers reference spectra are reported to help in peak assignment.

The PMMA-*co*-HEMA spectrum and the resonances attribution results in agreement with those already reported in literature [200,201]. However, the calculation of the molar ratios between the two comonomers leads to unreliable values, presumably due to an incomplete solubilization of the copolymer.

The copolymers were found insoluble neither in DMF nor in THF for all the ratios MMA/HEMA preventing the determination of molar masses. In particular, insolubility in THF, which is known to be a good solvent for the studied copolymers [201], suggests that side reactions happening during the copolymerization and leading to some extent of crosslinking.

3.2.1.1 Thermal stability of PMMA-*co*-HEMA copolymers

The influence of the addition of HEMA comonomer on thermal stability was evaluated for PMMA-*co*-HEMA copolymers. The temperatures corresponding to a weight loss of 5% ($T_{5\%}$) and peak maximum for the main weight loss (T_{max}) from the derivative TGA curves are included in the range 233 – 270°C and 372 – 400 °C, respectively. Detailed temperatures are listed in Table 9. TGA thermograms are depicted for the highest HEMA content, *i.e.* 39wt% (Figure 66). Besides the main weight loss, a weight loss at higher temperature is detected on the derivative curves of experiment done under nitrogen atmosphere between 445 and 550°C and in air between 414 and 420°C. The final residual weight is close to 0 for temperature higher than 550°C under nitrogen atmosphere and 420°C in air. Compared to PMMA, temperatures of the main weight loss result higher and similar to the ones found compared for PMMA-*co*-MAA copolymers, *e.g.* for the highest amount of MAA or HEMA T_{max} result 401°C vs 400°C under nitrogen atmosphere and 384°C vs 380°C under air. It is worth mentioning that the PMMA-*co*-HEMA 86/14wt% is characterized by $T_{5\%}$ lower than expected, *i.e.* lower than the PMMA ones. One can suggest that such a phenomenon is related to the presence of higher amount of residual comonomers which tend to evaporate at lower temperatures.

Table 9. TGA data for PMMA and PMMA-*co*-HEMA copolymers under $N_{2(g)}$ and air.

Composition	**$T_{5\%}$ (°C)**		**T_{max} (°C)**	
	N_2	**Air**	**N_2**	**Air**
PMMA	258	265	372	372
PMMA-*co*-HEMA 86/14	233	257	398	387
PMMA-*co*-HEMA 72/28	248	270	398	389
PMMA-*co*-HEMA 61/39	253	265	400	380

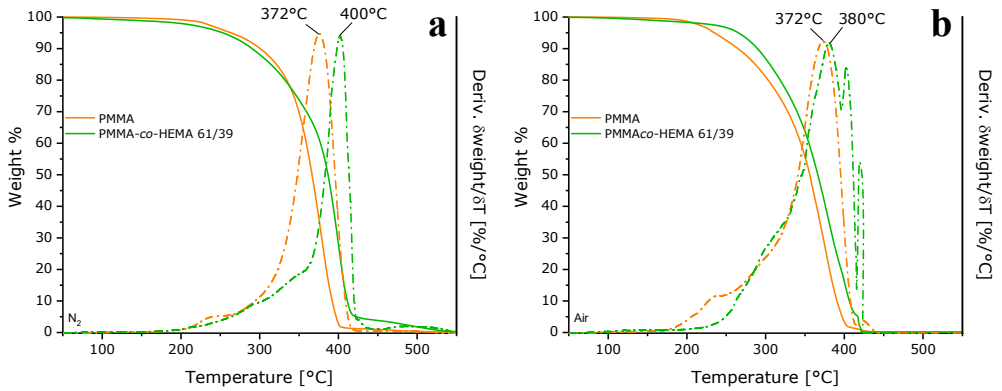


Figure 66. Thermogravimetric analyses of PMMA-*co*-HEMA 39wt% HEMA compared to PMMA ones in N_2 (a) and in air (b) (heating rate 10°C/min).

Compared to PMMA homopolymer, thermal degradation occurs at higher temperature when the HEMA comonomer is added with a more significant difference under nitrogen atmosphere compared to air in agreement with experimental results previously reported [200]. The decomposition of HEMA homopolymer polymer consists in two steps: 1/depolymerization at lower temperature which represents the main weight loss, 2/decomposition of the ester side chain at higher temperature following multiple reactions summarized in Figure 67 [202].

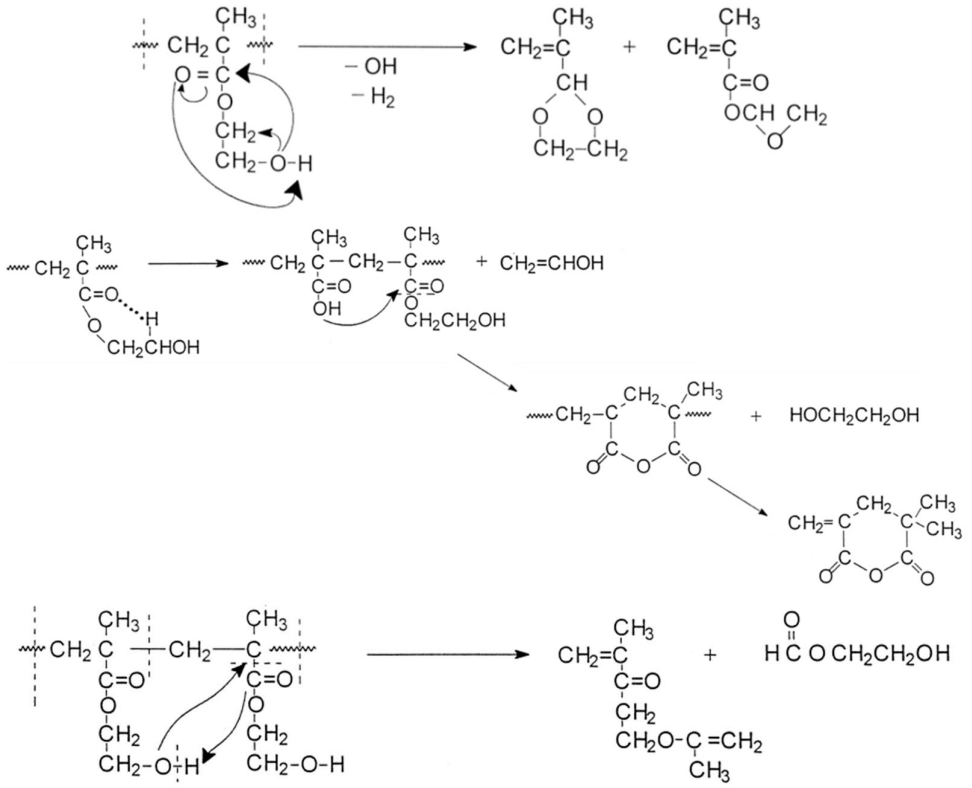


Figure 67. Decomposition reactions occurring in the side chain of HEMA units. *Adapted from A detailed study of thermal degradation of poly(2-hydroxyethyl methacrylate), 72, Demirelli K., Coşkun M., Kaya E., 75-80, Copyright (2001), with permission from Elsevier.*

Therefore, it is possible to associate the peaks corresponding to the main degradation to depolymerization in both atmospheres. The decomposition step observed at higher temperatures can be attributed to the decomposition of a cross-linked fraction formed in presence of HEMA units [202].

3.2.1.2 H-bond influence on copolymer properties

To further investigate the chemical structure, IR spectroscopy was performed. In the spectra (Figure 68), it is possible to identify the absorption peaks previously reported for PMMA listed in Table 6 [191]. The addition of HEMA comonomer results in the appearance of a broad peak between 3700 and 3100 cm^{-1} showing a higher intensity when HEMA content raises from 14 to 28 and 39wt% (Figure 68). This peak results from the superimposition of different contributions which can be attributed to the H-bonded hydroxyl groups of HEMA unit and absorbed water [200,201,203]. A shoulder to the C=O stretching peak (1724 cm^{-1}) appears at low wavenumbers and can be attributed to the presence of water (water bending is close to 1640 cm^{-1}) absorbed due to the presence of the polar comonomer [192].

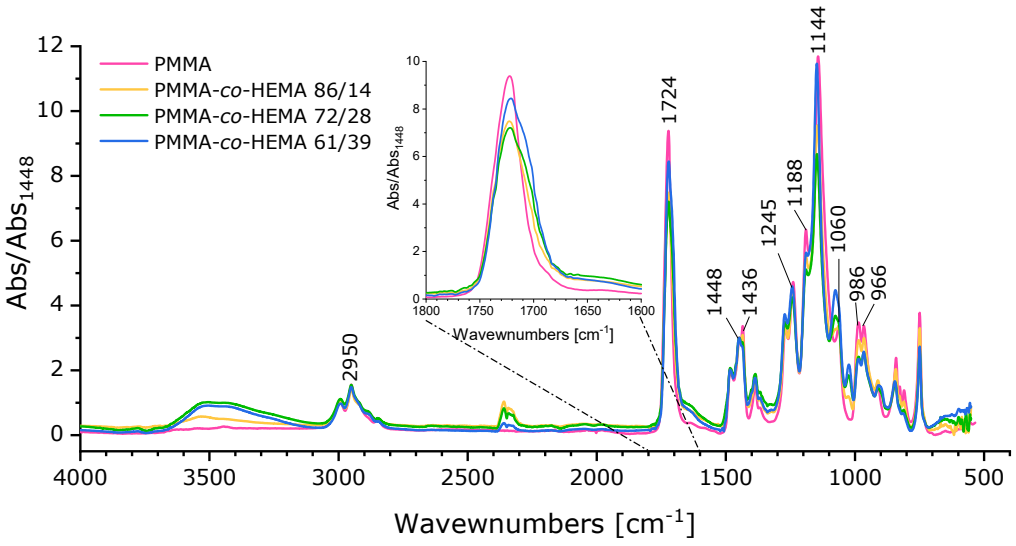


Figure 68. IR spectra (ATR mode) of PMMA-*co*-HEMA copolymers after copolymerization reaction with HEMA content from 14 to 39wt% compared to PMMA.

A peak appears between 2400 and 2300 cm^{-1} and can be ascribed to carbon dioxide present in the atmosphere detected due to the measuring conditions. Whether the sample is not perfectly planar, it could lead to a defective contact with the crystal resulting in air layer entrapped during the measurement.

DSC thermograms are reported in Figure 69 and show a single T_g for all the studied compositions. The T_gs determined from the second heating ramp are listed in Table 10. The values decrease increasing the HEMA fraction, coherently with the lower T_g of the HEMA homopolymer compared to the PMMA one (81°C vs. 100°C) [60,200].

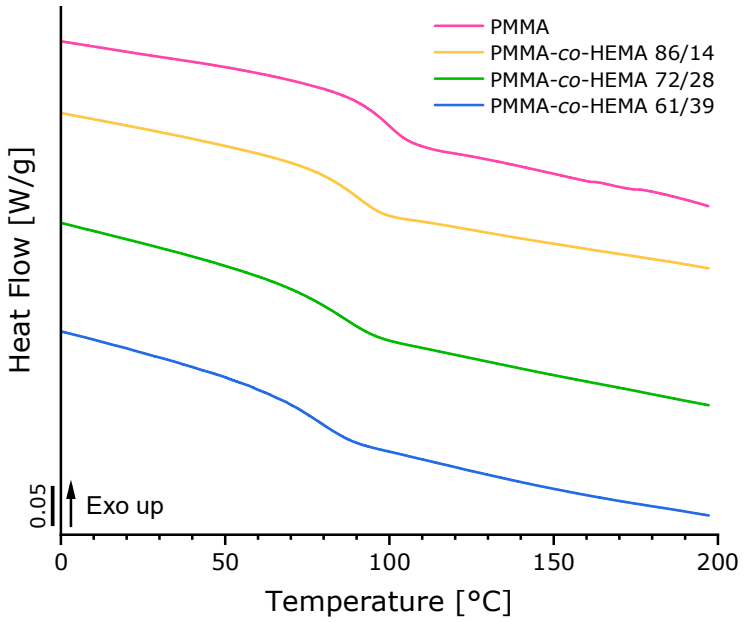


Figure 69. DSC thermograms of PMMA-*co*-HEMA at 14, 28, and 39wt% of HEMA (heating rate 10°C/min).

The obtained values are slightly lower compared to the ones calculated applying Fox's equation (Table 10), considering 100°C for PMMA and 81°C for PHEMA [200].

Table 10. T_gs values of PMMA-*co*-HEMA (14-39wt% HEMA) measured on the second DSC heating ramp and theoretical values calculated applying the Fox's equation.

Composition	**T_g DSC (°C)**	**T_g Fox's eq. (°C)**
PMMA	100	-
PMMA-*co*-HEMA 86/14	91	97
PMMA-*co*-HEMA 72/28	86	94
PMMA-*co*-HEMA 61/39	79	92

The Kwei's fit of the T_g variation as a function of the comonomers ratio is showed in Figure 70. The k and q fitting parameters are found equal to 1 and -51 respectively.

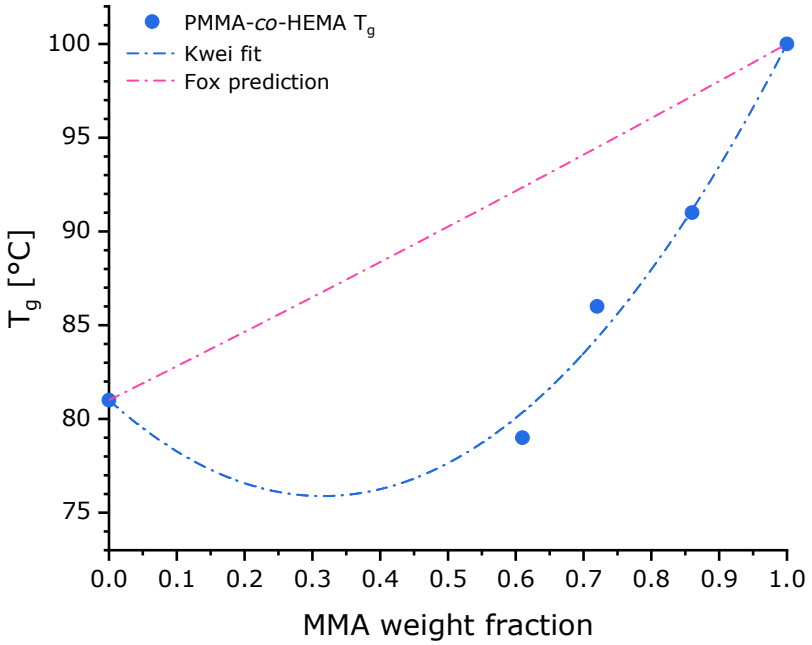


Figure 70. T_g versus composition curves of PMMA-*co*-HEMA based on experimental data fitted by Kwei's equation and theoretical prediction by Fox's equation.

The *k* value equal to 1 indicates that the two units contribute equally to the glass transition phenomenon. The negative value of *q* indicates that self-association interactions in similar units are stronger than intermolecular ones [60,195]. Therefore, we can assume that H-bonds are present in between the OH units of the HEMA units, while no significant interactions occur between the carboxylic group of MMA and the hydroxyl group of HEMA (scheme in Figure 71).

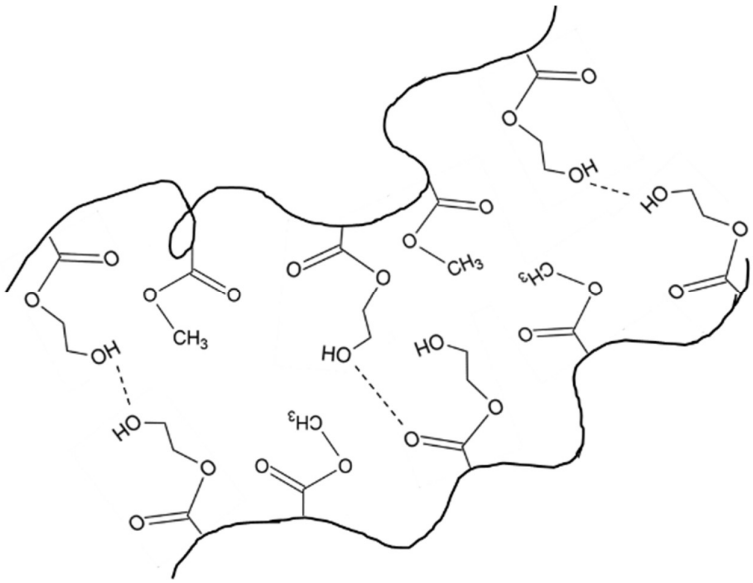


Figure 71. Scheme of intermolecular interactions in PMMA-*co*-HEMA.

Thermal conductivities (average of 3 measured values) were found equal to 0.214, 0.221, and 0.226 $W \cdot m^{-1} \cdot K^{-1}$ respectively for 14, 18, and 39wt% of HEMA (Figure 72).

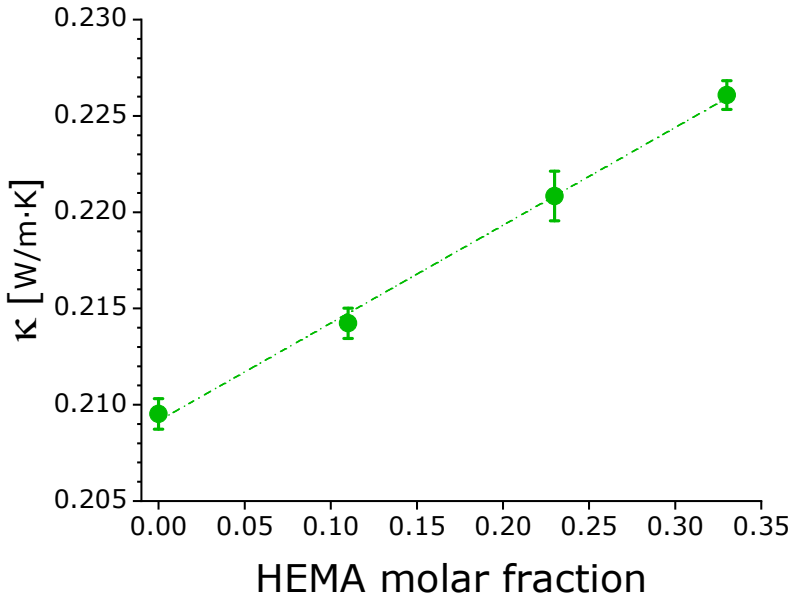


Figure 72. Thermal conductivity in PMMA-*co*-HEMA.

The thermal conductivity of the PMMA-*co*-HEMA copolymers results show no differences compared to PMMA-*co*-MAA copolymers suggesting that the addition of a more flexible chain in the H-forming unit has no influence on the bulk thermal conductivity of the polymethacrylate copolymers. It is worth mentioning that, in these copolymers, two different effects might compete: the introduction of strong inter-chain interactions, *i.e.* H-bonds, and that of a side chain, *i.e.* hydroxyethyl group. These two contributions may act in an opposite way on the final value of κ. The reinforcement of the interaction strength is expected to lead to an increment of the thermal conduction due to an improvement of inter-chain thermal conductance; on the contrary, the introduction of side chains may result in a smaller κ value due to an increment of chain terminations and consequently of scattering events [1,41]. Indeed, the presence of a side chains may lead to a higher number of chain terminations leading to an increase of phonon localization and scattering events [1,41]. However, given the small side chain introduced in the copolymers the negative contribution on κ should be negligible [1]. Therefore, the only contribution on the thermal conductivity should come from the introduction of inter-chain H-bonds. Indeed, as abovementioned, the results are found identical to the ones obtained for PMMA-*co*-MAA.

3.2.2 MMA-CEA copolymers

PMMA-*co*-CEA, 15, 30, and 41wt% of CEA, polymerized by cobalt-mediated polymerization applying identical synthesis conditions as those optimized for

PMMA and PMMA-*co*-MAA led to rigid samples with entrapped bubbles in the whole area of the sample (Figure 73).



Figure 73. PMMA-co-CEA 41wt% of CEA polymerized at 55/70°C.

Therefore, the temperature step profile of the synthesis was modified in order to suppress bubbles by controlling the formulation overheating. Different attempts have been performed applying different temperature profiles (2h at 55/70 (T_1), 55/60 (T_2), 30/40/60 (T_3), and T_{room}/25/30/35/40/45/60°C (T_4)). The evolution of the bubbles obtained in the different synthesis conditions are reported in Figure 74 for PMMA-*co*-CEA 59/41wt%. It is clear that the addition of isothermal steps at lower temperatures progressively determines a reduction in the bubbles size. However, despite their size reduction, a complete elimination was not achieved.

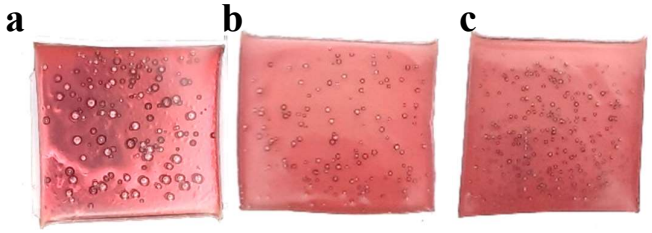
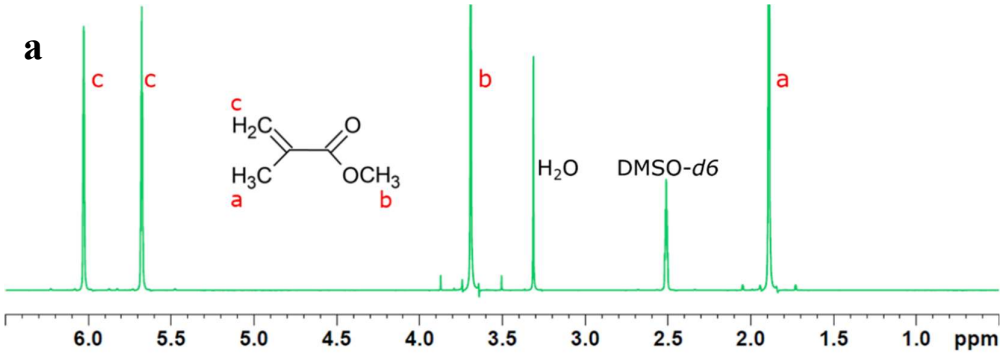
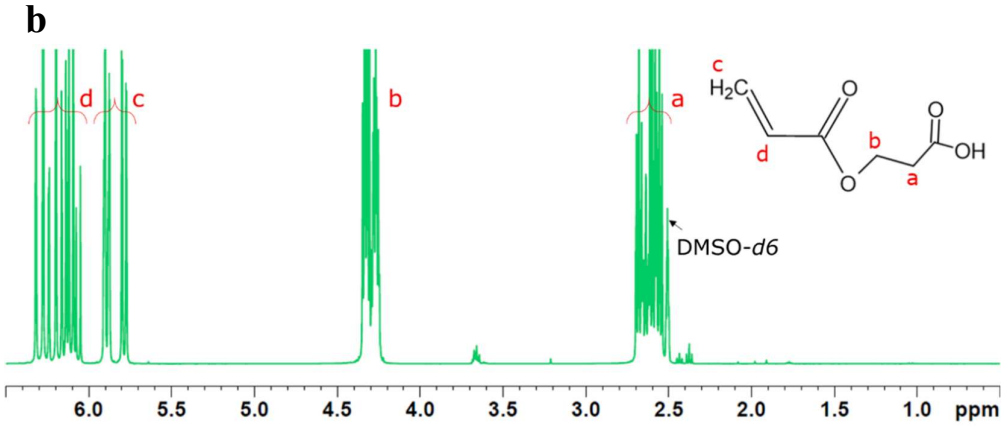


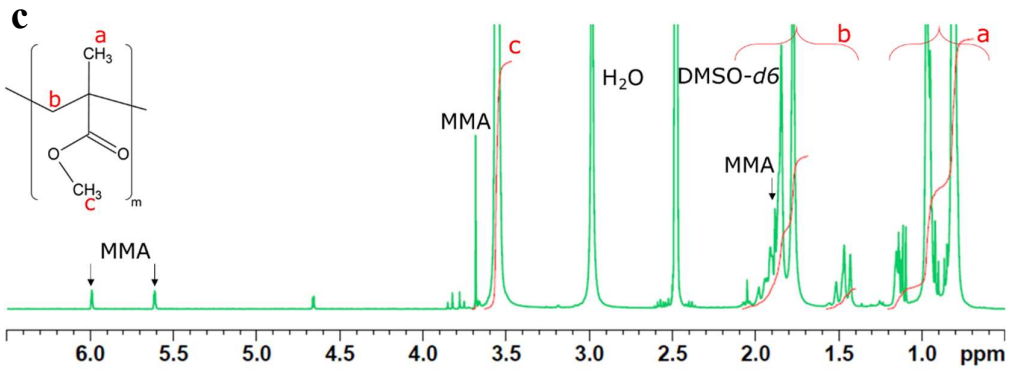
Figure 74. Bubbles evolution for PMMA-*co*-CEA 59/41wt% treated at 50/60 (A), 30/40/60 (B), and Troom/25/30/35/40/45/60°C (C).

The chemical structure after copolymerization was investigated by ^{1}H NMR spectroscopy (Figure 75). From the comparison with the spectra of the pure MMA and CEA (reported respectively in Figure 75a and b), residual monomers are found in the copolymer. The peaks corresponding to MMA are identified at 3.2 ppm, while the peaks between 6.3 and 5.8 ppm can be attributed to the contribution of residual MMA and CEA. Residual MMA and CEA were found to be 0.4mol% and 1.5mol%, respectively. The calculation of residual CEA in PMMA-*co*-CEA 15wt% of CEA is unreliable given the incertitude caused by the low intensity of the peaks.

For all compositions, the spectra (Figure 75c-f) show the peaks from MMA units corresponding to the α-methyl between 0.8 and 1.4 ppm and the -CH_2 from the backbone coming from both units between 1.4 and 2.3. Moreover, the peaks corresponding to the methyl of the side chain in PMMA can be identified at 3.6 ppm and the -CH_2 from the pending group in CEA close to 4.3 and 2.6 ppm [204]. Copolymers composition determined by ^{1}H NMR (Figure 75b, c, and d) for the ratio MMA:CEA were found to be 91:9, 78:22, and 67:33mol% respectively for the copolymerized 15, 30, and 41wt% of CEA in agreement with the expected values (11, 23, and 33mol%).


a
c
c
b
a
H2O
DMSO-d6
6.0
5.5
5.0
4.5
4.0
3.5
3.0
2.5
2.0
1.5
1.0
ppm


b
d
c
b
a
DMSO-d6
OH
6.0
5.5
5.0
4.5
4.0
3.5
3.0
2.5
2.0
1.5
1.0
ppm


c
a
b
c
MMA
H2O
DMSO-d6
b
a
MMA
MMA
6.0
5.5
5.0
4.5
4.0
3.5
3.0
2.5
2.0
1.5
1.0
ppm

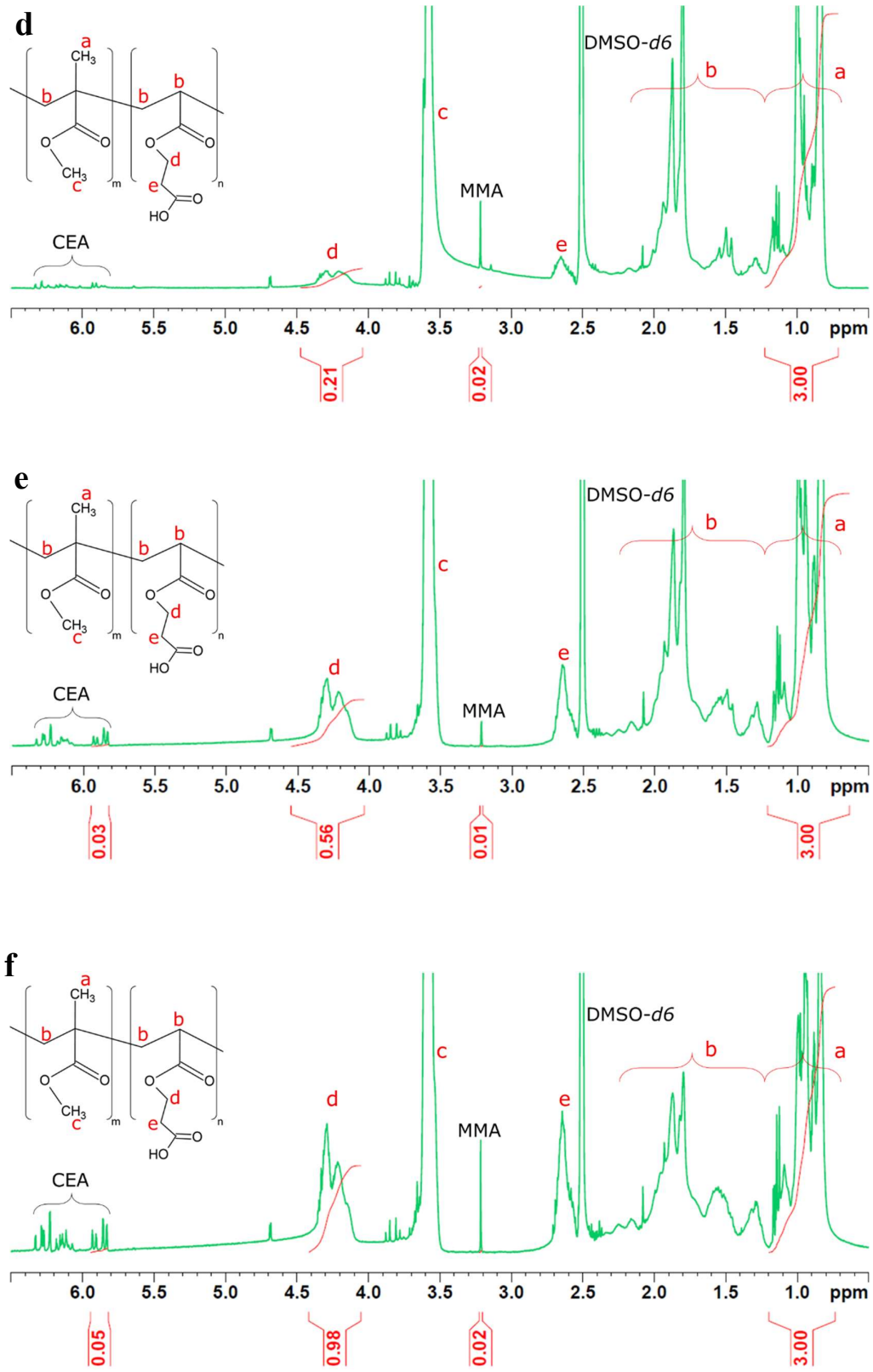


Figure 75. ^{1}H NMR spectra at 25°C for MMA (a) and at 90°C for CEA monomer (b), PMMA (c), PMMA-*co*-CEA 15 (d), 30 (d), and 41wt% (f) of CEA after copolymerization. (400 MHz, DMSO-*d6*). PMMA and comonomers reference spectra are reported to ease peak assignment.

Molar masses of PMMA and PMMA-*co*-CEA copolymers were obtained in DMF and are reported in Table 11.

Table 11. Molar masses PMMA-*co*-CEA polymerized applying different temperature profiles.

Composition	Temperature profile (°C)	M_n (g/mol)
PMMA	T_1 (55/70)	131200
PMMA-*co*-CEA 85/15	T_3 (30/40/60)	32600
PMMA-*co*-CEA 70/30	T_3 (30/40/60)	12400
PMMA-*co*-CEA 59/41	T_4 (T_{room}/25/30/35/40/45/60)	-

Compared to PMMA homopolymer, lower M_n are obtained when CEA comonomer is added in the chain. From the molar mass distribution showed in Figure 76, it is clear that, for the lowest content of CEA, the synthesis results in high dispersity with a large distribution of molar masses formed by the superimposition of multiple peaks. Therefore, given the large dispersion, the determined M_n is an approximate value. Moreover, for 30wt% of CEA the different temperature profiles applied led to a similar M_n value and in both cases to a monomodal distribution (Figure 76a). For the higher content of CEA 41wt%, the molar mass distribution shows a non-gaussian peak (Figure 76b) at an elution time close to the upper limit of the column. The M_n results in a value much higher than the upper limit identified by the calibration curve of PS, indicating that M_n of PMMA-*co*-CEA 41wt% of CEA is higher than $1.35 \cdot 10^6$ g/mol for both temperature profiles applied (T_3 and T_4).

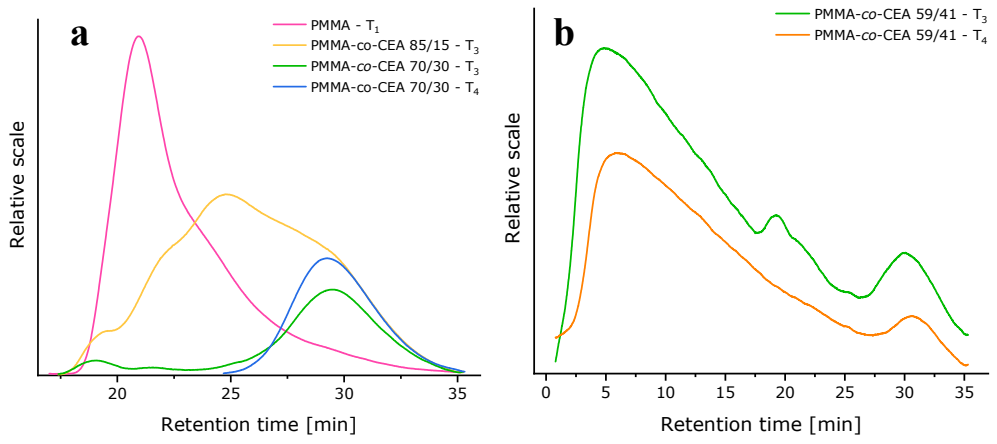


Figure 76. Molar mass distribution for PMMA, PMMA-*co*-CEA 15 and 30 (a) and 41wt% of CEA (b) polymerized applying different temperature profiles (PS standard, DMF as eluent and viscosimeter detection).

3.2.2.1 Thermal stability of PMMA-*co*-CEA

The influence of the addition of CEA comonomer on thermal stability was evaluated. The temperatures corresponding to a weight loss of 5% ($T_{5\%}$) and peak maximum for the main weight loss (T_{max}) from the derivative TGA curves resulted

included in the range 233 – 265°C and 340 – 379°C, respectively. Detailed temperatures are listed in Table 12.

Table 12. TGA data for PMMA and PMMA-*co*-CEA copolymers under $N_{2(g)}$ and air.

Composition	$T_{5\%}$ (°C)		T_{max} (°C)	
	N_2	Air	N_2	Air
PMMA	258	265	372	372
PMMA-*co*-CEA 85/15	248	248	378	365
PMMA-*co*-CEA 70/30	241	237	379	355
PMMA-*co*-CEA 59/41	233	225	370	340

Thermograms are reported for the highest CEA content, *i.e.* 41wt%, in Figure 77. A weight loss at higher temperatures is detected on the derivative curves under air between 450 and 535°C and under nitrogen atmosphere between 465 and 600°C. The curve final residual weight results close to 0 for temperature higher than 590°C under nitrogen atmosphere and 530°C under air. Compared to PMMA homopolymer, thermal decomposition occurs at lower temperature when the CEA comonomer is added. Moreover, the presence of multiple peaks indicates that the degradation takes place starting from 200°C and involves a much more complex mechanism compared to PMMA. The mechanism for MMA-CEA copolymer is not disclosed yet. However, considering the structure, multiple reactions can be observed. As for polyethylene acrylate, degradation of the side chain may occur before the main weight loss related to depolymerization [205]. Also, in the same way as for PMMA-*co*-MAA copolymer, the presence of a carboxylic acid units can lead to the formation of anhydride structure by the condensation of two -COOH units or of a -COOH with a $-COOCH_3$ unit. Moreover, the appearance of a small peak in the derivative curve after the main weight loss may suggest the formation of anhydride structures which can be degraded at high temperature under inert atmosphere compared an oxidative one [182].

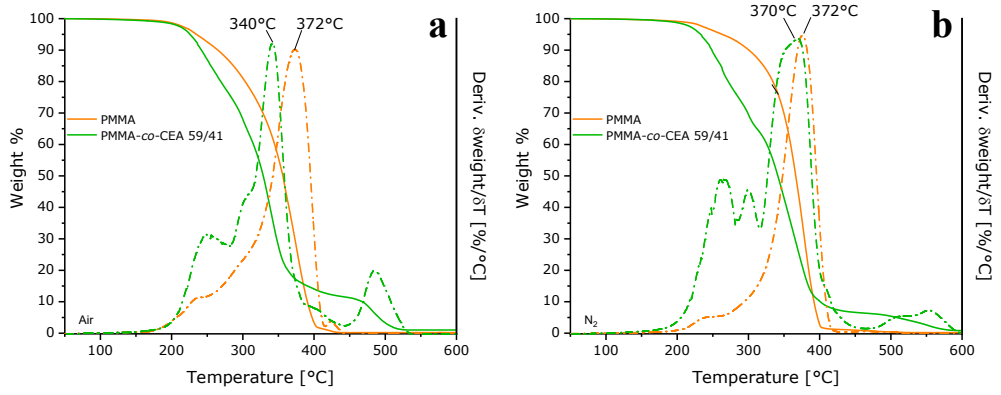


Figure 77. Thermogravimetric analyses of PMMA-*co*-CEA 41wt% CEA compared to PMMA ones in N_2 (a) and in air (c) (heating rate 10°C/min).

3.2.2.2 H-bond influence on copolymer properties

To further investigate the chemical structure, IR spectroscopy was performed (Figure 78). In the spectra, absorption peaks previously assigned to PMMA structure are identified and reported in Table 6 [191]. The addition of CEA comonomer leads to the appearance of a broad peak between 3100 and 3400 cm^{-1} when CEA content exceeds 30wt%. This broad peak can be correlated to the vibration of H-bonded -OH in carboxylic groups [206]. Also, a reduction of the peak intensities at 1060, 986, and 966 cm^{-1} is observed given the reduction of the α-methyl content when CEA is added. Focusing on the carbonyl region, it is possible to notice a broadening of the peak associated to the carbonyl absorption, which can be correlated to the superimposition of two peaks, the carbonyl in the MMA unit and the one from the CEA unit [206].

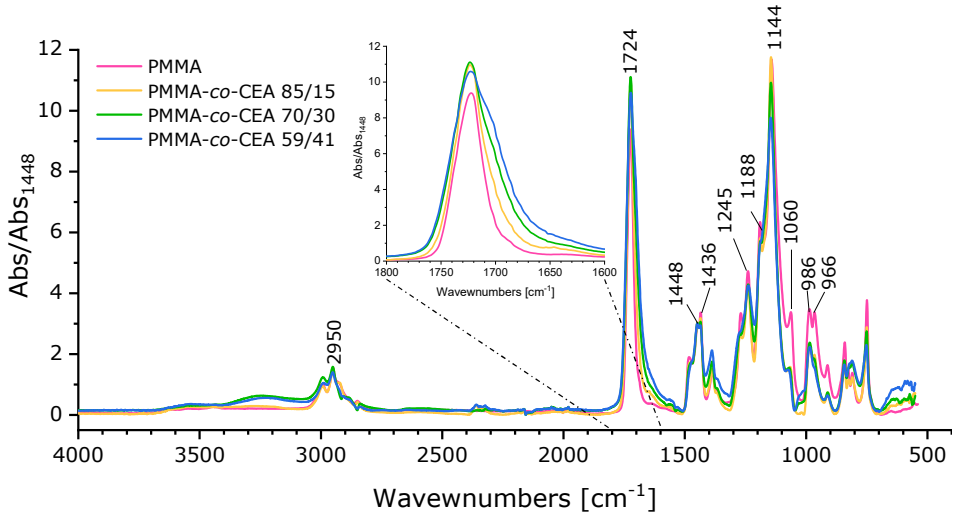


Figure 78. IR spectra (ATR mode) of PMMA-*co*-CEA copolymers after copolymerization reaction with CEA content from 15 to 41wt% compared to PMMA.

In a similar way to what it was observed for PMMA-*co*-HEMA, a peak appears between 2400 and 2300 cm^{-1} and can be ascribed to carbon dioxide detected due to the measuring condition according to the planarity of the sample.

DSC thermograms show a single T_g which decreases with CEA content (Figure 79).

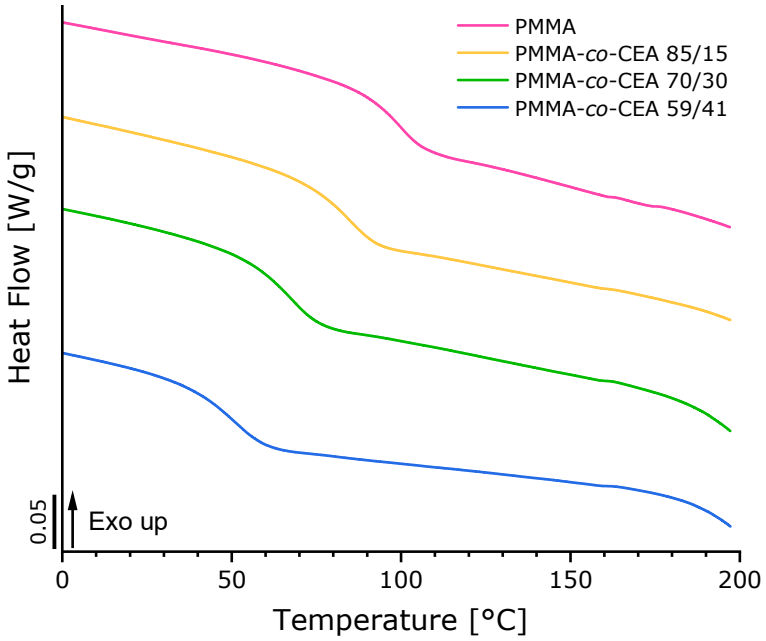


Figure 79. DSC thermograms of PMMA-*co*-CEA at 15 (a), 30 (b), and 41wt% of CEA (heating rate 10°C/min).

Experimental data and Fox's predictions for the T_g values are listed in Table 13. The theoretical values calculated by Fox's equation (using 100°C PMMA and 22°C for PCEA [207]) slightly overestimate the values measured on the second heating ramp of DSC thermograms. This deviation is larger for higher CEA content.

Table 13. T_gs values of PMMA-*co*-CEA (15-41wt% CEA) measured on the second heating ramp of DSC and theoretical values calculated applying Fox's equation.

Composition	**T_g DSC (°C)**	**T_g Fox's eq. (°C)**
PMMA	100	-
PMMA-*co*-CEA 85/15	84	86
PMMA-*co*-CEA 70/30	67	73
PMMA-*co*-CEA 59/41	52	64

The Kwei's fit of the T_g variation as a function of the comonomers ratio is plotted in Figure 80. The k and q fitting parameters are found equal to 1 and -54, respectively.

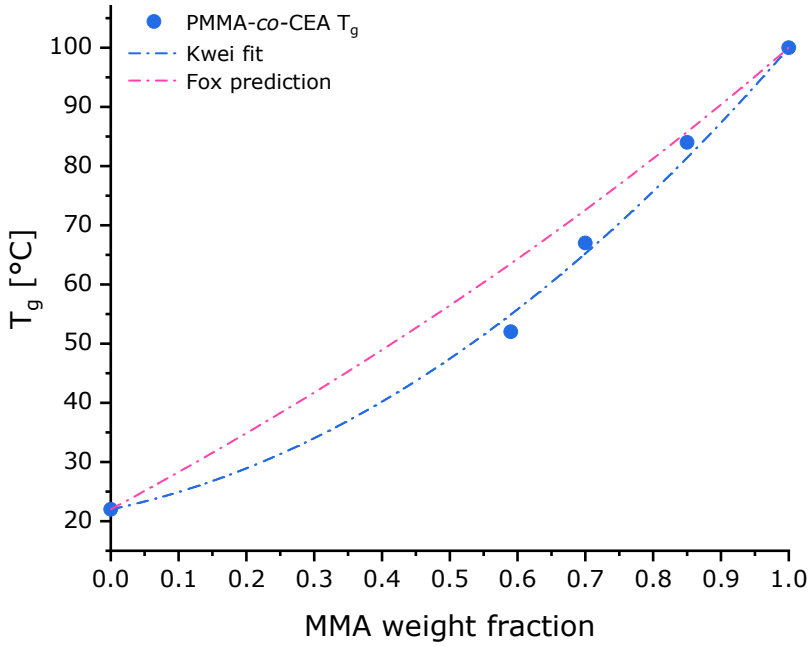


Figure 80. T_g versus composition curves of PMMA-*co*-CEA based on experimental data fitted by Kwei's equation and theoretical prediction by Fox's equation.

The *k* value equal to 1 indicates that the T_g is the result of an equal contribution of the two units. Instead, the negative value of *q* indicates that self-association interactions are stronger than intermolecular ones determining a free volume increase [60,195]. Therefore, we can assume that H-bonds are present in between the -COOH units of the CEA units and no interactions between the carboxylic groups of MMA and CEA are established.

The thermal conductivity of the copolymers was supposed to be measured in order to investigated the influence of a more flexible chain bringing in the system H-bonds and in a later step ionic bonds. However, the presence of bubbles in the sample prevent the accurate measurement of bulk thermal conductivity. Instead, pristine and neutralized copolymers films could be obtained from solution casting and thermal conductivity of the thin films can be measured, results will be discussed in Chapter 3.2.2.3.

3.2.2.3 Neutralized PMMA-*co*-CEA copolymers

Neutralization of PMMA-*co*-CEA (41wt% MAA) with 0.3M NaOH was evaluated by ATR IR spectroscopy analysis. The copolymer resulted successfully neutralized. In fact, the appearance of a new peak in carbonyl absorption region, namely at 1572 cm^{-1}, can attributed to asymmetric stretching of the carboxylate $-COO^-$ group (Figure 81) [49,60,161]. At the same time, the intensity of the peak at 1724 cm^{-1} notably decreases, this peak is the result of the convolution of the -C=O stretching in the ester group in MMA (1724 cm^{-1}) and in the H-bonded carboxylic group in CEA (at lower wavenumbers). Therefore, once the peak at lower wavenumbers is

removed the one at 1720 cm^{-1} decreases its intensity due to the loss one of the two contributions.

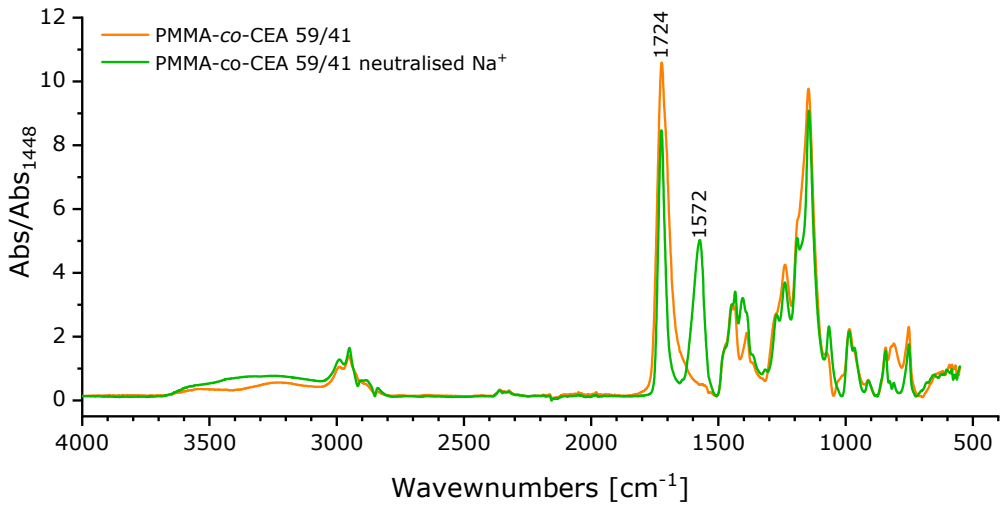


Figure 81. IR spectra (ATR mode) of pristine PMMA-*co*-CEA 41wt% of CEA and neutralized with NaOH 1:1.

The films obtained after overnight solvent evaporation for PMMA-*co*-CEA (15, 30, and 41wt% of CEA) and sodium neutralized PMMA-*co*-CEA 41wt% CEA were compression moulded. A better flow of the copolymer was observed for pristine and neutralized PMMA-*co*-CEA compared to pristine and neutralized PMMA-*co*-MAA thanks to the higher flexibility of the chains. However, despite the different attempts to optimize the moulding process parameters (moulding temperature was varied between 80 and 170°C), thickness homogeneity resulted still insufficient to perform thermal conductivity measurements on the thin film given the requirement of a thickness variation <1μm.

3.3 Conclusions

In this chapter, aiming to tailor the thermal conductivity in amorphous polymers by changing the strength and density of inter-chain interactions, the synthesis and characterization of methacrylic copolymers has been reported.

PMMA was selected as amorphous model and, in order to introduce stronger interactions than vdW in the polymethacrylate chain, free radical copolymerization was employed. Moreover, giving the requirements for the measurement of thermal conductivity in bulk (fully dense and defects free samples with minimum dimensions 40x40x4mm^3), polymerization was performed in bulk.

In the first designed copolymers, the comonomer (methacrylic acid) was chosen in order to introduce in the chain a unit able to form inter-chain H-bonds and, after neutralization, ionic interactions. Performing bulk free radical co-/polymerization, three different activation mechanisms have been investigated: BPO, BPO/tertiary amine, and MEKP/Co^{2+}. The first synthesis performed with BPO initiator proceeded at high temperature, led to high evaporation rate of reactive mixture during polymerization and resulted in porous materials unsuitable for

characterization. The second synthesis was performed at room temperature thanks to the redox reaction between BPO and the tertiary amine and resulted in the successfully reduction of the monomer evaporation, from 55 to 4.5wt%. However, despite the achievement of solid and dense materials, the presence of defects in the samples prevent the subsequent characterization. The last initiation mechanism evaluated ensured a more controlled radicals formation by using a temperature profile of isothermal steps. The temperature profile and the mould setup were adjusted in order to properly dissipate the heat generated during the exothermic reaction leading to the identification of optimal synthesis conditions, *i.e.* 2h at 55 and 2h at 70°C aluminium mould plates. Therefore, PMMA-*co*-MAA random copolymers were successfully copolymerised with a MAA content from 0 to a maximum of 30wt%, high degrees of conversion and high molar mass. An attempt of further increasing the MAA content was performed, with MAA equal to 40wt%, and the appearance of the second white phase into the samples was observed. From ^{1}H NMR, spectra MMA residual monomer was identified and calculated equal to 1.5mol%. The actual comonomers ratios were found to be 87:13, 74:26 and 63:37mol% respectively for the copolymerized 10, 20 and 30wt% of MAA. The values were slightly lower in terms of MMA mol% compared to the expected values due to higher MMA volatility compared to MAA one. Monomodal distributions of molar mass were found for PMMA and PMMA-*co*-MAA with 10 and 20wt% of MAA with M_n included between $9.8 \cdot 10^5$ and $2.6 \cdot 10^6$ g/mol. For the highest amount of MAA, 30wt%, the value was found higher than the upper limit of the column indicating a M_n higher than the detection limit. PMMA showed a thermal degradation coherent with that already described in literature. The main difference associated to the addition of MAA comonomer was identified in the formation of an anhydride structure which occurred around 220°C due to the condensation reactions characteristic of the carboxylic acid group. Next, the effect of the introduction of different amount of inter-chain H-bonds on final properties was evaluated. The presence of H-bonds established between the chains was proved by IR spectroscopy where a peak associated to the presence of H-bonded -COOH group appeared in the carbonyl region at 1697 cm^{-1}. Moreover, the derivation of Kwei's parameter q from the fit of experimental T_gs confirmed that strong inter-chain interactions were present in the copolymers. Lastly, a positive trend in bulk thermal conductivity was found with the increasing MAA content and thus H-bonding density. However, the increment of thermal conductivity following the addition of stronger inter-chain interactions, *i.e.* H-bonds, to weak vdW ones was limited.

Later, PMMA-*co*-MAA 30wt% MAA was successfully neutralized with sodium hydroxide as confirmed by IR spectroscopy by the appearance of a peak at 1560 cm^{-1} which is attributable to the stretching of the carboxylate -COO$^-$ group in MAA unit and replaced completely the peak at 1697 cm^{-1}. The neutralization led to the formation of ionic clusters which showed a second glass transition. Unfortunately, the neutralized materials resulted non-processable by compression moulding up to 300°C, likely due to the crosslinking effect associated to the ionic clusters, preventing the measurement of thermal conductivity on the films.

In a later stage, the MAA comonomer was replaced with different comonomers in order to investigate the impact of higher chain flexibility when intermolecular H-

bonds are present. The two comonomers chosen were characterized by the presence of a hydroxyl (HEMA) and a carboxylic acid group (CEA) at the end of an ethyl side chain. In both cases, the ratios MMA/comonomer were chosen to have correspondence with MAA mol% of PMMA-*co*-MAA in the three ratios. Additionally, in CEA copolymers, the effect on thermal conductivity of higher flexibility on neutralized copolymer with higher CEA content was evaluated.

PMMA-*co*-HEMA copolymers were effectively obtained for the same synthesis conditions as PMMA-*co*-MAA. ^{1}H NMR showed the peaks characteristic of the structure according to the ones reported in literature and the presence of residual comonomers. However, the calculation of the molar ratios between the two comonomers leads to unreliable values, presumably due to an incomplete solubilization of the copolymers. Moreover, given the insolubility in multiple solvents, the presence of crosslinking has been assumed in the structure and the molar mass of the copolymers were not evaluated. Thermal degradation of PMMA-*co*-HEMA copolymer occurred at higher temperature compared to PMMA with a higher difference under nitrogen atmosphere compared to air, in agreement with experimental results previously reported in literature. The IR spectra showed all the peaks associated to the methacrylic structure and the addition of HEMA unit resulted mainly into the addition of the peaks associated to the -OH stretching. From the Kwei's fit of T_g values, a negative value of q was derived indicating the preferential self-association in HEMA units rather than interactions with MMA one. Thermal conductivities were found identical to the values obtained for PMMA-*co*-MAA copolymers proving no impact from the side chain addition.

PMMA-*co*-CEA copolymers obtained by cobalt-mediated polymerization led to porous materials despite the multiple attempts to optimized the temperature profile applied. For this reason, bulk thermal conductivities could not be measured. ^{1}H NMR spectra showed the presence of residual MMA and CEA which were found to be 0.4mol% and 1.5mol%, respectively. Copolymers composition were found to be 91:9, 78:22, and 67:33mol% for the ratio MMA:CEA in agreement with the expected values (11, 23, and 33mol% of CEA). The molar masses were found to be lower than PMMA ones and characterized by higher polydispersity when CEA comonomer was added as 15 and 30wt%, while the highest content showed a non-gaussian peak at the upper limit of column suggesting a higher M_n. These findings suggest that the copolymerization method developed is not optimal in case of MMA and CEA monomers. Thermal degradation occurs at lower temperature when the CEA comonomer is copolymerised with MMA. The presence of multiple peaks on the thermogravimetric curves indicated that degradation started at 200°C and involved a much more complex mechanism compared to the PMMA. Moreover, similarly to PMMA-*co*-MAA, the presence of a carboxylic acid units can lead to the formation of anhydride structure. Indeed, the appearance of a small peak in the derivative curve at high temperature in the thermograms suggest the formation of anhydride structures which showed higher stability in temperature. IR spectra showed a broadening of the peak associated to the carbonyl absorption, which can be correlated to the superimposition of two peaks, the carbonyl in the MMA unit and the one from the CEA unit. Similarly to PMMA-*co*-HEMA copolymers, the

Kwei's fit resulted in a negative value of q indicating the preferential self-association between CEA units. PMMA-*co*-CEA for the higher CEA content was successfully neutralized with NaOH as confirmed by IR spectroscopy. The processability of the pristine and neutralized PMMA-*co*-CEA successfully increased compared to the PMMA-*co*-MAA case due to the presence of a more flexible chain. Therefore, thin films were successfully prepared by compression moulding in order to perform thermal conductivity measurements. However, thickness homogeneity resulted still insufficient for the application of the thin film method in TPS.

In conclusion, PMMA-*co*-MAA copolymer were successfully prepared up to 30wt% of MAA and characterized. The addition of H-bonds to vdW interactions in the polymethacrylate chain was confirmed by the change in T_g and in the IR spectrum and the value of Kwei's parameters. However, despite the positive trend observed in thermal conductivity by varying the comonomers ratio, the obtained increment was found limited comparable to the ones reported in literature for similar inter-chain interactions. Furthermore, the introduction of more flexibility in the chain, *i.e.* the replacement of MAA with HEMA in the copolymer, did not show an impact on final κ values. In both cases, the density of H-bonds may have been insufficient to significantly enhanced the bulk thermal transport. Regarding the introduction of ionic bonds in PMMA-*co*-MAA and PMMA-*co*-CEA, in both cases the processability of the neutralized copolymers precluded the preparation of sample suitable for testing and the consequent evaluation of their impact on κ.

In the next chapter, the preparation of fully organic nanocomposite (PMMA-*co*-MAA/CNF) will be presented where the presence of MAA units may lead to an advantageous dispersion given the possibility to form strong matrix-filler interaction, *i.e.* H-bonds. Then, the impact of nanofibers addition on macromolecular mobility and thermal conductivity will be investigated.

Chapter 4

Methacrylate-based CNF nanocomposites

Polymethylmethacrylate (PMMA) has been widely studied for the design of nanocellulose-based composites thanks to its optical transparency, its processability, its surface functionalization, and the necessity to overcome its main limitation related to its inadequate mechanical strength [112,140,148,149]. From the examples reported in Section 1.2.3., it is clear that, in polymer-based nanocomposites, the achievement of a proper dispersion and the strength of interfacial interactions are key parameters to guarantee a positive effect on the final properties [115,149]. Therefore, an improvement of mechanical properties, such as reinforcement effect, *i.e.* increase in Young's modulus, tensile strength, and impact strength [115,153,154,157,158], in hydrophobic matrices, such as PMMA, is reported. These findings are usually obtained also thanks to a chemical functionalization of the nanofiller surface or to the modification of the matrix or the nanocomposite morphology to guarantee proper surface interactions or the formation of chemical bonds and consequently an adequate stress transfer at the interface. To this purpose, cellulose surface is usually chemically modified to lower its surface polarity. Nevertheless, in a similar manner, the introduction of polar groups in non-polar matrices could be beneficial to promote interfacial interactions. According to the described background, an innovative solvent casting method to disperse CNF in methacrylic matrix is presented in this chapter without surface modification of CNF. PMMA-*co*-MAA (30wt% of MAA) was exploited given its dual-nature, polar and lowly polar, where a proper matrix-filler interaction is ensured by the presence of a carboxylic acid groups able to form H-bonds. CNF nanofibers are dispersed in the copolymer matrix thanks to a simple solvent casting method in a mixture of solvents (tetrahydrofuran/water and tetrahydrofuran/methanol) ensuring simultaneously a good solubility of all the components, eventually leading to proper dispersion of CNF, as proved by multiple microscopy analysis.

Furthermore, the effect of the introduction of H-bonds in the polymethacrylate chains has been previously discussed in Chapter 3 and already reported in literature for different PMMA-based copolymers. In fact, when PMMA is copolymerized with different types of comonomers, *i.e.* methacrylic acid (MAA), methacrylamide, 2-ureido-4[1*H*]-pyrimidinone methyl methacrylate (UPyMA), a large positive deviation from the theoretical calculation of T_g is generally observed and can be correlated with the presence of intermolecular H-bonds [56,58–60]. The main

modification obtained following the introduction of H-bond forming groups is the effect on the macromolecular mobility which leads to an increase of T_g [56,57].

Moreover, the presence of H-bonding interactions may give an additional contribution to final properties of composite materials thanks to the establishment of strong matrix/filler interactions. This effect has been already reported for various physical properties and different types of polymers. Dai *et al.* reported H-bonded graphene/PMMA where the presence of H-bonds at the interface allows a more efficient stress transfer, leading to an improvement of the mechanical reinforcement [208]. Ren *et al.* obtained enhanced mechanical properties, such as an increase in Young's modulus and tensile strength, in poly(vinyl alcohol) filled with carbon nanotubes when functionalized with a H-forming moieties (phenolic hydroxyl groups) thanks the strong interfacial interactions established via H-bond formation [209]. Neikirk *et al.* recorded an increase in strain at break and Young's modulus correlated to the presence of H-bonds between the silica particles and the poly(ε-caprolactone) matrix [210].

Based on these findings, once the good CNF dispersion in PMMA-*co*-MAA copolymer has been achieved, an investigation on main physical properties of the designed nanocomposite has been performed. In particular, a multi-technique approach has been employed in order to fully characterize their macromolecular mobility and their relaxations. Starting from PMMA, used as a simple amorphous model, the focus has been put on the influence on secondary relaxations of the introduction H-bond forming moieties (-COOH) in the chain and subsequently the addition of an organic polar filler (CNF) in the system in order to define the combination of their effects. Finally, the influence of the presence of filler on physical properties such as thermal conductivity has been evaluated.

4.1 Dispersion of CNF in a copolymer matrix

THF is a well-known good solvent for acrylics, including the PMMA-*co*-MAA copolymers. However, CNF shows stable suspension in highly polar solvent, *e.g.* water. Therefore pure THF is not suitable to achieve good suspension [211]. For this reason, solvent mixtures were investigated in order to solubilise or suspend simultaneously the two different components, *i.e.* polar nanofibers and less polar matrix. THF and water are fully miscible below 27°C as reported by Míguez *et al.* [212]. PMMA-*co*-MAA was found to be soluble in THF/water mixture up to 23vol% of water at room temperature, while precipitation rapidly occurs for higher water content. Similarly, THF and MeOH are fully miscible at room T and PMMA-*co*-MAA was found to be soluble in the mixture up to a maximum content of MeOH of 90vol%.

Based on the strong affinity of CNF with water, processing of nanocomposite films from THF/water solvent mixture was first explored. After the addition of CNF water suspension to the THF/water copolymer solution and overnight evaporation, opaque nanocomposite films were obtained independently on the CNF contents (5, 15 and 25wt%). Morphology of the film casted from 77/23vol% THF/water polymer solution with 5wt% CNF content is reported in Figure 82.

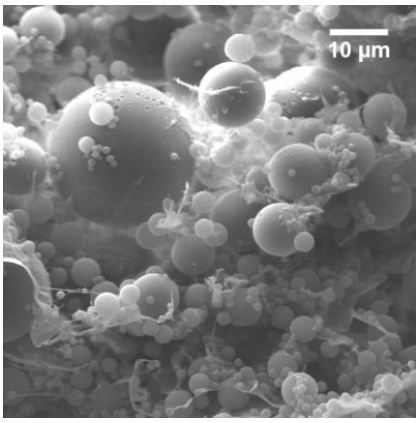


Figure 82. SEM images (secondary electrons) of PMMA-*co*-MAA + 5wt% of CNF evaporated from THF/water at 77/23vol%.

The fracture surface demonstrates the existence of phase separation leading to spherical domains (with a diameter size up to 25 µm). For a better understating of the phenomenon, the morphology of the neat copolymer matrix was investigated as a function of water fraction in the solvent mixture for three cases: namely 1/at the solubility limit of the matrix, *i.e.* in the 77/23vol% mixture, 2/at the minimum boiling azeotropic point at atmospheric pressure, 95/5vol% mixture [213], and 3/in pure THF (100vol%). From the SEM micrographs, showed in Figure 83, the copolymer film casted from the higher water content (23vol%) appears stratified in two different regions (Figure 83a) showing a 25µm-thick upper layer characterized by a microscopic porosity and a lower layer in the form of homogenous dense phase for the remaining thickness of the sample. SEM micrograph for lower water content (5vol% reported in Figure 83b) shows a fracture surface displaying plastic deformation of a homogenous phase. However, from a deeper investigation, it is possible to identify the appearance of similar spherical domains with a diameter ranging from nanometers up to 3µm for both ratios explored. The main difference lies in their amount and distribution. For the higher water content, the phase separated domains are present in large quantities and concentrated in the upper porous layer (Figure 83a), while for the lowest (95/5vol%) content, the analysed surface shows a homogenous dense phase with few randomly located phase separation (details of the inclusions are offered in Figure 83c). On the other hand, the copolymer film obtained by solvent casting from pure THF based solution (Figure 83d) shows a homogenous single phase in the whole sample section.

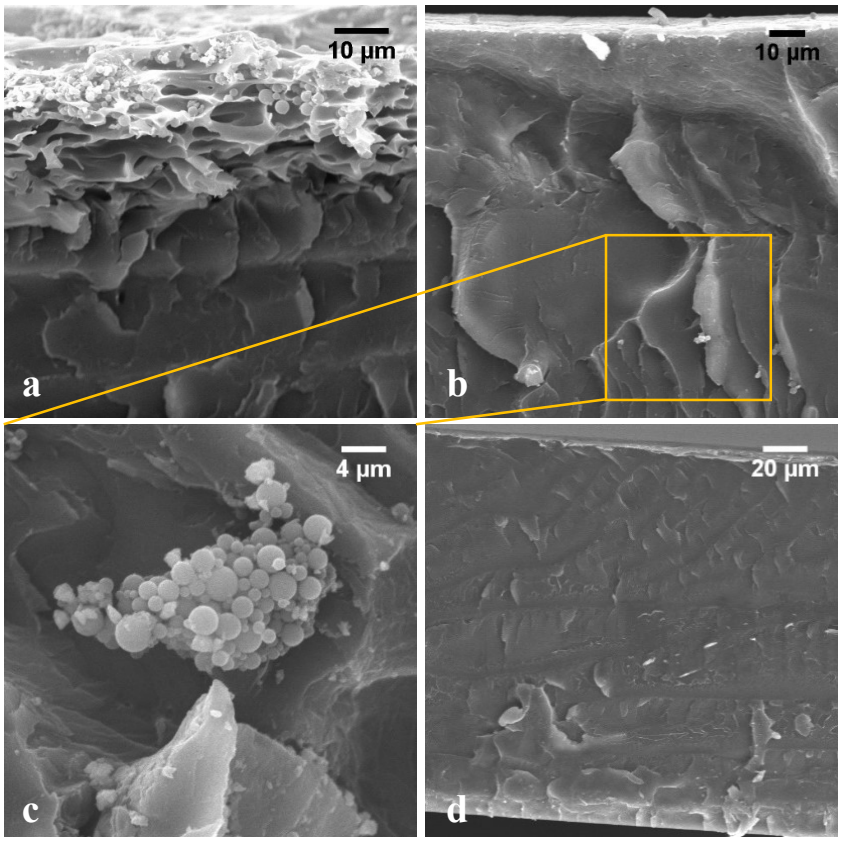


Figure 83. SEM images of neat PMMA-*co*-MAA evaporated from THF/water at 77/23vol% (a), 95/5vol% (azeotropic composition) (b) with details of spherical inclusions (c) and from pure THF (d).

We hypothesize that the phase separation phenomenon occurs due to the large difference in volatility of the two solvents (boiling point is 66°C for THF and 100°C for water). As THF has a higher vapor pressure compared to water, the solvent mixture evaporation leads to a progressive increase in water concentration in the solution. With the increase of water concentration, the less hydrophilic polymer chains, *i.e.* richer in MMA units, are not stable in solution and will aggregate as particles, whereas the more hydrophilic chains remain soluble and precipitate at a later stage leading to the appearance of a second phase richer in MAA units. Based on the mechanisms abovementioned, it is clear that the observed phase separation is driven by a different evaporation rate of the solvents. For this reason, a different solvent mixture was investigated to reduce the difference in volatility of the two solvents. A THF/methanol mixture was selected according to the limited boiling point difference (66.0 vs 64.7°C, respectively, with an azeotropic composition at 66/34vol%) and based on the possibility to exchange water in CNF suspension with MeOH as previously described by Roman *et al.* [163].

Prior to nanocomposite preparation, the morphology of the neat matrix was investigated for films casted at different THF/MeOH ratios (90, 70, and 50vol% of THF). The morphology shown on the fracture surface show for 90vol% of THF (Figure 84a) a homogeneous morphology characterized by the presence of a plastic deformation and microscopic pores left from the evaporation of the solvents. Similar results (reported in Figure 84b) were obtained for a content of THF at

70vol% with smaller pores and less in numbers. On the contrary, the film casted from 50/50vol% THF/MeOH solution (Figure 84c) also presents randomly distributed pores but two different fracture surfaces: a brittle fracture for the lower 1µm-thick layer and a 55µm-thick upper layer having a different fracture behaviour, *i.e.* displaying local plastic deformation.

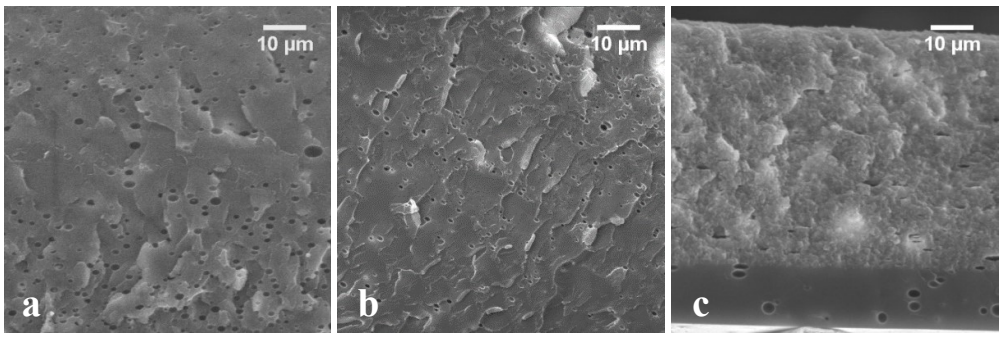


Figure 84. SEM images of neat PMMA-*co*-MAA casted from THF/MeOH 90/10 (a), 70/30 (b) and 50/50vol% (c) solutions.

The solvent exchange process for CNF suspension led to a visually homogeneous gel with an average CNF content in the solvent of about 1.8wt%. The solvent volatilization was completed at 70°C (Figure 85) and no evidence of water is found by IR spectroscopy collected on the gas phase produced during TGA, evidencing a successful substitution of water with methanol.

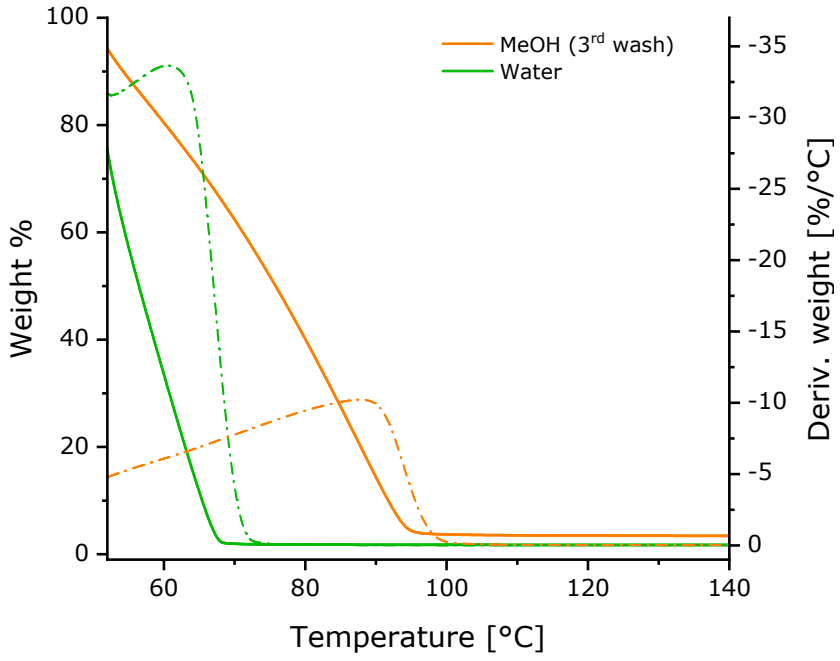


Figure 85. TGA thermograms for CNF water suspension and MeOH-wetted CNF after third washing (5°C/min).

A CNF suspension in methanol was exploited for the preparation of nanocomposites in THF/MeOH solution and different content of nanofibers (5, 10, and 15wt%). The solvent ratio was chosen as the middle of the interval in which the neat matrix showed a single homogenous phase (0-30vol% of MeOH), *i.e.* at 85/15vol% THF/MeOH ratio. SEM observations for PMMA-*co*-MAA nanocomposites based on 5, 10, and 15wt% casted from THF/MeOH 85/15vol% are reported in Figure 86. All the samples clearly appear homogenous according to the fracture surface of the film characterized by the presence of plastic deformation at submicronic scale. For all the fracture surfaces, the peculiar surface roughness can be correlated to the presence of the nanofibers in the matrix. However, it is possible to identify some smoother areas suggesting that the distribution of CNF is not fully homogenous in particular when 10 (Figure 86b) and 15wt% (Figure 86c) of CNF are introduced.

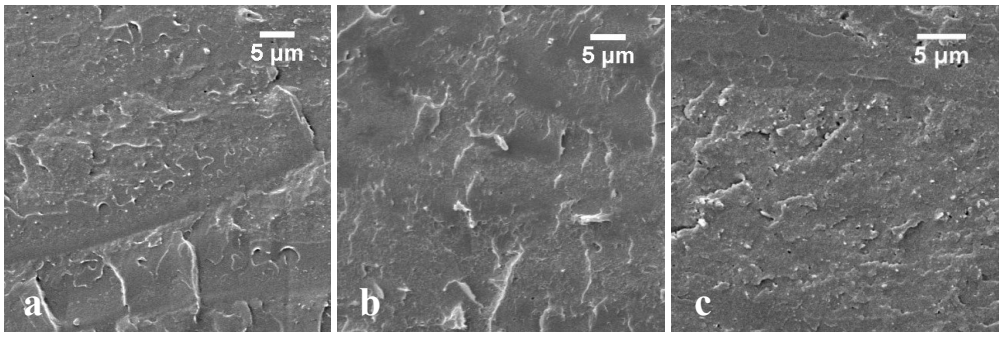


Figure 86. SEM images of fractured PMMA-*co*-MAA + 5 (a), 10 (b) and 15wt% (c) of CNF film casted from THF/MeOH 85/15vol% solutions.

The intermediate composition (10wt% of CNF) was selected for a deeper investigation combining multiple characterization techniques. The dispersion was examined for two different methanol concentrations in the solvent mixture, namely at 15 and 34vol%, with the maximum value corresponding to the azeotropic mixture at atmospheric pressure [214]. PMMA-*co*-MAA + 10wt% CNF casted from THF/MeOH 85/15vol% solution was observed at higher resolution by FE-SEM (Figure 87a), confirming a peculiar surface rugosity that can be associated to the organisation of dispersed CNF within the matrix. To further investigate the dispersion and interconnections of CNF, TEM analysis was carried out on the same sample and results are reported in Figure 87b. The fracture surface shows different areas with different concentrations of CNF. However, in the areas at higher concentration, CNF appear to be well dispersed and surrounded by the polymer indicating good matrix-filler interactions.

Similar analyses have been conducted on films with the same composition casted from THF/MeOH 66/34vol% solution. From the FE-SEM image shown in Figure 87c, the fracture surface is characterized by submicronic plastic deformation correlated to the presence of the CNF within the matrix. From TEM observations, it is possible to recognise some areas free of nanofibers showing a CNF distribution which is not homogeneous (Figure 87d). However, similarly to the film casted from

85/15vol% THF/MeOH solution, CNF appears dispersed and well embedded within the matrix.

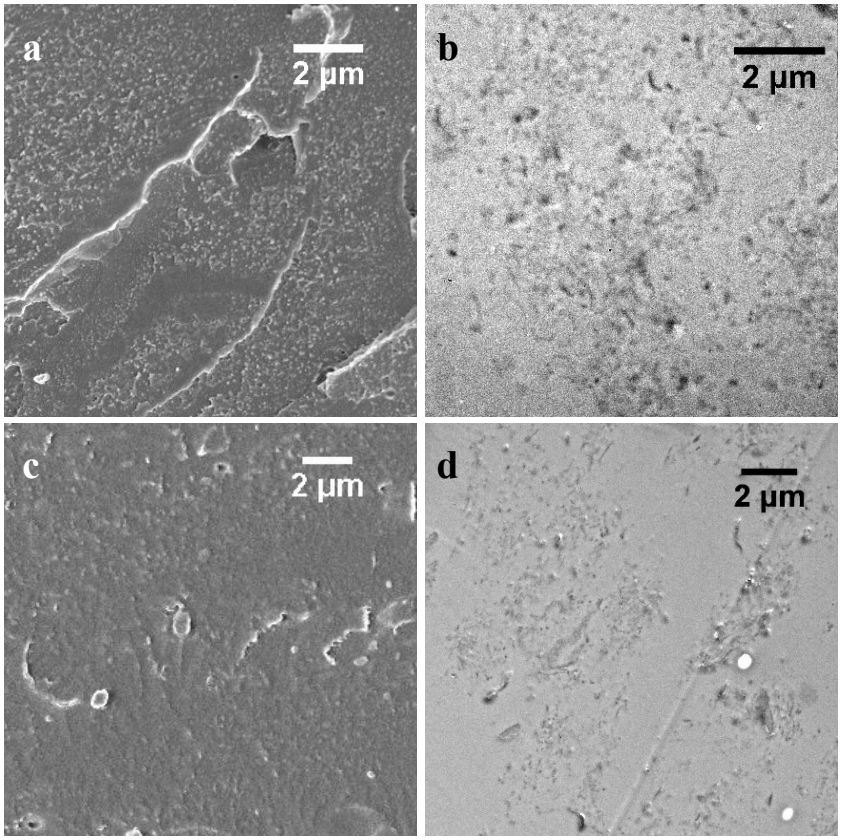


Figure 87. FE-SEM (a) and TEM (b) micrographs of PMMA-*co*-MAA + CNF 10wt% nanocomposites processed from THF/MeOH 85/15vol% solution. FE-SEM (c) and TEM (d) micrographs of PMMA-*co*-MAA + CNF 10wt% processed from THF/MeOH 66/34vol% solutions.

Solvent casting processes lead, in all the cases, to transparent films with the presence of few white spots related to a presence of micrometric pores. An example is showed Figure 88 for the nanocomposite (10wt% CNF) film casted from THF/MeOH 66/34vol% mixture.

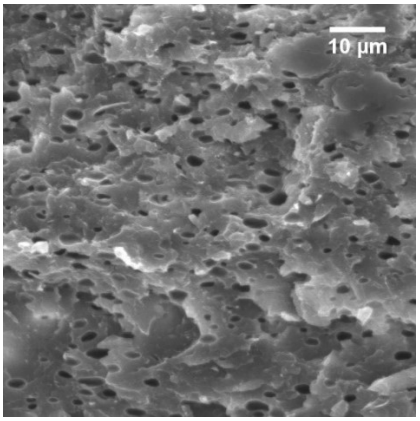


Figure 88. SEM micrograph showing residual porosity after solvent casting (THF/MeOH 66/34vol%) in PMMA-*co*-MAA + 10wt% CNF film before compression moulding.

After compression moulding, all the films are successfully densified and are fully transparent, as reported as an example for PMMA-*co*-MAA casted from THF/MeOH 70/30vol% and the nanocomposite (10wt% CNF) casted from 85/15vol% in Figure 89.



Figure 89. Transparent film of PMMA-*co*-MAA after compression moulding at 230°C (a) and with the addition of 10wt% of CNF after compression moulding at 230°C (b).

Additionally, UV-vis transmittance spectra were acquired to quantify films transparency (Figure 90). The spectra show a high value of transmittance in the whole range of wavelengths for all the compositions with a minimum at 98.7%. Quantitative evaluations of the samples transparency results 99.6% for the matrix and respectively 99.6, 99.5, and 99.1% when 5, 10, and 15wt% of CNF are added. Their values confirm the optical transparency in the visible wavelength interval for all the samples.

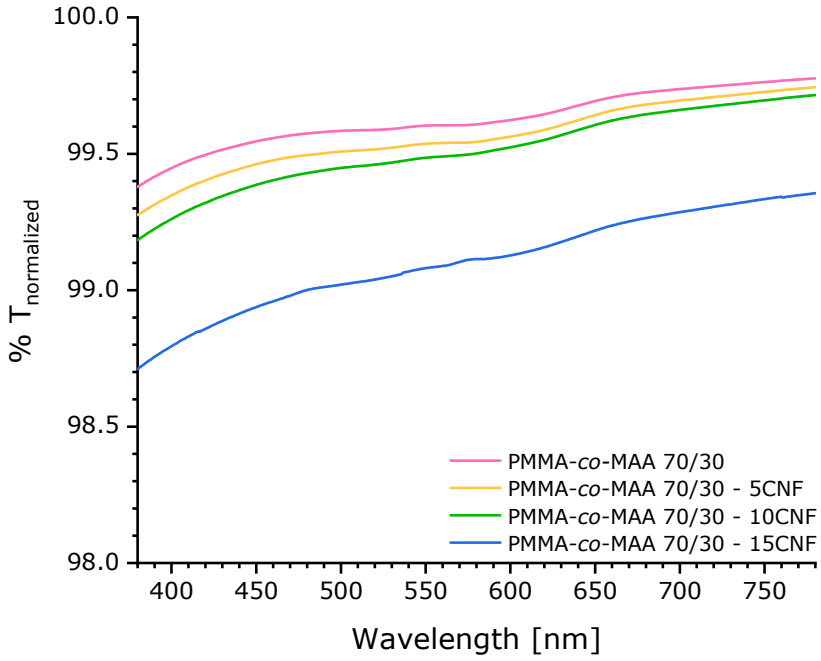


Figure 90. UV spectra of compression moulded films of PMMA-*co*-MAA (5, 10 and 15wt% of CNF).

After compression moulding, PMMA-*co*-MAA films were solubilised in DMSO and analysed by ^{1}H NMR (Figure 91). New peaks are identified which do not correspond to the ones of the copolymer. In fact, the two peaks (1.7-1.8 and 3.6

ppm) correspond to THF, suggesting that residual THF solvent is still present, while there is no evidence of MeOH (3.2 and 4.1 ppm) [215].

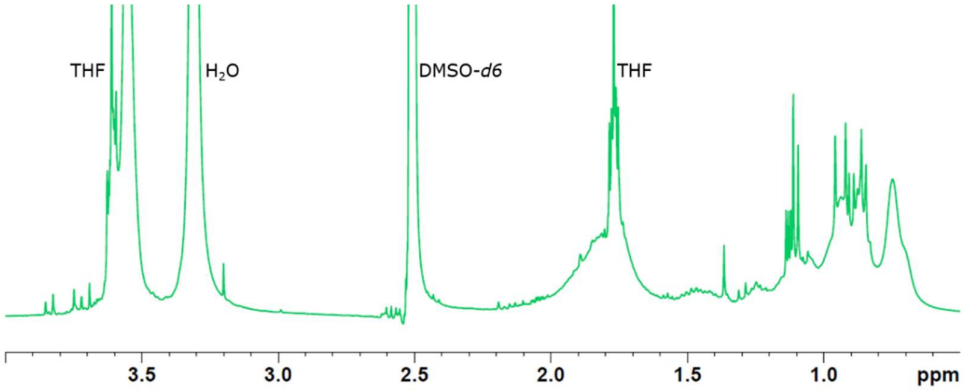


Figure 91. ^{1}H NMR spectrum at 25°C for PMMA-*co*-MAA after compression moulding of the film (400 MHz, DMSO-*d6*).

Possible copolymer evolution upon compression moulding at 230°C was evaluated by IR spectroscopy (Figure 92) performed on compression moulded films. Compared to the pristine copolymer (Figure 92), compression moulding caused a decrease of the intensity for the peak at 1697 cm^{-1} corresponding to the absorption of MAA groups as well as the appearance of new peaks at 1802, 1760, and 1015 cm^{-1} which correspond to anhydride groups [60]. The nanocomposite spectra (an example in Figure 92 for the 10wt% of CNF) show new absorption peaks ascribed to the presence of CNF in the matrix: two peaks at 1032 and 1055 cm^{-1} correspond to C-O-C vibration, a peak at 1105 cm^{-1} corresponding to C-O stretching, and a broad peak from 3060 to 3620 cm^{-1} related to the O-H stretching [216]. Furthermore, the peaks corresponding to the formation of the anhydride state can be recognised in the spectrum at 1802 and 1760 cm^{-1}, confirming the occurrence of limited condensation between carboxylic groups, as observed for the pristine polymer.

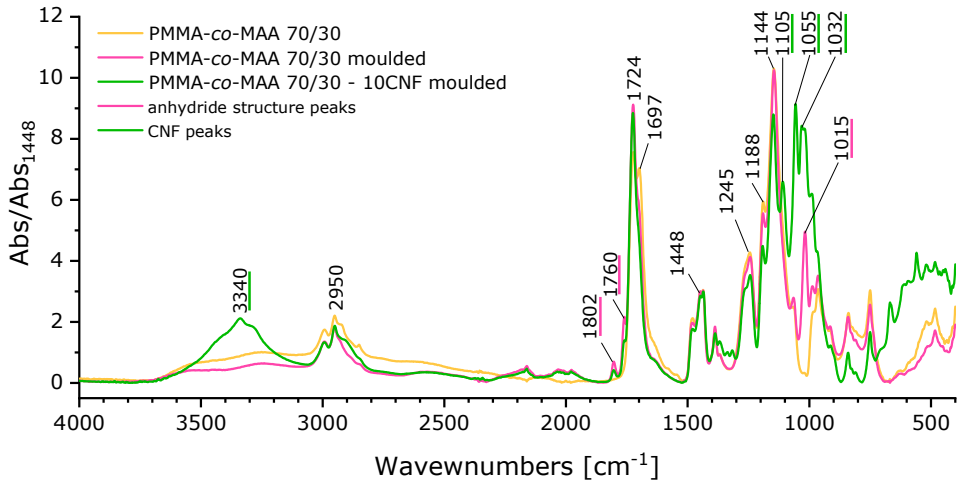


Figure 92. ATR spectra of PMMA-*co*-MAA 30wt% MAA before and after compression moulding at 230°C for 8 min and PMMA-*co*-MAA + 10wt% CNF after compression moulding at 230°C for 8 min.

Furthermore, compression moulded copolymer appears to be insoluble in DMF contrary to the as synthesized one. This phenomenon confirms the occurrence of a structural evolution but prevents the evaluation of its molar mass by SEC.

From these results, it is clear that a degradation mechanism occurs when the copolymer is heated at 230°C to perform compression moulding. Indeed, the changes in the structure can be correlated to the formation of both intra- and inter-chain anhydride groups, as suggested by the change in IR spectra, and non-solubility in DMF. These changes are in agreement with the mechanism of thermal degradation previously described for PMMA-*co*-MAA copolymers. In particular, upon heating, a condensation reaction can take place between two carboxylic units leading to the formation of an anhydride structure.

4.2 Thermal events in PMMA, PMMA-*co*-MAA and nanocomposite films

Prior to macromolecular mobility studies, changes in the materials properties related to the film preparation. In particular for solvent casting and compression moulding, pre- and post- films manufacturing were examined. Evolution of molar masses during compression moulding were evaluated in order to detect the occurrence of thermal degradation by depolymerization. Then, DSC thermograms were analysed to define the effect of residual solvents on the primary relaxation. Lastly, thermogravimetric analyses were performed in order to identify weight losses related to residual solvents at lower temperatures.

M_n of PMMA after compression moulding was analysed in THF and found to be equal to $1.41 \cdot 10^5$ g/mol. This value is slightly lower than that found for the as polymerized PMMA ($2.61 \cdot 10^5$ g/mol) suggesting that thermal degradation starts during moulding. As previously mentioned, PMMA-*co*-MAA and nanocomposites were found to be insoluble after compression, due to anhydride formation.

The T_g of PMMA, copolymer and nanocomposites films (pressed at 200°C for PMMA and 230°C for the other compositions) were measured by DSC analysis (Table 14).

Table 14. T_gs values of PMMA, PMMA-*co*-MAA (30wt% MAA), and nanocomposites measured during a first and a second heating ramp by DSC.

Composition	T_g on 1st heating (°C)	T_g on 2nd heating (°C)
PMMA	95	106
PMMA-*co*-MAA 70/30wt%	100	134
PMMA-*co*-MAA 70/30 - 5CNF	101	129
PMMA-*co*-MAA 70/30 - 10CNF	100	130
PMMA-*co*-MAA 70/30 - 15CNF	111	132

DSC analyses performed on films show a single T_g for all the analysed formulations (Figure 93). For PMMA-*co*-MAA film, the T_g is found at 134°C

during the second heating (Figure 93). This value is significantly lower compared to 150°C found for the pristine copolymer. It is worth mentioning that the T_g for compression moulded PMMA-*co*-MAA is closer to the prediction from Fox's equation (119°C). This fact suggests that the reduction by condensation of adjacent carboxylic groups may reduce the number of intermolecular H-bonds. Furthermore, the application of Kwei's equation in the case of film pressed at 230°C leads to a value of *q* equal to 45 for the copolymer at a ratio 70/30wt% MMA/MAA, which is considerably lower than the value found for the pristine PMMA-*co*-MAA (equal to 131) confirming a partial loss of intermolecular interactions. However, the positive value of *q* parameter indicates that intermolecular H-bonds are still present.

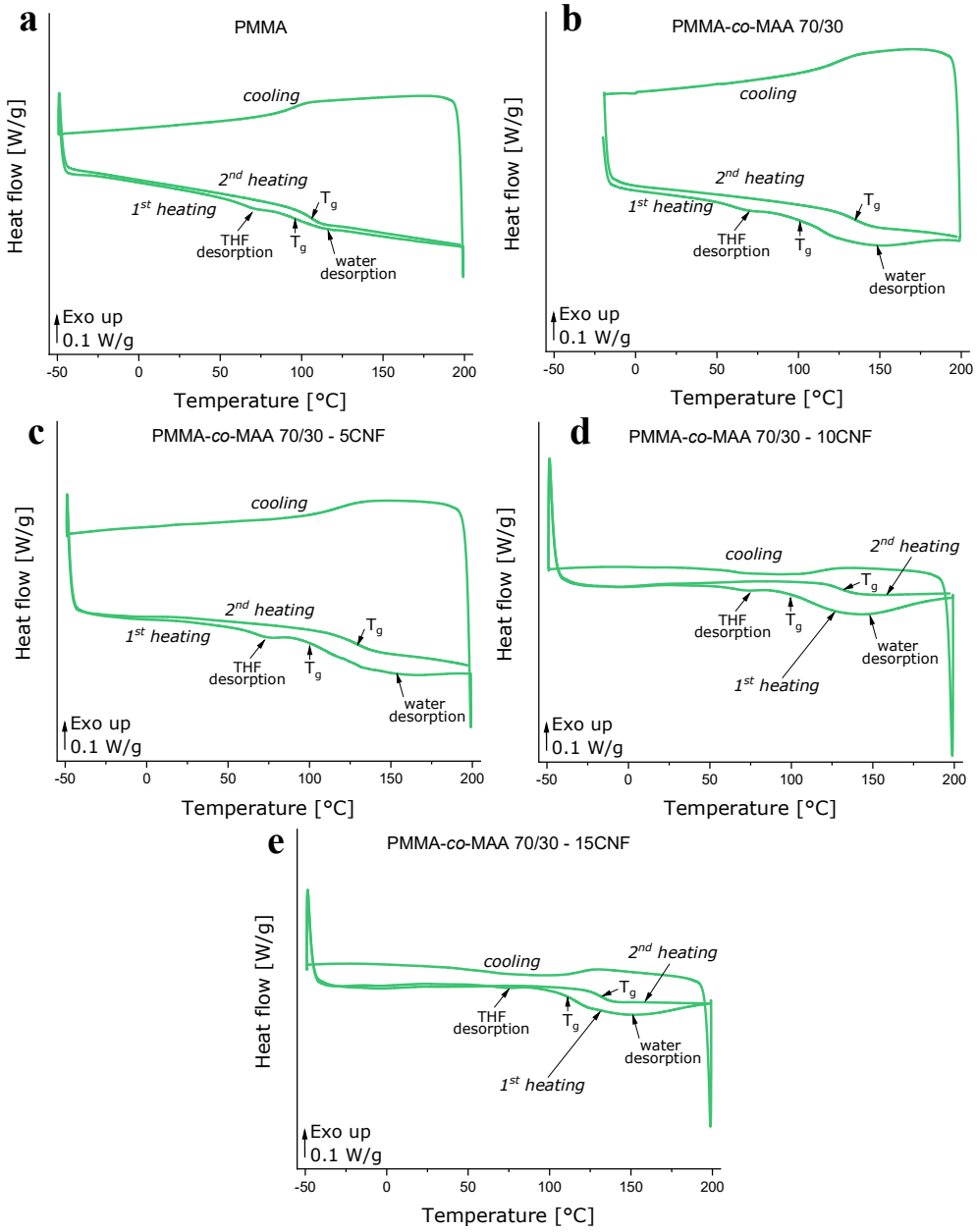


Figure 93. DSC thermograms for PMMA (a), PMMA-*co*-MAA (30wt% MAA) (b), and nanocomposites films with 5 (c), 10 (d) and 15 (e) wt% of CNF (heating rate 10°C/min).

T_gs obtained during the first and second heating ramps significantly differ for all the compositions: differences between 9 and 34°C were observed. This difference can be ascribed to the plasticizing effects of a residual solvent fraction. Indeed, THF traces (and no evidence of residual MeOH) were identified by NMR in the compression molded PMMA-*co*-MAA films (Figure 91), indicating that the drying step performed during the preparation was not able to ensure a complete elimination of the solvent. Another contribution could be the presence of absorbed water from the atmosphere, particularly when CNF were added due to their hydrophilic nature. From the DSC curves (Figure 95), on first heating two endothermic peaks corresponding to evaporation phenomena can be seen in all the cases. The first peak is centered between 70 and 75°C while the second one extends from 100 to 180°C. Also, the peak appearing at lower temperature is appreciably less intense than the other one, except for the PMMA where they show a similar intensity. Based on the higher volatile nature of THF compared to water (considering the large difference in their boiling point, 66°C for THF and 100°C for water) the peaks can be attributed respectively to THF and water desorption. These findings are also in agreement with the fact that PMMA seems to absorb a minor amount of water compared to the other compositions and explain the lowest ΔT_g between the values obtained during the first and the second heating ramps. This fact is in agreement with the lower water absorption expected from the apolar unit. The apolar MMA units are characterized by a lower hydrophilic nature compared to the polar MAA group. Furthermore, from the comparison of the T_gs detected during the second heating ramps, it can be seen that the introduction of MAA units in the PMMA chain significantly increases the T_g (around 30°C) thanks to the contribution of intermolecular H-bonds which can be formed between the carboxylic groups of the MAA units. When it comes to nanocomposites, the addition of CNF does not significantly change the T_g values.

The results from thermogravimetric analysis are reported in Figure 94 for PMMA, PMMA-*co*-MAA, and nanocomposites.

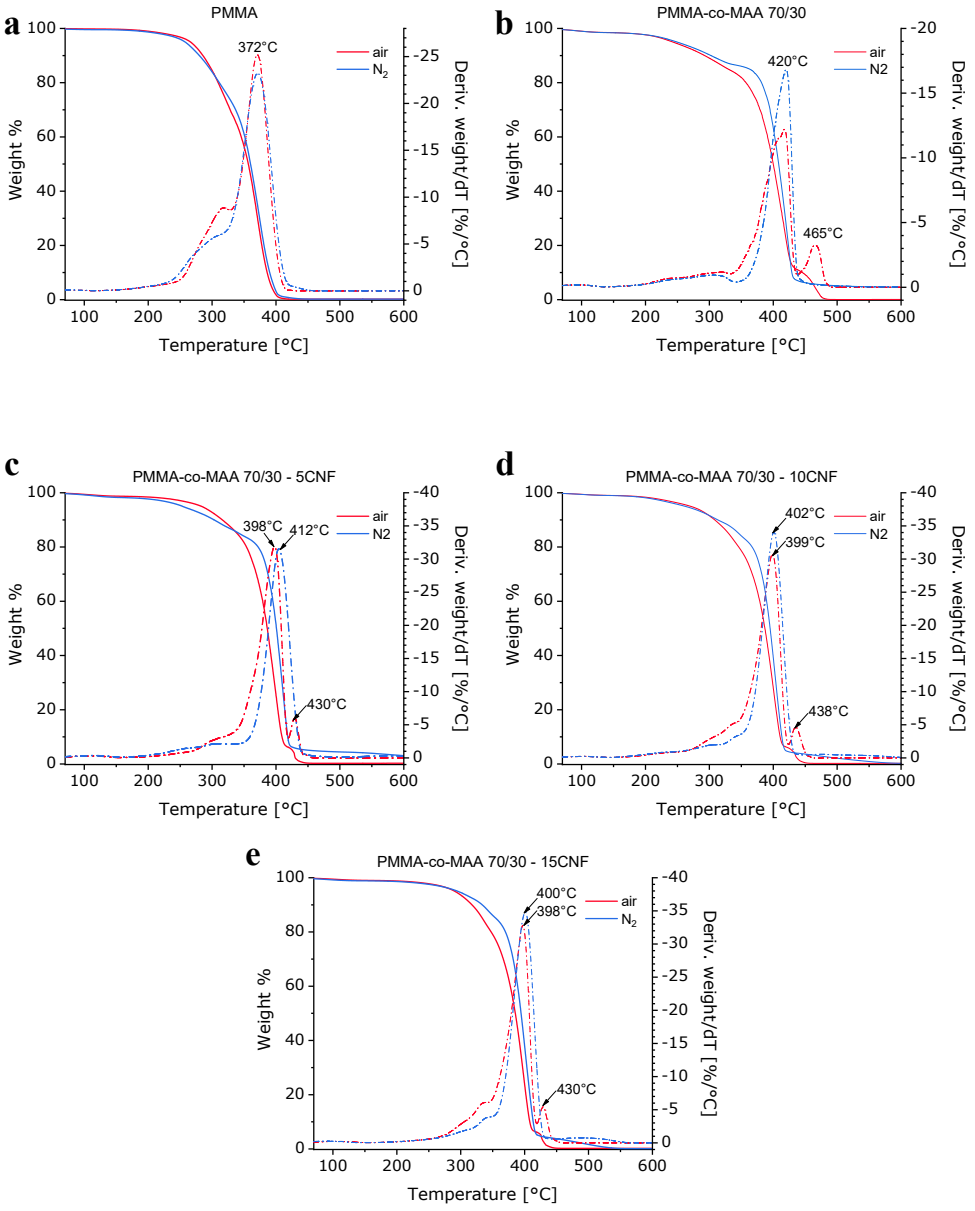


Figure 94. Thermogravimetric analyses on films of PMMA (a), PMMA-*co*-MAA (30wt% MAA) (b) and nanocomposite with 5 (c), 10 (d) and 15 (e) wt% of CNF in air and N_2 (heating rate 10°C/min).

The thermograms (Figure 94) show a weight loss at 100°C close to 0.3% for PMMA and 1% for the other compositions. This confirms the hypothesis that PMMA absorbs a minor amount of water compared to the other compositions as suggested by DSC results. From the derivative curves, it is also possible to identify the peaks corresponding to the main weight loss, associated with the thermal degradation of the polymer backbone. The corresponding temperatures (T_{degrad}) are listed in Table 15. The neat PMMA-*co*-MAA and the nanocomposites show, at higher temperatures, a third weight loss in air at 465°C for the matrix and in the vicinity of 450°C for the nanocomposites. Final residues above 550°C in air are below 0.3% for all the compositions and below 0.5% in nitrogen for all the films except the neat PMMA-*co*-MAA (which leaves a residual weight around 4%).

Table 15. TGA data for PMMA, PMMA-*co*-MAA and nanocomposites copolymers under $N_{2(g)}$ and air.

Composition	T_{degrad} air (°C)	T_{degrad} N_2 (°C)
PMMA	372	372
PMMA-*co*-MAA 70/30wt%	420	420
PMMA-*co*-MAA 70/30 - 5CNF	398	412
PMMA-*co*-MAA 70/30 - 10CNF	399	402
PMMA-*co*-MAA 70/30 - 15CNF	398	400

Thermal degradation of PMMA and PMMA-*co*-MAA has been already described in Chapter 3.1. These TGA are in agreement with the proposed degradation mechanisms. In the neat matrix and in the nanocomposites, the peak reported above 400°C in air can be also associated to the oxidation of the stable fraction derived by the anhydride structure. Based on TGA results, the temperature range for dielectric spectroscopy analyses was fixed with a maximum temperature below the T_{degrad} assuming that potential weight losses were limited to a percentage below 1% and associated to a loss of residual solvent.

4.3 Influence of CNF on molecular mobility

Relaxations of PMMA have been widely reported in the literature and four relaxation types have been observed. Starting from low temperatures, the first relaxation which has been reported is the δ-relaxation. It corresponds to the rotation of the methyl present in the ester group (Figure 95) and is usually not detected from dynamic mechanical analysis but only by NMR close to -190°C [217,218]. The second observed relaxation is the γ-relaxation. It is worth mentioning that, in polymethacrylates, its attribution has been subject of discussion in the literature [219–222]. However, the most likely hypothesis ascribes the relaxation to the non-cooperative motion of the α-methyl group covalently bonded to the main chain (Figure 95) [223–225]. Furthermore, some authors mentioned that the γ-relaxation depends on the complex interactions between the water molecules and the polar side groups, *i.e.* ester groups of PMMA [220,226]. As reported by Teixera *et al.*, its activation energy (E_a) is not affected by the side chain length having the ester group [219].

Next, the β-relaxation appears, which in polymethacrylates is ascribed to the non-cooperative rotational motion along the C-C bond linking the ester group to the chain backbone (Figure 95) [219,225–228]. Moreover, as reported by Ceccorulli *et al.*, the presence of absorbed water has no impact on the β-relaxation of PMMA, neither on the intensity nor on the location of the peak [220]. It is worth mentioning that Teixeira *et al.* reported different E_as for β-relaxation in different temperature ranges. Indeed, they observed for PMMA two different regimes with a relaxation characterized by a higher E_a at higher temperatures [219]. At the same time, Ceccoculli *et al.* reported a β'-relaxation for wet PMMA which appears as a shoulder on the β-relaxation peak at high temperatures which is characterized by a

lower frequency dependence. Given the high E_a of β'-relaxation, the authors ascribed the relaxation to a larger molecular unit, compared to the ones responsible for the secondary relaxations and correlated to the association of water molecules interacting with the ester group of PMMA [220]. A similar relaxation was also reported by Dudognon *et al.* and Li *et al.* [229,230].

Lastly, the α-relaxation corresponds to the cooperative motions of polymer chain segments, *i.e.* dynamic glass transition [222]. At higher temperatures, the merging of α- and β-relaxations can be observed due an increasing cooperativity involving a growing number of main chain bonds [218,219,231].

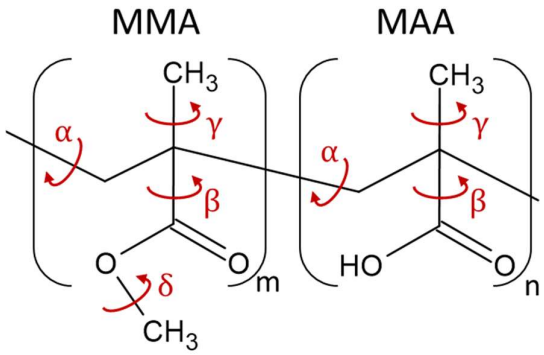


Figure 95. Relaxations in MMA units described in literature and possible relaxations in MAA units.

Three-dimensional plots of the imaginary part (ε'') of the relative dielectric permittivity obtained by dielectric spectroscopy are reported in Figure 96 as a function of temperature and frequency for PMMA, PMMA-*co*-MAA, and nanocomposites with 5, 10, and 15wt% of CNF. At low temperatures, two dielectric relaxations appear corresponding to the secondary relaxation processes (γ and β). Moreover, the 3D plots of the nanocomposites (Figure 96c and d) show at low frequencies a third relaxation (β') which merge with β-relaxation at high temperatures. For all the observed compositions, at higher temperatures, the α-relaxation is hidden by the conductivity (σ). For this reason, the data acquired by dielectric spectroscopy would not be sufficient to completely characterize the relaxations present in the analysed system. Therefore, in order to overcome this issue related to the primary relaxation and perform a complete study on macromolecular mobility, complementary DMA were carried out with the aim of deriving the relaxation times hardly detectable in the dielectric spectrum thanks to the Havriliak-Negami equation which relates them to the complex modulus.

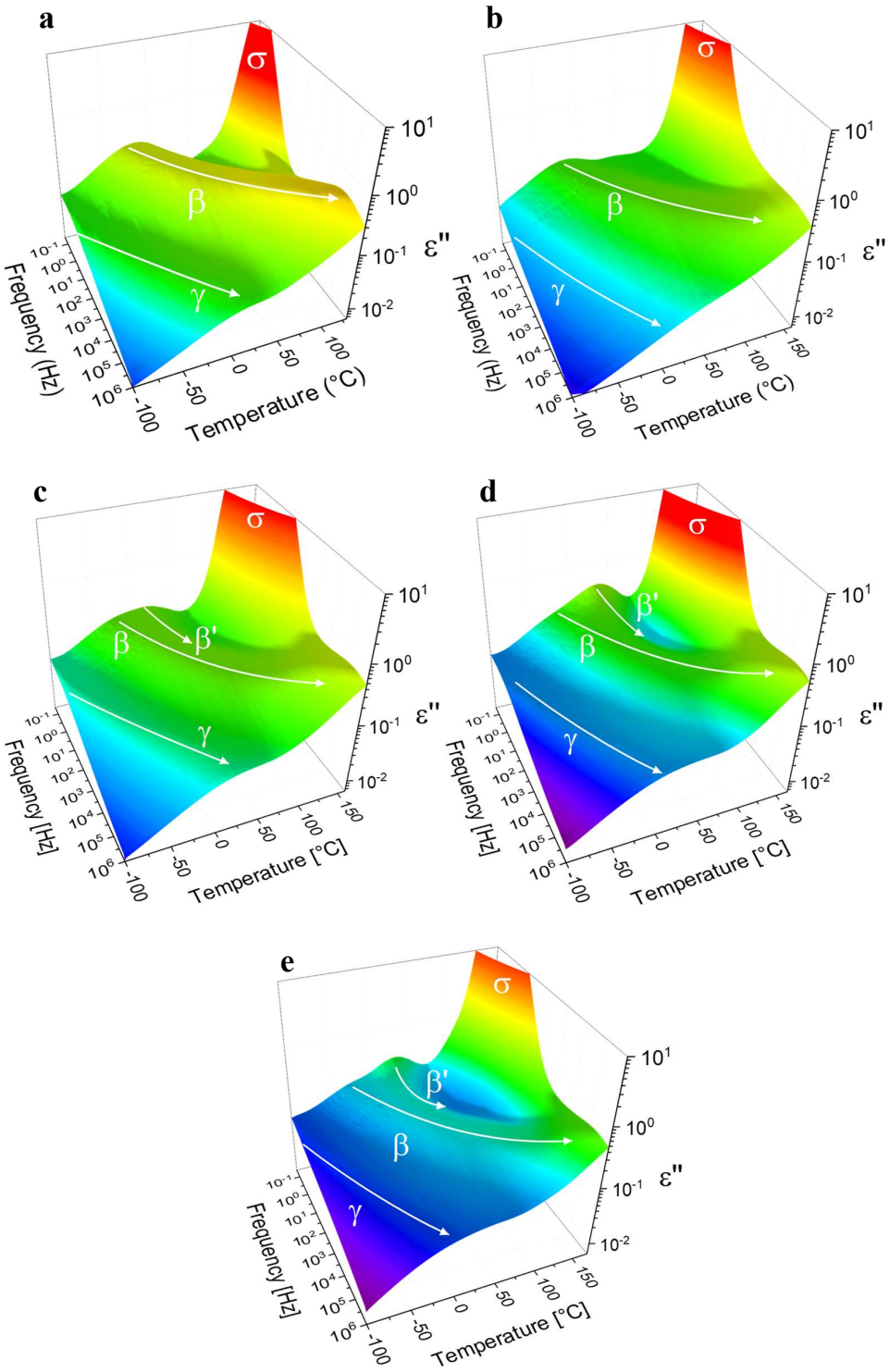


Figure 96. Dielectric relaxations maps for PMMA (a), neat PMMA-*co*-MAA (30wt% MAA) (b) and filled with 5 (c), 10 (d), and 15wt% (e) of CNF. Relaxation processes are indicated by white lines.

4.3.1 Secondary relaxations analysed by dielectric spectroscopy

The secondary relaxations were studied by dielectric spectroscopy. The relaxation times for the γ- and β-relaxations were obtained by Cole-Cole fitting the complex relative permittivity data with the equation [232]:

$$\varepsilon^*(\omega) = \varepsilon_\infty + \frac{\varepsilon_0 - \varepsilon_\infty}{1 + (i\omega\tau)^\alpha} \quad (30)$$

where ε_∞ and ε_0 are respectively the high- and the low-frequency permittivity, τ is the mean relaxation time, ω is the angular frequency which is equal to $2\pi f$ and α is the parameter depicting the width of the distribution. As reported in the literature for many polymers [219,220], the secondary relaxations in methacrylate polymers follow an Arrhenius-like temperature dependence. Therefore, the activation energy (E_a) was calculated by fitting the relaxation times with the Arrhenius equation [233]:

$$\tau = \tau_0 \, exp(\frac{E_a}{RT}) \quad (31)$$

where τ_0 is a pre-exponential factor, R the universal gas constant and T the temperature in Kelvin.

The β'-relaxation observed on the 3D plots for PMMA-*co*-MAA nanocomposites cannot be fitted using the Cole-Cole equation on ε^* spectra. Isofrequency curves at 0.04 Hz were examined and reported in Figure 97. The peak related to the β-relaxation appears in the same temperature range (from -70°C to 30°C) for the PMMA and the neat PMMA-*co*-MAA. From a comparison between the curves, it can be seen that, when CNF is present, an intense peak associated to the β'-relaxation is observed, while in PMMA and PMMA-*co*-MAA, a peak characterised by lower intensity appears close to 50°C.

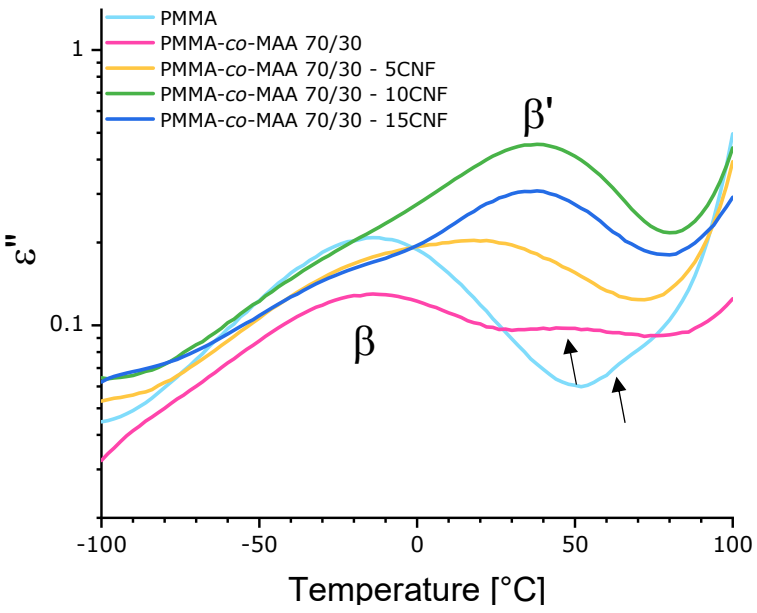


Figure 97. Dielectric thermogram, isofrequency at 0.04Hz of polymers and related nanocomposites. The presence of β'-relaxation is indicated (black arrows) for PMMA and PMMA-*co*-MAA.

The relaxation times for the β'-relaxation of PMMA-*co*-MAA with 10 and 15wt% of CNF were obtained by the analysis of the isofrequency curves where a clear peak was present: the temperature at peak maximum, T_{max}, was determined as the maximum of the frequency of the isofrequency curve. The associated relaxation times were calculated as $1/2\pi\tau$. For the 5wt% of CNF, the peaks corresponding to β' relaxation resulted close to the β-relaxation preventing its analysis.

The τ are plotted as a function of 1000/T in the Arrhenius diagram in Figure 98 and the associated E_a reported in Table 16.

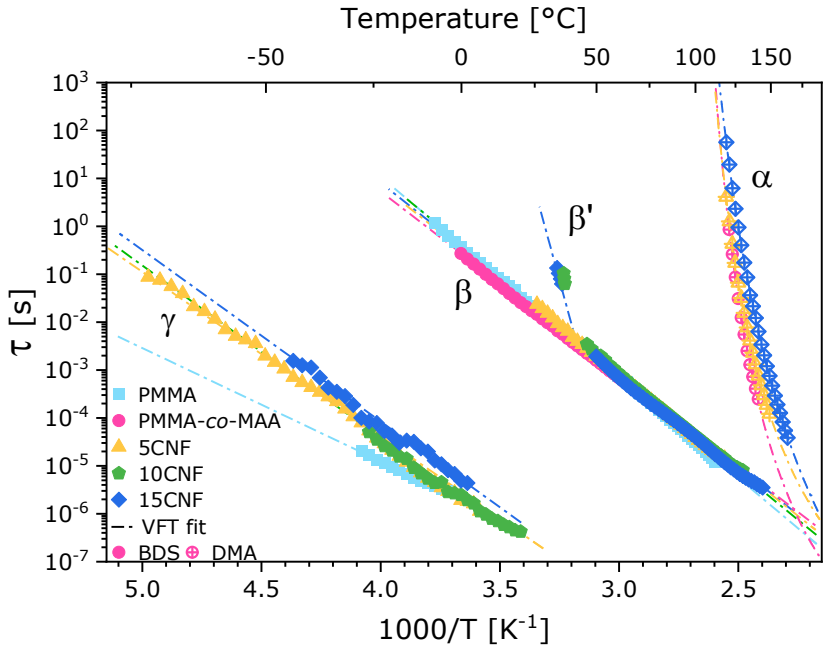


Figure 98. Arrhenius diagram of the secondary relaxations processes of polymers and related nanocomposites.

Table 16. Activation energies for γ, β, and β' relaxation of polymers and related nanocomposites.

Composition	Ea γ (kJ/mol)	Ea β (kJ/mol)	Ea β' (kJ/mol)
PMMA	44	79	-
PMMA-*co*-MAA	-	74	-
PMMA-*co*-MAA 70/30 - 5CNF	69	78	-
PMMA-*co*-MAA 70/30 - 10CNF	62	77	-
PMMA-*co*-MAA 70/30 - 15CNF	67	79	303

PMMA shows an E_a for the γ-relaxation equal to 44 kJ/mol which is consistent with the ~40 kJ/mol reported in literature [219,220]. For nanocomposites, E_a of γ-relaxation is increased by 45% regardless the CNF content. Unfortunately, we could not determine the E_a of the γ-relaxation of the PMMA-*co*-MAA due to its low intensity making it too convoluted with the β-relaxation. However, the relaxation is present in the pure copolymer and, as abovementioned, the γ-relaxation corresponds to a non-cooperative process and results as a water-related relaxation. The hypothesis is that the numerous hydroxyl groups present in the cellulose structure can interact with the absorbed water hindering the motion behind the loss process leading to a higher E_a. Unfortunately, due to the lack of data regarding the γ-relaxation of PMMA-*co*-MAA, it is not possible to clarify the behavior of the neat matrix. It is assumed that, as the absorption of water is less pronounced compared to the nanocomposites, due to the lower polarity and hydrophilicity of the copolymer compared to the one associated with CNF, the E_a may fall between the values found for PMMA and PMMA-*co*-MAA filled with CNF. E_a will be influenced by the amount of absorbed water molecules and the strength of the H-bonding formed with them.

For PMMA, the activation energy E_a of β-relaxation is found to be in good agreement with the values previously reported in literature, *i.e.* 81 kJ/mol by Teixeira *et al.* and by Comer *et al.* [219,222,225,226,234]. Regarding the neat PMMA-*co*-MAA, despite the addition of a polar group in the chain, the E_a of β-relaxation remains constant (Table 16). It seems that the two units, $-COOCH_3$ and -COOH, share similar relaxation times over the temperature range resulting in a single peak, with a possible overlap of their contributions. A similar phenomenon was reported by Kolařík *et al.* for methacrylate copolymers based on hydroxyethyl methacrylate and MAA where the β-relaxation appears as a single peak given the similarity in the origin of the relaxation [235]. Also, Kihira *et al.* reported that the introduction of MAA units in the poly(ethyl methacrylate-*co*-MAA) copolymer did not affect the β-relaxation [236]. Also, once CNF are added to PMMA-*co*-MAA, a similar phenomenon of overlapping occurs in the most part of the frequency range, but at low frequencies, the two contributions become distinct peaks (Figure 97). Where a unique peak is present, E_a of the β-relaxation is similar to the one reported for PMMA and the matrix, and can be attributed to the relaxation of MMA and MAA units. Moreover, the obtained α parameter from Cole-Cole fit (equation (30)) is found to be higher for PMMA compared to the PMMA-*co*-MAA copolymer and

its nanocomposites and the observed difference is constant in the whole temperature range in which the β-relaxation is displayed. For example, at 80°C it is equal to 0.42 for PMMA and between 0.34 and 0.35 for PMMA-*co*-MAA and its nanocomposites. This finding suggests a broadening of the peak associated to the β-relaxation when MAA comonomer is present confirming the initial hypothesis. Indeed, this effect can be ascribed to the presence of two different groups which show a single peak as result of their average contribution. Focusing on the peak observed in PMMA and PMMA-*co*-MAA close to 50°C (Figure 97), it appears here as a shoulder on the β-relaxation peak for higher temperature similarly to what has been already reported in literature as β'-relaxation, therefore it can be ascribed to the same relaxation mechanism [220,229,230]. Regarding the nanocomposites, the activation energy of the β'-relaxation is not calculated for the nanocomposite with 10wt% of CNF due to an insufficient numbers of relaxation times; while for the copolymer with the higher amount of CNF (15wt%), is 303 kJ/mol, *i.e.* almost 4 times higher than that of the β-relaxation. It should be considered that in the same temperature interval, a β relaxation associated to cellulose has been already reported in literature [237,238]. However, the relaxation ascribed to cellulose is characterized by an E_a comparable to that of the β-relaxation of PMMA-*co*-MAA copolymer matrix close to 74 kJ/mol. The β'-relaxation showed in the nanocomposites can be ascribed to the rotation of the ester group characterised by a high E_a due to hindering effect caused by the presence of H-bonds. These can occur between the -COOH groups of MAA and the hydroxyl superficial groups of CNF or the molecules of absorbed water, as schematised in Figure 99. Also, this relaxation appears to be dependent on CNF concentration. Indeed, higher density of H-bond forming groups characterise the system when a higher content of nanofibers is added. Moreover, the CNF hydrophilic character may lead to a great amount of absorbed water. Additional considerations about the main groups involved in the H-bonds will be discussed further on in the analysis on the α-relaxation.

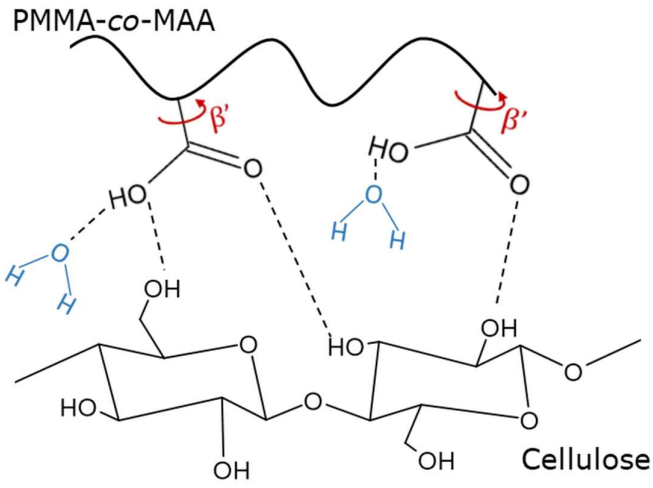


Figure 99. Schematic interactions between MAA carboxylic group in PMMA-*co*-MAA and CNF surface hydroxyl groups and water molecules.

For all the studied compositions, a comprehensive description of the secondary relaxation processes has been achieved thanks to BDS measurements. However, given the conductivity (σ) at high temperatures (between $1.3 \cdot 10^{-12}$ and $1.1 \cdot 10^{-10}$ S/cm), which hides the α-relaxation, an alternative method was used in order to determine the corresponding relaxation times.

4.3.2 Alpha relaxation analysis from dynamic mechanical spectroscopy

The mechanical manifestation of the glass transition (α-relaxation) was analysed by DMA thanks to the application of the TTS principle with a focus on the influence of the CNF addition in the copolymer matrix. The shift factors were obtained from the elaboration of the master curves and the Williams-Landel-Ferry equation was applied to derive the empirical constants C_1 and C_2 (Table 17):

$$\log(a_T) = \log\left(\frac{\tau(T)}{\tau(T_{ref})}\right) = \frac{-C_1(T - T_{ref})}{C_2 + (T - T_{ref})} \quad (32)$$

where a_T is the shift factor and T_{ref} is the reference temperature [239].

Table 17. Fitting parameters from WLF.

	C_1	C_2 (K)	T_{ref} (°C)
PMMA-*co*-MAA	7.7	48.7	133
PMMA-*co*-MAA + 5wt% CNF	8.7	51.9	129
PMMA-*co*-MAA + 15wt% CNF	11.1	69.3	133

The Havriliak-Negami was fitted on the complex mechanical modulus (E^*) master curves in order to determine the relaxation time at T_{ref} [233]:

$$E^*(\omega) = \frac{E_0 - E_\infty}{[1 + (i\omega\tau_{HN})^\alpha]^\beta} + E_\infty \quad (33)$$

where E_0 and E_∞ are respectively the rubbery and glassy plateau, τ_{HN} is the mean relaxation time, α and β are parameters related to the width and the asymmetry of the relaxation and ω is the angular frequency.

In the first place, the recorded isothermal segments were horizontally shifted to obtain the master curves for the storage (E') and the loss (E'') moduli, which are reported in Figure 100. The addition of CNF in the copolymer leads to an increase in the storage modulus, E', on the rubbery plateau. PMMA-*co*-MAA with 10wt% of CNF displays incomplete E' and E'' master curves and not suitable to perform accurate fits. Therefore, this nanocomposite will not be further analysed. The addition of CNF results in a mechanical reinforcement of the matrix which is clearly observed at low frequencies in correspondence to the rubbery plateau and it appears

influenced by the content of CNF, indeed a stronger effect is detected for the highest nanofibers wt%.

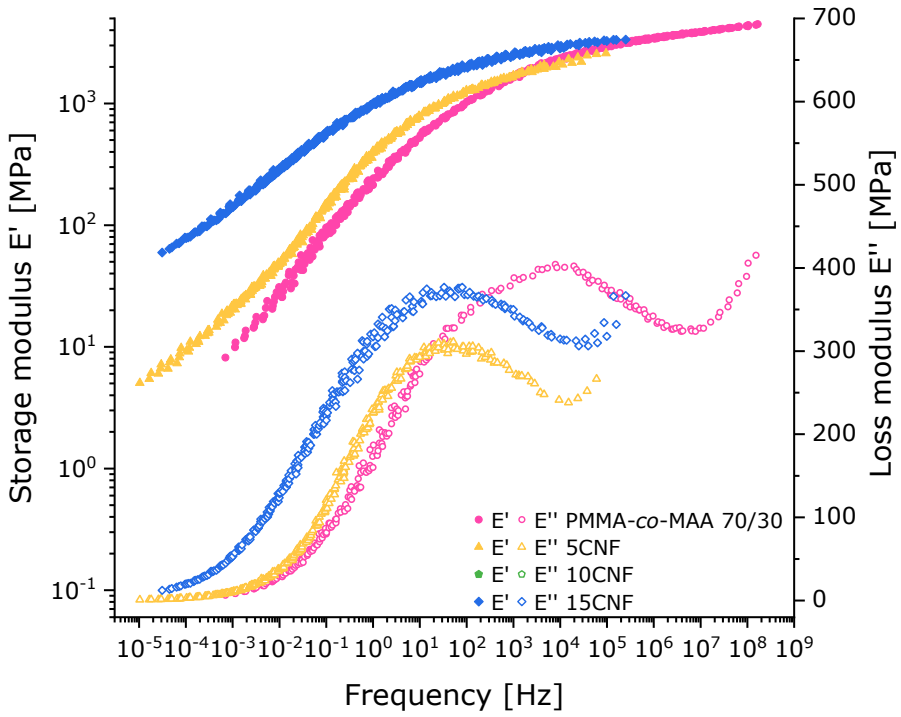


Figure 100. Storage (solid dots) and loss modulus (open dots) master curves of copolymer and related nanocomposites.

The influence of MAA units in MAA copolymer has already been described in literature as a shift of the E'' peak to higher temperature. This effect is usually ascribed to the interactions of the MAA units which contribute to an increase of the copolymer T_g, as also reported by DSC analyses in Chapter 3 with a ΔT_g about 50°C when 30wt% of MAA is added. The carboxylic groups present in the MAA unit tends to form a dimer via H-bonding which hinders the primary relaxation of the chain [236,240,241].

The relaxation time at T_{ref} was determined by fitting the complex modulus (E^*) of the master curves with the Havriliak-Negami equation (33) [233]. The shift factors were then used to obtain the relaxation times at the other temperatures, thanks to equation (32) [233,239]:

$$a_T = \tau(T)/\tau(T_{ref}) \leftrightarrow \tau(T) = a_T \cdot \tau(T_{ref}). \quad (34)$$

The obtained relaxation times are reported in the Arrhenius plots in Figure 98 and Figure 101.

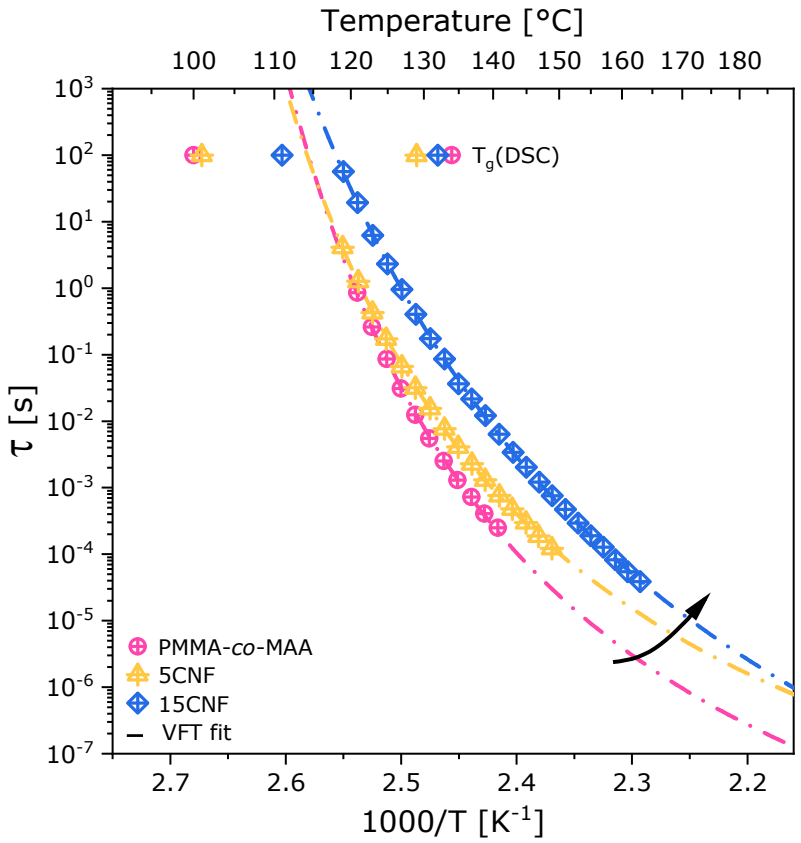


Figure 101. Arrhenius plot of alpha relaxations of copolymer and related nanocomposites.

The addition of CNF causes a shift of relaxation times to higher temperature compared to the neat copolymer matrix. The VFT fitting curves are placed in between the values of T_gs from DSC derived on the first and the second heating ramps and fixed at a relaxation time of 100s. The VFT fit falling in between the two DSC T_gs can be related to the different testing conditions of the two methods, *i.e.* DSC and DMA. In fact, the T_g determined by the first heating ramp by DSC is lowered due to the plasticizing effect linked to the presence of residual THF and absorbed water. Anyway, they can fully evaporate while the higher temperatures are reached and more mobility is given to the macromolecules allowing the shift of a higher value on the second heating free from the abovementioned effect. Instead, the DMA curves, performed after compression moulding to remove porosity and homogenise the film thickness, are recorded during a single heating ramp. The heating rate during DMA measurements is considerably slower than the DSC one and the air flux present in the chamber allows a gradual evaporation while the temperature is increasing bringing the sample in a condition that can be considered intermediate between the two DSC steps. Unfortunately, a second DMA heating ramp could not be performed on the same sample given the high degree of

deformation observed in the film at the end of the first heating ramp. Despite the limited differences observed in T_gs during the second heating of DSC (see Table 14) for PMMA-*co*-MAA and 10wt% and 15wt% CNF nanocomposites, it is interesting to notice that the analysis of the relaxation times of the α-relaxation underlines the influence of CNF on molecular dynamic. Indeed, at the same temperature, the nanocomposites display a higher relaxation time compared to the one of the matrix which increases with the nanofiber content. Therefore, the presence of CNF and the possibility to generate interactions with the matrix via H-bonding leads to a slower molecular dynamics of the amorphous phase (PMMA-*co*-MAA).

Besides, α-relaxation generally obeys the Vogel-Fulcher-Tammann (VFT) law [242]:

$$\tau = \tau_0 \, exp\left(\frac{1}{\alpha_f (T - T_0)}\right) \tag{35}$$

where τ_0 is the relaxation time for infinite frequency, T_0 is the so-called Vogel temperature or ideal glass transition temperature (approximately 50°C below the T_g) and α_f is the thermal expansion coefficient of the free volume. Prior to VFT fitting, the Stickel's function was applied to confirm the VFT behavior [243,244]. In a Stickel's diagram ($d\ln(f_{VFT})/dT^{-1}$ vs 1000/T), the VFT law describes a linear dependence where the slope and the y-intercept are function of the VFT parameters, while an Arrhenius law leads to a constant value. Consequently, the points not lying on the linear regression were discarded (Figure 102).

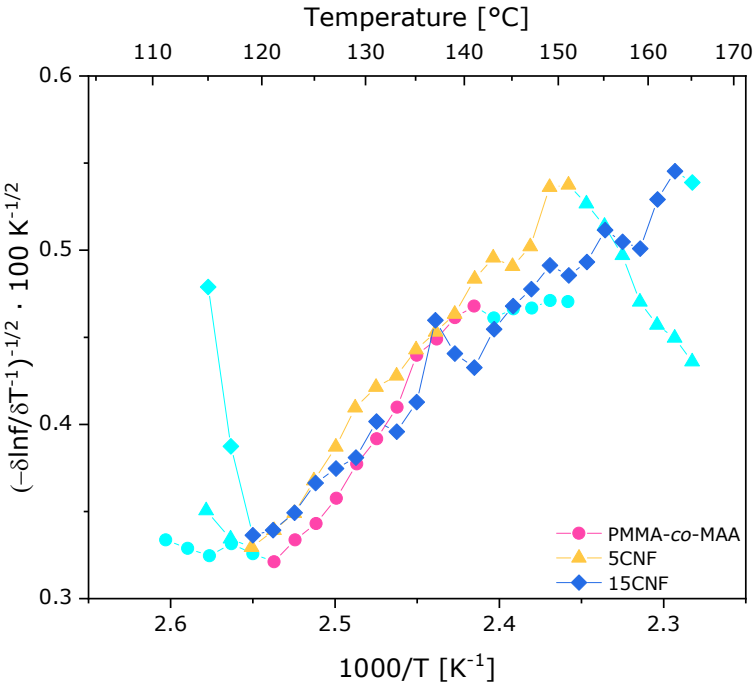


Figure 102. Stickel diagram for copolymer and related nanocomposites.

Then, VFT equation was used to fit the remaining points and the obtained parameters are listed in Table 18. Moreover, the fragility was calculated at T equal to T_g given the relation [245]:

$$m = \frac{dlog\ (\tau)}{d(T_g/T)} \quad (36).$$

Results are reported in Table 18.

Table 18. VFT parameters from fit determined for copolymer and related nanocomposites.

Composition	τ_0 (s)	α_f (°C^{-1})	T_0 (°C)	m
PMMA-*co*-MAA	1.5E-11	1.02E-3	81	150
PMMA-*co*-MAA + 5wt% CNF	1.3E-10	1.04E-3	79	130
PMMA-*co*-MAA + 15wt% CNF	1.4E-12	5.96E-4	65	103

The α_f remained unchanged with the addition of 5wt% of CNF, while significantly decreased with the highest content of nanofibers. These finding suggest that, when a higher content of CNF is added, the interactions present in the system are able to decrease the expansion of the free volume and hinder the mobility of the amorphous phase. These results are confirmed by the lower value of m found following the addition of CNF. Indeed, the lower fragility of the nanocomposites suggests that the presence of CNF make the nanocomposites stronger material according to the Angell definition [245]. Moreover, this effect can be correlated with the presence of interactions able to hinder the segmental mobility and explained by the presence of H-bonds between the nanofibers and the copolymer which increase the rigidity of the system. Similar observations were reported by Ghorbel *et al.* for PVA/CNF nanocomposites [246]. Moreover, the lower value of m indicates a higher Arrhenius character of the α-relaxation which has been previously reported for CNF and correlated to a higher density of H-bonds [247].

Regarding the β'-relaxation observed in the nanocomposites, it has been discussed in section 4.3.1 that the hindering of the ester groups relaxation is ascribed to the introduction of H-bonds formed either with -OH groups of CNF or absorbed water molecules. However, in view of the results obtained by the analysis of the effect of CNF on the primary relaxation, it seems more likely that they are caused by the interaction with the former, *i.e.* CNF hydroxyl groups. Indeed, if significant amount of absorbed water were present in the system, they would affect as well in a detectable way the α-relaxation causing a plasticization effect.

The observation of the T_gs values by DSC analysis during the second heating ramp, *i.e.* without plasticizing effect induced by residual solvents, suggested that the α-relaxation was surprisingly unaffected by the addiction of CNF. However, a deeper investigation of the relaxation times associated to their relaxation was able to reveal differences between the nanocomposites. Indeed, the addition of CNF in PMMA-*co*-MAA copolymer successfully led to an increase of the relaxation times for the α-relaxation showing a stronger behaviour, *i.e.* lower fragility, with higher

nanoparticles content. These findings were supported as well by the appearance of an intense peak ascribed to the β'-relaxation in the nanocomposites which was found to be determined by the presence of strong interactions between the matrix and the nanofibers, *i.e.* H-bonds.

4.4 Thermal conductivity of thin films

Thermal conductivities measured by Hot Disk applying the thin film method are reported in Table 19 (as an average value of 3 measured points. PMMA and PMMA-*co*-MAA selected as matrix (30wt% MAA) were also tested in order to obtain reference values measured in the same conditions. Between nanocomposite formulations, κ is reported only for the 10wt% of CNF. For the other CNF contents, the thicknesses inhomogeneity prevents the acquisition of a reliable value.

Table 19. Thermal conductivities measured on thin films by Hot Disk method for PMMA, PMMA-*co*-MAA, and nanocomposite with 10wt% of CNF.

Composition	Thickness (μm)	κ ($W \cdot m^{-1} \cdot K^{-1}$)
PMMA	125	0.198
PMMA-*co*-MAA 70/30	150	0.198
PMMA-*co*-MAA 70/30 - 10CNF	195	0.211

From the comparison of PMMA and copolymer matrix values (Figure 103), it is clear that the slight increment observed in bulk with the addition of 30wt% of MAA is not confirmed in film form. In fact, the two polymers show identical κ values (Table 19), with relatively large uncertainties associated to the variant of the Hot Disk method. This finding may be associated to the formation of anhydride structure in PMMA-*co*-MAA copolymer. Indeed, as previously showed from IR analyses, the peaks associated to the anhydride structure are detected in the film after compression moulding. Moreover, the relevant ΔT_g between the experimental value and the Fox's prediction observed in the bulk form, which has been correlated to the presence of intermolecular H-bonds (as confirmed by Kwei *q* parameter), is lowered when passing to the film form confirming the effect of anhydride presence on intermolecular interactions. The elimination of bridging H-bonds between the macromolecules can cause the loss on the positive contribution on the thermal conduction.

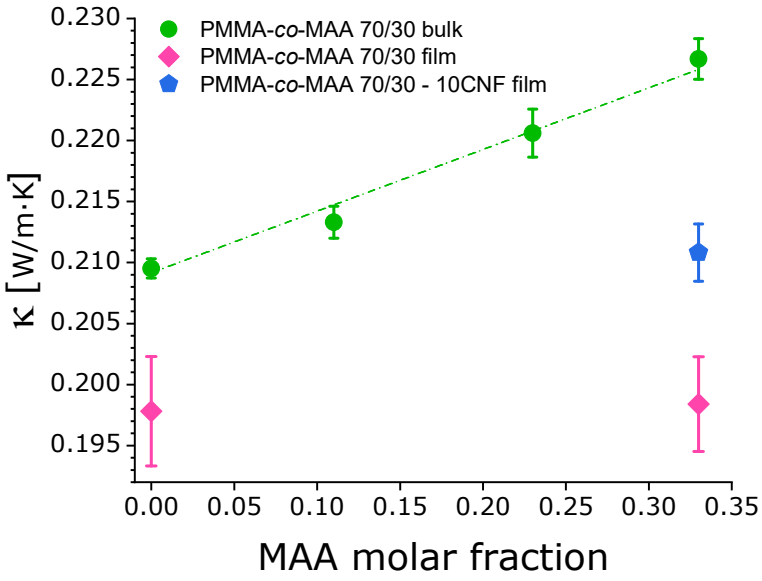


Figure 103. Thermal conductivity of PMMA-*co*-MAA copolymers in bulk and as thin films as function of MAA content and for PMMA-*co*-MAA with 10wt% of CNF.

A minimum expected value of 0.216 $W \cdot m^{-1} \cdot K^{-1}$ was calculated applying the series model (21) for the addition of 10wt% of CNF, using 2.200 $W \cdot m^{-1} \cdot K^{-1}$ for CNF as reported by Adachi *et al.* (measured along the CNF axis) [18] and 0.198 $W \cdot m^{-1} \cdot K^{-1}$ for the matrix. The volume fraction of the filler was calculated starting from the mass fraction and considering 1.60 g/cm^3 as density for CNF and 1.25 g/cm^3 for the matrix [18,248]. Despite the presence of H-bonds interactions proved by the appearance of a β' relaxation in BDS measurements, the addition of 10wt% of CNF in the PMMA-*co*-MAA matrix did not lead to a significant increase of κ which resulted lower than the minimum value expected. Similarly to observation proposed for PMMA-*co*-MAA, also in the nanocomposite films, the formation of anhydride structure has been observed leading to a reduction in the H-bonding density. The nanocomposite thermal conductivity will mainly depend on the intrinsic one of both components but also by the thermal contact resistance at the interface matrix/filler and among the fillers [1,10]. Assuming that a partial loss of H-bonds is induced during the moulding process, the thermal contact resistance matrix/filler will not be reduced thanks to strong interfacial interactions and will play a determining role in preventing the increment of overall thermal conduction.

4.5 Conclusions

The PMMA-*co*-MAA copolymer with the highest content of MAA (*i.e.* 30wt%) was selected to prepare CNF-based nanocomposites. The presence of the second monomer unit (MAA) characterized by a higher polarity was designed in order to ensure better matrix filler interactions via H-bonding and promote the dispersion of polar fillers in such highly hydrophobic matrix.

The dispersion was achieved in solution and the nanocomposite films were prepared by solvent casting. Given the different polarities of the two components, a mixture of solvents was used in order to ensure simultaneously solubilization of the copolymer and dispersion of CNF. The first tested solvents mixture was THF/water since the first is a well-known solvent for acrylics and the second for CNF dispersion. The copolymer showed solubility up to 23vol% of water and the dispersion was evaluated for nanocomposites with different CNF contents (5, 15, and 25wt%). Phase separation with spherical domains up to 25 μm was observed in nanocomposites casted from THF/water (23vol% of water) mixture regardless the CNF content. For a better understanding of the phenomenon, the pristine matrix was casted from different THF/water ratios (5 and 23vol%) and in pure THF. The copolymer casted from the highest water fraction (23vol%) showed a stratification in two different phases. In case of 5vol% water-based solution, the surface fracture appeared homogenous with few randomly located spherical inclusions which are smaller compared with the previous case. The copolymer casted from pure THF showed a homogenous morphology in the whole film section. Given these observations and the hypothesis that this phase separation phenomenon occurs due to the difference in the volatility of the two solvents present in the mixture, water was replaced with MeOH thanks to the possible exchange of the two solvents in CNF suspension and the close boiling point of THF and MeOH.

Prior nanocomposite preparation, the morphology of the pristine matrix casted by different ratios of THF/MeOH (90, 70, and 50vol% of THF) was evaluated. For films processed with 70 and 90vol% of MeOH, the fracture surface showed a homogenous phase characterized by the presence of plastic deformation. The range for the solution used for the preparation of nanocomposite films was selected between the pure THF and the azeotropic composition (34vol% of MeOH).

CNF suspension was successfully exchanged from water to MeOH suspension and the dispersion process from THF/MeOH mixture was tested for different vol% of solvents and different CNF contents (5, 10, and 15wt%). As evidenced by electron microscopy, a good CNF dispersion was obtained for films casted from THF/MeOH solution over the range of 85/15 to 66/34vol% and with CNF content up to 15wt%. Moreover, FESEM microscopy shows that CNF are embedded in the matrix confirming matrix/nanofiber interfacial interactions. In all the studied compositions, the achievement of a good dispersion was confirmed by the high degree of transparency obtained (higher than 99.1% in terms of transparency in the visible range). Therefore, the introduction of a polar comonomer in PMMA chains can ensure a good dispersion of polar fillers such as CNF in a nonpolar polymethacrylate matrix without surface pre-treatment or the use of a compatibilizer as interfacial agent. The preparation of CNF-based nanocomposites was successfully achieved by the development of this new methodology based on a solvent mixture which, despite the simplicity of the method, overcame the obstacle of mixing two components with different nature, *i.e.* polarity.

A multi-technique and multiscale methodology was then used to fully characterize the macromolecular mobility and the relaxations of the designed system. Indeed, the macromolecular mobility of PMMA, PMMA-*co*-MAA, and

PMMA-*co*-MAA polymer matrices containing 5, 10, and 15wt% of CNF was studied thanks to the integration of mechanical and dielectrical techniques. In particular, the employment of the Havriliak-Negami's equation describing the mechanical complex modulus and the mathematical equivalence of the WLF and VFT equations allowed a comprehensive characterization of the α-relaxation and its derivation as $\ln(\tau(1/T))$ typical of dielectric analysis. Regarding the secondary relaxations, all the analysed composition reported the same E_a for the β-relaxation. This indicating that the β-relaxation in MMA and MAA units is characterized by the same relaxation times temperature dependency and that the addition of CNF did not cause a change for the MMA and the free MAA units involved. Indeed, the β-relaxation in the copolymer and the nanocomposites resulted as average contribution from the relaxation in present in the MMA and in the MAA units, as further confirmed by the changes in the α parameter from Cole-Cole fitting. Interestingly, an additional β'-relaxation characterized by an E_a nearly four times higher than the $E_a(\beta)$ has been identified at low frequencies in the nanocomposites. This relaxation was ascribed to the hindered rotation of the ester group due to the formation of H-bonds between the -COOH groups of MAA and the hydroxyl superficial groups of CNF, as confirmed by the analysis of the α-relaxation. Indeed, the γ-relaxation shown a major change in terms of E_a which increased about 45% between the PMMA and the nanocomposite. This important increase can be correlated to the interactions between the superficial -OH of the CNF and the water molecules able to hindered the motion at the base of the relaxation. The α-relaxation was evaluated with a focus on the effect coming from the addition of CNF in PMMA-*co*-MAA. DSC results suggested that the presence of nanofibers did not affect the amorphous phase; however, deeper analyses of the its relaxation times (α-relaxation) were able to reveal the effect of CNF which led to slow down the relaxation process. Moreover, the nanocomposites presented lower thermal expansion coefficient of the free volume and were found to be stronger materials according the Angell definition thanks to the establishment of strong interactions with the matrix, *i.e.* H-bonds.

Lastly, the effect of CNF addition on the thermal conduction, κ, was evaluated and the thermal conductivity was measured for films of PMMA, PMMA-*co*-MAA (30wt% MAA) and with the addition of 10wt% of CNF. Identical κ values were found for PMMA and PMMA-*co*-MAA, apparently suggesting that the elimination of bridging H-bonds between the macromolecules due to the anhydride formation in the copolymer causes the loss on the positive contribution on the thermal conduction. For nanocomposites, despite the presence of interfacial H-bonds interactions proved by the appearance of a β' relaxation in BDS measurements, the addition of 10wt% of CNF in PMMA-*co*-MAA matrix did not show a significant increase of κ. Similarly to observation proposed for PMMA-*co*-MAA, in the nanocomposite films the formation of anhydride structure has been observed leading to a reduction in the H-bonding density. Considering that nanocomposite thermal conductivity will mainly depend on the intrinsic κ of both components but also by the thermal contact resistance at the interface matrix/filler and among the fillers. The H-bonds present in the nanocomposite film are probably not sufficient

to reduce the thermal contact resistance at the interface preventing the increment of overall thermal conduction.

In conclusion, an innovative method to disperse polar CNF into PMMA-*co*-MAA matrix has been reported. Indeed, the use of a solvent mixture approach allowed the achievement of a good dispersion despite the different polarity of the two components of the designed nanocomposites. Also, thanks to the combination of DMA and BDS techniques, it was possible to perform a complete characterization of the molecular mobilities. The main result was obtained showing the influence of the CNF on the α-relaxation which led to an increase of relaxation times. Finally, the thermal conductivity of nanocomposites was found unaffected by the nanofibers addition probably due to a loss of H-bonds density as a result of the anhydride formation in the polymethacrylate chains.

Chapter 5

Conclusions

This PhD thesis focused on the understanding of relationships between intermolecular interactions and physical properties in polymer and nanocomposites by tailoring these ones from their strength and number. In particular, the role of inter-chain interactions on the thermal conductivity has been investigated. In amorphous polymers, the addition of stronger intermolecular interactions to weak vdW forces may lead to the achievement of a continuous thermal network with a resulting increase in the final thermal conductivity of the whole material. For this purpose, starting from PMMA, used as a simple amorphous model, methacrylic copolymers were synthesised where the introduction of H-bond forming moieties, *i.e.* carboxylic acid groups. By varying the ratio between the two comonomers, different concentration of H-bonds was introduced along the chain and the effect of their content on the final properties was evaluated. Furthermore, the possibility to neutralize the -COOH group leading to the introduction of ionic interactions allowed the exploration of the effect of even stronger ionic interactions. The requirements for the measurement of thermal conductivity as bulk property have guided the choice of polymerization synthesis to free radical polymerization in bulk. Three different activation mechanisms have been investigated: benzoyl peroxide, benzoyl peroxide /tertiary amine, and methyl ethyl ketone peroxide/Co^{2+}. The first synthesis performed at high temperature led to porous materials unsuitable for characterizations. The second synthesis was performed at room temperature successfully reducing the monomer evaporation observed in the first case. However, despite the achievement of stiff and dense materials, the presence of defects in the materials prevent subsequent characterizations. The last type of synthesis evaluated ensured a gradual radical formation by using a temperature profile of isothermal steps. The temperature profile and the mould setup were adjusted leading to the identification of optimal synthesis conditions. Then PMMA-*co*-MAA random copolymers were successfully copolymerised with a MAA content from 0 to a maximum of 30wt% with high degree of conversion and high molar masses. The copolymerized materials were then fully characterized and, in particular, the effect of inter-chains H-bonds was addressed. The presence of H-bonds established as intermolecular interactions was proved by IR spectroscopy and by the derivation of Kwei's parameters from experimental T_gs. Lastly, a positive trend in bulk thermal conductivity was found with the increasing MAA content. Later, PMMA-*co*-MAA 30wt% MAA was successfully neutralized with sodium hydroxide leading to the presence of ionic clusters which resulted in the appearance of a second T_g. Unfortunately, the neutralized materials were found to be non-

processable by compression moulding preventing the measurement of thermal conductivity.

In a later stage, the MAA comonomer was replaced with different comonomers and the influence of a higher chain flexibility when intermolecular H-bonds are present was evaluated. The two comonomers chosen were characterized by the presence of hydroxyl (HEMA) and carboxylic acid (CEA) groups at the end of the ethyl side chain. In both cases, the MMA/comonomer ratios were chosen accordingly with MAA mol% of PMMA-*co*-MAA in the three ratios. Additionally, for CEA copolymers, the effect of higher flexibility on neutralized copolymer with higher -COOH content and on their properties was investigated. PMMA-*co*-HEMA copolymers were effectively obtained in the same synthesis conditions as PMMA-*co*-MAA copolymer. However, these copolymers were found to be only partially soluble in common solvents, suggesting partial crosslinking was obtained during polymerisation. The Kwei's fit resulted in a negative value of q indicating the preferential self-association of the HEMA units rather than interactions with MMA one. Thermal conductivities were found identical to the values obtained for PMMA-*co*-MAA copolymers showing that there is no influence of the side chain addition. PMMA-*co*-CEA copolymers obtained by cobalt-mediated polymerization resulted in porous materials despite the multiple attempts to optimized the temperature profile applied. For this reason, bulk thermal conductivities could not be measured. Similarly to PMMA-*co*-HEMA copolymers, the Kwei's fit resulted in a negative value of q indicating the preferential self-association between CEA units, *i.e.* carboxylic groups. PMMA-*co*-CEA copolymer having the higher CEA content was successfully neutralized with NaOH. The addition of the side chain resulted in a better flow of the copolymer for both pristine and neutralized PMMA-*co*-CEA compared to pristine and neutralized PMMA-*co*-MAA. However, thickness homogeneity was still insufficient to allow reliable measurements of thermal conductivity in thin films.

PMMA-*co*-MAA 30wt% of MAA copolymer was considered to prepare CNF-based nanocomposites given its amphiphilic nature which ensured proper matrix-filler interactions by the presence of carboxylic acid units able to form H-bonds. The processing route was based on solvent casting technique where the dispersion was achieved from a mixture of two solvents in order to ensure simultaneously solubilization of the copolymer and dispersion of the CNF despite their different natures, *i.e.* a low polar matrix and strongly polar nanofibers. Dispersion of CNF nanofibers in PMMA-*co*-MAA films casted from THF/water displayed a phase separation upon solvent removal, due to the change in solvent mixture composition caused by the different vapour pressure of the two solvents. To limit this inconvenient, MeOH was exploited instead of water, having a boiling point closer to the THF as till being able to disperse CNF after water exchange process. CNF suspension in MeOH was successfully obtained. The new solvent mixture, *i.e.* THF/MeOH, was used to disperse the cellulose nanofibers in PMMA-*co*-MAA. Considering the two solvents selected, the process takes also an advantage from to their high volatile character which facilitates the solvents removal by evaporation. Nanocomposite films were prepared by solvent casting for different THF/MeOH

ratios and the dispersion of CNF was evaluated by multiple microscopy techniques. As evidenced by electron microscopy, a good CNF dispersion was obtained from proceeding in THF/MeOH solution over the range of 85/15 to 66/34vol% with CNF content up to 15wt%. Moreover, FESEM microscopy shows that CNF are embedded in the matrix confirming good matrix-filler interactions. The developed methodology successfully led to the achievement of a good dispersion despite the differences in their nature, *i.e.* polar nanofiber in a poorly polar matrix, with the advantages of being a simple procedure and without the necessity of compatibilization steps.

The macromolecular mobility in PMMA, PMMA-*co*-MAA and PMMA-*co*-MAA containing 5, 10, and 15wt% of CNF was fully characterized thanks to the combination of mechanical and dielectrical spectroscopy. In particular, this was possible applying the correlation between the mechanical complex modulus and the relaxation time described by the Havriliak-Negami's equation and the mathematical equivalence between the WLF and VFT laws, which made possible the achievement of a comprehensive characterization of the α-relaxation. Regarding the secondary relaxations, the activation energy (E_a) for the β-relaxation was found constant for all the compositions due to a similar relaxation time characterising the relaxation of the ester group either in MMA and in MAA units. Interestingly, the nanocomposites showed at low frequencies an additional β'-relaxation characterized by an E_a nearly four times higher than the $E_a(\beta)$. This relaxation process was attributed to the H-bond interactions hindering the β-relaxation of the PMMA-*co*-MAA chain due to the establishment of H-bonds interactions at the interface matrix/nanofibers. Moreover, a significant change was found for the γ-relaxation in presence of CNF, as the E_a of the relaxation increased about 45% compared to PMMA. This important increase may be correlated to the interactions between the superficial -OH of the CNF and the water molecules able to hinder the motion responsible of the γ-relaxation. At the same time, DMA spectroscopy was used in order to evaluate the effect of the addition of CNF on the primary relaxation, α, of PMMA-*co*-MAA copolymers. The master curves showed that the presence of the nanofibers led to a mechanical reinforcement in the matrix on the rubbery state with the generation of a rubbery plateau dependent on the CNF content. A deeper investigation about the macromolecular mobility has been essential in order to highlight the influence of CNF and the presence of interfacial H-bonding. Indeed, despite the similar T_gs characterising the matrix and the nanocomposites, their relaxation times appeared higher following the addition of CNF. These findings suggested that matrix/nanofibers H-bond interactions result into a slower molecular dynamics.

Lastly, the influence of CNF addition on thermal conduction was evaluated and thermal conductivity was measured for films of PMMA, PMMA-*co*-MAA (30wt% MAA), and this copolymer with the addition of 10wt% of CNF. Compared to PMMA, limited or no advantages in thermal conductivity were observed for PMMA-*co*-MAA. While the bulk measure suggested a slight thermal conductivity improvement, the same was not confirmed after reprocessing by compression moulding, which is possibly explained by the reduction of H-bonding between the

macromolecules as a consequence of the anhydride formation during thermal degradation of the copolymer. For the nanocomposites, despite the presence of H-bonds interactions proved by the appearance of a β' relaxation process by BDS, the addition of 10wt% of CNF in the PMMA-*co*-MAA matrix did not show a significant augmentation of κ. Considering that nanocomposite thermal conductivity will mainly depend on the intrinsic κ of both components but also by the thermal contact resistance at the interface matrix/filler and among the fillers, the H-bonds present in the nanocomposite film are probably not sufficient to reduce the thermal contact resistance at the interface, thus preventing the thermal conductivity enhancement.

Based on the results obtained in this thesis, the enhancements of thermal conductivity obtainable by the modification of the interchain interactions between chains in amorphous matrices remains an extremely complex challenge. While the improvement in the interconnection between polymer chains and the inclusion of a moderate fraction of highly crystalline CNF are generally expected to provide additional channels for heat transfer within the polymer structure, the change in conformational states and associated phonon scattering phenomena appears to dominate the heat exchange performance. Anyway, a fundamental understanding of the phenomenon remains of strong interest since only thanks to an accurate description of the mechanism it will be possible to design polymer-based system with improved thermal properties. Therefore, similar interactions may be explored in polymeric materials having a better processability allowing the preparation of sample characterised by a higher quality, *i.e.* homogenous thickness. At the same time, different measurement techniques having other requirements in terms of sample shape and dimensions could be considered, *e.g.* 3ω-method which allows the analysis of thinner films.

References

1. Huang, C.; Qian, X.; Yang, R. Thermal Conductivity of Polymers and Polymer Nanocomposites. *Materials Science and Engineering: R: Reports* **2018**, *132*, 1–22, doi:10.1016/j.mser.2018.06.002.
2. Hussain, A.R.J.; Alahyari, A.A.; Eastman, S.A.; Thibaud-Erkey, C.; Johnston, S.; Sobkowicz, M.J. Review of Polymers for Heat Exchanger Applications: Factors Concerning Thermal Conductivity. *Applied Thermal Engineering* **2017**, *113*, 1118–1127, doi:10.1016/j.applthermaleng.2016.11.041.
3. Moore, A.L.; Shi, L. Emerging Challenges and Materials for Thermal Management of Electronics. *Materials Today* **2014**, *17*, 163–174, doi:10.1016/j.mattod.2014.04.003.
4. Chen, H.; Ginzburg, V.V.; Yang, J.; Yang, Y.; Liu, W.; Huang, Y.; Du, L.; Chen, B. Thermal Conductivity of Polymer-Based Composites: Fundamentals and Applications. *Progress in Polymer Science* **2016**, *59*, 41–85, doi:10.1016/j.progpolymsci.2016.03.001.
5. Wei, X.; Zhang, T.; Luo, T. Chain Conformation-Dependent Thermal Conductivity of Amorphous Polymer Blends: The Impact of Inter- and Intra-Chain Interactions. *Phys. Chem. Chem. Phys.* **2016**, *18*, 21–46, doi:10.1039/C6CP06643G.
6. Guo, Y.; Zhou, Y.; Xu, Y. Engineering Polymers with Metal-like Thermal Conductivity—Present Status and Future Perspectives. *Polymer* **2021**, *233*, 124168, doi:10.1016/j.polymer.2021.124168.
7. Toberer, E.S.; Baranowski, L.L.; Dames, C. Advances in Thermal Conductivity. *Annu. Rev. Mater. Res.* **2012**, *42*, 179–209, doi:10.1146/annurev-matsci-070511-155040.
8. Xu, X.; Zhou, J.; Chen, J. Thermal Transport in Conductive Polymer–Based Materials. *Adv. Funct. Mater.* **2020**, *30*, 1904704, doi:10.1002/adfm.201904704.
9. Zhang, T.; Luo, T. Role of Chain Morphology and Stiffness in Thermal Conductivity of Amorphous Polymers. *J. Phys. Chem. B* **2016**, *120*, 803–812, doi:10.1021/acs.jpcb.5b09955.
10. Xu, X.; Chen, J.; Zhou, J.; Li, B. Thermal Conductivity of Polymers and Their Nanocomposites. *Adv. Mater.* **2018**, *30*, doi:https://doi.org/10.1002/adma.201705544.
11. Palacios, A.; Cong, L.; Navarro, M.E.; Ding, Y.; Barreneche, C. Thermal Conductivity Measurement Techniques for Characterizing Thermal Energy Storage Materials – A Review. *Renewable and Sustainable Energy Reviews* **2019**, *108*, 32–52, doi:10.1016/j.rser.2019.03.020.
12. Balandin, A.A. Thermal Properties of Graphene and Nanostructured Carbon Materials. *Nature Mater* **2011**, *10*, 569–581, doi:10.1038/nmat3064.
13. Shi, A.; Li, Y.; Liu, W.; Lei, J.; Li, Z.-M. High Thermal Conductivity of Chain-Aligned Bulk Linear Ultra-High Molecular Weight Polyethylene. *Journal of Applied Physics* **2019**, *125*, 245110, doi:10.1063/1.5108520.
14. Singh, V.; Bougher, T.L.; Weathers, A.; Cai, Y.; Bi, K.; Pettes, M.T.; McMenamin, S.A.; Lv, W.; Resler, D.P.; Gattuso, T.R.; et al. High Thermal Conductivity of Chain-Oriented Amorphous Polythiophene. *Nature Nanotech* **2014**, *9*, 384–390, doi:10.1038/nnano.2014.44.

15. Henry, A.; Chen, G. High Thermal Conductivity of Single Polyethylene Chains Using Molecular Dynamics Simulations. *Phys. Rev. Lett.* **2008**, *101*, 235502, doi:10.1103/PhysRevLett.101.235502.
16. Shen, S.; Henry, A.; Tong, J.; Zheng, R.; Chen, G. Polyethylene Nanofibres with Very High Thermal Conductivities. *Nature Nanotech* **2010**, *5*, 251–255, doi:10.1038/nnano.2010.27.
17. Shrestha, R.; Li, P.; Chatterjee, B.; Zheng, T.; Wu, X.; Liu, Z.; Luo, T.; Choi, S.; Hippalgaonkar, K.; De Boer, M.P.; et al. Crystalline Polymer Nanofibers with Ultra-High Strength and Thermal Conductivity. *Nat Commun* **2018**, *9*, 1664, doi:10.1038/s41467-018-03978-3.
18. Adachi, K.; Daicho, K.; Furuta, M.; Shiga, T.; Saito, T.; Kodama, T. Thermal Conduction through Individual Cellulose Nanofibers. *Applied Physics Letters* **2021**, *118*, 053701, doi:10.1063/5.0042463.
19. Antlauf, M.; Andersson, O. Thermal Conductivity of Porous and Dense Networks of Cellulose Nanocrystals. *Macromolecules* **2022**, *55*, 5326–5331, doi:10.1021/acs.macromol.2c00153.
20. Lv, W.; Henry, A. Examining the Validity of the Phonon Gas Model in Amorphous Materials. *Sci Rep* **2016**, *6*, 37675, doi:10.1038/srep37675.
21. Hsieh, W.-P.; Losego, M.D.; Braun, P.V.; Shenogin, S.; Keblinski, P.; Cahill, D.G. Testing the Minimum Thermal Conductivity Model for Amorphous Polymers Using High Pressure. *Phys. Rev. B* **2011**, *83*, 174205, doi:10.1103/PhysRevB.83.174205.
22. Toberer, E.S.; Zevalkink, A.; Snyder, G.J. Phonon Engineering through Crystal Chemistry. *J. Mater. Chem.* **2011**, *21*, 15843, doi:10.1039/c1jm11754h.
23. Xu, Y.; Wang, X.; Zhou, J.; Song, B.; Jiang, Z.; Lee, E.M.Y.; Huberman, S.; Gleason, K.K.; Chen, G. Molecular Engineered Conjugated Polymer with High Thermal Conductivity. *Sci. Adv.* **2018**, *4*, eaar3031, doi:10.1126/sciadv.aar3031.
24. Xu, Y.; Kraemer, D.; Song, B.; Jiang, Z.; Zhou, J.; Loomis, J.; Wang, J.; Li, M.; Ghasemi, H.; Huang, X.; et al. Nanostructured Polymer Films with Metal-like Thermal Conductivity. *Nat Commun* **2019**, *10*, 1771, doi:10.1038/s41467-019-09697-7.
25. Tritt, T.M.; Weston, D. Measurement Techniques and Considerations for Determining Thermal Conductivity of Bulk Materials. In *Thermal Conductivity*; Tritt, T.M., Ed.; Physics of Solids and Liquids; Springer US, 2004; pp. 187–203 ISBN 978-0-306-48327-1.
26. Yüksel, N. The Review of Some Commonly Used Methods and Techniques to Measure the Thermal Conductivity of Insulation Materials. In *Insulation Materials in Context of Sustainability*; Almusaed, A., Almssad, A., Eds.; InTech, 2016 ISBN 978-953-51-2624-9.
27. dos Santos, W.N. Thermal Properties of Polymers by Non-Steady-State Techniques. *Polymer Testing* **2007**, *26*, 556–566, doi:10.1016/j.polymertesting.2007.02.005.
28. Nunes dos Santos, W.; Mummery, P.; Wallwork, A. Thermal Diffusivity of Polymers by the Laser Flash Technique. *Polymer Testing* **2005**, *24*, 628–634, doi:10.1016/j.polymertesting.2005.03.007.
29. Al-Ajlan, S.A. Measurements of Thermal Properties of Insulation Materials by Using Transient Plane Source Technique. *Applied Thermal Engineering* **2006**, *26*, 2184–2191, doi:10.1016/j.applthermaleng.2006.04.006.

30. Bohac, V.; Gustavsson, M.K.; Kubicar, L.; Gustafsson, S.E. Parameter Estimations for Measurements of Thermal Transport Properties with the Hot Disk Thermal Constants Analyzer. *Review of Scientific Instruments* **2000**, *71*, 2452–2455, doi:10.1063/1.1150635.
31. Zhao, D.; Qian, X.; Gu, X.; Jajja, S.A.; Yang, R. Measurement Techniques for Thermal Conductivity and Interfacial Thermal Conductance of Bulk and Thin Film Materials. *Journal of Electronic Packaging* **2016**, *138*, 040802, doi:10.1115/1.4034605.
32. Gong, L.; Wang, Y.; Cheng, X.; Zhang, R.; Zhang, H. Porous Mullite Ceramics with Low Thermal Conductivity Prepared by Foaming and Starch Consolidation. *J Porous Mater* **2014**, *21*, 15–21, doi:10.1007/s10934-013-9741-z.
33. Zheng, Q.; Kaur, S.; Dames, C.; Prasher, R.S. Analysis and Improvement of the Hot Disk Transient Plane Source Method for Low Thermal Conductivity Materials. *International Journal of Heat and Mass Transfer* **2020**, *151*, 119331, doi:10.1016/j.ijheatmasstransfer.2020.119331.
34. Gustafsson, S.E. Transient Plane Source Techniques for Thermal Conductivity and Thermal Diffusivity Measurements of Solid Materials. *Review of Scientific Instruments* **1991**, *62*, 797–804, doi:10.1063/1.1142087.
35. Ahadi, M.; Andisheh-Tadbir, M.; Tam, M.; Bahrami, M. An Improved Transient Plane Source Method for Measuring Thermal Conductivity of Thin Films: Deconvoluting Thermal Contact Resistance. *International Journal of Heat and Mass Transfer* **2016**, *96*, 371–380, doi:10.1016/j.ijheatmasstransfer.2016.01.037.
36. Feng, B.; Zhang, Y.-H.; Tu, J.; Fan, L.-W.; Yu, Z.-T. Determination on the Thermal Conductivity and Thermal Contact Resistance of Thin Composite Phase Change Films as a Thermal Interfacial Material. *Case Studies in Thermal Engineering* **2022**, *33*, 101979, doi:10.1016/j.csite.2022.101979.
37. Gustavsson, J.S. On the Use of the Hot Disk Thermal Constants Analyser for Measuring the Thermal Conductivity of Thin Samples of Electrically Insulating Materials. In Proceedings of the Thermal conductivity 24; Pittsburg, Pennsylvania, USA, 1997; pp. 116–122.
38. Zhang, H.; Li, M.-J.; Fang, W.-Z.; Dan, D.; Li, Z.-Y.; Tao, W.-Q. A Numerical Study on the Theoretical Accuracy of Film Thermal Conductivity Using Transient Plane Source Method. *Applied Thermal Engineering* **2014**, *72*, 62–69, doi:10.1016/j.applthermaleng.2014.01.058.
39. Kiessling, A.; Simavilla, D.N.; Vogiatzis, G.G.; Venerus, D.C. Thermal Conductivity of Amorphous Polymers and Its Dependence on Molecular Weight. *Polymer* **2021**, *228*, 123881, doi:10.1016/j.polymer.2021.123881.
40. Canetta, C.; Guo, S.; Narayanaswamy, A. Measuring Thermal Conductivity of Polystyrene Nanowires Using the Dual-Cantilever Technique. *Review of Scientific Instruments* **2014**, *85*, 104901, doi:10.1063/1.4896330.
41. Ma, H.; Tian, Z. Effects of Polymer Topology and Morphology on Thermal Transport: A Molecular Dynamics Study of Bottlebrush Polymers. *Applied Physics Letters* **2017**, *110*, 091903, doi:10.1063/1.4976946.
42. Guo, Z.; Lee, D.; Liu, Y.; Sun, F.; Sliwinski, A.; Gao, H.; Burns, P.C.; Huang, L.; Luo, T. Tuning the Thermal Conductivity of Solar Cell Polymers through Side Chain Engineering. *Phys. Chem. Chem. Phys.* **2014**, *16*, 7764–7771, doi:10.1039/C4CP00393D.
43. Chen, X.P.; Liang, Q.H.; Jiang, J.K.; Wong, C.K.Y.; Leung, S.Y.Y.; Ye, H.Y.; Yang, D.G.; Ren, T.L. Functionalization-Induced Changes in the Structural

and Physical Properties of Amorphous Polyaniline: A First-Principles and Molecular Dynamics Study. *Sci Rep* **2016**, *6*, 20621, doi:10.1038/srep20621.
44. Chen, X.P.; Jiang, J.K.; Liang, Q.H.; Yang, N.; Ye, H.Y.; Cai, M.; Shen, L.; Yang, D.G.; Ren, T.L. First-Principles Study of the Effect of Functional Groups on Polyaniline Backbone. *Sci Rep* **2015**, *5*, 16907, doi:10.1038/srep16907.
45. Xie, X.; Yang, K.; Li, D.; Tsai, T.-H.; Shin, J.; Braun, P.V.; Cahill, D.G. High and Low Thermal Conductivity of Amorphous Macromolecules. *Phys. Rev. B* **2017**, *95*, 035406, doi:10.1103/PhysRevB.95.035406.
46. Kim, G.-H.; Lee, D.; Shanker, A.; Shao, L.; Kwon, M.S.; Gidley, D.; Kim, J.; Pipe, K.P. High Thermal Conductivity in Amorphous Polymer Blends by Engineered Interchain Interactions. *Nature Mater* **2015**, *14*, 295–300, doi:10.1038/nmat4141.
47. Xie, X.; Li, D.; Tsai, T.-H.; Liu, J.; Braun, P.V.; Cahill, D.G. Thermal Conductivity, Heat Capacity, and Elastic Constants of Water-Soluble Polymers and Polymer Blends. *Macromolecules* **2016**, *49*, 972–978, doi:10.1021/acs.macromol.5b02477.
48. Mu, L.; He, J.; Li, Y.; Ji, T.; Mehra, N.; Shi, Y.; Zhu, J. Molecular Origin of Efficient Phonon Transfer in Modulated Polymer Blends: Effect of Hydrogen Bonding on Polymer Coil Size and Assembled Microstructure. *J. Phys. Chem. C* **2017**, *121*, 14204–14212, doi:10.1021/acs.jpcc.7b03726.
49. Shanker, A.; Li, C.; Kim, G.-H.; Gidley, D.; Pipe, K.P.; Kim, J. High Thermal Conductivity in Electrostatically Engineered Amorphous Polymers. *Sci. Adv.* **2017**, *3*, e1700342, doi:10.1126/sciadv.1700342.
50. Kikugawa, G.; Desai, T.G.; Keblinski, P.; Ohara, T. Effect of Crosslink Formation on Heat Conduction in Amorphous Polymers. *Journal of Applied Physics* **2013**, *114*, 034302, doi:10.1063/1.4813505.
51. Tang, N.; Peng, Z.; Guo, R.; An, M.; Chen, X.; Li, X.; Yang, N.; Zang, J. Thermal Transport in Soft PAAm Hydrogels. *Polymers* **2017**, *9*, 688, doi:10.3390/polym9120688.
52. Corsaro, C.; Neri, G.; Santoro, A.; Fazio, E. Acrylate and Methacrylate Polymers' Applications: Second Life with Inexpensive and Sustainable Recycling Approaches. *Materials* **2021**, *15*, 282, doi:10.3390/ma15010282.
53. Ali, U.; Karim, K.J.Bt.A.; Buang, N.A. A Review of the Properties and Applications of Poly (Methyl Methacrylate) (PMMA). *Polymer Reviews* **2015**, *55*, 678–705, doi:10.1080/15583724.2015.1031377.
54. Deka, N.; Bera, A.; Roy, D.; De, P. Methyl Methacrylate-Based Copolymers: Recent Developments in the Areas of Transparent and Stretchable Active Matrices. *ACS Omega* **2022**, *7*, 36929–36944, doi:10.1021/acsomega.2c04564.
55. Abusafieh, A.; Gobran, R.; Kalidindi, S.R. Synthesis and Characterization of a Poly(Methyl Methacrylate-Acrylic Acid) Copolymer for Bioimplant Applications. *J. Appl. Polym. Sci.* **1997**, *63*, 75–87, doi:10.1002/(SICI)1097-4628(19970103)63:1<75::AID-APP8>3.0.CO;2-P.
56. Kuo, S.-W.; Kao, H.-C.; Chang, F.-C. Thermal Behavior and Specific Interaction in High Glass Transition Temperature PMMA Copolymer. *Polymer* **2003**, *44*, 6873–6882, doi:10.1016/j.polymer.2003.08.026.
57. Kuo, S.-W.; Tsai, H.-T. Complementary Multiple Hydrogen-Bonding Interactions Increase the Glass Transition Temperatures to PMMA Copolymer Mixtures. *Macromolecules* **2009**, *42*, 4701–4711, doi:10.1021/ma900640a.

58. Kuo, S.-W.; Tsai, H.-T. Self-Complementary Multiple Hydrogen Bonding Interactions Increase the Glass Transition Temperatures to Supramolecular Poly(Methyl Methacrylate) Copolymers. *J. Appl. Polym. Sci.* **2012**, *123*, 3275–3282, doi:10.1002/app.35001.
59. Yeh, S.-L.; Zhu, C.-Y.; Kuo, S.-W. Transparent Heat-Resistant PMMA Copolymers for Packing Light-Emitting Diode Materials. *Polymers* **2015**, *7*, 1379–1388, doi:10.3390/polym7081379.
60. Huang, C.-F.; Chang, F.-C. Comparison of Hydrogen Bonding Interaction between PMMA/PMAA Blends and PMMA-Co-PMAA Copolymers. *Polymer* **2003**, *44*, 2965–2974, doi:10.1016/S0032-3861(03)00188-5.
61. Tsou, L.; Ma, X.; Sauer, J.A.; Hara, M. Blends of Poly(Methyl Methacrylate) (PMMA) with PMMA Ionomers: Mechanical Properties. *J. Polym. Sci. B Polym. Phys.* **1998**, *36*, 1235–1245, doi:10.1002/(SICI)1099-0488(199805)36:7<1235::AID-POLB13>3.0.CO;2-9.
62. Nah, Y.-H.; Kim, J.-S.; Jo, B.-W.; Kim, J.; Lee, Y. Effects of Contact Surface Area of Chains on the Mechanical Properties of Poly(Methyl Methacrylate-Co -Acrylate) Ionomers. *Polymer Bulletin* **1999**, *42*, 213–219, doi:10.1007/s002890050455.
63. Ma, X.; Sauer, J.A.; Hara, M. Poly(Methyl Methacrylate) Based Ionomers. 1. Dynamic Mechanical Properties and Morphology. *Macromolecules* **1995**, *28*, 3953–3962, doi:10.1021/ma00115a031.
64. Assael, M.J.; Botsios, S.; Gialou, K.; Metaxa, I.N. Thermal Conductivity of Polymethyl Methacrylate (PMMA) and Borosilicate Crown Glass BK7. *Int J Thermophys* **2005**, *26*, 1595–1605, doi:10.1007/s10765-005-8106-5.
65. Cahill, D.G.; Pohl, R.O. Thermal Conductivity of Amorphous Solids above the Plateau. *Phys. Rev. B* **1987**, *35*, 4067–4073, doi:10.1103/PhysRevB.35.4067.
66. Andersson, S.P.; Ross, R.G. Thermal Conductivity and Heat Capacity per Unit Volume of Poly(Methyl Methacrylate) under High Pressure. *Int J Thermophys* **1994**, *15*, 949–962, doi:10.1007/BF01447105.
67. Hu, M.; Yu, D.; Wei, J. Thermal Conductivity Determination of Small Polymer Samples by Differential Scanning Calorimetry. *Polymer Testing* **2007**, *26*, 333–337, doi:10.1016/j.polymertesting.2006.11.003.
68. Putnam, S.A.; Cahill, D.G.; Ash, B.J.; Schadler, L.S. High-Precision Thermal Conductivity Measurements as a Probe of Polymer/Nanoparticle Interfaces. *Journal of Applied Physics* **2003**, *94*, 6785–6788, doi:10.1063/1.1619202.
69. Wu, M.; Huang, H.-X.; Tong, J.; Ke, D.-Y. Enhancing Thermal Conductivity and Mechanical Properties of Poly(Methyl Methacrylate) via Adding Expanded Graphite and Injecting Water. *Composites Part A: Applied Science and Manufacturing* **2017**, *102*, 228–235, doi:10.1016/j.compositesa.2017.08.010.
70. Zhou, Y.; Wang, H.; Wang, L.; Yu, K.; Lin, Z.; He, L.; Bai, Y. Fabrication and Characterization of Aluminum Nitride Polymer Matrix Composites with High Thermal Conductivity and Low Dielectric Constant for Electronic Packaging. *Materials Science and Engineering: B* **2012**, *177*, 892–896, doi:10.1016/j.mseb.2012.03.056.
71. Tang, Y.; Xiao, C.; Ding, J.; Hu, K.; Zheng, K.; Tian, X. Synergetic Enhancement of Thermal Conductivity in the Silica-Coated Boron Nitride (SiO2@BN)/Polymethyl Methacrylate (PMMA) Composites. *Colloid Polym Sci* **2020**, *298*, 385–393, doi:10.1007/s00396-020-04617-4.

72. Hong, W.-T.; Tai, N.-H. Investigations on the Thermal Conductivity of Composites Reinforced with Carbon Nanotubes. *Diamond and Related Materials* **2008**, *17*, 1577–1581, doi:10.1016/j.diamond.2008.03.037.
73. Guthy, C. Thermal Conductivity of Single-Walled Carbon Nanotube/PMMA Nanocomposites. *Journal of Heat Transfer* **2007**, 1096–1099.
74. Pielichowska, K. Polymer Nanocomposites: Preparation, Characterisation and Applications. *Nanomaterials* **2022**, *12*, 1900, doi:10.3390/nano12111900.
75. Safdari, M.; Al-Haik, M.S. A Review on Polymeric Nanocomposites. In *Carbon-Based Polymer Nanocomposites for Environmental and Energy Applications*; Elsevier, 2018; pp. 113–146 ISBN 978-0-12-813574-7.
76. Kayalvizhi Nangai, E.; Saravanan, S. Synthesis, Fabrication and Testing of Polymer Nanocomposites: A Review. *Materials Today: Proceedings* **2023**, *81*, 91–97, doi:10.1016/j.matpr.2021.02.261.
77. Vinyas, M.; Athul, S.J.; Harursampath, D.; Loja, M.; Nguyen Thoi, T. A Comprehensive Review on Analysis of Nanocomposites: From Manufacturing to Properties Characterization. *Mater. Res. Express* **2019**, *6*, 092002, doi:10.1088/2053-1591/ab3175.
78. Muhammed Shameem, M.; Sasikanth, S.M.; Annamalai, R.; Ganapathi Raman, R. A Brief Review on Polymer Nanocomposites and Its Applications. *Materials Today: Proceedings* **2021**, *45*, 2536–2539, doi:10.1016/j.matpr.2020.11.254.
79. Mohammed, L.; Ansari, M.N.M.; Pua, G.; Jawaid, M.; Islam, M.S. A Review on Natural Fiber Reinforced Polymer Composite and Its Applications. *International Journal of Polymer Science* **2015**, *2015*, 1–15, doi:10.1155/2015/243947.
80. Fu, S.; Sun, Z.; Huang, P.; Li, Y.; Hu, N. Some Basic Aspects of Polymer Nanocomposites: A Critical Review. *Nano Materials Science* **2019**, *1*, 2–30, doi:10.1016/j.nanoms.2019.02.006.
81. Dantas De Oliveira, A.; Augusto Gonçalves Beatrice, C. Polymer Nanocomposites with Different Types of Nanofiller. In *Nanocomposites - Recent Evolutions*; Sivasankaran, S., Ed.; IntechOpen, 2019 ISBN 978-1-78985-011-6.
82. Kalia, S.; Boufi, S.; Celli, A.; Kango, S. Nanofibrillated Cellulose: Surface Modification and Potential Applications. *Colloid Polym Sci* **2014**, *292*, 5–31, doi:10.1007/s00396-013-3112-9.
83. Kausar, A. A Review of High Performance Polymer Nanocomposites for Packaging Applications in Electronics and Food Industries. *Journal of Plastic Film & Sheeting* **2020**, *36*, 94–112, doi:10.1177/8756087919849459.
84. Kumar, A.; Sharma, K.; Dixit, A.R. A Review on the Mechanical Properties of Polymer Composites Reinforced by Carbon Nanotubes and Graphene. *Carbon Lett.* **2021**, *31*, 149–165, doi:10.1007/s42823-020-00161-x.
85. Hiremath, A.; Murthy, A.A.; Thipperudrappa, S.; K N, B. Nanoparticles Filled Polymer Nanocomposites: A Technological Review. *Cogent Engineering* **2021**, *8*, 1991229, doi:10.1080/23311916.2021.1991229.
86. Liu, W.; Liu, K.; Du, H.; Zheng, T.; Zhang, N.; Xu, T.; Pang, B.; Zhang, X.; Si, C.; Zhang, K. Cellulose Nanopaper: Fabrication, Functionalization, and Applications. *Nano-Micro Lett.* **2022**, *14*, 104, doi:10.1007/s40820-022-00849-x.
87. Lin, W. Modeling of Thermal Conductivity of Polymer Nanocomposites. In *Modeling and Prediction of Polymer Nanocomposite Properties*; Mittal, V., Ed.; Wiley, **2013**; pp. 169–200 ISBN 978-3-527-33150-5.

88. Burger, N.; Laachachi, A.; Ferriol, M.; Lutz, M.; Toniazzo, V.; Ruch, D. Review of Thermal Conductivity in Composites: Mechanisms, Parameters and Theory. *Progress in Polymer Science* **2016**, *61*, 1–28, doi:10.1016/j.progpolymsci.2016.05.001.
89. Chu, K.; Jia, C.; Li, W. Effective Thermal Conductivity of Graphene-Based Composites. *Applied Physics Letters* **2012**, *101*, 121916, doi:10.1063/1.4754120.
90. Nan, C.-W.; Liu, G.; Lin, Y.; Li, M. Interface Effect on Thermal Conductivity of Carbon Nanotube Composites. *Applied Physics Letters* **2004**, *85*, 3549–3551, doi:10.1063/1.1808874.
91. Peterson, R.E.; Anderson, A.C. The Kapitza Thermal Boundary Resistance. *J Low Temp Phys* **1973**, *11*, 639–665, doi:10.1007/BF00654451.
92. Pietrak, K.; Wisniewski, T.S. A Review of Models for Effective Thermal Conductivity of Composite Materials. **2015**.
93. Kapitza, P.L. The study of heat transfer in helium II. In *Helium 4*; Elsevier, **1971**; pp. 114–153 ISBN 978-0-08-015816-7.
94. Kim, P.; Shi, L.; Majumdar, A.; McEuen, P.L. Thermal Transport Measurements of Individual Multiwalled Nanotubes. *Phys. Rev. Lett.* **2001**, *87*, 215502, doi:10.1103/PhysRevLett.87.215502.
95. Yu, C.; Shi, L.; Yao, Z.; Li, D.; Majumdar, A. Thermal Conductance and Thermopower of an Individual Single-Wall Carbon Nanotube. *Nano Lett.* **2005**, *5*, 1842–1846, doi:10.1021/nl051044e.
96. Shahil, K.M.F.; Balandin, A.A. Graphene–Multilayer Graphene Nanocomposites as Highly Efficient Thermal Interface Materials. *Nano Lett.* **2012**, *12*, 861–867, doi:10.1021/nl203906r.
97. Liu, Z.; Guo, Q.; Shi, J.; Zhai, G.; Liu, L. Graphite Blocks with High Thermal Conductivity Derived from Natural Graphite Flake. *Carbon* **2008**, *46*, 414–421, doi:10.1016/j.carbon.2007.11.050.
98. Haggenmueller, R.; Guthy, C.; Lukes, J.R.; Fischer, J.E.; Winey, K.I. Single Wall Carbon Nanotube/Polyethylene Nanocomposites: Thermal and Electrical Conductivity. *Macromolecules* **2007**, *40*, 2417–2421, doi:10.1021/ma0615046.
99. Han, Z.; Fina, A. Thermal Conductivity of Carbon Nanotubes and Their Polymer Nanocomposites: A Review. *Progress in Polymer Science* **2011**, *36*, 914–944, doi:10.1016/j.progpolymsci.2010.11.004.
100. Luo, T.; Lloyd, J.R. Enhancement of Thermal Energy Transport Across Graphene/Graphite and Polymer Interfaces: A Molecular Dynamics Study. *Adv. Funct. Mater.* **2012**, *22*, 2495–2502, doi:10.1002/adfm.201103048.
101. Yu, J.; Huang, X.; Wu, C.; Wu, X.; Wang, G.; Jiang, P. Interfacial Modification of Boron Nitride Nanoplatelets for Epoxy Composites with Improved Thermal Properties. *Polymer* **2012**, *53*, 471–480, doi:10.1016/j.polymer.2011.12.040.
102. Antlauf, M.; Boulanger, N.; Berglund, L.; Oksman, K.; Andersson, O. Thermal Conductivity of Cellulose Fibers in Different Size Scales and Densities. *Biomacromolecules* **2021**, *22*, 3800–3809, doi:10.1021/acs.biomac.1c00643.
103. Bahar, E.; Ucar, N.; Onen, A.; Wang, Y.; Oksüz, M.; Ayaz, O.; Ucar, M.; Demir, A. Thermal and Mechanical Properties of Polypropylene Nanocomposite Materials Reinforced with Cellulose Nano Whiskers. *J. Appl. Polym. Sci.* **2012**, *125*, 2882–2889, doi:10.1002/app.36445.

104. Shimazaki, Y.; Miyazaki, Y.; Takezawa, Y.; Nogi, M.; Abe, K.; Ifuku, S.; Yano, H. Excellent Thermal Conductivity of Transparent Cellulose Nanofiber/Epoxy Resin Nanocomposites. *Biomacromolecules* **2007**, *8*, 2976–2978, doi:10.1021/bm7004998.
105. Klemm, D.; Heublein, B.; Fink, H.-P.; Bohn, A. Cellulose: Fascinating Biopolymer and Sustainable Raw Material. *Angew. Chem. Int. Ed.* **2005**, *44*, 3358–3393, doi:10.1002/anie.200460587.
106. Jedvert, K.; Heinze, T. Cellulose Modification and Shaping – a Review. *Journal of Polymer Engineering* **2017**, *37*, 845–860, doi:10.1515/polyeng-2016-0272.
107. Shaghaleh, H.; Xu, X.; Wang, S. Current Progress in Production of Biopolymeric Materials Based on Cellulose, Cellulose Nanofibers, and Cellulose Derivatives. *RSC Adv.* **2018**, *8*, 825–842, doi:10.1039/C7RA11157F.
108. Aziz, T.; Farid, A.; Haq, F.; Kiran, M.; Ullah, A.; Zhang, K.; Li, C.; Ghazanfar, S.; Sun, H.; Ullah, R.; et al. A Review on the Modification of Cellulose and Its Applications. *Polymers* **2022**, *14*, 3206, doi:10.3390/polym14153206.
109. Hou, D.-F.; Li, M.-L.; Yan, C.; Zhou, L.; Liu, Z.-Y.; Yang, W.; Yang, M.-B. Mechanochemical Preparation of Thermoplastic Cellulose Oleate by Ball Milling. *Green Chem.* **2021**, *23*, 2069–2078, doi:10.1039/D0GC03853A.
110. Oksman, K.; Aitomäki, Y.; Mathew, A.P.; Siqueira, G.; Zhou, Q.; Butylina, S.; Tanpichai, S.; Zhou, X.; Hooshmand, S. Review of the Recent Developments in Cellulose Nanocomposite Processing. *Composites Part A: Applied Science and Manufacturing* **2016**, *83*, 2–18, doi:10.1016/j.compositesa.2015.10.041.
111. Lee, H.-J.; Lee, H.-S.; Seo, J.; Kang, Y.-H.; Kim, W.; Kang, T. State-of-the-Art of Cellulose Nanocrystals and Optimal Method for Their Dispersion for Construction-Related Applications. *Applied Sciences* **2019**, *9*, 426, doi:10.3390/app9030426.
112. Jamaluddin, N.; Hsu, Y.-I.; Asoh, T.-A.; Uyama, H. Optically Transparent and Toughened Poly(Methyl Methacrylate) Composite Films with Acylated Cellulose Nanofibers. *ACS Omega* **2021**, *6*, 10752–10758, doi:10.1021/acsomega.1c00325.
113. Lin, N.; Dufresne, A. Physical and/or Chemical Compatibilization of Extruded Cellulose Nanocrystal Reinforced Polystyrene Nanocomposites. *Macromolecules* **2013**, *46*, 5570–5583, doi:10.1021/ma4010154.
114. Pei, A.; Malho, J.-M.; Ruokolainen, J.; Zhou, Q.; Berglund, L.A. Strong Nanocomposite Reinforcement Effects in Polyurethane Elastomer with Low Volume Fraction of Cellulose Nanocrystals. *Macromolecules* **2011**, *44*, 4422–4427, doi:10.1021/ma200318k.
115. Dong, H.; Sliozberg, Y.R.; Snyder, J.F.; Steele, J.; Chantawansri, T.L.; Orlicki, J.A.; Walck, S.D.; Reiner, R.S.; Rudie, A.W. Highly Transparent and Toughened Poly(Methyl Methacrylate) Nanocomposite Films Containing Networks of Cellulose Nanofibrils. *ACS Appl. Mater. Interfaces* **2015**, *7*, 25464–25472, doi:10.1021/acsami.5b08317.
116. Ramesh, S.; Radhakrishnan, P. Cellulose Nanoparticles from Agro-Industrial Waste for the Development of Active Packaging. *Applied Surface Science* **2019**, *484*, 1274–1281, doi:10.1016/j.apsusc.2019.04.003.
117. Randhawa, A.; Dutta, S.D.; Ganguly, K.; Patil, T.V.; Patel, D.K.; Lim, K.-T. A Review of Properties of Nanocellulose, Its Synthesis, and Potential in

Biomedical Applications. *Applied Sciences* **2022**, *12*, 7090, doi:10.3390/app12147090.
118. Nasir, M.; Hashim, R.; Sulaiman, O.; Asim, M. Nanocellulose. In *Cellulose-Reinforced Nanofibre Composites*; Elsevier, **2017**; pp. 261–276 ISBN 978-0-08-100957-4.
119. Islam, M.T.; Alam, M.M.; Patrucco, A.; Montarsolo, A.; Zoccola, M. Preparation of Nanocellulose: A Review. *aatcc j res* **2014**, *1*, 17–23, doi:10.14504/ajr.1.5.3.
120. Salimi, S.; Sotudeh-Gharebagh, R.; Zarghami, R.; Chan, S.Y.; Yuen, K.H. Production of Nanocellulose and Its Applications in Drug Delivery: A Critical Review. *ACS Sustainable Chem. Eng.* **2019**, *7*, 15800–15827, doi:10.1021/acssuschemeng.9b02744.
121. Magalhães, A.I.; Carvalho, J.C.; Melo Pereira, G.V.; Karp, S.G.; Câmara, M.C.; Medina, J.D.C.; Soccol, C.R. Lignocellulosic Biomass from Agro-industrial Residues in South America: Current Developments and Perspectives. *Biofuels, Bioprod. Bioref.* **2019**, *13*, 1505–1519, doi:10.1002/bbb.2048.
122. Bondeson, D.; Syre, P.; Niska, K.O. All Cellulose Nanocomposites Produced by Extrusion. *J Biobased Mat Bioenergy* **2007**, *1*, 367–371, doi:10.1166/jbmb.2007.011.
123. Bondeson, D.; Oksman, K. Dispersion and Characteristics of Surfactant Modified Cellulose Whiskers Nanocomposites. *Composite Interfaces* **2007**, *14*, 617–630, doi:10.1163/156855407782106519.
124. Oksman, K.; Mathew, A.P.; Bondeson, D.; Kvien, I. Manufacturing Process of Cellulose Whiskers/Polylactic Acid Nanocomposites. *Composites Science and Technology* **2006**, *66*, 2776–2784, doi:10.1016/j.compscitech.2006.03.002.
125. Salmén, L.; Stevanic, J.S. Effect of Drying Conditions on Cellulose Microfibril Aggregation and "Hornification." *Cellulose* **2018**, *25*, 6333–6344, doi:10.1007/s10570-018-2039-1.
126. Thomas, P.; Duolikun, T.; Rumjit, N.P.; Moosavi, S.; Lai, C.W.; Bin Johan, M.R.; Fen, L.B. Comprehensive Review on Nanocellulose: Recent Developments, Challenges and Future Prospects. *Journal of the Mechanical Behavior of Biomedical Materials* **2020**, *110*, 103884, doi:10.1016/j.jmbbm.2020.103884.
127. Peterson, A.; Mehandzhiyski, A.Y.; Svenningsson, L.; Ziolkowska, A.; Kádár, R.; Lund, A.; Sandblad, L.; Evenäs, L.; Lo Re, G.; Zozoulenko, I.; et al. A Combined Theoretical and Experimental Study of the Polymer Matrix-Mediated Stress Transfer in a Cellulose Nanocomposite. *Macromolecules* **2021**, *54*, 3507–3516, doi:10.1021/acs.macromol.0c02305.
128. Robles, E.; Urruzola, I.; Labidi, J.; Serrano, L. Surface-Modified Nano-Cellulose as Reinforcement in Poly(Lactic Acid) to Conform New Composites. *Industrial Crops and Products* **2015**, *71*, 44–53, doi:10.1016/j.indcrop.2015.03.075.
129. Lee, K.-Y.; Blaker, J.J.; Bismarck, A. Surface Functionalisation of Bacterial Cellulose as the Route to Produce Green Polylactide Nanocomposites with Improved Properties. *Composites Science and Technology* **2009**, *69*, 2724–2733, doi:10.1016/j.compscitech.2009.08.016.
130. de la Orden, M.U.; González Sánchez, C.; González Quesada, M.; Martínez Urreaga, J. Novel Polypropylene–Cellulose Composites Using Polyethylenimine as Coupling Agent. *Composites Part A: Applied Science*

and Manufacturing **2007**, *38*, 2005–2012, doi:10.1016/j.compositesa.2007.05.008.
131. Qiu, W.; Zhang, F.; Endo, T.; Hirotsu, T. Effect of Maleated Polypropylene on the Performance of Polypropylene/Cellulose Composite. *Polym. Compos.* **2005**, *26*, 448–453, doi:10.1002/pc.20119.
132. Venkatesh, A.; Thunberg, J.; Moberg, T.; Klingberg, M.; Hammar, L.; Peterson, A.; Müller, C.; Boldizar, A. Cellulose Nanofibril-Reinforced Composites Using Aqueous Dispersed Ethylene-Acrylic Acid Copolymer. *Cellulose* **2018**, *25*, 4577–4589, doi:10.1007/s10570-018-1875-3.
133. Keener, T.J.; Stuart, R.K.; Brown, T.K. Maleated Coupling Agents for Natural Fibre Composites. *Composites Part A: Applied Science and Manufacturing* **2004**, *35*, 357–362, doi:10.1016/j.compositesa.2003.09.014.
134. Peng, Y.; Gallegos, S.A.; Gardner, D.J.; Han, Y.; Cai, Z. Maleic Anhydride Polypropylene Modified Cellulose Nanofibril Polypropylene Nanocomposites with Enhanced Impact Strength. *Polym. Compos.* **2016**, *37*, 782–793, doi:10.1002/pc.23235.
135. Dufresne, A. *Polymer Nanocomposites from Biological Sources*; 2009;
136. Aitomäki, Y.; Oksman, K. Reinforcing Efficiency of Nanocellulose in Polymers. *Reactive and Functional Polymers* **2014**, *85*, 151–156, doi:10.1016/j.reactfunctpolym.2014.08.010.
137. Tingaut, P.; Zimmermann, T.; Lopez-Suevos, F. Synthesis and Characterization of Bionanocomposites with Tunable Properties from Poly(Lactic Acid) and Acetylated Microfibrillated Cellulose. *Biomacromolecules* **2010**, *11*, 454–464, doi:10.1021/bm901186u.
138. Jonoobi, M.; Mathew, A.P.; Abdi, M.M.; Makinejad, M.D.; Oksman, K. A Comparison of Modified and Unmodified Cellulose Nanofiber Reinforced Polylactic Acid (PLA) Prepared by Twin Screw Extrusion. *J Polym Environ* **2012**, *20*, 991–997, doi:10.1007/s10924-012-0503-9.
139. Qu, P.; Zhou, Y.; Zhang, X.; Yao, S.; Zhang, L. Surface Modification of Cellulose Nanofibrils for Poly(Lactic Acid) Composite Application. *J. Appl. Polym. Sci.* **2012**, *125*, 3084–3091, doi:10.1002/app.36360.
140. Anžlovar, A.; Huskić, M.; Žagar, E. Modification of Nanocrystalline Cellulose for Application as a Reinforcing Nanofiller in PMMA Composites. *Cellulose* **2016**, *23*, 505–518, doi:10.1007/s10570-015-0786-9.
141. Lönnberg, H.; Fogelström, L.; Berglund, L.; Malmström, E.; Hult, A. Surface Grafting of Microfibrillated Cellulose with Poly(ε-Caprolactone) – Synthesis and Characterization. *European Polymer Journal* **2008**, *44*, 2991–2997, doi:10.1016/j.eurpolymj.2008.06.023.
142. Tang, H.; Butchosa, N.; Zhou, Q. A Transparent, Hazy, and Strong Macroscopic Ribbon of Oriented Cellulose Nanofibrils Bearing Poly(Ethylene Glycol). *Adv. Mater.* **2015**, *27*, 2070–2076, doi:10.1002/adma.201404565.
143. Eichhorn, S.J.; Dufresne, A.; Aranguren, M.; Marcovich, N.E.; Capadona, J.R.; Rowan, S.J.; Weder, C.; Thielemans, W.; Roman, M.; Renneckar, S.; et al. Review: Current International Research into Cellulose Nanofibres and Nanocomposites. *J Mater Sci* **2010**, *45*, 1–33, doi:10.1007/s10853-009-3874-0.
144. Feldman, D. Cellulose Nanocomposites. *Journal of Macromolecular Science, Part A* **2015**, *52*, ebi-ebi, doi:10.1080/10601325.2015.984542.
145. Peterson, A.; Östergren, I.; Lotsari, A.; Venkatesh, A.; Thunberg, J.; Ström, A.; Rojas, R.; Andersson, M.; Berglund, L.A.; Boldizar, A.; et al. Dynamic

Nanocellulose Networks for Thermoset-like yet Recyclable Plastics with a High Melt Stiffness and Creep Resistance. *Biomacromolecules* **2019**, *20*, 3924–3932, doi:10.1021/acs.biomac.9b00993.
146. Trovatti, E.; Oliveira, L.; Freire, C.S.R.; Silvestre, A.J.D.; Pascoal Neto, C.; Cruz Pinto, J.J.C.; Gandini, A. Novel Bacterial Cellulose–Acrylic Resin Nanocomposites. *Composites Science and Technology* **2010**, *70*, 1148–1153, doi:10.1016/j.compscitech.2010.02.031.
147. Lu, P.; Hsieh, Y.-L. Cellulose Nanocrystal-Filled Poly(Acrylic Acid) Nanocomposite Fibrous Membranes. *Nanotechnology* **2009**, *20*, 415604, doi:10.1088/0957-4484/20/41/415604.
148. Erbas Kiziltas, E.; Kiziltas, A.; Bollin, S.C.; Gardner, D.J. Preparation and Characterization of Transparent PMMA–Cellulose-Based Nanocomposites. *Carbohydrate Polymers* **2015**, *127*, 381–389, doi:10.1016/j.carbpol.2015.03.029.
149. Huang, T.; Kuboyama, K.; Fukuzumi, H.; Ougizawa, T. PMMA/TEMPO-Oxidized Cellulose Nanofiber Nanocomposite with Improved Mechanical Properties, High Transparency and Tunable Birefringence. *Cellulose* **2018**, *25*, 2393–2403, doi:10.1007/s10570-018-1725-3.
150. Sain, S.; Ray, D.; Mukhopadhyay, A. Improved Mechanical and Moisture Resistance Property of *in Situ* Polymerized Transparent PMMA/Cellulose Composites. *Polym. Compos.* **2015**, *36*, 1748–1758, doi:10.1002/pc.23102.
151. Littunen, K.; Hippi, U.; Saarinen, T.; Seppälä, J. Network Formation of Nanofibrillated Cellulose in Solution Blended Poly(Methyl Methacrylate) Composites. *Carbohydrate Polymers* **2013**, *91*, 183–190, doi:10.1016/j.carbpol.2012.08.032.
152. Wang, W.; Liang, T.; Zhang, B.; Bai, H.; Ma, P.; Dong, W. Green Functionalization of Cellulose Nanocrystals for Application in Reinforced Poly(Methyl Methacrylate) Nanocomposites. *Carbohydrate Polymers* **2018**, *202*, 591–599, doi:10.1016/j.carbpol.2018.09.019.
153. Shih, Y.F.; Chou, M.Y.; Lian, H.Y.; Hsu, L.R.; Chen-Wei, S.M. Highly Transparent and Impact-Resistant PMMA Nanocomposites Reinforced by Cellulose Nanofibers of Pineapple Leaves Modified by Eco-Friendly Methods. *Express Polym. Lett.* **2018**, *12*, 844–854, doi:10.3144/expresspolymlett.2018.72.
154. Banerjee, M.; Sain, S.; Mukhopadhyay, A.; Sengupta, S.; Kar, T.; Ray, D. Surface Treatment of Cellulose Fibers with Methylmethacrylate for Enhanced Properties of *in Situ* Polymerized PMMA/Cellulose Composites. *J. Appl. Polym. Sci.* **2014**, *131*, n/a-n/a, doi:10.1002/app.39808.
155. Fujisawa, S.; Togawa, E.; Kimura, S. Large Specific Surface Area and Rigid Network of Nanocellulose Govern the Thermal Stability of Polymers: Mechanisms of Enhanced Thermomechanical Properties for Nanocellulose/PMMA Nanocomposite. *Materials Today Communications* **2018**, *16*, 105–110, doi:10.1016/j.mtcomm.2018.05.002.
156. Boujemaoui, A.; Ansari, F.; Berglund, L.A. Nanostructural Effects in High Cellulose Content Thermoplastic Nanocomposites with a Covalently Grafted Cellulose–Poly(Methyl Methacrylate) Interface. *Biomacromolecules* **2019**, *20*, 598–607, doi:10.1021/acs.biomac.8b00701.
157. Fahma, F.; Hori, N.; Iwata, T.; Takemura, A. The Morphology and Properties of Poly(Methyl Methacrylate)-Cellulose Nanocomposites Prepared by Immersion Precipitation Method. *J. Appl. Polym. Sci.* **2012**, n/a-n/a, doi:10.1002/app.38312.

158. Kim, D.W.; Shin, J.; Choi, S.Q. Nano-Dispersed Cellulose Nanofibrils-PMMA Composite from Pickering Emulsion with Tunable Interfacial Tensions. *Carbohydrate Polymers* **2020**, *247*, 116762, doi:10.1016/j.carbpol.2020.116762.
159. Sain, S.; Sengupta, S.; Ray, D.; Kar, A.; Mukhopadhyay, A. Cellulose Nanofiber Reinforced Ecofriendly Green PMMA Nanocomposites. *AMR* **2013**, *747*, 387–390, doi:10.4028/www.scientific.net/AMR.747.387.
160. Zoller, A.; Gigmes, D.; Guillaneuf, Y. Simulation of Radical Polymerization of Methyl Methacrylate at Room Temperature Using a Tertiary Amine/BPO Initiating System. *Polym. Chem.* **2015**, *6*, 5719–5727, doi:10.1039/C5PY00229J.
161. Kim, C.-H.; Kim, H.-T.; Park, J.-K.; Moon, S.-I.; Yoon, M.-S. Preparation and Ionic Conductivities of the Plasticized Polymer Electrolytes Based on Poly(Methyl Methacrylate-Co-Alkali Metal Methacrylate). *J. Polym. Sci. B Polym. Phys.* **1996**, *34*, 2709–2714, doi:10.1002/(SICI)1099-0488(19961130)34:16<2709::AID-POLB3>3.0.CO;2-K.
162. Kim, C.-H.; Park, J.-K.; Moon, S.-I.; Yoon, M.-S. Study on Ion Conduction Behavior of the Plasticized Polymer Electrolytes Based on Poly(Methylmethacrylate-Co-Alkali Metal Methacrylate) by FT-IR Spectroscopy. *Electrochimica Acta* **1998**, *43*, 1421–1427, doi:10.1016/S0013-4686(97)10078-0.
163. Roman, C.; García-Morales, M.; Eugenio, M.E.; Ibarra, D.; Martín-Sampedro, R.; Delgado, M.A. A Sustainable Methanol-Based Solvent Exchange Method to Produce Nanocellulose-Based Ecofriendly Lubricants. *Journal of Cleaner Production* **2021**, *319*, 128673, doi:10.1016/j.jclepro.2021.128673.
164. Zhang, L.; Ruesch, M.; Zhang, X.; Bai, Z.; Liu, L. Tuning Thermal Conductivity of Crystalline Polymer Nanofibers by Interchain Hydrogen Bonding. *RSC Adv.* **2015**, *5*, 87981–87986, doi:10.1039/C5RA18519J.
165. Liu, J.; Yang, R. Length-Dependent Thermal Conductivity of Single Extended Polymer Chains. *Phys. Rev. B* **2012**, *86*, 104307, doi:10.1103/PhysRevB.86.104307.
166. Eisenberg, A.; Hird, B.; Moore, R.B. A New Multiplet-Cluster Model for the Morphology of Random Ionomers. *Macromolecules* **1990**, *23*, 4098–4107, doi:10.1021/ma00220a012.
167. Cherfi, A.; Févotte, G. On-Line Conversion Monitoring of the Solution Polymerization of Methyl Methacrylate Using near-Infrared Spectroscopy. *Macromol. Chem. Phys.* **2002**, *203*, 1188, doi:10.1002/1521-3935(200206)203:9<1188::AID-MACP1188>3.0.CO;2-N.
168. Gong, M.; Zhang, D.; Zhang, J.; Li, J.; Chen, X. Optimization of Initiator Contents in Room Temperature Polymerization of Methyl Methacrylate. *Polymers and Polymer Composites* **2022**, *30*, 096739112211432, doi:10.1177/09673911221143201.
169. Gyurova, A.Y.; Halacheva, S.; Mileva, E. Aqueous Solutions of Random Poly(Methyl Methacrylate-Co-Acrylic Acid): Effect of the Acrylic Acid Content. *RSC Adv.* **2017**, *7*, 13372–13382, doi:10.1039/C7RA00180K.
170. Slobodian, P.; Svoboda, P.; Riha, P.; Boruta, R.; Saha, P. Synthesis of PMMA-Co-PMAA Copolymer Brush on Multi-Wall Carbon Nanotubes. *JSEMAT* **2012**, *02*, 221–226, doi:10.4236/jsemat.2012.223034.
171. Ahamad Said, M.N.; Hasbullah, N.A.; Rosdi, M.R.H.; Musa, M.S.; Rusli, A.; Ariffin, A.; Shafiq, M.D. Polymerization and Applications of Poly(Methyl

Methacrylate)–Graphene Oxide Nanocomposites: A Review. *ACS Omega* **2022**, *7*, 47490–47503, doi:10.1021/acsomega.2c04483.
172. Shrivastava, A. Polymerization. In *Introduction to Plastics Engineering*; Elsevier, **2018**; pp. 17–48 ISBN 978-0-323-39500-7.
173. Hmayed, A.A.R.; Norsic, S.; Monteil, V.; Raynaud, J. Ethylene Free Radical Polymerization in Supercritical Ethylene/CO_2 Mixture. *Polym. Chem.* **2020**, *11*, 1001–1009, doi:10.1039/C9PY00976K.
174. Denisov, E.T.; Denisova, T.G.; Pokidova, T.S. *Handbook of Free Radical Initiators*; Wiley-Interscience: Hoboken, N.J, **2003**; ISBN 978-0-471-20753-5.
175. Libnau, F.O.; Kvalheim, O.M.; Christy, A.A.; Toft, J. Spectra of Water in the Near- and Mid-Infrared Region. *Vibrational Spectroscopy* **1994**, *7*, 243–254, doi:10.1016/0924-2031(94)85014-3.
176. Otsuka, M.; Kato, F.; Matsuda, Y. Comparative Evaluation of the Degree of Indomethacin Crystallinity by Chemoinfometrical Fourie-Transformed near-Infrared Spectroscopy and Conventional Powder X-Ray Diffractiometry. *AAPS PharmSci* **2000**, *2*, 80–87, doi:10.1208/ps020109.
177. Martin, J.L. Kinetic Analysis of Two DSC Peaks in the Curing of an Unsaturated Polyester Resin Catalyzed with Methylethylketone Peroxide and Cobalt Octoate. *Polym. Eng. Sci.* **2007**, *47*, 62–70, doi:10.1002/pen.20667.
178. Guo, R.; Wang, Y.; Qi, Y.; Talma, A.G.; Zhang, J. Initiation Mechanisms of Styrene with Methyl Ethyl Ketone Peroxide-Cobalt System. *Macromol. Res.* **2018**, *26*, 680–689, doi:10.1007/s13233-018-6103-3.
179. Cousinet, S.; Ghadban, A.; Fleury, E.; Lortie, F.; Pascault, J.-P.; Portinha, D. Toward Replacement of Styrene by Bio-Based Methacrylates in Unsaturated Polyester Resins. *European Polymer Journal* **2015**, *67*, 539–550, doi:10.1016/j.eurpolymj.2015.02.016.
180. Cho, H.H.; Kim, S.H.; Heo, J.H.; Moon, Y.E.; Choi, Y.H.; Lim, D.C.; Han, K.-H.; Lee, J.H. A One-Step Colorimetric Acid–Base Titration Sensor Using a Complementary Color Changing Coordination System. *Analyst* **2016**, *141*, 3890–3897, doi:10.1039/C6AN00744A.
181. Klesper, E.; Johnsen, A.; Gronski, W.; Wehrli, F.W. Evaluation of Triads in Methyl Methacrylate/Methacrilic Acid Copolymers by 1H-NMR in Different Solvents and 13C-NMR. *Makromol. Chem.* **1975**, *176*, 1071–1119, doi:10.1002/macp.1975.021760418.
182. Krul', L.P.; Yakimtsova, L.B.; Egorova, E.L.; Matusevich, Yu.I.; Selevich, K.A.; Kurtikova, A.L. Preparation and Thermal Degradation of Methyl Methacrylate-Methacrylic Acid Copolymers. *Russ J Appl Chem* **2009**, *82*, 1636–1643, doi:10.1134/S1070427209090237.
183. Zhang, Z.; Zhang, W.; Zhu, X.; Cheng, Z.; Zhu, J. "Living"/Controlled Free Radical Polymerization of MMA in the Presence of Cobalt(II) 2-Ethylhexanoate: A Switch from RAFT to ATRP Mechanism. *J. Polym. Sci. A Polym. Chem.* **2007**, *45*, 5722–5730, doi:10.1002/pola.22320.
184. Chaiken, R.F.; Andersen, W.H.; Barsh, M.K.; Mishuck, E.; Moe, G.; Schultz, R.D. Kinetics of the Surface Degradation of Polymethylmethacrylate. *The Journal of Chemical Physics* **1960**, *32*, 141–146, doi:10.1063/1.1700888.
185. Kashiwagi, T.; Inaba, A.; Hatada, K.; Kitayama, T. Effects of Weak Linkages on the Thermal and Oxidative Degradation of Poly(Methyl Methacrylates). *Macromolecules* **1986**, *19*.
186. Suresh, S.S.; Mohanty, S.; Nayak, S.K. Investigation into the Mechanical and Thermal Properties of Poly(Methyl Methacrylate) Recovered from Light

Guidance Panels with a Focus on Future Remanufacturing and Sustainable Waste Management. *Jnl Remanufactur* **2017**, *7*, 217–233, doi:10.1007/s13243-017-0041-7.
187. Song, J.; Fischer, Ch.-H.; Schnabel, W. Thermal Oxidative Degradation of Poly(Methyl Methacrylate). *Polymer Degradation and Stability* **1992**, *36*, 261–266, doi:10.1016/0141-3910(92)90065-D.
188. Hatada, K.; Kitayama, T.; Fujimoto, N.; Nishiura, T. Stability and Degradation of Polymethacrylates with Controlled Structure. *Journal of Macromolecular Science, Part A* **1993**, *30*, 645–667, doi:10.1080/10601329308021252.
189. Jamieson, A.; McNeill, I.C. The Thermal Degradation of Copolymers of Methyl Methacrylate with Methacrylic Acid. *European Polymer Journal* **1974**, *10*, 217–225, doi:10.1016/0014-3057(74)90089-5.
190. Lazzari, M.; Kitayama, T.; He, S.; Hatada, K.; Chiantore, O. The Effect of Stereoregularity on the Thermal Behavior of Poly(Methacrylic Acid)s: I. Thermal Analysis Studies. *Polymer Bulletin* **1997**, *39*, 85–91, doi:10.1007/s002890050124.
191. Sayyah, S.M. Infrared Spectroscopic Studies on Some Thermally Degraded Poly(Methyl Methacrylate) Doped with N,N,N′,N′- Tetraoxaloyl Para Sulphanilamide. *Egypt. J. Chem.* **2012**, *55*, 603–623, doi:10.21608/ejchem.2012.1176.
192. Max, J.-J.; Chapados, C. Isotope Effects in Liquid Water by Infrared Spectroscopy. IV. No Free OH Groups in Liquid Water. *The Journal of Chemical Physics* **2010**, *133*, 164509, doi:10.1063/1.3505321.
193. Brostow, W.; Chiu, R.; Kalogeras, I.M.; Vassilikou-Dova, A. Prediction of Glass Transition Temperatures: Binary Blends and Copolymers. *Materials Letters* **2008**, *62*, 3152–3155, doi:10.1016/j.matlet.2008.02.008.
194. Penzel, E.; Rieger, J.; Schneider, H.A. The Glass Transition Temperature of Random Copolymers: 1. Experimental Data and the Gordon-Taylor Equation. *Polymer* **1997**, *38*, 325–337, doi:10.1016/S0032-3861(96)00521-6.
195. Weng, L.; Vijayaraghavan, R.; MacFarlane, D.R.; Elliott, G.D. Application of the Kwei Equation to Model the Tg Behavior of Binary Blends of Sugars and Salts. *Cryobiology* **2014**, *68*, 155–158, doi:10.1016/j.cryobiol.2013.12.005.
196. Wu, P.-P.; Zhao, D.-M.; Li, L.-X.; Wang, H.-S.; Liu, G.-D. Preparation of Blends of Poly(Methyl Methacrylate) Copolymers with High Glass Transition Temperatures and Low Hydrophilicity. *Polym Eng Sci* **2013**, *53*, 2370–2377, doi:10.1002/pen.23502.
197. Gatica, N.; Alvarado, N.; Sepúlveda, D. Blends of Poly(Methyl Methacrylate-Co-Methacrylic Acid) and Two Dihydric Phenols: Thermal and Infrared Spectroscopic Studies. *J. Chil. Chem. Soc.* **2006**, *51*, doi:10.4067/S0717-97072006000300003.
198. Spencer, M.W.; Wetzel, M.D.; Troeltzsch, C.; Paul, D.R. Effects of Acid Neutralization on the Properties of K+ and Na+poly(Ethylene-Co-Methacrylic Acid) Ionomers. *Polymer* **2012**, *53*, 569–580, doi:10.1016/j.polymer.2011.12.013.
199. Kim, S.-H.; Kim, J.-S. Relationships between the Glass Transition Temperatures and the Type of Cations in Poly(Ethyl Acrylate) Ionomers. *Macromolecules* **2003**, *36*, 2382–2386, doi:10.1021/ma021744v.
200. Vargün, E.; Sankir, M.; Aran, B.; Sankir, N.D.; Usanmaz, A. Synthesis and Characterization of 2-Hydroxyethyl Methacrylate (HEMA) and Methyl Methacrylate (MMA) Copolymer Used as Biomaterial. *Journal of*

Macromolecular Science, Part A **2010**, *47*, 235–240, doi:10.1080/10601320903526998.
201. Doğanci, E.; Gorur, M. Synthesis, Characterization, and Chemosensing Application of Poly(Methyl Methacrylate-Co-Hydroxyethyl Methacrylate) with Dansyl Side Group. *J. Turk. Chem. Soc., Sect. A: Chem.* **2016**, *3*, 565, doi:10.18596/jotcsa.28202.
202. Demirelli, K.; Coşkun, M.; Kaya, E. A Detailed Study of Thermal Degradation of Poly(2-Hydroxyethyl Methacrylate). *Polymer Degradation and Stability* **2001**, *72*, 75–80, doi:10.1016/S0141-3910(00)00204-4.
203. Achilias, D.; Siafaka, P. Polymerization Kinetics of Poly(2-Hydroxyethyl Methacrylate) Hydrogels and Nanocomposite Materials. *Processes* **2017**, *5*, 21, doi:10.3390/pr5020021.
204. North, S.M.; Armes, S.P. One-Pot Synthesis and Aqueous Solution Properties of PH-Responsive Schizophrenic Diblock Copolymer Nanoparticles Prepared *via* RAFT Aqueous Dispersion Polymerization. *Polym. Chem.* **2021**, *12*, 5842–5850, doi:10.1039/D1PY01114F.
205. McNeill, I.C.; Mohammed, M.H. A Comparison of the Thermal Degradation Behaviour of Ethylene-Ethyl Acrylate Copolymer, Low Density Polyethylene and Poly(Ethyl Acrylate). *Polymer Degradation and Stability* **1995**, *48*, 175–187, doi:10.1016/0141-3910(95)00030-P.
206. Kim, D.; Kim, S.; Jo, S.; Woo, J.; Noh, I. Effect of Cross-Linking Spacers on Biocompatibility of Chitosan-Spacer-Poly(Ethylene Oxide) Hydrogel. *Macromol. Res.* **2011**, *19*, 573–581, doi:10.1007/s13233-011-0606-5.
207. Voorhaar, L. High-Throughput Polymer Synthesis for Supramolecular Materials, Universiteit Gent.
208. Dai, Z.; Wang, G.; Liu, L.; Hou, Y.; Wei, Y.; Zhang, Z. Mechanical Behavior and Properties of Hydrogen Bonded Graphene/Polymer Nano-Interfaces. *Composites Science and Technology* **2016**, *136*, 1–9, doi:10.1016/j.compscitech.2016.09.005.
209. Ren, J.; Yu, D. Effects of Enhanced Hydrogen Bonding on the Mechanical Properties of Poly (Vinyl Alcohol)/Carbon Nanotubes Nanocomposites. *Composite Interfaces* **2018**, *25*, 205–219, doi:10.1080/09276440.2017.1356099.
210. Neikirk, C.C.; Chung, J.W.; Priestley, R.D. Thermomechanical Behavior of Hydrogen-Bond Based Supramolecular Poly(ε-Caprolactone)-Silica Nanocomposites. *RSC Adv.* **2013**, *3*, 16686, doi:10.1039/c3ra42031k.
211. Reichardt, C. Empirical Parameters of Solvent Polarity as Linear Free-Energy Relationships. *Angew. Chem. Int. Ed. Engl.* **1979**, *18*, 98–110, doi:10.1002/anie.197900981.
212. Míguez, J.M.; Piñeiro, M.M.; Algaba, J.; Mendiboure, B.; Torré, J.P.; Blas, F.J. Understanding the Phase Behavior of Tetrahydrofuran + Carbon Dioxide, + Methane, and + Water Binary Mixtures from the SAFT-VR Approach. *J. Phys. Chem. B* **2015**, *119*, 14288–14302, doi:10.1021/acs.jpcb.5b07845.
213. Matsuda, H.; Kamihama, N.; Kurihara, K.; Tochigi, K.; Yokoyama, K. Measurement of Isobaric Vapor-Liquid Equilibria for Binary Systems Containing Tetrahydrofuran Using an Automatic Apparatus. *J. Chem. Eng. Japan / JCEJ* **2011**, *44*, 131–139, doi:10.1252/jcej.10we162.
214. Krug, J.; Palm, C. Separation of a Mixture of Methanol and Tetrahydrofuran into Its Constituents (U.S. Patent No. 5559254A) **1996**.
215. Babij, N.R.; McCusker, E.O.; Whiteker, G.T.; Canturk, B.; Choy, N.; Creemer, L.C.; Amicis, C.V.D.; Hewlett, N.M.; Johnson, P.L.; Knobelsdorf,

J.A.; et al. NMR Chemical Shifts of Trace Impurities: Industrially Preferred Solvents Used in Process and Green Chemistry. *Org. Process Res. Dev.* **2016**, *20*, 661–667, doi:10.1021/acs.oprd.5b00417.
216. Wulandari, W.T.; Rochliadi, A.; Arcana, I.M. Nanocellulose Prepared by Acid Hydrolysis of Isolated Cellulose from Sugarcane Bagasse. *IOP Conf. Ser.: Mater. Sci. Eng.* **2016**, *107*, 012045, doi:10.1088/1757-899X/107/1/012045.
217. Liu, W.; Zhang, L. Mechanisms of the Complex Thermo-Mechanical Behavior of Polymer Glass Across a Wide Range of Temperature Variations. *Polymers* **2018**, *10*, 1153, doi:10.3390/polym10101153.
218. Halary, J.L. *Polymer Materials : Macroscopic Properties and Molecular Interpretations*; John Wiley & Sons, **2011**;
219. Teixeira, S.S.; Dias, C.J.; Dionisio, M.; Costa, L.C. New Method to Analyze Dielectric Relaxation Processes: A Study on Polymethacrylate Series: New Method to Analyze Dielectric Relaxation Processes. *Polym. Int.* **2013**, *62*, 1744–1749, doi:10.1002/pi.4479.
220. Ceccorulli, G.; Pizzoli, M. Effect of Water on the Relaxation Spectrum of Poly(Methylmethacrylate). *Polymer Bulletin* **2001**, *47*, 283–289, doi:10.1007/s289-001-8183-9.
221. Muisener, P.A.O.; Clayton, L.; D'Angelo, J.; Harmon, J.P.; Sikder, A.K.; Kumar, A.; Cassell, A.M.; Meyyappan, M. Effects of Gamma Radiation on Poly(Methyl Methacrylate)/Single-Wall Nanotube Composites. *J. Mater. Res.* **2002**, *17*, 2507–2513, doi:10.1557/JMR.2002.0365.
222. Namouchi, F.; Jilani, W.; Guermazi, H. Thermally Stimulated Depolarization Current and Dielectric Spectroscopy Used to Study Dipolar Relaxations and Trap Level Distribution in PMMA Polymer. *Journal of Non-Crystalline Solids* **2015**, *427*, 76–82, doi:10.1016/j.jnoncrysol.2015.07.004.
223. Kalogeras, I.M. Contradicting Perturbations of the Segmental and Secondary Relaxation Dynamics of Polymer Strands Constrained in Nanopores. *Acta Materialia* **2005**, *53*, 1621–1630, doi:10.1016/j.actamat.2004.12.012.
224. Wypych, A.; Duval, E.; Boiteux, G.; Ulanski, J.; David, L.; Mermet, A. Effect of Physical Aging on Nano- and Macroscopic Properties of Poly(Methyl Methacrylate) Glass. *Polymer* **2005**, *46*, 12523–12531, doi:10.1016/j.polymer.2005.10.116.
225. Vassilikou-Dova, A.; Kalogeras, I.M. Dielectric Analysis (DEA). In *Thermal Analysis of Polymers*; Menczel, J.D., Prime, R.B., Eds.; Wiley, **2009**; pp. 497–613 ISBN 978-0-471-76917-0.
226. Ionita, D.; Cristea, M.; Banabic, D. Viscoelastic Behavior of PMMA in Relation to Deformation Mode. *J Therm Anal Calorim* **2015**, *120*, 1775–1783, doi:10.1007/s10973-015-4558-4.
227. Wypych-Puszkarz, A.; Cetinkaya, O.; Yan, J.; Udovytska, R.; Jung, J.; Jenczyk, J.; Nowaczyk, G.; Jurga, S.; Ulański, J.; Matyjaszewski, K.; et al. Molecular Dynamics and Structure of Poly(Methyl Methacrylate) Chains Grafted from Barium Titanate Nanoparticles. *Molecules* **2022**, *27*, 6372, doi:10.3390/molecules27196372.
228. Mijovic, J.; Sy, J.-W.; Kwei, T.K. Reorientational Dynamics of Dipoles in Poly(Vinylidene Fluoride)/Poly(Methyl Methacrylate) (PVDF/PMMA) Blends by Dielectric Spectroscopy. *Macromolecules* **1997**, *30*, 3042–3050, doi:10.1021/ma961774w.
229. Dudognon, E.; Bernès, A.; Lacabanne, C. Nature of Molecular Mobility Through the Glass Transition in Poly(*n* -Alkyl Methacrylates): A Study by

Dielectric Spectroscopies. *Journal of Macromolecular Science, Part B* **2004**, *43*, 591–604, doi:10.1081/MB-120030008.
230. Li, C.; Wu, J.; Zhao, J.; Zhao, D.; Fan, Q. Effect of Inorganic Phase on Polymeric Relaxation Dynamics in PMMA/Silica Hybrids Studied by Dielectric Analysis. *European Polymer Journal* **2004**, *40*, 1807–1814, doi:10.1016/j.eurpolymj.2004.04.011.
231. Bergman, R.; Alvarez, F.; Alegría, A.; Colmenero, J. The Merging of the Dielectric α- and β-Relaxations in Poly-(Methyl Methacrylate). *The Journal of Chemical Physics* **1998**, *109*, 7546–7555, doi:10.1063/1.477376.
232. Volkov, A.S.; Koposov, G.D.; Perfil'ev, R.O.; Tyagunin, A.V. Analysis of Experimental Results by the Havriliak–Negami Model in Dielectric Spectroscopy. *Opt. Spectrosc.* **2018**, *124*, 202–205, doi:10.1134/S0030400X18020200.
233. Szabo, J.P.; Keough, I.A. Method for Analysis of Dynamic Mechanical Thermal Analysis Data Using the Havriliak–Negami Model. *Thermochimica Acta* **2002**, *392–393*, 1–12, doi:10.1016/S0040-6031(02)00064-3.
234. Comer, A.C.; Heilman, A.L.; Kalika, D.S. Dynamic Relaxation Characteristics of Polymer Nanocomposites Based on Poly(Ether Imide) and Poly(Methyl Methacrylate). *Polymer* **2010**, *51*, 5245–5254, doi:10.1016/j.polymer.2010.08.053.
235. Kolarík, J. Effect of Side Chain Concentration on the Intensity and Temperature of the Low-Temperature Dispersion of Polymethacrylate Copolymers. *Journal of Macromolecular Science, Part B* **1971**, *5*, 355–365, doi:10.1080/00222347108212542.
236. Kihira, Y.; Yamamura, H.; Murakami, I. Effect of Introducing Acrylic and Methacrylic Acid Groups on Molecular Relaxation of Poly(Ethyl Methacrylate). *J. Polym. Sci. B Polym. Phys.* **1986**, *24*, 867–876, doi:10.1002/polb.1986.090240412.
237. Jafarpour, G.; Dantras, E.; Boudet, A.; Lacabanne, C. Study of Dielectric Relaxations in Cellulose by Combined DDS and TSC. *Journal of Non-Crystalline Solids* **2007**, *353*, 4108–4115, doi:10.1016/j.jnoncrysol.2007.06.026.
238. Einfeldt, J.; Kwasniewski, A. Characterization of Different Types of Cellulose by Dielectric Spectroscopy. **2002**.
239. Angell, C.A. Why C1 = 16–17 in the WLF Equation Is Physical—and the Fragility of Polymers. *Polymer* **1997**, *38*, 6261–6266, doi:10.1016/S0032-3861(97)00201-2.
240. Arai, K.; Eisenberg, A. Dielectric Properties and Conductivity of Styrene-Methacrylic Acid Copolymers and Partially Neutralized Salts. *Journal of Macromolecular Science, Part B* **1980**, *17*, 803–832, doi:10.1080/00222348008212838.
241. Kihira, Y.; Yamamura, H.; Murakami, I. Effect of the Acid Dimer on the Alpha-Relaxation Process of the Methyl Methacrylate-Acrylic Acid Copolymer. *Makromol. Chem.* **1985**, *186*, 423–432, doi:10.1002/macp.1985.021860220.
242. Dupenne, D.; Roggero, A.; Dantras, E.; Lonjon, A.; Pierré, T.; Lacabanne, C. Dynamic Molecular Mobility of Polyurethane by a Broad Range Dielectric and Mechanical Analysis. *Journal of Non-Crystalline Solids* **2017**, *468*, 46–51, doi:10.1016/j.jnoncrysol.2017.04.022.

243. Stickel, F.; Fischer, E.W.; Richert, R. Dynamics of Glass-forming Liquids. I. Temperature-derivative Analysis of Dielectric Relaxation Data. *The Journal of Chemical Physics* **1995**, *102*, 6251–6257, doi:10.1063/1.469071.
244. Roggero, A.; Caussé, N.; Pébère, N.; Dantras, E. VFT to Arrhenius Crossover at the Dynamic Glass Transition of an Epoxy Network as Revealed by Dielectric Experiments in Continuous Immersion. *Polymer* **2022**, *241*, 124542, doi:10.1016/j.polymer.2022.124542.
245. Böhmer, R.; Ngai, K.L.; Angell, C.A.; Plazek, D.J. Nonexponential Relaxations in Strong and Fragile Glass Formers. *The Journal of Chemical Physics* **1993**, *99*, 4201–4209, doi:10.1063/1.466117.
246. Ghorbel, N.; Kallel, A.; Boufi, S. Molecular Dynamics of Poly(Vinyl Alcohol)/Cellulose Nanofibrils Nanocomposites Highlighted by Dielectric Relaxation Spectroscopy. *Composites Part A: Applied Science and Manufacturing* **2019**, *124*, 105465, doi:10.1016/j.compositesa.2019.05.033.
247. Jafarpour, G.; Dantras, E.; Boudet, A.; Lacabanne, C. Molecular Mobility of Poplar Cell Wall Polymers Studied by Dielectric Techniques. *Journal of Non-Crystalline Solids* **2008**, *354*, 3207–3214, doi:10.1016/j.jnoncrysol.2008.01.008.
248. Lum, S.K.; Duncan-Hewitt, W.C. A Comparison of Elastic Moduli Derived from Theory, Microindentation, and Ultrasonic Testing. *Pharm Res.* **1996**, *13*, 1739–1745, doi:10.1023/A:1016465412544.

Annexe

Résumé de la thèse en Français

État de l'art

Les polymères sont traditionnellement considérés comme des matériaux d'isolation thermique en raison de leur faible conductivité thermique apparente comprise entre 0,1 et 0,5 $W \cdot m^{-1} \cdot K^{-1}$. Il faut cependant considérer que les polymères ne sont pas intrinsèquement de mauvais conducteurs de chaleur. En fait, la faible conductivité thermique apparente résulte principalement de la dispersion fréquente des caloporteurs aux extrémités de la chaîne et des enchevêtrements. En effet, de nombreuses études ont été publiées faisant état d'une excellente conductivité thermique le long du squelette polymère encourageant la communauté scientifique à poursuivre les recherches dans ce domaine. Ce chapitre vise à donner un aperçu des connaissances actuelles concernant la conduction thermique dans les polymères et les principaux facteurs affectant cette propriété.

Transport thermique dans les polymères

La conductivité thermique peut être définie comme « la vitesse à laquelle la chaleur est transférée par conduction à travers une surface unitaire de section transversale d'un matériau, lorsqu'un gradient de température sort perpendiculairement à la zone ». La conductivité thermique est la somme des différentes contributions au transfert de chaleur dans le matériau, par exemple conduction électronique ou phononique. Les polymères étant généralement des isolants électriques, la principale contribution au transfert de chaleur est imputable à la propagation des modes vibrationnels dans le matériau. Le mécanisme à l'origine du transport thermique dans les matériaux polymères n'est pas encore entièrement compris et, étant donné leur structure amorphe, il n'est pas possible de décrire avec précision la vibration atomique sous forme de phonons. Une distinction importante doit être faite entre le transport thermique dans le domaine cristallin et la région amorphe ou les polymères. Dans les régions amorphes, la présence de multiples sites de diffusion (tels que des extrémités de chaîne, des enchevêtrements et des volume libre) détermine un libre parcours moyen des phonons plus court et une fréquence plus élevée d'événements de diffusion (Figure S1).

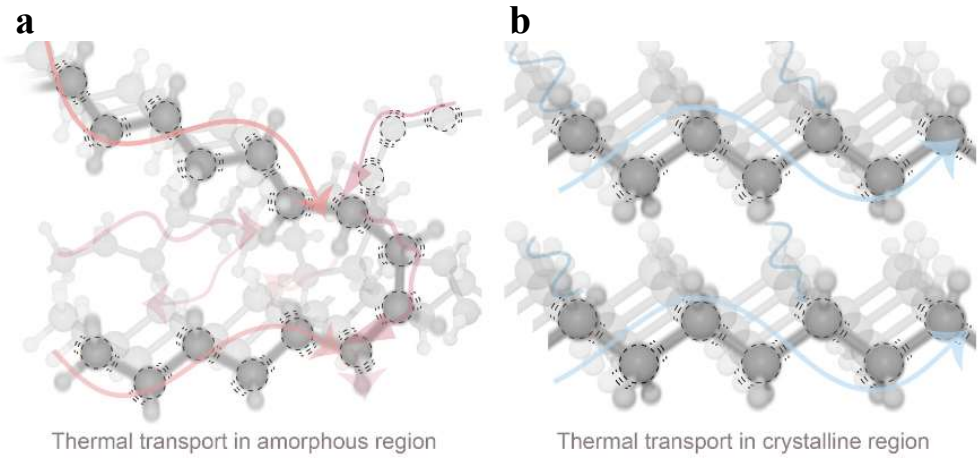


Figure S1. Transfert de chaleur au niveau moléculaire. Diffusion du caloporteur dans un polymère amorphe en raison de la présence de défauts et de désordres dans la structure (a). Conduction thermique efficace le long des chaînes dans les domaines cristallins (b). *Reprinted from Engineering polymers with metal-like thermal conductivity—Present status and future perspectives, 233, Guo Y., Zhou Y., Xu Y., 124168, Copyright (2021), with permission from Elsevier.*

Les techniques appliquées pour mesurer la conductivité thermique peuvent être regroupées en deux catégories principales (Figure S2) : les techniques en régime permanent et les techniques en régime non stationnaire (ou méthodes transitoires). Les méthodes en régime permanent sont basées sur des mesures effectuées dans un état d'équilibre thermique complet et un flux de chaleur constant établi à travers l'échantillon. Une de ses principales limites réside dans le fait qu'il est très sensible à la résistance thermique de contact (TCR) et aux pertes thermiques parasites qui peuvent affecter la mesure. Dans les techniques en régime non stationnaire, les propriétés thermiques du matériau sont mesurées lors d'un état transitoire d'échange thermique.

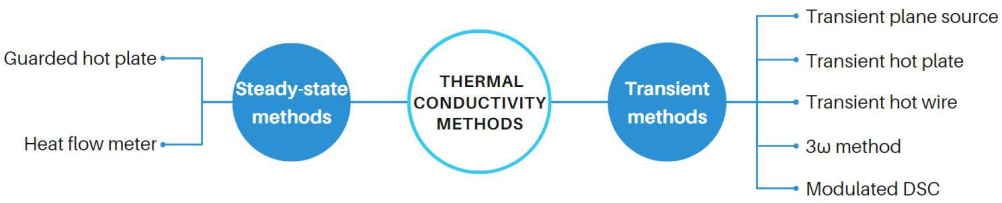


Figure S2. Classification des méthodes de mesure de la conductivité thermique.

La méthode de la source plane transitoire représente l'une des techniques les plus utilisées étant donné l'intervalle de travail le plus large en termes de conductivités thermiques mesurées. La source plane transitoire (TPS), également connue sous le nom d'analyseur à disque chaud ou sonde Gustafsson, est une technique expérimentale largement utilisée pour la détermination de la conductivité thermique et de la diffusivité. L'appareil (Figure S3) est constitué d'une source de tension constante (V), de deux voltmètres (V_1 et V_2), d'une résistance étalon ($R_{e,s}$) et d'un capteur avec sa propre résistance (R_e).

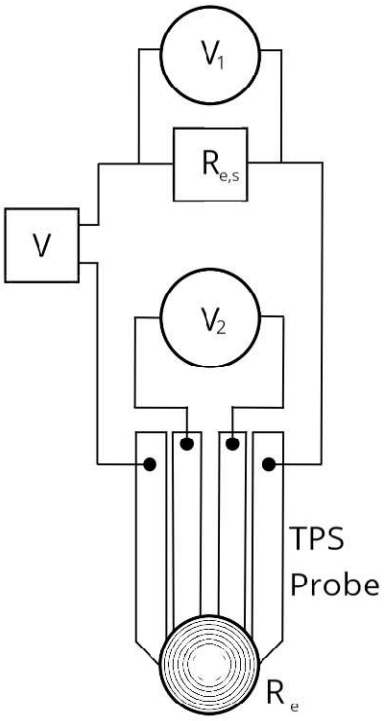


Figure S3. Schéma de l'appareil TPS.

Le capteur (Figure S4a) a une double nature : source de chaleur pour augmenter la température de l'échantillon et thermomètre à résistance afin d'enregistrer la dépendance temps-température. En effet, lors de la mesure, un courant constant est imposé dans la spirale déterminant une augmentation de température dépendante de la capacité thermique et de la conductivité thermique des deux échantillons en contact avec la sonde. Par conséquent, en enregistrant la variation de température du capteur et sa dépendance temporelle, les propriétés thermiques de l'échantillon peuvent être extraites.

La conductivité thermique de films minces de matériau isolant électrique peut être mesurée par la méthode TPS grâce à une variante de la méthode utilisée pour les échantillons épaisse. Cependant, afin d'obtenir des valeurs précises, certaines exigences doivent être respectées : la conductivité thermique de l'échantillon doit être inférieure à 2 $W \cdot m^{-1} \cdot K^{-1}$ et l'épaisseur du film doit être comprise entre 20 et 600 µm avec une valeur d'épaisseur connue avec une précision de 1 µm. La configuration de la mesure (Figure S4b) est constituée de la sonde placée entre deux films minces du matériau de test, puis prise en sandwich entre deux blocs cylindriques d'un matériau de fond thermoconducteur qui est généralement de l'acier inoxydable.

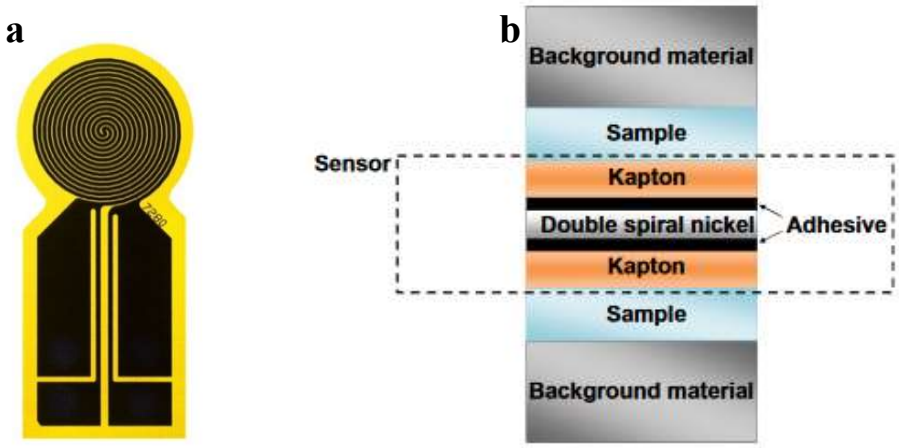


Figure S4. Capteur TPS conçu pour les méthodes à couches minces (a). Configuration schématique de la mesure de couches minces dans la technique TPS (b). *Reprinted from An improved transient plane source method for measuring thermal conductivity of thin films: Deconvoluting thermal contact resistance, 96, Ahadi M., Andisheh-Tadbir M., Tam M., Bahrami M., 371-380, Copyright (2016), with permission from Elsevier.*

Avant la mesure, l'installation est assemblée et laissée libre pour atteindre des conditions isothermes. La mesure est ensuite effectuée : un courant traverse la spirale de nickel entraînant une élévation de température, puis la résistance électrique est enregistrée et la conductivité thermique du film peut être extraite. Les paramètres de test doivent être choisis afin de garantir une différence de température à travers le film mince comprise entre 1 et 3 K.

Il a été reconnu que plusieurs facteurs jouent un rôle sur la conduction thermique (Figure S5), par exemple la masse molaire, la morphologie, l'orientation des chaînes principale et latérales, etc.

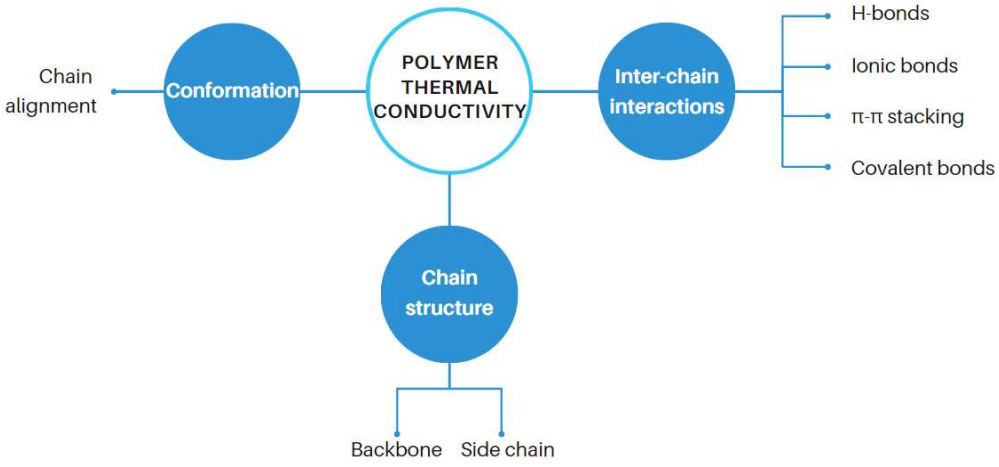


Figure S5. Facteurs physiques déterminant le mécanisme de conduction thermique dans les polymères.

La structure désordonnée typique d'un polymère amorphe provoque une localisation intense des modes vibrationnels responsables du transfert de chaleur entraînant une faible conduction thermique. Par conséquent, la possibilité d'agir sur l'orientation des chaînes afin d'augmenter l'ordre structurel est une voie. Dans les polymères amorphes, la faible conductivité thermique est principalement

attribuable aux pertes associées aux faibles interactions inter-chaînes et à la diffusion récurrente de phonons. Par conséquent, l'ajout de fortes interactions intermoléculaires à celles de vdW pourrait conduire à une augmentation de la conductivité thermique grâce à deux effets : 1/amélioration de la conductance thermique inter-chaînes, 2/raidissement de la chaîne et suppression conséquente de la rotation segmentaire conduisant à une diminution diffusion. Malgré la nécessité d'investigations plus approfondies, plusieurs études ont déjà largement démontré que l'augmentation des interactions inter-chaînes est bénéfique en termes de conduction thermique dans les polymères amorphes.

Les polyméthacrylates représentent une classe de matériaux utilisés dans divers domaines, par exemple implants biomédicaux, applications électroniques, etc. Leurs propriétés physiques et chimiques peuvent fortement varier selon la nature des substituants de la chaîne latérale. De plus, la présence du groupe α-méthyle directement lié sur la chaîne principale empêche la cristallisation et la libre rotation autour du squelette C-C conduisant à une structure amorphe. L'ester de l'acide polyméthacrylique (PMAA), le polyméthylméthacrylate (PMMA), est actuellement le polymère méthacrylate le plus utilisé grâce à la combinaison de ses propriétés physiques et chimiques. L'absence de phase cristalline, qui présente une contribution supplémentaire distincte, permet d'isoler plus facilement la contribution d'un seul facteur, à savoir l'introduction de groupements formant des liaisons H ou de renforts.

Polymères nanocomposites pour des propriétés modulables

Les matériaux nanocomposites ont été intensivement étudiés au cours des dernières décennies grâce à leur combinaison prometteuse de propriétés finales et à la possibilité d'être proposés pour un large éventail d'applications, par ex. électronique, automobile, applications médicales, etc. De plus, il a été rapporté que l'ajout de nanoparticules dans des matrices polymères améliore diverses propriétés, telles que la résistance à la traction, la stabilité thermique, la résistance chimique, la conductivité thermique ou électrique. La réalisation d'une dispersion appropriée des nanocharges est essentielle afin de tirer parti du potentiel des nanoparticules. Pour cette raison, la méthode de préparation doit être soigneusement sélectionnée en fonction de l'aptitude à la transformation de la matrice, du type de nanoparticules à disperser et des propriétés finales souhaitées.

La préparation de nanocomposites s'est avérée une stratégie prometteuse afin d'améliorer la conductivité thermique des polymères grâce à l'ajout d'une charge thermoconductrice. Il est important de garder à l'esprit que la conductivité thermique du nanocomposite dépendra non seulement de la conductivité intrinsèque des composants, mais également de plusieurs facteurs tels que la quantité de charge, son état de dispersion et les interactions matrice/charge. De plus, la variation de la concentration des nanoparticules a également une influence sur la possibilité de former un réseau pendant de nanoparticules qui affecte de manière significative sur le transport thermique dans le matériau. Pour toutes ces raisons, la description d'un

modèle théorique capable de prédire efficacement la valeur finale de la conductivité thermique reste un défi.

Outre les nanoparticules traditionnellement proposées (métalliques ou céramiques) dans la conception de nanocomposites thermoconducteurs, la possibilité d'améliorer la conductivité thermique dans les nanocomposites entièrement organiques suscite une attention croissante. Entre autres, les nanocharges à base de cellulose ont été identifiées comme des charges thermoconductrices prometteuses en raison de leur structure cristalline formée de molécules de cellulose alignées unidirectionnellement formant une structure fortement tassée grâce à la formation de liaisons H.

La cellulose est un polymère d'origine biologique dérivé de ressources abondantes et renouvelables, qui a attiré une attention considérable au cours de la dernière décennie grâce à sa combinaison de propriétés uniques, notamment d'excellentes propriétés mécaniques et thermiques et une chimie de surface polyvalente. Les nanoparticules de cellulose représentent une option fascinante pour la préparation de composites « tout polymère ». Malheureusement, le traitement des fibres cellulosiques et en particulier de la nanocellulose est extrêmement difficile, en raison de fortes interactions secondaires entraînant une mauvaise compatibilité avec les polymères thermoplastiques conventionnels considérés comme matrice. La fonctionnalisation chimique de la cellulose ou l'utilisation d'agents compatibilisant peuvent être envisagées pour améliorer les interactions avec le polymère et réduire les auto-interactions (Figure S6). Malgré la nécessité de prétraitements, l'ajout de CNF a été rapporté pour différents objectifs : propriétés mécaniques améliorées, stabilité thermique plus élevée et propriétés de barrière aux gaz élevées. En outre, l'effet des nanoparticules de cellulose sur la conductivité thermique a commencé à être étudié et différentes études ont rapporté un impact positif sur la conduction thermique suite à l'ajout de CNF.

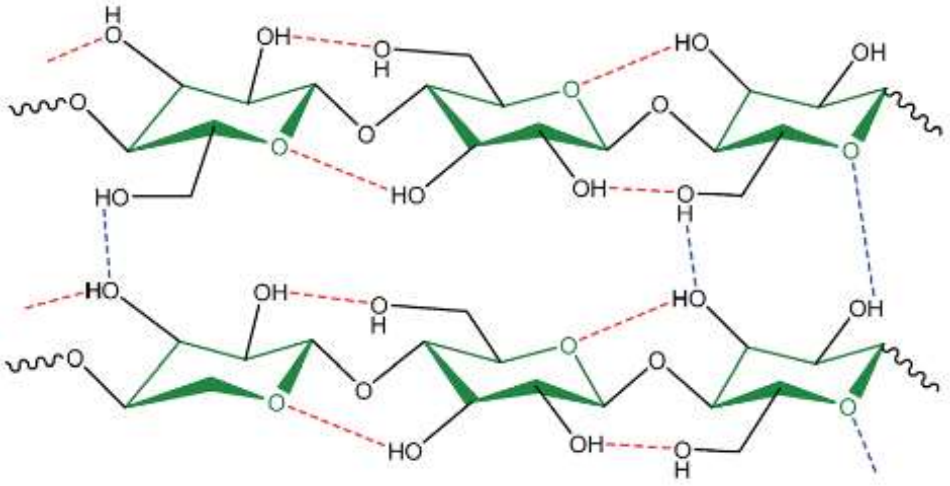


Figure S6. Liaison H intra et inter-chaînes dans la structure cellulosique. *Reproduced from Ref. [107] with permission from the Royal Society of Chemistry.*

Diverses études ont été rapportées sur la préparation de composites à base de nanocellulose à l'aide d'une matrice méthacrylique. L'objectif principal de ces études était l'impact de l'ajout de nanoparticules de cellulose sur les propriétés mécaniques, optiques et thermiques des nanocomposites à base de méthacrylate. Concernant les propriétés thermiques, les résultats rapportés se réfèrent exclusivement à la stabilité thermique et à la modification de la T_g. Au début de cet état de l'art de thèse, les résultats sur la conductivité thermique dans les nanocomposites CNF à base de méthacrylate n'ont pas encore été rapportés.

Matériels et méthodes

Dans le présent travail, il y a une tentative de modulation de la conduite thermique dans les polymères améliorés en intégrant les interactions intramoléculaires. Le PMMA a servi de modèle, grâce à la possibilité de copolymériser facilement le MMA avec divers comonomères. L'ajout d'interactions de liaisons H intermoléculaires avec quel vdW est à l'origine de l'ajout de groupes d'acide carbossilique dans la chaîne en faisant la copolymérisation de MMA avec MAA. Nous avons exploré divers rapports MMA:MAA pour personnaliser la quantité de droits H introduits et trouvés une corrélation avec leur contenu et la conduite thermique finale affichée par le copolymère.

Ensuite, un processus de neutralisation a été mis en place afin de remplacer les liaisons H par des interactions inter-chaînes plus fortes, c'est-à-dire des liaisons ioniques, dans le copolymère à plus forte teneur en groupes -COOH. Des films de PMMA et de PMMA-*co*-MAA vierges et de PMMA-*co*-MAA neutralisés au sodium ont été préparés par des techniques de coulée au solvant et utilisés pour effectuer des mesures de conductivité thermique sur des films minces.

À un stade ultérieur, le comonomère MAA a été remplacé par de nouveaux comonomères (méthacrylate de 2-hydroxyéthyle HEMA et acrylate de 2-carboxyéthyle CEA) afin d'évaluer l'impact d'une flexibilité de chaîne plus élevée lorsque des liaisons H intermoléculaires étaient présentes. De plus, dans le PMMA-*co*-CEA, l'effet d'une flexibilité plus élevée a également été évalué sur le copolymère neutralisé ayant la teneur la plus élevée en CEA.

Dans un deuxième temps, le PMMA-*co*-MAA ayant la teneur en MAA la plus élevée (30 % en poids) a été sélectionné pour la préparation d'un nanocomposite entièrement organique avec ajout de CNF. La dispersion des nanofibres a été réalisée en solution dans un mélange de solvants et des films nanocomposites contenant différentes quantités de CNF (5, 10 et 15 % en poids) ont été obtenus par coulée de solvant. La dispersion a été évaluée dans des films à partir de différents mélanges de solvants. Ensuite, la variation de la mobilité macromoléculaire et de la conductivité thermique a été étudiée pour les différentes teneurs en CNF.

Copolymères acrylate pour améliorer les interactions

La corrélation entre la force des interactions intermoléculaires et les propriétés physiques a été largement rapportée dans la littérature, comme indiqué précédemment. En particulier, en se concentrant sur la conduction thermique dans les polymères amorphes, l'ajout d'interactions plus fortes à des interactions vdW faibles pourrait conduire à la réalisation d'un réseau thermique continu résultant d'une augmentation de la conductivité thermique. Il apparaît que dans les polymères amorphes, un facteur qui joue un rôle essentiel dans la détermination de la valeur finale de la conductivité thermique est la force des interactions intermoléculaires, d'autant plus que les faibles valeurs de conductivité thermique ne sont pas le résultat d'une mauvaise conduction le long du squelette du polymère mais résultent principalement de diffusion de phonons.

Sur la base de ces résultats, dans le présent travail, une tentative d'adaptation de la conductivité thermique dans les polymères amorphes a été réalisée par l'ingénierie d'interactions intramoléculaires. Dans cette étude, le PMMA a été sélectionné comme modèle amorphe grâce à sa chimie bien connue qui permet un contrôle aisé des interactions entre chaînes macromoléculaires. L'introduction de fragments formant H dans la structure a été réalisée grâce à la copolymérisation du MMA avec un comonomère (MAA) comportant des groupes -COOH (Figure S7). De plus, la copolymérisation du MMA et du MAA dans différents rapports permet de faire varier la quantité de liaisons H introduites dans la chaîne et de définir une relation entre la teneur en liaisons H et les propriétés finales du copolymère. Par ailleurs, la possibilité de neutraliser le groupe -COOH conduisant à l'introduction d'interactions ioniques (Figure S7), où les cations peuvent former des multiplets qui agissent comme agent de réticulation, permet d'explorer l'effet d'interactions intermoléculaires plus fortes sur la conduction thermique. Dans le même temps, les unités -COOH restantes pourraient préserver les interactions de liaison H observées dans le copolymère vierge. À un stade ultérieur, les comonomères MAA ont été remplacés par différents comonomères (Figure S7) et l'impact de la flexibilité de la chaîne lorsque des liaisons H intermoléculaires sont présentes a été évalué. Les deux comonomères choisis se caractérisent par l'existence d'un groupe hydroxyle et d'un groupe acide carboxylique en extrémité d'une chaîne latérale éthyle, respectivement pour HEMA et CEA.

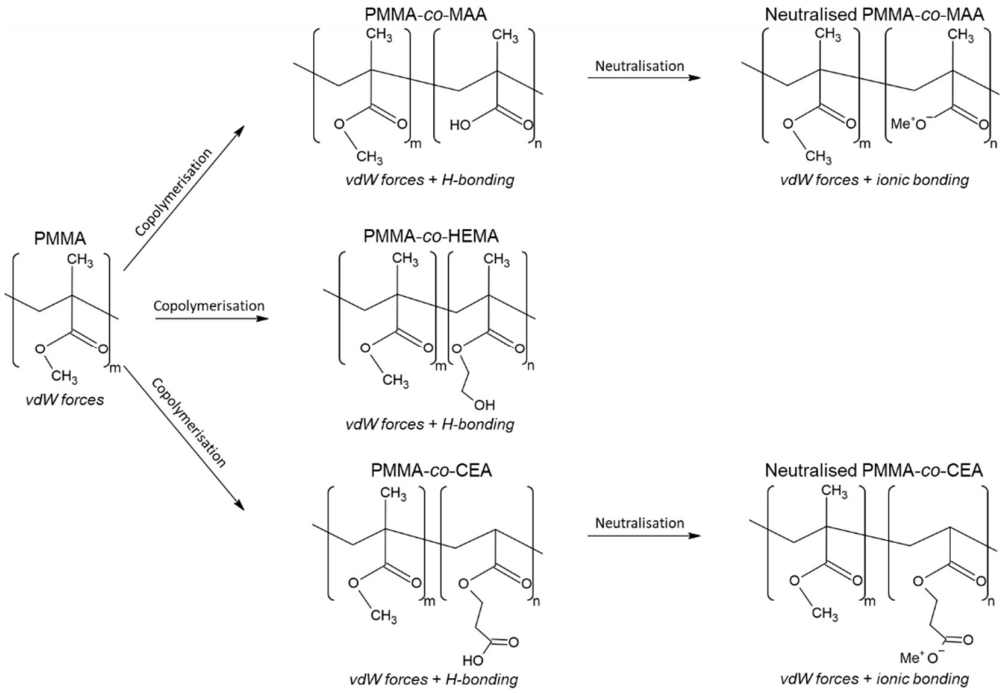


Figure S7. Evolution de la structure corrélée à l'introduction de liaisons H et de liaisons ioniques dans la macromolécule.

Copolymères MMA-MAA

La polymérisation radicalaire en masse a été sélectionnée pour la synthèse de ces nouveaux matériaux et trois méthodes différentes caractérisées par un mécanisme d'initiation différent seront présentées.

Dans une première tentative, le PMMA a été polymérisé grâce à un procédé d'activation thermique utilisant une formulation simple constituée du monomère et d'un initiateur de peroxyde de diacyle (formule générale $R_1C(O)OOC(O)R_2$, BPO) présent en deux teneurs différentes, 0,13 et 0,30 % en mole. Quelle que soit la quantité de peroxyde utilisée dans la formulation, les échantillons présentent une structure très poreuse inadaptée aux caractérisations physique. De plus, comme attendu, dans le réacteur ouvert utilisé, l'évaporation des monomères s'est produite en compétition avec la polymérisation. En effet, la perte de masse lors de la polymérisation a été calculée égale à 55 %.

La deuxième tentative a été réalisée avec une polymérisation à température ambiante grâce à une activation redox peroxyde/amine. La perte de masse pendant la polymérisation a été réduite avec succès et s'est avérée égale à 4,5 %. Cependant, les échantillons présentent certains défauts liés au retrait de la formulation lors de la polymérisation. Afin de mieux contrôler la réaction, une formulation plus complexe a ensuite été étudiée.

Enfin, le PMMA a été polymérisé par polymérisation radicalaire contrôlé par le cobalt qui est activée thermiquement par la décomposition d'une molécule de peroxyde, le MEKP. Le MEKP catalysé par le 2-éthylhexanoate de Cobalt(II) (MEKP/Co^{2+}) représente l'un des initiateurs les plus utilisés notamment dans les polyesters insaturés. Dans ce système, les principaux radicaux formés globalement

à partir du système initiateur MEKP/Co^{2+} sont les radicaux méthyle, éthyle et hydroxyle, qui seront les espèces responsables de l'activation de la polymérisation.

Le PMMA synthétisé entre des plaques de verre suivant un profil de température de 2h à 55°C et 2h à 80°C a présente des inclusions de bulles dans les échantillons comme indiqué sur la Figure S8a. En supposant que la chaleur générée lors de la réaction exothermique n'est pas correctement évacuée par les plaques de verre, l'exothermie de la réaction conduit jusqu'au point d'ébullition pendant que le mélange réactif atteint le point de gel. Pour cette raison, différentes tentatives ont été faites afin de contrôler la chaleur générée lors de la réaction et d'améliorer sa dissipation. Les conditions de synthèse optimales ont été atteintes en remplaçant les plaques de moule par des plaques en aluminium et le profil de température (2h à 55°C et 2h à 70°C). Dans ces nouvelles conditions, le PMMA est sous forme rigide, totalement dense et transparent pour des plaques de 5 mm d'épaisseur (Figure S8c).

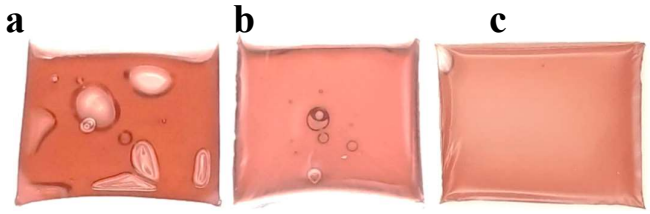


Figure S8. PMMA polymérisé en moule en verre à 55/80°C (a), en moule en aluminium à 55/80 (b) et à 55/70°C (c).

Une fois la configuration optimale définie pour le PMMA, toutes les formulations de copolymères (10, 20 et 30 % en poids de MAA) ont été copolymérisées avec succès en appliquant les mêmes conditions pour donner des échantillons totalement denses et transparents. Ainsi, l'utilisation d'un cadre carré fermé où le mélange réactif était injecté et la réduction de 60% du temps de réaction ont permis une diminution de la masse de monomère évaporé qui a été réduite de 55 à 12% en poids. Une tentative pour augmenter encore le rapport en termes de teneur en MAA a été réalisée en préparant un copolymère PMMA-*co*-MAA à 60 : 40 % en poids, ce qui a malheureusement conduit à une séparation de phases.

Après synthèse, les copolymères ont été entièrement caractérisés. Des analyses RMN ^{1}H ont été effectuées pour définir le rapport des comonomères et la fraction de comonomères résiduels. Les compositions des copolymères pour le rapport MMA:MAA se sont révélées être respectivement de 87:13, 74:26 et 63:37% en moles pour les 10, 20 et 30% en poids de MAA copolymérisés. En outre, le MMA résiduel est inférieur à 1,5% en mole, alors qu'aucune preuve de MAA résiduel n'a été trouvée. Concernant la structure macromoléculaire, sur la base des constantes de copolymérisation rapportées par Krul *et al.* (r_{MMA}=0,84 et r_{MAA}=0,62) et étant donné leur produit <1, il est possible de prédire la formation de la microstructure des copolymères statistiques.

Des distributions monomodales des masses molaires ont été trouvées pour le PMMA et les PMMA-*co*-MAA avec 10 et 20 % en poids de MAA (respectivement $2,6 \cdot 10^6$, $1,3 \cdot 10^6$ et $0,98 \cdot 10^6$ g/mol). Cependant, pour une teneur plus élevée en

MAA (30 % en poids), les valeurs de M_n obtenues se sont révélées bien supérieures à la limite supérieure des colonnes. Il est probable que le M_n soit donc supérieur à la limite de détection des colonnes, ce qui conduit à un temps de rétention trop faible pour être analysé par méthode d'étalonnage. Pour cette raison, le PMMA-*co*-MAA 30% en poids de MAA, M_n a également été évaluée dans le DMF. De manière similaire au THF, M_n à une valeur bien supérieure à la limite supérieure identifiée par la courbe d'étalonnage PS, suggérant que M_n du PMMA-*co*-MAA est supérieur à la limite de détection (égale à $1{,}35 \cdot 10^6$ g/ mole).

La stabilité thermique a été étudiée par TGA pour le PMMA et le copolymère PMMA-*co*-MAA. Le PMMA se caractérise par un mécanisme de dépolymérisation bien connu qui convertit toute la masse initiale en espèces volatiles et n'est pas affecté par la présence d'oxygène comme le suggère le fait que la température des pics de perte de poids principale est identique dans les deux atmosphères. Le mécanisme de dégradation qui se produit pour les copolymères MMA-MAA est décrit dans la littérature. Il a été rapporté que les copolymères PMMA-*co*-MAA libèrent des produits volatils au-dessus de 220°C et les espèces chimiques formées peuvent être différentes selon les chemins impliqués ; dans tous les cas, cette réaction de condensation conduit à la même structure anhydride (Figure S9).

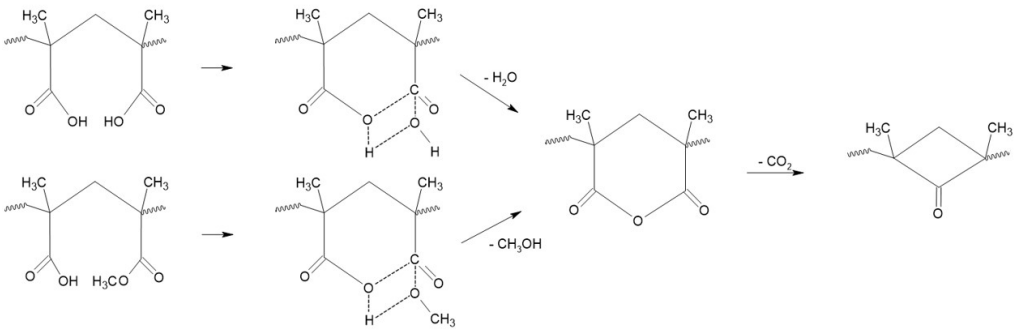


Figure S9. Réaction de formation d'anhydride via un état de transition et décarboxylation des cycles anhydride.

Au-dessus de 300°C, le mécanisme de dégradation fait référence à la décomposition de la structure de l'anhydride qui se produit simultanément au début de la volatilisation du squelette polymère par dépolymérisation. Les cycles anhydride peuvent se décarboniser partiellement, conduisant à la formation d'une fraction plus stable qui sera volatilisée dans des conditions thermo-oxydantes supérieures à 400°C ou à une température plus élevée dans une atmosphère inerte comme le montre l'analyse TGA.

Des recherches plus approfondies sur la structure chimique du copolymère ont été réalisées par spectroscopie infrarouge. Les spectres IR (Figure S10) ont montré tous les pics caractéristiques des groupes méthacrylique. En se concentrant sur la région d'absorption du carbonyle, le pic au nombre d'onde inférieur (1 697 cm^{-1}) peut être attribué aux unités acide, tandis que celui à 1 724 cm^{-1} est lié au groupe ester du MMA. De plus, le pic correspondant au groupe carboxylique présente une intensité directement liée à la teneur en MAA.

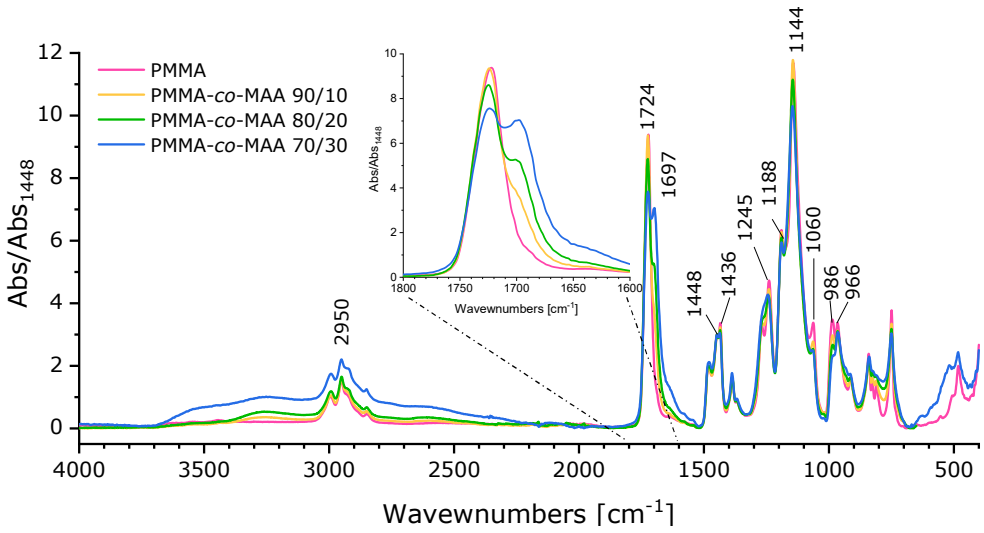


Figure S10. Spectres IR (mode ATR) des copolymères PMMA-*co*-MAA après réaction de copolymérisation avec une teneur en MAA de 0 à 30 % en poids.

Les thermogrammes DSC montrent une T_g unique pour toutes les compositions qui est comprise dans la plage 100 – 150°C et augmente avec la teneur en MAA (Table S1).

Table S1. Valeurs de T_g du PMMA et du copolymère PMMA-*co*-MAA (0-30% en poids de MAA) mesurées sur la deuxième rampe de chauffage du DSC et valeurs théoriques calculées en appliquant l'équation de Fox.

Composition	**T_g DSC (°C)**	**T_g Fox eq.(°C)**
PMMA	100	-
PMMA-*co*-MAA 90/10	113	106
PMMA-*co*-MAA 80/20	134	112
PMMA-*co*-MAA 70/30	150	119

Pour les copolymères, une T_g théorique a été calculée en appliquant l'équation de Fox, cependant les valeurs expérimentales sont supérieures aux prévisions. Afin de prendre en compte la contribution des interactions intermoléculaires, l'équation de Kwei a été utilisée pour ajuster la tendance expérimentale et dériver les paramètres *k* et *q* qui sont respectivement égaux à 1 et 131, en accord avec les valeurs précédemment rapportées par Huang *et al.* pour des mêmes copolymères. La valeur positive du paramètre *q* suggère que les interactions intermoléculaires sont plus fortes que celles d'auto-association, confirmant ainsi la présence de fortes liaisons H formées entre les unités MMA et MAA. La valeur de *k* égale à 1 indique que les deux unités contribuent de manière égale au phénomène de transition vitreuse.

La présence de liaisons H établies entre les chaînes a été prouvée par spectroscopie IR et l'effet correspondant sur la transition vitreuse a été évalué par DSC. À ce stade, l'impact de l'introduction de telles interactions intermoléculaires sur la conductivité thermique a été évalué.

Des conductivités thermiques ont été trouvées égales à 0,209 pour le PMMA et à 0,213, 0,221 et 0,227 $W \cdot m^{-1} \cdot K^{-1}$ ont été mesurées respectivement pour du copolymère avec10, 20 et 30 % en poids de MAA (Figure S11). La légère augmentation observée peut être corrélée à l'ajout d'interactions intermoléculaires plus fortes, c'est-à-dire les liaisons H, aux interactions faibles déjà présentes, c'est-à-dire de vdW. Cependant, malgré la tendance positive observée dans ce système, les incréments (Figure S11) sont limités par rapport à la variation précédente de conductivité thermique associée aux liaisons H inter-chaînes comme montré dans la littérature. L'ajout d'interactions de liaisons H plus fortes à celles de vdW peut ne pas suffire si des nombreuse liaisons H ne sont pas présentes en avec une distribution uniforme.

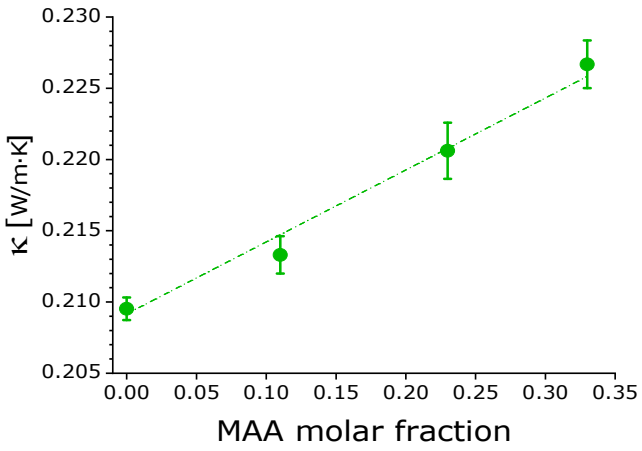


Figure S11. Conductivité thermique en PMMA-*co*-MAA.

La neutralisation du PMMA-*co*-MAA (30 % en poids de MAA) avec 0,2 M de NaOH a été vérifiée par analyse ATR. Le copolymère a été neutralisé avec succès. En effet, le pic des groupements carboxyliques à 1697 cm^{-1} présents dans le copolymère PMMA-*co*-MAA vierge disparaît et un nouveau pic à 1560 cm^{-1} apparaît (Figure S12), qui peut être attribué à l'étirement asymétrique du groupement carboxylate $-COO^-$ du MAA.

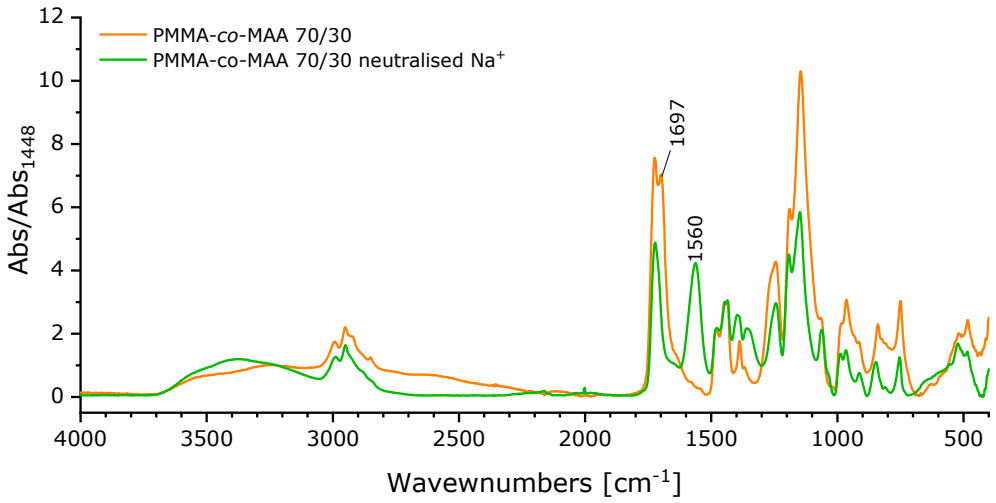


Figure S12. Spectres IR (mode ATR) de PMMA-*co*-MAA vierge et neutralisé avec de l'hydroxyde de NaOH 1 :1.

Le thermogramme DSC montre la présence de deux T_g, 130 et 160°C. La présence d'une seconde transition vitreuse est cohérente avec le modèle de clusters multiplets décrit par Eisenberg et Moore pour les ionomères statistiques. Lorsque la quantité de multiplets dans la matrice augmente et qu'ils commencent à être suffisamment proches pour chevaucher leurs couches de mobilité restreinte. À ce stade, ils créent un cluster qui peut agir comme une deuxième phase indépendante avec une T_g distincte.

Les films neutralisés obtenus après une nuit d'évaporation des solvants ont ensuite été moulés par compression à différentes températures, de 180 à 300°C. Cette étape s'avère indispensable pour réaliser des mesures de conductivité thermique qui nécessitent une grande homogénéité de l'épaisseur du film. Cependant, malgré les nombreuses tentatives visant à augmenter la durée et la température de moulage, il n'a pas été possible d'obtenir un résultat final adapté aux tests. En effet, la présence d'amas semble agir comme des agents de réticulation, ce qui donne lieu à un matériau de type réticulé non transformable.

Comonomères alternatifs : une évaluation de l'influence de la flexibilité de la chaîne sur les propriétés physiques

De nouveaux comonomères (Figure S13) ont été explorés afin de concevoir un système dans lequel les groupements formant des liaisons H sont présents dans une chaîne plus flexible et de surmonter simultanément les problèmes liés à la non-transformabilité du PMMA-*co*-MAA. En particulier, les unités MAA ont été remplacées soit par du méthacrylate de 2-hydroxyéthyle (HEMA), soit par de l'acrylate de 2-carboxyéthyle (CEA). Dans les deux copolymères, il sera possible d'évaluer l'influence de l'ajout d'une chaîne latérale plus longue et l'augmentation conséquente de la flexibilité sur les propriétés finales alors que les liaisons H intermoléculaires sont encore présentes. De plus, dans les copolymères à base de CEA, l'effet d'une flexibilité plus élevée sur un copolymère neutralisé avec une teneur plus élevée en CEA et ses propriétés seront étudiées. Pour les deux cas, les

ratios MMA/comonomère ont été choisis pour avoir le même % molaire que pour le MAA dans le PMMA-*co*-MAA, à savoir à 11, 23 et 33% molaire ce qui correspond à 14, 28 et 39% massique d'HEMA et 15, 30 et 41 % du CEA.

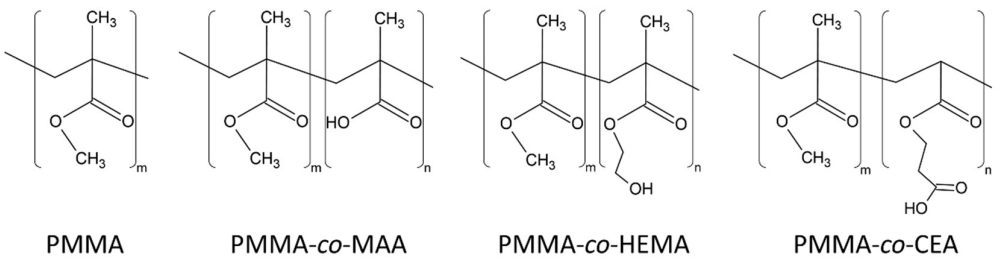


Figure S13. Structure chimique du PMMA et copolymères conçus.

Les copolymères PMMA-*co*-HEMA avec 14, 28 et 39 % en poids de HEMA ont été copolymérisés avec succès (Figure S14) par polymérisation contrôlée par le cobalt en maintenant des conditions de synthèse identiques à celles optimisées pour le PMMA et le PMMA-*co*-MAA.



Figure S14. PMMA-*co*-HEMA 39% en poids d'HEMA provenant d'une polymérisation en masse.

La structure chimique a été étudiée par spectroscopie RMN ^{1}H. Par comparaison avec les spectres du MMA et HEMA purs, on retrouve des monomères résiduels dans le copolymère. Les spectres PMMA-*co*-HEMA sont en accord avec ceux déjà rapportés dans la littérature. Cependant, le calcul des rapports molaires entre les deux comonomères conduit à des valeurs peu fiables, probablement dues à une solubilisation incomplète du copolymère qui se traduit par une intensité incohérente des pics. Les copolymères ne se sont révélés insolubles dans le DMF ne le THF pour tous les ratios MMA/HEMA empêchant la détermination des masses molaires.

L'effet de l'ajout de comonomère HEMA sur la stabilité thermique a été évalué pour les copolymères PMMA-*co*-HEMA. Par rapport au PMMA pur, la dégradation thermique se produit à des températures plus élevées lorsque le comonomère HEMA est ajouté, avec une différence plus significative sous atmosphère d'azote que dans l'air, en accord avec les résultats expérimentaux rapportés précédemment. La décomposition du polymère à base de HEMA comprend deux étapes : 1/la dépolymérisation à basse température qui représente la principale perte de poids, 2/la décomposition de la chaîne latérale ester à plus haute température suite à de multiples réactions.

Pour étudier plus en détail la structure chimique, une spectroscopie IR a été réalisée. Dans les spectres (Figure S15), il est possible d'identifier les pics d'absorption précédemment rapportés pour la structure PMMA. L'ajout de comonomère HEMA entraîne l'apparition d'un large pic entre 3 700 et 3 100 cm^{-1} montrant une intensité plus élevée lorsque la teneur en HEMA augmente de 14 à 28 et 39 % en poids. Ce pic est la superposition de différentes contributions des groupes hydroxyle interagissant par des liaisons H de l'unité HEMA et à l'eau absorbée.

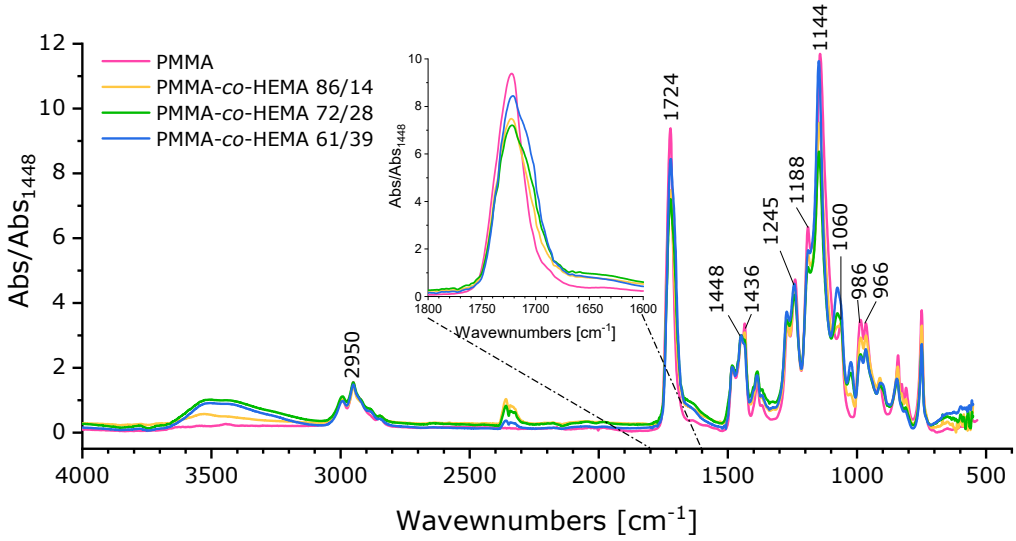


Figure S15. Spectres IR (mode ATR) des copolymères PMMA-*co*-HEMA après réaction de copolymérisation avec une teneur en HEMA de 14 à 39% en poids par rapport au spectre PMMA.

Les thermogrammes DSC montrent une seule T_g pour toute la composition étudiée. Les T_gs extraites sur la deuxième rampe de chauffage sont répertoriées dans le Table S2. Les valeurs diminuent en augmentant la fraction HEMA, de manière cohérente avec la T_g plus faible de l'homopolymère d'HEMA par rapport à celui du PMMA (81°C vs. 100°C).

Table S2. Valeurs T_gs du PMMA-*co*-HEMA (14-39% en poids HEMA) mesurées sur la deuxième rampe de chauffage du DSC et valeurs théoriques calculées en appliquant l'équation de Fox.

Composition	**T_g DSC (°C)**	**T_g Fox eq. (°C)**
PMMA	100	-
PMMA-*co*-HEMA 86/14	91	97
PMMA-*co*-HEMA 72/28	86	94
PMMA-*co*-HEMA 61/39	79	92

Les valeurs obtenues sont légèrement inférieures à celles calculées en appliquant l'équation de Fox (Table S2), en utilisant 100°C pour le PMMA et 81°C pour le PHEMA. Les paramètres d'ajustement *k* et *q*, obtenus en appliquant l'équation de Kwei, se trouvent respectivement égaux à 1 et -51. La valeur *k* égale

à 1 indique que les deux unités contribuent de manière égale au phénomène de transition vitreuse. La valeur négative de *q* indique que les interactions d'auto-association dans des unités similaires sont plus fortes que les interactions intermoléculaires.

Les conductivités thermiques ont été trouvées égales à 0,214, 0,221 et 0,226 $W \cdot m^{-1} \cdot K^{-1}$ respectivement pour 14, 18 et 39 % en poids d'HEMA (Figure S16).

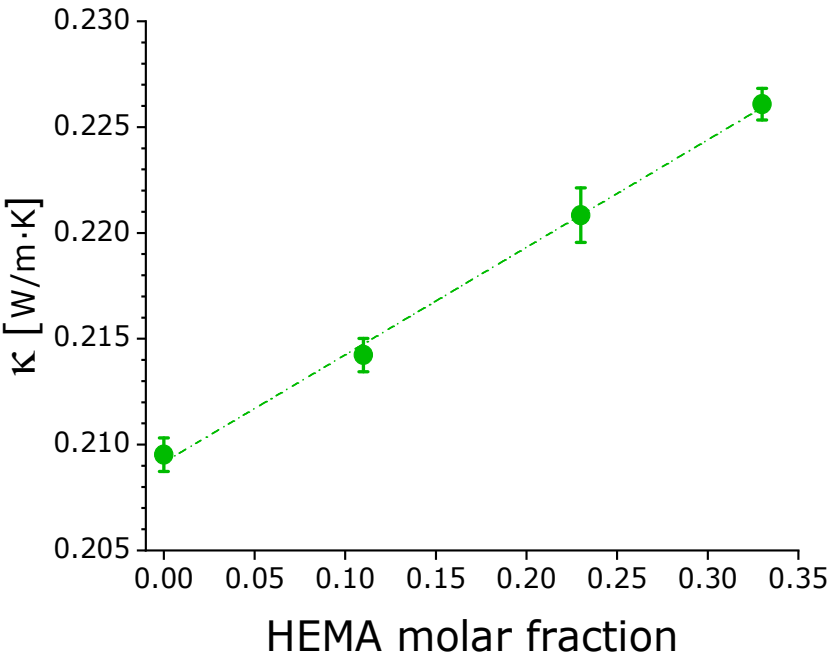


Figure S16. Conductivité thermique en PMMA-*co*-HEMA.

Les résultats de conductivité thermique ne montrent aucune différence par rapport aux copolymères PMMA-*co*-MAA, ce qui suggère que l'ajout d'une chaîne plus flexible dans l'unité de formation de H n'a aucune influence sur la conductivité thermique globale dans les copolymères polyméthacrylate. Il convient de mentionner que, dans ces copolymères, deux effets différents peuvent entrer en compétition : l'introduction de fortes interactions inter-chaînes, c'est-à-dire par liaisons H, et celle d'une chaîne latérale, c'est-à-dire le groupe hydroxyéthyle. Cependant, étant donné la faible longueur de la chaîne latérale introduite dans les copolymères, la contribution négative sur κ devrait être négligeable. Par conséquent, la seule contribution sur la conductivité thermique devrait provenir de l'introduction de liaisons H intermoléculaire.

Les copolymères PMMA-*co*-CEA, 15, 30 et 41 % en poids de comonomère CEA, polymérisés par polymérisation contrôlée par le cobalt en appliquant des conditions de synthèse identiques à celles optimisées pour le PMMA et le PMMA-*co*-MAA, ont conduit à des échantillons rigides avec des bulles piégées dans toute la zone de l'échantillon (Figure S17). Par conséquent, le profil des étapes de température de la synthèse a été modifié afin de supprimer les bulles en contrôlant la surchauffe de la réaction. Cependant, malgré les différentes tentatives pour

modifier les conditions de synthèse, une élimination complète des bulles n'a pas été possible.

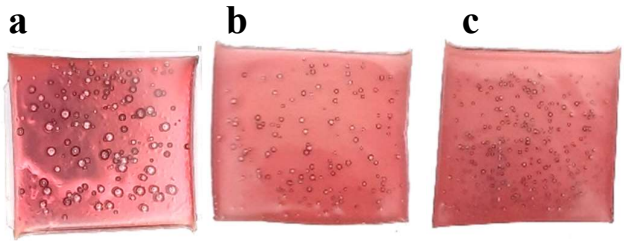


Figure S17. Evolution des bulles pour PMMA-*co*-CEA 59/41wt% traité à 50/60 (A), 30/40/60 (B), et T_{room}/25/30/35/40/45/60°C (C).

La structure chimique après copolymérisation a été étudiée par spectroscopie RMN ^{1}H. Des résidus de MMA et de CEA respectivement de 0,4 % en mole et 1,5 % en mole sont mesure. La composition des copolymères déterminée par RMN ^{1}H pour le rapport MMA:CEA s'est avérée être de 91:9, 78:22 et 67:33 % en moles respectivement pour les 15, 30 et 41 % en poids de comonomère CEA en accord avec les valeurs attendues (11, 23 et 33mol%).

Les masses molaires des copolymères PMMA-*co*-CEA ont été obtenues dans le DMF et sont rapportées dans le Table S3. Par rapport à l'homopolymère PMMA, un M_n inférieur est obtenu lorsque le comonomère CEA est ajouté dans la chaîne. D'après l'indice de polydispersité (M_n/M_w), il ressort également que, pour la plus faible teneur en CEA, la synthèse aboutit à une forte dispersité avec une large distribution des masses molaires. Pour la teneur plus élevée en CEA (41% en poids), la distribution des masses molaires montre un pic non gaussien à un temps d'élution proche de la limite supérieure de colonne.

Table S3. Masses molaires PMMA-*co*-CEA polymérisées en appliquant différents profils de température (PS standards).

Composition	**Temperature profile (°C)**	**M_n (g/mol)**	**M_w/M_n**
PMMA	T_1 (55/70)	261000	1.62
PMMA-*co*-CEA 85/15	T_3 (30/40/60)	32600	9.81
PMMA-*co*-CEA 70/30	T_3 (30/40/60)	12400	2.32
PMMA-*co*-CEA 59/41	T_4 (T_{room}/25/30/35/40/45/60)	-	-

L'effet de l'ajout du comonomère CEA sur la stabilité thermique a été évalué. Par rapport au PMMA pur, la décomposition thermique se produit à une température plus basse lorsque le comonomère CEA est ajouté. De plus, la présence de multiples pics indique que la dégradation a lieu à partir de 200°C et implique un mécanisme beaucoup plus complexe que celui du PMMA. L'apparition d'un petit pic dans la courbe dérivée après la perte de poids principale peut suggérer la formation de structures anhydrides qui se dégradent à hautes températures sous atmosphère inerte par rapport à une structure oxydante, similaire au PMMA-*co*-MAA.

Pour étudier plus en détail la structure chimique, la spectroscopie IR a été réalisée. Dans les spectres (Figure S18), les pics d'absorption précédemment attribués à la structure PMMA sont identifiés. L'ajout du comonomère CEA entraîne l'apparition d'un large pic entre 3 100 et 3 400 cm^{-1} lorsque la teneur en CEA dépasse 30 % en poids. Ce large pic peut être corrélé à la vibration -OH liée à H dans les groupes carboxyliques. En se concentrant sur la région des carbonyles, il est possible de constater un élargissement du pic associé à l'absorption du carbonyle, qui peut être corrélé à la superposition de deux pics, celui du carbonyle dans l'unité MMA et celui de l'unité CEA.

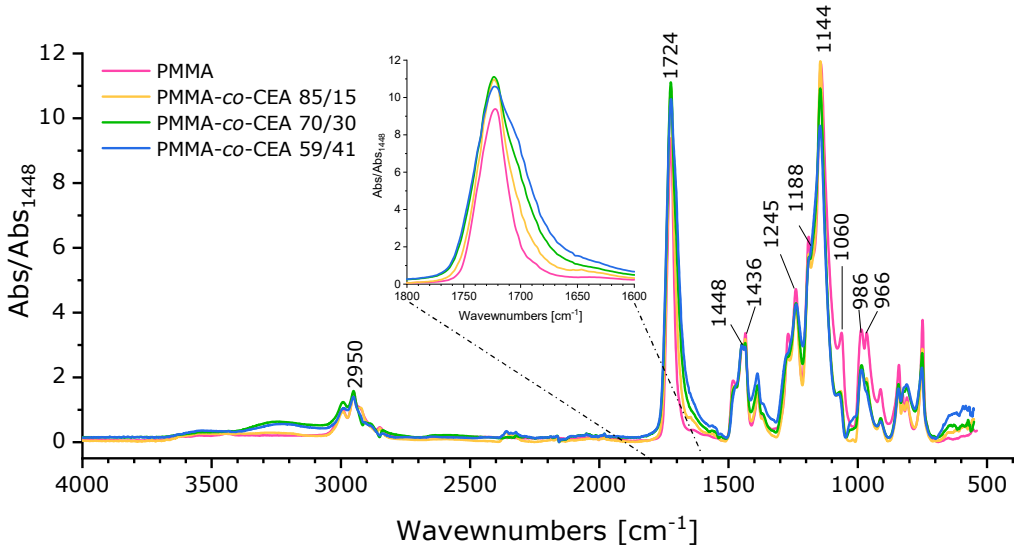


Figure S18. Spectres IR (mode ATR) des copolymères PMMA-*co*-CEA après réaction de copolymérisation avec une teneur en comonomère CEA de 15 à 41 % en poids par rapport au spectre PMMA.

Les thermogrammes DSC montrent une seule T_g qui diminue avec la teneur en CEA. Les données expérimentales et les prévisions de Fox pour les valeurs de T_g sont répertoriées dans le Table S4. Les valeurs théoriques calculées par l'équation de Fox (en utilisant du PMMA à 100°C et 22°C pour le PCEA) surestiment légèrement les valeurs calculées sur la deuxième rampe de chauffage DSC. Cet écart est plus grand pour une teneur plus élevée en CEA.

Table S4. T_g du PMMA-*co*-CEA (15-41% en poids de CEA) mesurées sur la deuxième rampe de chauffage du DSC et valeurs théoriques calculées en appliquant l'équation de Fox.

Composition	**T_g DSC (°C)**	**T_g Fox eq. (°C)**
PMMA	100	-
PMMA-*co*-CEA 85/15	84	86
PMMA-*co*-CEA 70/30	67	73
PMMA-*co*-CEA 59/41	52	64

L'ajustement Kwei de la variation de T_g en fonction du rapport des comonomères a été calculé. Les paramètres d'ajustement k et q se trouvent

respectivement égaux à 1 et -54. La valeur *k*, égale à 1, indique que la T_g est le résultat d'une contribution égale des deux unités. Au lieu de cela, la valeur négative de *q* indique que les interactions d'auto-association sont plus fortes que les interactions intermoléculaires, déterminant une augmentation de volume libre.

La conductivité thermique des copolymères devait être mesurée afin d'étudier l'effet de la flexibilité de la chaîne apportant dans le système des liaisons H et dans un second temps des liaisons ioniques. Cependant, la présence de bulles dans l'échantillon empêche une mesure précise de la conductivité thermique globale.

La neutralisation du copolymère PMMA-*co*-CEA (41 % en poids de MAA) avec 0,3 M de NaOH a été évaluée par analyse ATR. Le copolymère a été neutralisé avec succès. En fait, l'apparition d'un nouveau pic dans la région d'absorption du carbonyle (Figure S19), à savoir à 1572 cm^{-1}, peut être attribuée à un étirement asymétrique de t. Les films obtenus par évaporation pendant 12h du solvant pour le copolymère PMMA-*co*-CEA (15, 30 et 41 % en poids de CEA) et du PMMA-*co*-CEA neutralisé au sodium à 41 % en poids de CEA ont été moulés par compression.

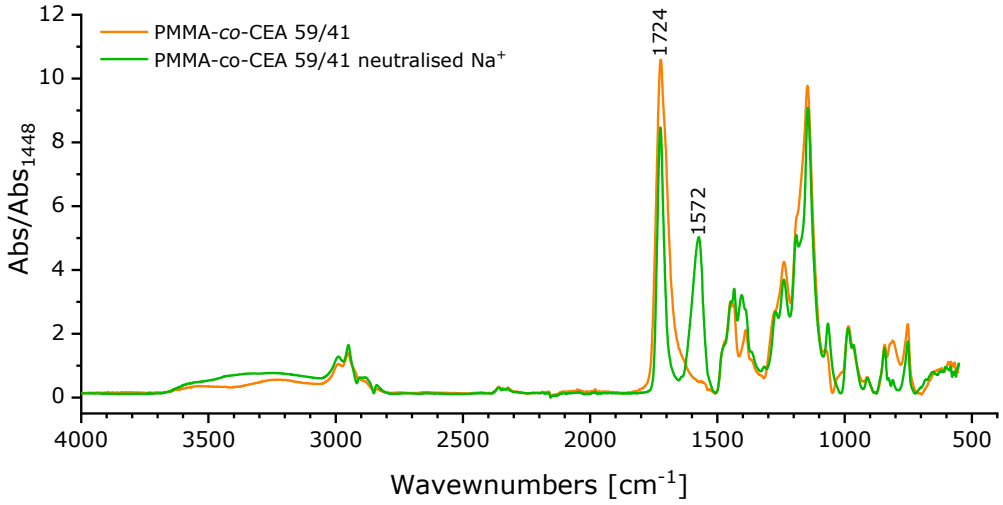


Figure S19. Spectres IR (mode ATR) du copolymère PMMA-*co*-CEA vierge 41% en poids de CEA et neutralisé avec NaOH 1:1.

Les films obtenus par évaporation du solvant pendant une nuit pour le PMMA-*co*-CEA (15, 30 et 41 % en poids de CEA) et le PMMA-*co*-CEA neutralisé par le sodium à 41 % en poids de CEA ont été moulés par compression. Cependant, malgré les différentes tentatives d'optimisation des paramètres du processus de moulage (la température de moulage a été explorée entre 80 et 170°C), l'homogénéité de l'épaisseur s'est avérée encore insuffisante pour effectuer des mesures de conductivité thermique sur film mince étant donné l'exigence d'une variation d'épaisseur <1 µm.

En conclusion, des copolymère PMMA-*co*-MAA ont été préparés avec succès jusqu'à 30 % en poids de MAA et caractérisés. L'ajout de liaisons H aux interactions vdW dans la chaîne polyméthacrylate a été confirmé par la variation de T_g et du spectre IR ainsi que par la valeur des paramètres de Kwei. Cependant, malgré la tendance positive observée pour la conductivité thermique en faisant varier le

rapport des comonomères, l'incrément obtenu s'est avéré limité, comparable à ceux rapportés dans la littérature pour des interactions inter-chaînes similaires. De plus, l'introduction de plus de flexibilité dans la chaîne, c'est-à-dire le remplacement du MAA par du HEMA dans le copolymère, n'a pas montré d'effet sur les valeurs finales de κ. Dans les deux cas, la densité des liaisons H pourrait avoir été insuffisante pour améliorer considérablement le transport thermique. Concernant l'introduction de liaisons ioniques dans le PMMA-*co*-MAA et le PMMA-*co*-CEA, dans les deux cas, la transformabilité des copolymères neutralisés a empêché la préparation d'échantillons adaptés aux mesures de κ.

Nanocomposites polyméthacrylate à base de CNF

Le polyméthacrylate de méthyle (PMMA) a été largement étudié pour la conception de nanocomposites à base de nanocellulose grâce à la transparence optique, la transformabilité, la fonctionnalisation de surface et la nécessité de surmonter sa principale limitation liée à une résistance mécanique insuffisante. Dans les nanocomposites matrice polymère, l'obtention d'une bonne dispersion et l'intensité des interactions interfaciales sont des paramètres-clé pour garantir un effet positif sur les propriétés physique finales. À cette fin, la surface de la cellulose est généralement modifiée chimiquement pour réduire sa polarité de surface. De la même manière, l'introduction des groupement polaires dans les matrices non polaires pourrait être bénéfique pour favoriser les interactions interfaciales. Dans le contexte décrit, une méthode innovante de mise en œuvre par voie solvant pour disperser le CNF dans une matrice polyméthacrylate est présentée dans ce chapitre. Le PMMA-*co*-MAA (30% en poids de MAA) est proposé comme matrice étant donné sa double nature, polaire et faiblement polaire, d'où des fortes interactions matrice-charge est assurée par la présence d'unités d'acide carboxylique capables de former de fortes liaisons H. Les nanofibres CNF sont dispersées par une simple méthode de coulée de solvant dans un mélange de solvants (tétrahydrofurane/eau et tétrahydrofurane/méthanol) assurant simultanément une bonne solubilité de tous les composants et conduisant aussi à une bonne dispersion des CNF (comme le montre les analyses en microscopie multiple). De plus, la présence d'interactions de liaison H peut apporter une contribution supplémentaire aux propriétés finales des matériaux composites grâce à l'établissement de fortes interactions matrice/charge. Cet effet a déjà été rapporté pour diverses propriétés physiques et différents types de polymères. Sur la base de ces résultats, une fois la bonne dispersion des CNF dans le copolymère PMMA-*co*-MAA, une analyse des propriétés physiques du nanocomposite a été réalisée. En particulier, une approche multi-techniques a été utilisée afin de caractériser finement la mobilité macromoléculaire et les processus de relaxations. A partir du PMMA, utilisé comme matériau modèle amorphe simple, l'accent a été mis sur l'effet de l'introduction des comonomères formant des liaisons H (-COOH) dans la chaîne et par la suite de l'ajout dans un tel système d'une nanocharge polaire organique (CNF), afin de définir la combinaison de leurs effets. Enfin, l'effet de l'introduction de nanocharges sur les propriétés physiques telles que la conductivité thermique a été évalué.

Dispersion de CNF dans des matrices copolymères

Le THF est un bon solvant bien connu pour les acryliques, y compris les copolymères PMMA-*co*-MAA. Cependant, le CNF se présent sous forme d'une suspension stable dans un solvant hautement polaire, par ex. l'eau. Le THF pur ne convient pas pour obtenir une bonne suspension. Pour cette raison, des mélanges de solvants ont été étudiés afin de dissoudre ou de suspendre simultanément les deux composants différents, à savoir la matrice moins polaire et les nanofibres polaires. Le PMMA-*co*-MAA s'est avéré soluble dans le mélange THF/eau jusqu'à 23 % en volume d'eau à température ambiante, tandis que la précipitation se produit rapidement pour une teneur en eau plus élevée. De même, le THF et le MeOH sont entièrement miscibles à température ambiante et le PMMA-*co*-MAA s'est révélé soluble dans le mélange jusqu'à une teneur maximale en MeOH de 90 % en volume. Compte-tenu de la forte affinité des CNF pour l'eau, la préparation de films nanocomposites à partir d'un mélange de THF/eau a été explorée pour la première fois. La morphologie du film coulé à partir d'une solution de polymère à 77/23 % en volume de THF et d'eau avec une teneur en CNF de 5 % en poids est rapportée, Figure S20.

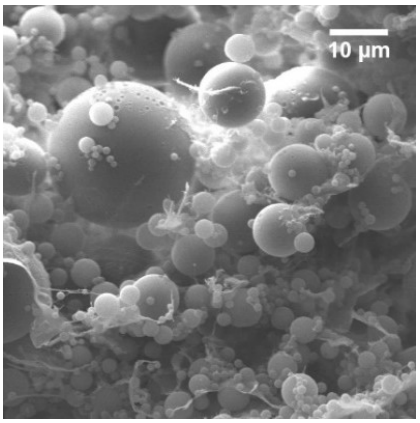


Figure S20. Images SEM (électrons secondaires) du nanocomposite PMMA-*co*-MAA + 5 % en poids de CNF pur évaporé du mélange dans THF/eau à 77/23% en volume.

La surface de fracture montre la présence d'une séparation de phases avec des domaines sphériques allant jusqu'à 25 µm. La morphologie de la matrice copolymère seul a été étudiée en fonction de la fraction d'eau dans le mélange de solvants pour trois cas : à savoir 1/à la limite de solubilité de la matrice, soit dans le mélange 77/23vol%, 2/au point azéotropique d'ébullition minimale à pression atmosphérique, mélange 95/5vol% et 3/en THF pur. Le film de copolymère coulé à partir de la teneur en eau plus élevée (23 % en volume) apparaît stratifié dans deux couches différentes montrant une séparation de phase macroscopique. Pour une teneur en eau plus faible (5 % en volume), la surface de fracture présente une déformation plastique d'une phase homogène. Cependant, à partir d'une analyse plus approfondie, il est possible d'identifier l'apparition de domaines sphériques similaires avec un diamètre allant du nanomètre jusqu'à 3 µm pour les deux rapports explorés. Le film de copolymère obtenu par coulée de solvant à partir d'une solution

à base de THF pur présente une phase unique homogène dans toute la section du film. Nous émettons l'hypothèse que le phénomène de séparation de phases se produit en raison de la grande différence de volatilité des deux solvants (le point d'ébullition est de 66°C pour le THF et de 100°C pour l'eau). Comme le THF a une pression de vapeur plus élevée que celle de l'eau, l'évaporation du mélange de solvants entraîne une augmentation progressive de la concentration en eau dans la solution.

Un mélange de solvants différent a été étudié pour réduire la différence de volatilité des deux solvants. Un mélange THF/méthanol a été sélectionné. Compte-tenu de la différence limitée des points d'ébullition (66,0 vs 64,7 °C, respectivement) et sur la base de la possibilité d'échanger l'eau d'une suspension de CNF avec du MeOH comme décrit précédemment par Roman *et al.*. Avant la préparation du nanocomposite, la morphologie de la matrice pure a été étudiée pour des films coulés à différents rapports THF/MeOH (90, 70 et 50 % en volume de THF). Les surfaces de fracture présentent pour les 90vol% de THF une morphologie homogène caractérisée par la présence d'une déformation plastique et de pores microscopiques issus de l'évaporation des solvants. Des résultats similaires ont été obtenus pour une teneur en THF à 70% en volume. A l'opposé, le film coulé à partir d'une solution 50/50vol% THF/MeOH présente également des pores répartis de manière aléatoire mais deux surfaces de fracture différentes : une fracture fragile pour la couche inférieure de 1 µm d'épaisseur et une couche supérieure de 55 µm d'épaisseur ayant un comportement de rupture différent, c'est-à-dire présentant une déformation plastique locale.

Le processus d'échange de solvant pour la suspension de CNF a conduit à un gel visuellement homogène avec une teneur moyenne en CNF dans le solvant d'environ 1,8 % en poids. L'évaporation du solvant a été faite à 70 °C et aucune trace d'eau n'a été trouvée par spectroscopie IR, ce qui témoigne d'une substitution réussie de l'eau par du méthanol. Une suspension de CNF dans le méthanol a été envisagée pour la préparation de nanocomposites dans une solution THF/MeOH avec un ratio de solvants fixé à 85/15% en volume et différentes teneurs en nanofibres (5, 10 et 15% en poids, Figure S21). Tous les échantillons apparaissent clairement homogènes et présentent une surface de fracture caractérisée par la présence d'une déformation plastique à l'échelle submicronique. Pour toutes les surfaces de fracture, la rugosité particulière de la surface peut être corrélée à la présence des nanofibres dans la matrice. Cependant, il est possible d'identifier des zones plus lisses suggérant que la distribution des CNF n'est pas totalement homogène, en particulier lorsque 10 (Figure S21b) et 15 % en poids (Figure S21c) de CNF sont introduits.

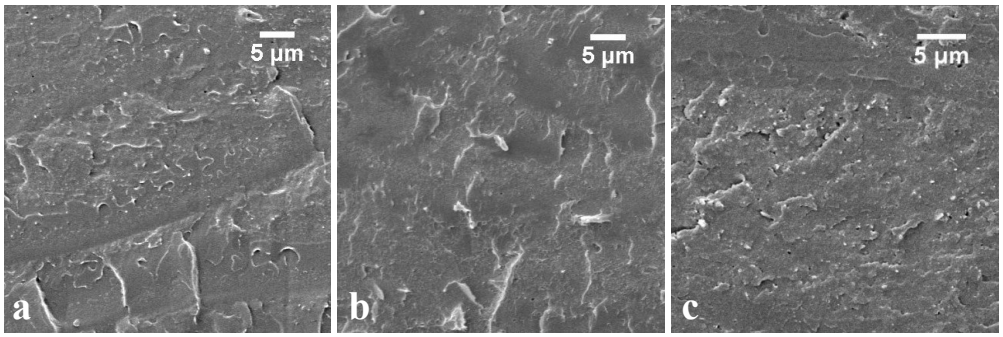


Figure S21. Images SEM de nanocomposites PMMA-*co*-MAA + 5 (a), 10 (b) et 15 % en poids (c) de CNF coulés à partir de solutions THF/MeOH 85/15 % en volume.

La composition intermédiaire (10 % en poids de CNF) a été sélectionnée pour effectuer une enquête plus approfondie combinant plusieurs techniques de caractérisation. La dispersion a été examinée pour deux concentrations différentes de méthanol dans le mélange de solvants, à savoir à 15 et 34 % en volume, la valeur maximale correspondant au mélange azéotropique à pression atmosphérique. Le nanocomposite PMMA-*co*-MAA + 10 % en poids de CNF coulé à partir d'une solution THF/MeOH 85/15 % en volume a été observé avec une résolution plus élevée par FE-SEM (Figure S22a), qui confirme une rugosité de surface particulière qui peut être associée à l'organisation de CNF dispersés au sein du matrice. L'analyse TEM (Figure S22b) a montré une morphologie des zones avec différentes concentrations de CNF. Cependant, dans les zones à concentration plus élevée, les CNF semblent bien dispersés et entourés par le polymère, indiquant de bonnes interactions matrice-nanocharge. Des analyses similaires ont été réalisées sur des films de même composition coulés à partir d'une solution THF/MeOH 66/34% en volume. D'après l'image FE-SEM présentée sur la Figure S22c, la surface de fracture est caractérisée par une déformation plastique submicronique corrélée à la présence des CNF au sein de la matrice. A partir des observations TEM, il est possible de reconnaître certaines zones exemptes de nanofibres présentant une distribution de CNF qui n'est pas homogène (Figure S22d). Cependant, à l'instar du film coulé à partir d'une solution THF/MeOH à 85/15 % en volume, les CNF semblent dispersés et entièrement intégrés dans la matrice.

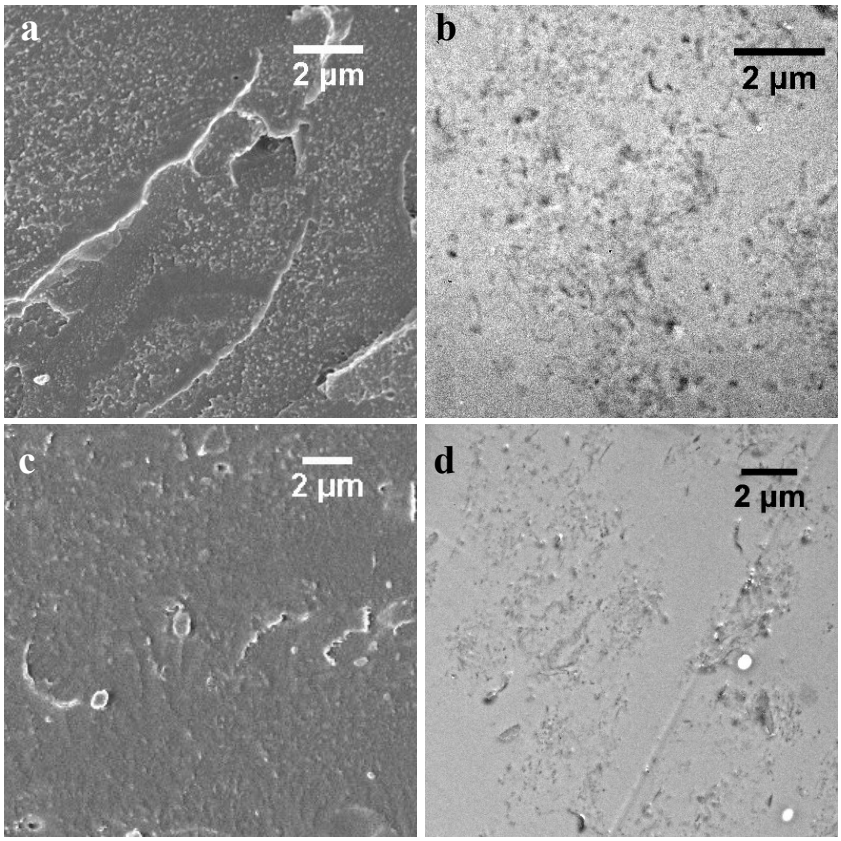


Figure S22. Micrographies FE-SEM (a) et TEM (b) de nanocomposites PMMA-*co*-MAA + CNF à 10 % en poids traités à partir d'une solution THF/MeOH 85/15 % en volume. Micrographies FE-SEM (c) et TEM (d) de PMMA-*co*-MAA + CNF 10 % en poids traitées à partir de solutions THF/MeOH 66/34 % en volume.

De plus, des spectres de transmission UV-visible ont été acquis pour quantifier la transparence des films (Figure S23). Les spectres montrent une valeur élevée de transmission dans toute la gamme de longueurs d'onde pour toutes les compositions avec un minimum à 98,7 %. Les évaluations quantitatives de la transparence des échantillons donnent des résultats de 99,6 % pour la matrice et respectivement de 99,6, 99,5 et 99,1 % lorsque 5, 10 et 15 % en poids de CNF sont ajoutés. Les valeurs confirment la transparence optique dans l'intervalle de longueur d'onde visible pour tous les échantillons.

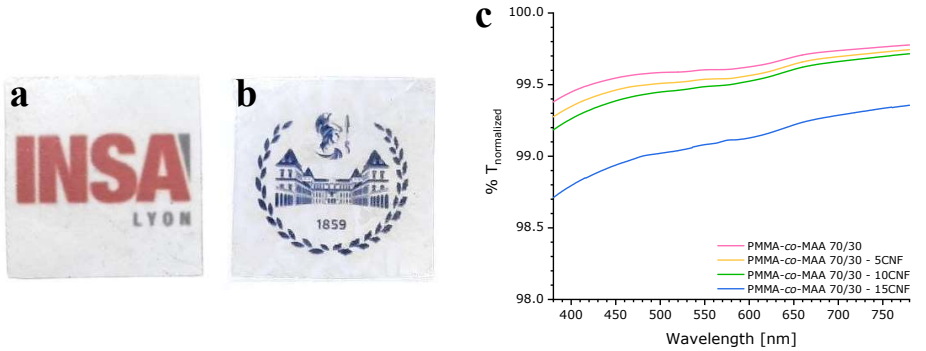


Figure S23. Film transparent de PMMA-*co*-MAA après moulage par compression à 230°C (a) et avec ajout de 10 % en poids de CNF après moulage par compression à 230°C (b). Spectres UV de films moulés par compression de PMMA-*co*-MAA (5, 10 et 15 % en poids de CNF) (c).

Les films PMMA-*co*-MAA ont été analysés par RMN ^{1}H. De nouveaux pics sont identifiés et ne correspondent pas à ceux du copolymère. En fait, les deux pics (1,7-1,8 et 3,6 ppm) correspondent au THF, ce qui suggère que le solvant résiduel du THF est toujours présent, alors qu'il n'y a aucune trace de MeOH (3,2 et 4,1 ppm).

L'évolution possible du copolymère lors du moulage par compression à 230°C a été évaluée par spectroscopie IR réalisée sur des films moulés par compression. Les pics correspondant à la formation de l'état anhydride peuvent être identifie dans le spectre à 1802 et 1760 cm^{-1}, confirmant l'apparition d'une condensation limitée entre les groupes carboxyliques, comme observé pour le polymère seul. Les spectres des nanocomposites montrent de nouveaux pics d'absorption attribués à la présence de CNF dans la matrice : deux pics à 1032 et 1055 cm^{-1} correspondent à la vibration C-O-C, un pic à 1105 cm^{-1} correspondant à l'étirement C-O, et un large pic de 3060 à 3620 cm^{-1} lié à l'étirement O-H. De plus, le copolymère moulé par compression semble être insoluble dans le DMF contrairement à celui tel que synthétisé (c.à.d. sous étape de chauffage supplémentaire). Ce phénomène confirme l'apparition d'une évolution structurale et empêche l'évaluation des masses molaires par SEC. Ces changements sont en accord avec le mécanisme de dégradation thermique décrit précédemment pour les copolymères PMMA-*co*-MAA. En particulier, lors du chauffage, une réaction de condensation peut avoir lieu entre deux groupements carboxyliques conduisant à la formation d'un anhydride.

Influence des CNF sur la dynamique moléculaire

Avant les études de mobilité moléculaire, les changements dans les propriétés des matériaux liés à la préparation du film, en particulier lors du moulage au solvant et du moulage par compression, ainsi que dans la fabrication des pré- et post-films, ont été examinés. L'évolution des masses molaires lors du moulage par compression a été évaluée afin de détecter la présence d'une dégradation thermique par mécanisme de dépolymérisation. Ensuite, des thermogrammes DSC ont été analysés pour définir l'effet des solvants résiduels sur la relaxation primaire. Enfin, des analyses thermogravimétriques ont été réalisées afin d'identifier les pertes de solvants résiduels à plus basses températures. M_n du PMMA moulé après compression a été analysée dans le THF et trouvée égale à $1{,}41 \cdot 10^5$ g/mol. La valeur s'avère légèrement inférieure à celle du PMMA tel que polymérisé ($2{,}61 \cdot 10^5$ g/mol), suggérant que la dégradation thermique commence pendant le moulage. Comme mentionné précédemment, le PMMA-*co*-MAA et les nanocomposites associés se sont révélés insolubles après compression, en raison de la formation d'une structure anhydride.

Les transition vitreuse (T_g) des films de PMMA, copolymères et nanocomposites pressés à 200°C ont été mesurées par DSC. Ces analyses effectuées sur les films montrent une seule T_g dans toutes les formulations analysées et les valeurs sont rapportées dans le Table S5. Pour le film PMMA-*co*-MAA, la T_g se retrouve à 134°C au deuxième chauffage. Cette valeur est nettement inférieure à celle de 150 °C trouvée pour le copolymère vierge. Il convient de mentionner que

la T_g pour le PMMA-*co*-MAA moulé par compression est plus proche de la prédiction de l'équation de Fox (119°C). Ce fait suggère que la réduction par condensation de groupes carboxyliques adjacents peut réduire le nombre de liaisons H intermoléculaires. De plus, l'application de l'équation de Kwei dans le cas d'un film pressé à 230°C conduit à une valeur de *q* égale à 45 pour le copolymère à un ratio 70/30% poids MMA/MAA, ce qui est considérablement inférieur à la valeur trouvée pour le PMMA-*co*-MAA vierge (égal à 131) confirmant une perte partielle des interactions intermoléculaires. Cependant, la valeur positive du paramètre q indique que des liaisons H sont toujours présentes entre chaînes. De plus, l'ajout de CNF dans la matrice PMMA-*co*-MAA 70/30wt% n'a pas d'effet sur sa T_g indiquant que l'ajout de CNF n'influence pas la T_g au deuxième chauffage (Table S5).

Il est à noter que les T_gs définies lors du premier et du deuxième chauffage diffèrent significativement pour toutes les compositions. En effet, une différence de 9 à 34°C peut être observée. Cette différence peut être décrite comme le résultat d'effets plastifiant provenant de la présence d'une fraction résiduelle de solvant. En effet, des traces de THF sont identifiées par RMN dans les films moulés par compression de PMMA-*co*-MAA, comme rapporté ci-dessus, indiquant que l'étape de séchage réalisée lors de la préparation n'est pas en mesure d'assurer une élimination complète du solvant. Une autre contribution peut être attribuée à la présence d'eau absorbée provenant de l'atmosphère, en particulier lorsque les CNF sont ajoutés en raison de leur nature hydrophile. En effet, à partir des analyse DSC, on observe dans tous les cas deux pics endothermiques correspondant à un phénomène d'évaporation. Le premier pic est centré entre 70 et 75°C tandis que le second s'étend entre 100 et 180°C. De plus, le pic apparaissant à plus basse température est sensiblement moins intense que l'autre, sauf pour le PMMA où ils présentent une amplitude similaire. Sur la base de la nature plus volatile du THF par rapport à l'eau (compte tenu de la grande différence de point d'ébullition, 66°C pour le THF et 100°C pour l'eau), les pics peuvent être attribués respectivement au THF et à la désorption de l'eau. Ces résultats sont également en accord avec le fait que le PMMA semble absorber une quantité d'eau mineure par rapport aux autres compositions et explique le ΔT_g le plus faible entre les valeurs obtenues sur la première et la deuxième rampe de chauffage (Table S5). Ceci est cohérent avec la plus faible absorption d'eau attendue de l'unité apolaire, les unités apolaires MMA se caractérisent par une nature hydrophile inférieure par rapport au groupe polaire MAA. Par ailleurs, de la comparaison des T_gs détectées sur les deuxièmes rampes de chauffe, on constate que l'introduction d'unités MAA dans la chaîne PMMA augmente significativement la T_g (environ 30°C) grâce à l'apport de liaisons H intermoléculaires qui peuvent se former entre les groupes carboxyliques des unités MAA. Lorsqu'il s'agit de nanocomposites, l'ajout de CNF ne modifie pas significativement les valeurs de T_g.

Table S5. Événements thermiques identifiés par les analyses DSC et TGA.

	T_g (°C) 1er chauffage	T_g (°C) 2eme chauffage	T_{degrad} (°C) air	T_{degrad} (°C) N_2
PMMA	95	106	372	372
PMMA-*co*-MAA	100	134	420	420
5CNF	101	129	398	412
10CNF	100	130	399	402
15CNF	111	132	398	400

Les résultats d'analyse thermogravimétrique sont rapportés sur les Figure S24.

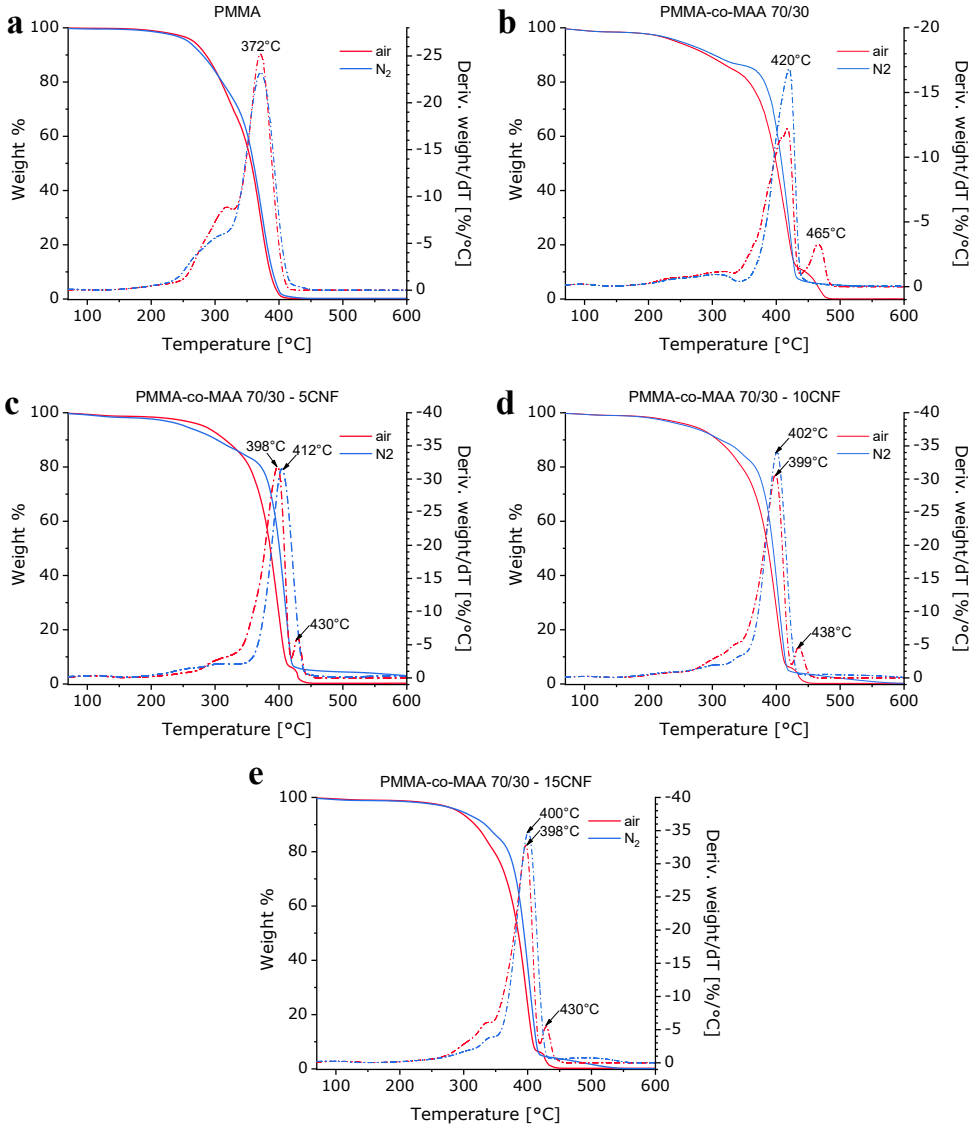


Figure S24. Analyses thermogravimétriques sur films de PMMA (a), PMMA-*co*-MAA (b) et nanocomposite avec 5 (c), 10 (d) et 15 (e) % poids de CNF dans l'air et N_2 (chauffage 10°C/min).

Les thermogrammes de la Figure S24 montrent une première perte de poids à 100°C de l'ordre de 0,3% pour le PMMA et 1% pour les autres compositions attribuées à la désorption de l'eau, confirmant l'hypothèse selon laquelle le PMMA absorbe moins d'eau par rapport aux autres compositions comme suggéré par DSC. A partir des dérivées de perte de masse, il est également possible d'identifier les pics correspondant à la perte de poids principale, associée à la dégradation thermique du squelette polymère. Les températures correspondantes (T_{degrad}) sont répertoriées dans la Table S5.

Le copolymère PMMA-*co*-MAA seul et les nanocomposites associés présentent, à des températures plus élevées, une troisième perte de poids aux alentours de 450°C sous l'air. Les résidus finaux au dessus de 550°C dans l'air sont inférieurs à 0,3% pour toutes les compositions et inférieurs à 0,5% dans l'azote pour tous les films sauf le PMMA-*co*-MAA pur qui laisse un poids résiduel autour de 4%. La dégradation thermique du PMMA et du PMMA-*co*-MAA a déjà été décrite. Ces analyses sont en accord avec les mécanismes de dégradation décrits. Le troisième pic observé sous air dans le PMMA-*co*-MAA seul et les nanocomposites peut être associé à l'oxydation de la fraction stable issue de la structure anhydride. Sur la base des résultats TGA, la plage de température pour la spectroscopie diélectrique a été fixée avec une température maximale inférieure à la T_{degrad} en supposant que les pertes de poids éventuelles étaient limitées à un pourcentage inférieur à 1 % et associées à une perte de solvant résiduel.

Les relaxations du PMMA ont été largement rapportées dans la littérature et quatre types de relaxation ont été observés. A partir de basses températures, la première relaxation rapportée est la δ-relaxation. Elle correspond à la rotation du méthyle présent dans le groupe ester (Figure S25). La deuxième relaxation observée est la relaxation γ attribuée au mouvement non coopératif du groupe α-méthyle lié de manière covalente à la chaîne principale. Certains auteurs ont mentionné que la relaxation γ dépend de l'interaction complexe entre les molécules d'eau et les groupes latéraux polaires, c'est-à-dire les groupes ester du PMMA. Ensuite, la β-relaxation apparaît, qui, dans les polyméthacrylates, est attribuée au mouvement de rotation non coopératif le long de la liaison C-C reliant le groupe ester au squelette de la chaîne. Enfin, apparait la relaxation α, qui correspond au mouvement coopératif des segments de la chaîne polymère, c'est-à-dire à la transition vitreuse dynamique. À des températures plus élevées, la superposition des relaxations α et β peut être observée en raison d'une coopérativité croissante impliquant un nombre augmenté de liaisons de la chaîne principale.

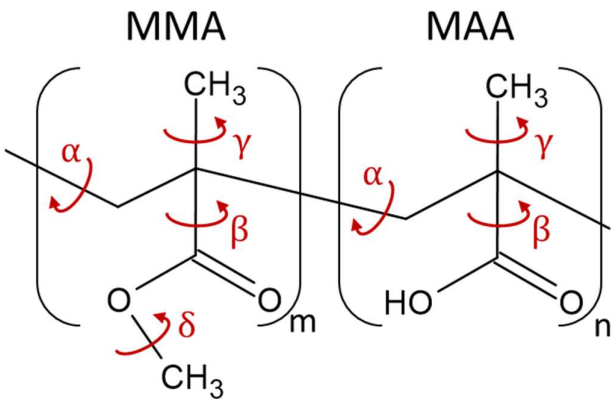


Figure S25. Relaxations moléculaires observée pour un copolymère en PMMA-*co*-MAA.

Des tracés tridimensionnels de la partie imaginaire (ε") de la permittivité diélectrique relative obtenue par spectroscopie diélectrique sont présentés dans la Figure S26en fonction de la température et de la fréquence pour l'homopolymère PMMA, le copolymère PMMA-*co*-MAA et les nanocomposites avec 5, 10 et 15 poids % du CNF.

A basse température, deux relaxations diélectriques apparaissent correspondant aux processus de relaxation secondaires (γ et β). De plus, les tracés 3D des nanocomposites (Figure S26c, d et f) montrent aux basses fréquences une troisième relaxation (β') qui se confond avec la relaxation β aux hautes températures. Pour toutes les compositions observées, à température plus élevée, la relaxation primaire (α) est masquée par la conductivité (σ). Pour cette raison, les données acquises par spectroscopie diélectrique ne seraient pas suffisantes pour caractériser complètement les relaxations présentes dans le système analysé. Ainsi, afin de pallier ce problème lié à la relaxation primaire et réaliser une étude complète de la mobilité macromoléculaire et de ses processus, des analyse mécanique dynamiques complémentaires ont été réalisées dans le but d'accéder aux temps de relaxation indétectables pour spectroscopie diélectrique grâce à l'équation de Havriliak-Negami qui les relie au module complexe.

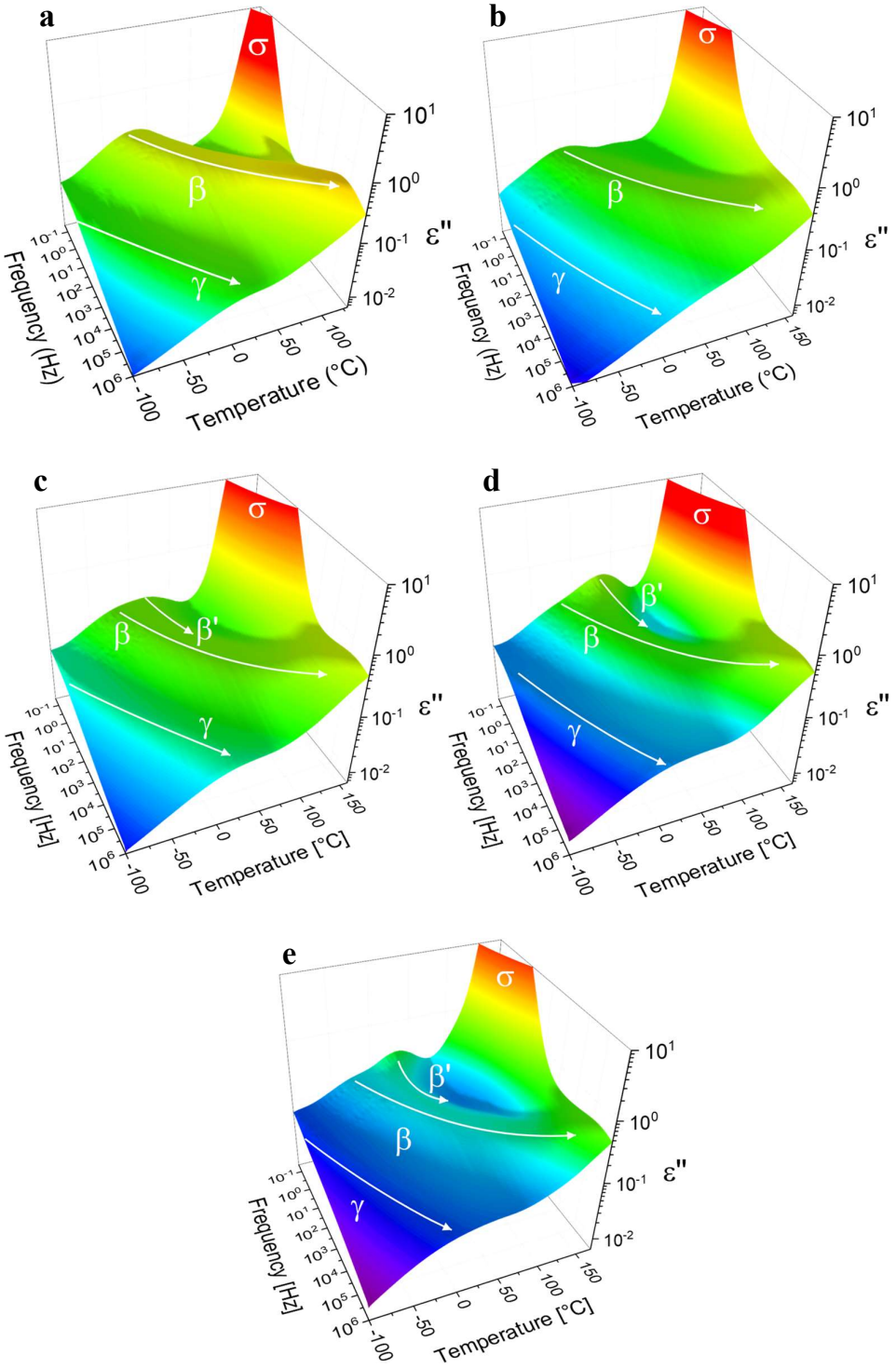


Figure S26. Carte des relaxations diélectriques pour le PMMA (a), le copolymère PMMA-*co*-MAA seul (b) et celui-ci chargé de 5 (c), 10 (d) et 15 % en poids (e) de CNF. Les processus de relaxation sont indiqués par des lignes blanches.

Les relaxations secondaires ont été étudiées par spectroscopie diélectrique. Les temps de relaxation pour les relaxations γ et β ont été obtenus par le modèle de Cole-Cole en ajustant les données complexes de permittivité relative. Il est de plus montrée que les relaxations secondaires dans le polyméthacrylates obéissent à une dépendance avec la température de type Arrhenius.

Les temps de relaxation τ sont tracés en fonction de 1000/T dans le diagramme d'Arrhenius de la Figure S27.

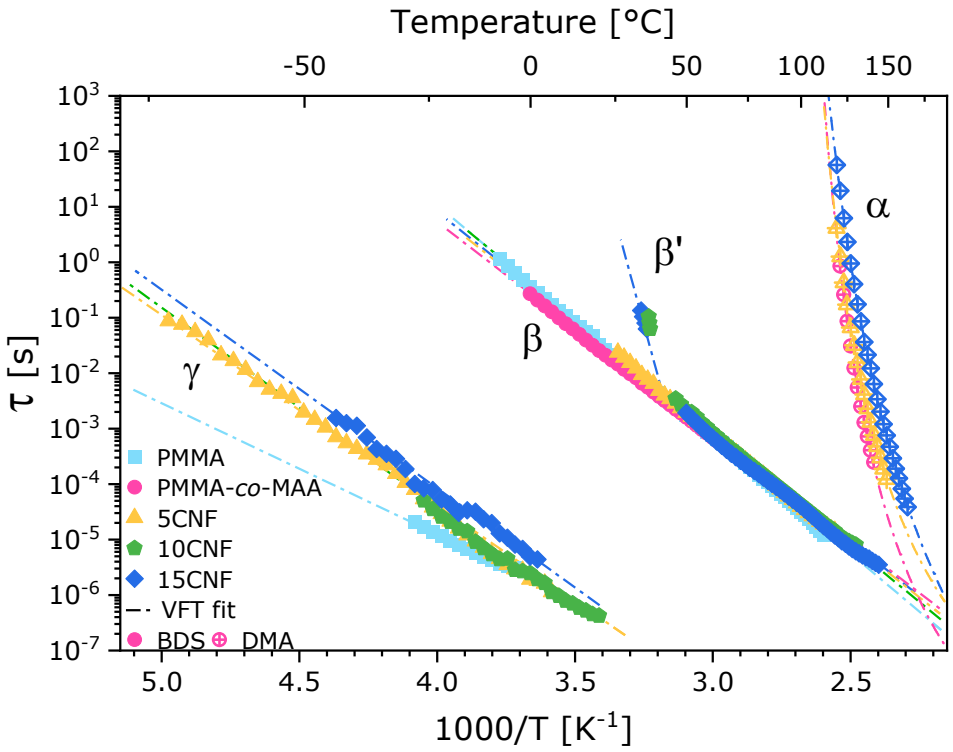


Figure S27. Diagramme d'Arrhénius des processus de relaxations secondaires.

Le PMMA montre une E_a pour la relaxation γ égale à 44 kJ/mol, ce qui est cohérent avec les ~40 kJ/mol rapportés dans la littérature. Dans les nanocomposites, E_a de la relaxation γ est augmentée de 45 % quelle que soit la quantité de CNF. Malheureusement, nous n'avons pas pu déterminer l'E_a de la relaxation γ du copolymère PMMA-*co*-MAA en raison de sa faible intensité le rendant trop intriqué avec la relaxation β. L'hypothèse est que les nombreux groupes hydroxyle présents dans la structure cellulosique peuvent interagir avec l'eau absorbée, empêchant le mouvement derrière le processus de perte déterminant pour conduire à une E_a plus élevée. Le PMMA E_a de la relaxation β s'avère être en bon accord avec les valeurs précédemment rapportées dans la littérature et le copolymère PMMA-*co*-MAA a la même E_a. De plus, une fois que les CNF sont ajoutés au copolymère PMMA-*co*-MAA, un phénomène similaire de chevauchement apparaît sur la majeure partie de la plage de fréquences, mais aux basses fréquences, les deux contributions deviennent des pics distincts.

L'énergie d'activation de la relaxation β' pour le copolymère avec la quantité la plus élevée de CNF (15% en poids) est de 303 kJ/mol. La relaxation β' montrée dans les nanocomposites peut être attribuée à la rotation du groupe ester caractérisé par une E_a élevée en raison de l'effet d'entrave causé par la présence de liaisons H. Ceux-ci peuvent se produire entre les groupes -COOH de MAA et les groupes hydroxyles superficiels de CNF ou les molécules d'eau absorbée. Ainsi, cette

relaxation semble dépendre de la concentration de CNF. En effet, une densité plus élevée de groupes formant des liaisons H caractérise le système lorsqu'une teneur plus élevée en nanofibres est ajoutée. De plus, le caractère hydrophile du CNF peut conduire à une grande quantité d'eau absorbée. Des considérations supplémentaires sur les principaux groupes impliqués dans les obligations H seront discutées plus loin dans l'analyse sur l'assouplissement.

Pour toutes les compositions étudiées, une description complète des processus de relaxations secondaires a été réalisée grâce aux mesures BDS. Cependant, étant donné la conductivité (σ) à haute température, qui masque la relaxation α, une méthode alternative a été utilisée afin d'extraire les temps de relaxation correspondants.

La manifestation mécanique de la transition vitreuse (α-relaxation) a été analysée par DMA grâce à l'application du principe TTS en mettant l'accent sur l'effet de l'ajout de CNF au copolymère. Le modèle Havriliak-Negami a été ajusté sur les courbes maîtresses du module mécanique complexe (E*) afin de déterminer le temps de relaxation à T_{ref}. En se concentrant sur l'ajout de CNF, il en résulte un renforcement mécanique de la matrice qui est clairement observé aux basses fréquences en correspondance du plateau à l'état caoutchoutique qui apparaît dépendant de la teneur en CNF. En effet un effet plus fort est détecté pour les nanofibres les plus élevées.

Les temps de relaxation obtenus sont rapportés dans les tracés d'Arrhenius des Figure S27 et Figure S28.

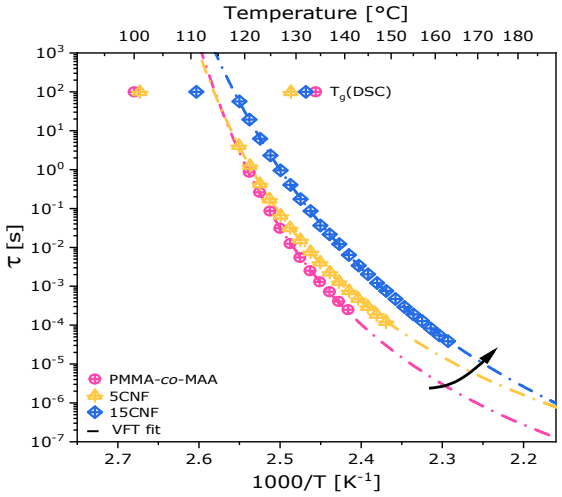


Figure S28. Diagramme d'Arrhenius des relaxations alpha.

Malgré les différences limitées observées pour les T_gs lors d'un deuxième chauffage DSC suite à l'ajout du CNF, il est intéressant de remarquer que l'analyse des temps de relaxation corrélés à la relaxation α est capable de révéler la présence d'un comportement différent. En effet, à même température, le nanocomposite présente un temps de relaxation plus élevé par rapport à la matrice qui augmente avec la teneur en nanofibres. Par conséquent, la présence de CNF et la possibilité d'interactions avec la matrice copolymère via des liaisons H conduisent à une

dynamique moléculaire plus lente de la phase amorphe (PMMA-*co*-MAA). Aussi, la plus grande fragilité des nanocomposites peut s'expliquer par la présence de liaisons H entre les nanofibres et le copolymère qui augmentent la rigidité du système et entravent la mobilité du copolymère.

Conductivité thermique des films minces

Les conductivités thermiques κ mesurées par la méthode du Hot Disk pour couches minces sont reportées dans le Table S6. Le PMMA et le PMMA-*co*-MAA sélectionnés comme matrice (30% en poids de MAA) du nanocomposites ont également été testés afin d'obtenir des valeurs de référence mesurées dans les mêmes conditions. Entre les formulations nanocomposites, κ n'est rapporté que pour les 10 % en poids de CNF. Pour les autres teneurs en CNF, l'inhomogénéité des épaisseurs s'est révélée trop élevée pour permettre l'acquisition d'une valeur fiable.

Table S6. Conductivités thermiques mesurées sur films minces par Hot Disk.

Composition	Épaisseur (µm)	κ ($W \cdot m^{-1} \cdot K^{-1}$)
PMMA	125	0.198
PMMA-*co*-MAA 70/30	150	0.198
PMMA-*co*-MAA 70/30 - 10CNF	195	0.211

D'après l'observation des valeurs du PMMA et du copolymère comme matrice (Figure S29), il est évident que le léger incrément obtenu avec l'ajout de 30 % en poids de MAA est perdu lors du passage de la forme massive à la forme film mince. Cette découverte peut être associée à la formation d'une structure anhydride dans le copolymère film PMMA-co-MAA. Une valeur minimale attendue a été calculée en appliquant le modèle de série et s'est avérée égale à 0,216 $W \cdot m^{-1} \cdot K^{-1}$ pour l'ajout de 10 % en poids de CNF, en utilisant 2,200 $W \cdot m^{-1} \cdot K^{-1}$ pour le CNF tel que rapporté par Adachi avec un seul CNF et 0,198 $W \cdot m^{-1} \cdot K^{-1}$ pour la matrice.

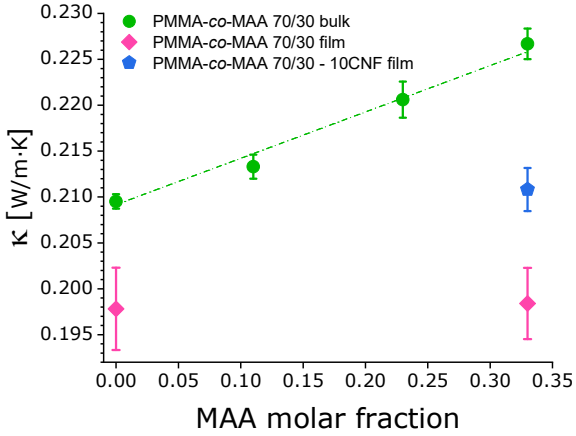


Figure S29. Conductivité thermique des copolymères PMMA-*co*-MAA en vrac et sous forme de films minces en fonction de la teneur en MAA et pour le PMMA-*co*-MAA avec 10% en poids de CNF.

Malgré la présence d'interactions de type liaisons H prouvée par l'apparition d'une relaxation β' dans les mesures BDS, l'ajout de 10% en poids de CNF dans la matrice PMMA-*co*-MAA n'a pas montré d'augmentation significative de κ qui s'est avérée inférieure au minimum valeur attendue. La conductivité thermique du nanocomposite dépendra principalement des valeurs intrinsèque des deux composants mais également de la résistance thermique de contact à l'interface matrice/charge et entre les charges. En supposant qu'une perte au moins partielle des liaisons H soit provoquée par le processus de moulage, la résistance de contact thermique matrice/charge ne sera pas réduite et jouera un rôle déterminant pour empêcher l'augmentation de la conduction thermique globale.

Conclusion

Cette thèse de doctorat s'est concentrée sur la compréhension des relations entre interactions intermoléculaires et propriétés physiques des polymères, dans le but d'adapter ces dernières en modifiant la nature et la densité. En particulier, le rôle des interactions intermoléculaire sur la conductivité thermique a été étudié. Dans les polymères amorphes, l'ajout d'interactions intermoléculaires plus fortes que celles de vdW faibles pourrait conduire à la réalisation d'un réseau thermique continu avec pour conséquence une augmentation de la valeur finale de conductivité thermique. À cette fin, à partir du PMMA, utilisé comme modèle de polymère amorphe simple, des copolymères méthacryliques ont été synthétisé dans lesquels l'introduction d'unité portant du groupement formant des liaisons H, c'est-à-dire des d'acides carboxyliques, conduit à l'ajout d'interactions inter-chaînes de plus forte énergie en comparaison de interactions vdW. De plus, en faisant varier le rapport entre les deux comonomères, un nombre différent de liaisons H est introduit dans la chaîne et l'effet de celui-ci sur les propriétés finales peut être évalué. De plus, la possibilité de neutraliser le groupement -COOH conduisant à l'introduction d'interactions ioniques permet d'explorer l'effet d'interactions encore plus fortes. Les exigences pour la mesure de κ comme propriété de volume en termes d'échantillons à mettre en forme ont guidé le choix de la synthèse vers la polymérisation radicalaire en masse. Trois mécanismes d'activation différents ont été étudiés : BPO, BPO/amine tertiaire et MEKP/Co^{2+}. La première synthèse réalisée à haute température a conduit à des matériaux poreux impropres aux caractérisations. La deuxième synthèse a été conduite à température ambiante, réduisant avec succès l'évaporation du monomère observée dans le premier cas. Cependant, malgré l'obtention de matériaux rigides et denses, la présence de défauts dans les échantillons empêche les caractérisations ultérieures. La dernière méthode de synthèse explorée avec MEKP/Co^{2+} a assuré une formation progressive de radicaux en utilisant un profil de température avec plusieurs étapes isothermes. Le profil de température et la configuration du moule ont été ajustés, conduisant à l'identification des conditions de synthèse optimales. Ensuite, les copolymères statistiques PMMA-*co*-MAA ont été synthétisé avec succès avec une teneur en MAA de 0 (homopolymère PMMA) à un maximum de 30% en poids, des degrés de conversion et des masses molaires élevés. Les copolymères ont ensuite été entièrement caractérisés et, en particulier, l'effet des liaisons H inter-chaînes a été mis en évidence. La présence de liaisons H établies entre les chaînes a été prouvée par spectroscopie IR et par la dérivation des paramètres de Kwei à partir de l'ajustement des T_gs expérimentaux. Enfin, une tendance positive sur la conductivité thermique globale a été confirmée avec l'augmentation de la teneur en MAA. Plus tard, le copolymère PMMA-*co*-MAA 30% en poids de MAA a été neutralisé avec succès avec l'hydroxyde de sodium, conduisant à la présence de cluster ioniques qui ont entraîné l'apparition d'une seconde T_g. Malheureusement, les matériaux neutralisés ne pouvaient plus être mis en forme par moulage-compression, empêchant la mesure de la conductivité thermique sur les films.

Ultérieurement, le comonomère MAA a été remplacé par différents comonomères et l'effet d'une flexibilité de chaîne plus élevée lorsque des liaisons H intermoléculaires sont présentes a été évalué. Les deux comonomères choisis ont été caractérisés par la présence d'un groupe hydroxyle (avec le comonomère HEMA) et d'un groupe acide carboxylique (avec le comonomère CEA) en bout de chaîne latérale éthyle. Dans les deux cas, les ratios MMA/comonomère ont été choisis pour correspondre au % molaire MAA de PMMA-*co*-MAA dans les trois ratios. De plus, dans les copolymères à base de CEA, l'effet d'une flexibilité plus élevée sur les copolymères neutralisés avec une teneur plus élevée en CEA et sur leurs propriétés a été étudié. Les copolymères PMMA-*co*-HEMA ont été efficacement obtenus dans les mêmes conditions de synthèse que le copolymère PMMA-*co*-MAA. Compte tenu de l'insolubilité dans plusieurs solvants, la présence d'une réticulation a été supposée compte-tenu de la présence de monomère diacrylate résiduel dans le HEMA. L'ajustement Kwei a abouti à une valeur négative de q indiquant l'auto-association préférentielle des unités HEMA plutôt que les interactions avec celle du MMA. Les conductivités thermiques se sont alors révélées identiques aux valeurs obtenues pour les copolymères PMMA-*co*-MAA, prouvant l'absence d'effet de la chaîne latérale. Les copolymères PMMA-*co*-CEA obtenus par polymérisation contrôlée par le cobalt ont donné lieu à des matériaux poreux malgré les multiples tentatives d'optimisation du profil de température appliqué. Pour cette raison, les conductivités thermiques globales n'ont pas pu être obtenues. De la même manière que pour les copolymères PMMA-*co*-HEMA, l'ajustement Kwei a abouti à une valeur négative de q indiquant l'auto-association préférentielle entre les groupes fortes par l'unités CEA. Le copolymère PMMA-*co*-CEA avec la teneur plus élevée en CEA a été neutralisé avec succès avec NaOH. Ce groupement latéral entraîne un écoulement en température du copolymère PMMA-*co*-CEA vierge et neutralisé par rapport au copolymère PMMA-*co*-MAA vierge et neutralisé. Cependant, l'homogénéité de l'épaisseur s'avère encore insuffisante pour effectuer des mesures de conductivité thermique sur les films.

Des copolymères PMMA-*co*-MAA 30 % en poids de MAA ont été utilisés pour préparer des nanocomposites à base de nanofibres de cellulose (CNF). La double nature, polaire et non polaire, du copolymère garantis des interactions interfaciales matrice-charge appropriées grâce à la présence d'unités d'acide carboxylique capables de former de fortes liaisons H. La voie de traitement était basée sur la technique de coulée d'une solution en solvant où la dispersion était réalisée à partir d'un mélange de deux solvants afin d'assurer évaporation simultanément la solubilisation du copolymère et la dispersion du CNF. La dispersion des nanofibres CNF dans des films PMMA-*co*-MAA coulés à partir d'un solution THF/eau présente une séparation de phase en raison du taux d'évaporation différent des deux solvants. Afin de procéder avec une approche de mélange de deux solvants, le MeOH a été sélectionné en place de l'eau grâce à son point d'ébullition plus proche de celui du THF et à la possibilité de redisperser le CNF via un processus d'échange de solvant. La suspension de CNF dans MeOH a été obtenue avec succès. Le nouveau mélange de solvants, à savoir THF/MeOH, a été utilisé pour disperser les nanofibres de cellulose dans le copolymère PMMA-*co*-MAA. Compte tenu des

deux solvants sélectionnés, le procédé bénéficie également de leur caractère hautement volatil qui facilite l'élimination des solvants par évaporation. Des films nanocomposites ont ainsi été préparés et coulés pour différents rapports THF/MeOH et la dispersion du CNF a été évaluée par plusieurs techniques de microscopie. Comme le montre la microscopie par transmission, une bonne dispersion de CNF a été obtenue en procédant dans une solution THF/MeOH dans la plage de 85/15 à 66/34 % en volume avec une teneur en CNF allant jusqu'à 15 % en poids. De plus, la microscopie FESEM a montré que les CNF sont intégrés dans la matrice, confirmant de bonnes interactions interfaciales matrice-charge. Ainsi, l'introduction d'un comonomère polaire dans les chaînes PMMA peut assurer une bonne dispersion de charges polaires telles que les CNF dans une matrice polyméthacrylate majoritairement apolaire sans prétraitement de surface des nanofibres ni utilisation d'un compatibilisant comme agent interfacial.

La mobilité moléculaire du PMMA, du copolymère PMMA-*co*-MAA et du copolymère PMMA-*co*-MAA contenant 5, 10 et 15% en poids de CNF a été entièrement caractérisée grâce à la combination de spectroscopies mécaniques et diélectriques. En particulier, grâce à la corrélation entre la description du module complexe mécanique et du temps de relaxation décrit par l'équation de Havriliak-Negami et l'équivalence entre les lois WLF et VFT, il a été possible d'effectuer une caractérisation complète de la relaxation principale α, associée a T_g. Concernant les relaxations secondaires, l'énergie d'activation E_a pour la relaxation β s'est avéré constante pour tous les matériaux analysés. Il est intéressant de noter que les nanocomposites ont montré aux basses fréquences une relaxation β' supplémentaire caractérisée par une E_a près de quatre fois supérieure celle de β. Cela peut résulter d'interactions de type liaisons H entravant la relaxation β des chaînes de la matrice PMMA-*co*-MAA ou d'un mécanisme lié à l'eau déjà décrit pour le PMMA dans la littérature.

Au lieu de cela, un changement significatif a été trouvé pour la relaxation γ en présence de CNF. En fait, l'E_a de la relaxation augmente d'environ 45 % par rapport au PMMA. L'augmentation importante pourrait être corrélée aux interactions entre les -OH superficiels des CNF et les molécules d'eau capables de déterminer les mouvements responsables de la relaxation. La forme du pic a empêché la détermination de E_a pour la matrice, cependant, sa valeur est supposée être intermédiaire entre le PMMA et le nanocomposite étant donné sa nature liée à l'eau.

Des analyses spectroscopiques DMA ont été utilisées afin d'évaluer l'effet de l'ajout de CNF sur la relaxation principale du PMMA-*co*-MAA. Les courbes maîtresses ont montré que la présence des nanofibres entraînait un renforcement mécanique de la matrice dans le domaine caoutchoutique (plateau) en fonction de la teneur en CNF. De plus, l'analyse des temps de relaxation pour les relaxations α a révélé l'effet des CNF. En effet, malgré des T_gs similaires pour la matrice et les nanocomposites, leurs temps de relaxation sont apparus plus élevés suite à l'ajout de CNF. Ces résultats suggèrent que la possibilité d'établir des liaisons H matrice/nanofibre entraîne une dynamique moléculaire plus lente.

Enfin, l'effet de l'ajout de CNF sur la conduction thermique a été évalué et la conductivité thermique a été mesurée pour des films de PMMA, PMMA-*co*-MAA

(30% en poids de MAA) et avec l'ajout de 10% en poids de CNF. Des valeurs κ identiques ont été déterminées pour le PMMA et le PMMA-*co*-MAA, montrant que l'élimination des liaisons H intermoléculaire en raison de la formation d'anhydride dans le copolymère entraîne une perte de contribution positive à la conduction thermique. Dans la formulation nanocomposite, malgré la présence d'interactions de liaisons H prouvées par l'apparition d'une relaxation β' par mesures BDS, l'ajout de 10% en poids de CNF dans la matrice PMMA-*co*-MAA n'a pas montré d'augmentation significative de κ. À l'instar de l'observation proposée pour le PMMA-*co*-MAA, la formation d'une structure anhydride a également été observée dans les films nanocomposites, entraînant une réduction de la densité de liaisons H. Considérant que le nanocomposite κ dépendra principalement du κ intrinsèque des deux composants mais aussi de la résistance de contact thermique à l'interface matrice/charge et entre les charges, les liaisons H présentes dans le nanocomposite ne sont probablement pas suffisantes pour réduire le contact thermique de résistance à l'interface empêchant l'augmentation de la conduction thermique globale.

Sur la base des résultats obtenus dans cette thèse, les améliorations de la conductivité thermique obtenues par la modification des interactions entre les chaînes dans les matrices amorphes restent un défi extrêmement complexe. Alors que l'amélioration de l'interconnexion entre les chaînes de polymères et l'inclusion d'une fraction modérée de CNF hautement cristallin devraient généralement fournir des canaux supplémentaires pour le transfert de chaleur dans la structure du polymère, le changement des états conformationnels et les phénomènes de diffusion de phonons associés semblent dominer les performances d'échange thermique. Quoi qu'il en soit, une compréhension fondamentale du phénomène reste d'un grand intérêt puisque ce n'est que grâce à une description précise du mécanisme qu'il sera possible de concevoir un système à base de polymère avec des propriétés thermiques améliorées. Par conséquent, des interactions similaires peuvent être explorées dans des matériaux polymères ayant une meilleure aptitude au traitement permettant la préparation d'échantillons caractérisés par une qualité supérieure, c.-à-d. une épaisseur homogène. Dans le même temps, différentes techniques de mesure ayant d'autres exigences en termes de forme et de dimensions de l'échantillon pourraient être envisagées, par example 3-ω méthode qui permet d'analyser de films plus minces.

FOLIO ADMINISTRATIF

THESE DE L'INSA LYON, MEMBRE DE L'UNIVERSITE DE LYON

NOM : CAVALLO DATE de SOUTENANCE : 01/12/2023

Prénoms : Valentina

TITRE : Tailoring intermolecular interactions in methacrylate-based copolymers and nanocomposites: Effect on molecular dynamics and thermal properties

NATURE : Doctorante Numéro d'ordre : 2023ISAL0103

Ecole doctorale : ED MATERIAUX DE LYON

Spécialité : Matériaux

RESUME : Une corrélation entre l'intensité et la nature des interactions intermoléculaires et les propriétés physiques, comme la conductivité thermique, a été rapportée pour des polymères amorphes. En particulier, une augmentation de la conductivité thermique a été associée à l'ajout d'interactions plus fortes par rapport aux liaisons de Van der Walls faibles, c'est-à-dire des liaisons hydrogène et ioniques. Dans ce travail, une tentative d'adapter la conductivité thermique dans les polymères amorphes a été réalisée par ingénierie des interactions intermoléculaires. Le poly(méthylméthacrylate) PMMA a été utilisé comme modèle et des copolymères poly(méthylméthacrylate-*co*-acide méthacrylique) (PMMA-*co*-MAA) ont été synthétisés par copolymérisation radicalaire afin d'introduire des liaisons H inter-chaînes et, après neutralisation, des liaisons ioniques. Des copolymères ont été obtenus avec succès jusqu'à 30 % en poids de MAA et caractérisés. Différents comonomères ont été utilisés pour évaluer l'influence d'une unité flexible apportant des liaisons H, le 2-hydroxyéthylméthacrylate (HEMA) ou le 2-carboxyéthylacrylate (CEA). La conductivité thermique a légèrement augmenté en augmentant la teneur en MAA et HEMA, tandis que pour les copolymères CEA, la présence de défauts a empêché la mesure. Le copolymère PMMA-*co*-MAA a été utilisé comme matrice pour les nanocomposites à base de cellulose afin d'adapter la compatibilité des charges, grâce à la présence de liaisons H entre l'unité MAA et la surface de la cellulose. Des nanofibres de cellulose (CNF) jusqu'à 15 % en poids ont été efficacement dispersées par coulée de solvant dans un mélange de deux solvants (tétrahydrofurane/méthanol). La conduction thermique n'a montré aucun changement significatif après l'introduction des CNF. L'analyse mécanique dynamique (DMA) et la spectroscopie diélectrique à large bande (BDS) ont été utilisées en combinaison pour caractériser pleinement la dynamique moléculaire du PMMA-*co*-MAA copolymère suite à l'introduction de liaisons H inter-chaînes et à l'ajout ultérieur de CNF.

MOTS-CLÉS : methacrylate copolymer, thermal conductivity, interchain interactions, cellulose nanofibers, nanocomposites, macromolecular mobility

Laboratoire (s) de recherche : IMP - Ingénierie des Matériaux Polymères (UMR5223)

Directeur de thèse: Prof. PRUVOST Sébastien

Président de jury : LACABANNE Colette

Composition du jury :

LACABANNE, Colette	Professeure	Université Toulouse 3	Examinatrice
HERNANDEZ SANTANA, Marianella	Professeure	Instituto de Ciencia y Tecnología de Polímeros	Rapporteuse
LO RE, Giada	Professeure	Chalmers University of Technology	Rapporteuse
PRUVOST, Sébastien	Professeur	INSA Lyon	Directeur de thèse
GERARD, Jean-François	Professeur	INSA Lyon	Co-directeur de thèse
FINA, Alberto	Professeur	Politecnico di Torino	Co-directeur de thèse